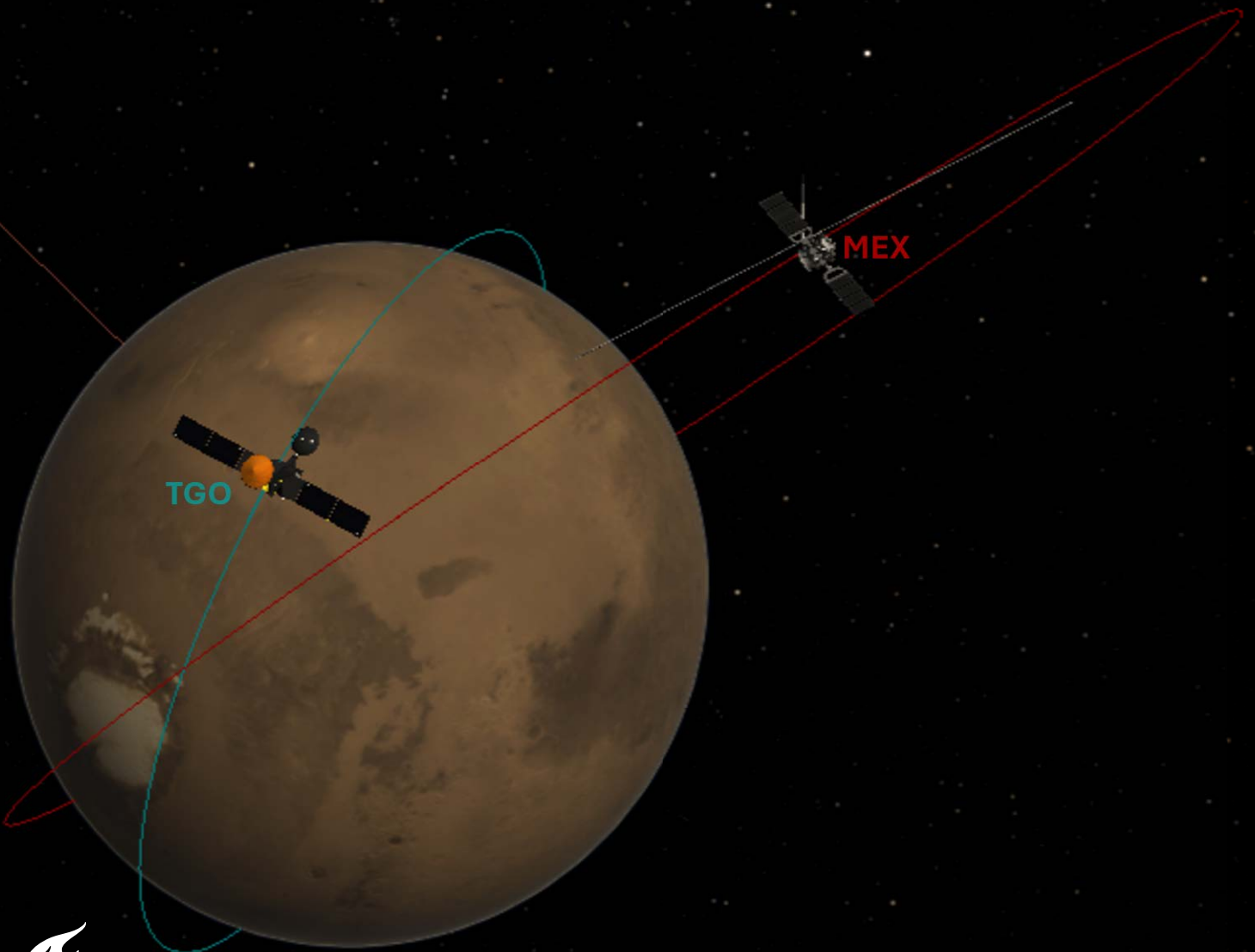# MSc Thesis

Probing shallow subsurface water on Mars through bi-static radar measurements at UHF wavelengths

Dominique Julianne Nieuwenhuizen

MEX

TGO

TUDelft

MSc Thesis

Probing shallow subsurface water on Mars through bi-static radar measurements at UHF wavelengths

by

Dominique Julianne Nieuwenhuizen

to obtain the degree of Master of Science at the Delft University of Technology,
to be defended on the 25th of September, 2025

An electronic version of this thesis is made available at https://repository.tudelft.nl/

TUDelft

Preface

After a little over six years, this thesis officially marks the end of my time at the Delft University of Technology's Faculty of Aerospace Engineering. As my BSc thesis took me to our neighbor Venus, it was only fitting to come full ~~circle~~ orbit for my MSc thesis and also visit our other neighbor: Mars. However, as I traversed this 'journey' through the (inner) Solar system, I held base living in Delft, and briefly Berlin, getting acquainted not only these with amazing cities or the beautiful universe around us, but also the person I see in the mirror. Looking back, I can say there were many (tough) lessons to be learned, wonderful people to meet and of course dreams to be progressed, and I would like to thank all those who have been there to support me along the way.

First of all, I would like to thank Håkan Svedhem for laying the foundation for the MEX-TGO BSR research, and even more so his role as my supervisor, helping me brainstorm through this branch of research which was initially so foreign to me. I would like to also express my gratitude to Bert Vermeersen for supporting the administrative side and attending the nerve-wracking official TU Delft meetings, as well as Wouter van der Wal and Bart Root for taking part in my thesis assessment committee.

My thanks also goes out to the people at ESA ESAC, specifically Alejandro (Alex) Cardesin-Moinelo for the MEX-TGO BSR measurement planning and Alfredo Escalante Lopez for providing his equal-emission code and insights to using SPICE. Additionally, I want to thank Jacob Parrot at ESA ESTEC for his assistance in decrypting and interpreting the AGC data for the BSR measurement processing.

On the personal side, my deepest gratitude goes out to my family and friends for their continuous support throughout the entirety of my studies, and especially the thesis.

Dear friends, thank you for being there during both minor and major bumps along the road. Whether it was by having meals together, listening to a passionate monologue on the latest encountered inconvenience during a coffee break, or just taking a walk around the faculty. Thank you for the distraction, the much-needed social interaction, support, but most all for simply being there with your friendship.

Thank you to my family, most of all for reminding me whenever I came home feeling overwhelmed and under-performing that: *"Je kan niet meer doen dan je best"*. The only reason I have been able to do so both in the years before and those during my studies is because of you, and I am forever grateful for that.

Lastly, a thank you to the reader. I hope this work provides you with some new insight or inspiration of your own, maybe even taking part in the continuation of the MEX-TGO BSR shallow subsurface water ice research!

Dominique Julianne Nieuwenhuizen
Delft, September 2025

Summary

In the early 70s, Mariner 9 made history as the first spacecraft (S/C) to orbit another planet [162], opening humanities' eyes to Mars and leading scientists to hypothesize over its (aquatic) history [7, 25, 63, 99, 126]. Current consensus dictates shallow subsurface water ice to be present from the poles to ±40° latitude, but presence at mid- to equatorial latitudes is debated [96] and correlation between different measurements, particularly at shallow depths, is poor. The aim of this MSc thesis, titled "Probing shallow subsurface water on Mars through bi-static radar measurements at Ultra High Frequency (UHF) Wavelengths", is to assess the feasibility of utilizing Bi-Static Radar (BSR) measurements between Mars Express (MEX) and the ExoMars Trace Gas Orbiter (TGO) for Martian subsurface water (ice) research. The research objective states:

Compare current knowledge, particularly the Gamma-Ray Spectrometer (GRS) and Fine Resolution Epithermal Neutron Detector (FREND) maps, on shallow subsurface water ice at mid to equatorial latitudes on Mars

by

planning, performing and processing Bi-Static Radar (BSR) measurements between the Mars Express (MEX) and the ExoMars Trace Gas Orbiter (TGO) spacecraft, using numerical simulations of the Martian subsurface

The MEX-TGO BSR dual-S/C setup (Figure 1) allows for global access and a much less restricted observation geometry compared to Earth-based receivers [24, 129]. MEX transmits a continuous signal with its lander relay antenna (requiring no new dedicated instrument) at Ultra High Frequency $f = 437.1 MHz$ in conventional nadir-pointing attitude, probing only a few metres into the Martian subsurface, shallow depths which cannot be mapped by conventional low-frequency radar. The signal is partially absorbed and reflected, yielding an echo that is dependent on the average permittivity affected by the presence water ice (and even more so liquid water). TGO receives the echo and measures its Automatic Gain Control (AGC) value, which can be directly related to the received signal power [156], determining water (ice) content by pure amplitude analysis.
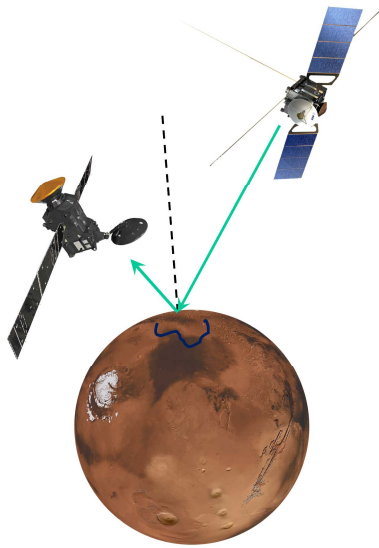
Figure 1: MEX-TGO BSR measurement via the Martian subsurface

To attain the objective; the following research questions (RQ) are defined:

- **RQ1:** When can the best bi-static radar measurements be performed between MEX and TGO?
  - RQ1.1: Which regions fit the interest of past and future missions?
  - RQ1.2: What are the relevant selection criteria for quality measurements?
  - RQ1.3: How can MEX-TGO BSR measurements be modelled?
- **RQ2:** How can bi-static radar measurements be processed to retrieve the amount and form of H_2O?
  - RQ2.1: How does the received signal amplitude depend on the sampled area's dielectric constant?
  - RQ2.2: How does the dielectric constant depend on water and other constituents of the subsurface?
  - RQ2.3: What is the confidence level of the MEX-TGO BSR results?
- **RQ3:** How do processed MEX-TGO BSR results match the state-of-the-art scientific knowledge?

The research is divided into three phases: The literary background of Martian water research and how MEX-TGO BSR complements this, measurement planning and performing, and lastly, modelling and data analysis.

Phase 1: 'History and Water Presence' & 'Humanity's Exploration of Mars'

Unlike its current state, early Mars is believed to have been a warm paradise, with river valleys and a thick atmosphere [67, 128]. At present, the thin (primarily CO_2) atmosphere causes water (ice) to instantly vaporize/sublimate at the surface, making it cold, dry and arid [128], limiting water supplies to:

- **(Non-)polar ice:** Subsurface water ice (especially at high latitudes) and polar layered deposits
- **Atmospheric water vapor and adsorbed subsurface water:** Exchanged diffusively on a seasonal basis
- **Hydrated mineral deposits:** A global abundance of minerals altered by aquatic activity

Mars is the single most explored planet inside the Solar system (aside from Earth), and water (ice) research has been performed both from orbit and in-situ. The most relevant measurement methods are:

- **Neutron spectroscopy:** Mars lacks protection from a magnetic field or thick atmosphere and is consistently bombarded by Galactic Cosmic Rays (GCR) [94, 95]. These interact with its shallow subsurface constituents, particularly hydrogen [49, 95], causing emission of fast/(epi)thermal neutron fluxes and gamma rays [15, 94, 127]. Thus, by mapping neutron emissions the wt% of water the subsurface contains if all detected hydrogen is present as H_2O can be derived, i.e. the Water Equivalent Hydrogen (WEH) level [96].

- **Radar sounding:** Radar instruments come in one of two types: Mono-static (co-located transmitter and receiver; such as MARSIS (Mars Advanced Radar for Subsurface and Ionosphere Sounding) and SHARAD (Mars SHAllow RADar sounder)) or bi-static (the transmitter and receiver are not co-located; as for MEX-TGO BSR). The transmitter transmits radio pulses or a continuous radar signal [73, 108]. After subsurface reflections have taken place, the receiver captures the echo and from the data, discontinuities in the dielectric constant can be identified, resulting from the compositional and structural change inflicted by water (ice) layers [108], allowing a direct measure of water (ice) content variations.

The most relevant prior missions for shallow water deposits (deep water has been studied extensively by MARSIS and SHARAD), which are to be correlated with MEX-TGO BSR, are both neutron spectrometers:

- The **Gamma-Ray Spectrometer (2001 Mars Odyssey)** was the first to globally map the Martian subsurface hydrogen abundance [15, 127], yielding maps such as shown in Figure 2. It located large non-polar water ice deposits, scattered in the mid-latitudinal to equatorial region, varying in concentration [49, 50, 95].

- The **Fine Resolution Epithermal Neutron Detector (ExoMars Trace Gas Orbiter)** maps WEH levels in the shallow subsurface at high spatial resolution to allow for identifying local hydrogen-rich areas, correlate with local topography and study landing sites [86, 94, 96, 97]. Global FREND data is shown in Figure 3, largely consistent with GRS, but noting higher local concentrations, e.g. at the Valles Marineris.
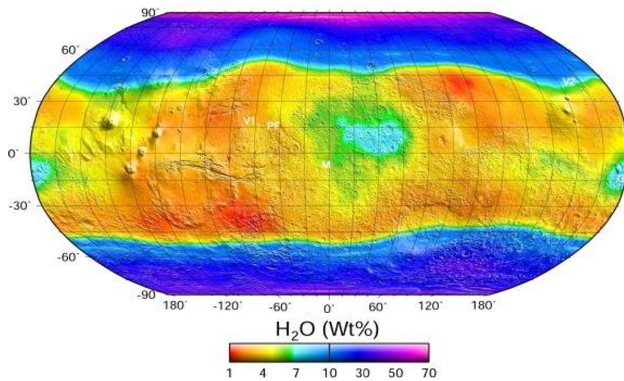

Figure 2: Global map of water (ice) in the Martian subsurface based on GRS data, retrieved from Martin [90]
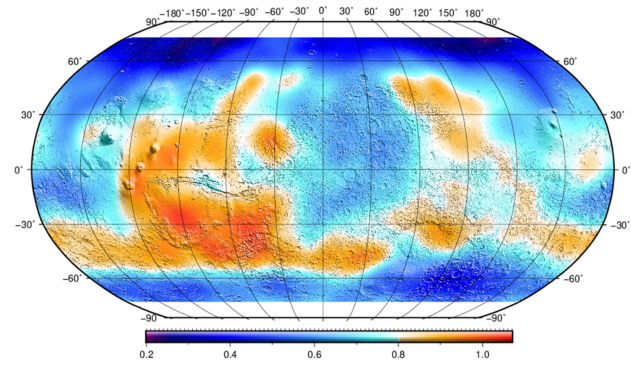

Figure 3: Global map of water(ice) in the Martian subsurface based on FREND data, retrieved from Svedhem [144]

Phase 2: 'MEX-TGO Bi-Static Radar Targets' & 'Measurement Planning'

MEX-TGO BSR targets are defined to complement prior (near-equatorial) research, and mapped in Figure 4 along with the specular point tracks for all performed BSR measurements. These are the equal-emission points of highest expected reflection, i.e. the points on the mean Martian surface where the incidence and reflection angles are equal, and the surface normal and vectors to both S/C all lay in-plane. The campaigns include:

- **Non-ideal measurements:** BSR campaign 1 follows from the MEX-TGO Mutual Occultation experiment, as during MTP257/76 (Medium Term Plan; MTP 257 for MEX and MTP 76 for TGO) measurements were performed at the incorrect switch-ON time, causing the signal to reflect via the surface. BSR campaign 2 contains two additional non-ideal measurements in MTP272/91, only requiring a closest pass ≤1000 km.

- **Ideal measurements:** For the ideal measurements, a Python model, employing SPICE[1], constrains feasible measurement geometries and target location coverage. For July 2025, eight measurement opportunities were identified with a well-spread ground track distribution and relatively favorable geometry. For August 2025, seven less favorable measurement opportunities were identified. The opportunities were requested from the ESA European Space Astronomy Centre (ESAC) and ultimately, one opportunity was accepted, designated BSR campaign 3. Other opportunities were in conflict with lander visibility periods [21, 22], thus an alternative non-ideal measurement was included in MTP277/96 [22]: BSR campaign 4.

Overall the model is deemed a good first iteration, but requires further development. Lander visibility periods should be included and requirements should be re-quantified/defined, most importantly characterizing the upper equal-emission angle bound to limit scattering effects and lower bound to limit LHCP conversion effects.

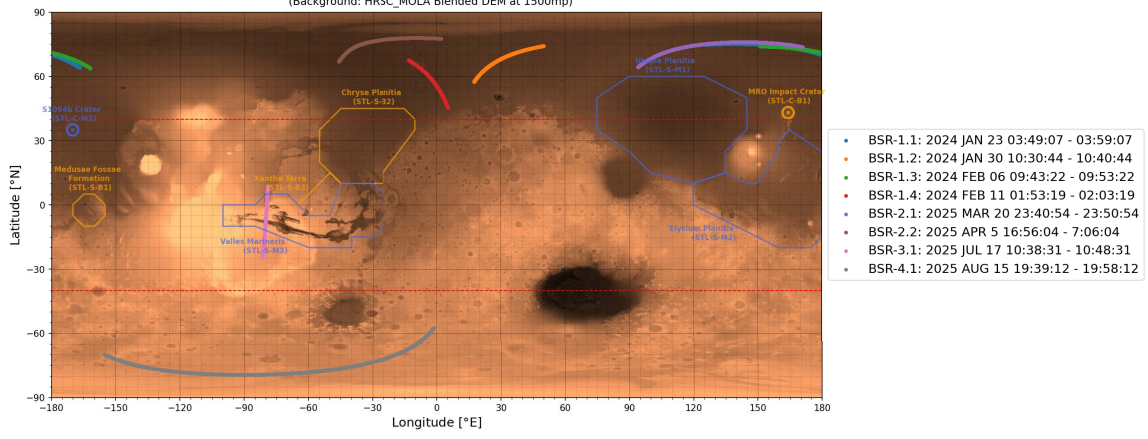[1] https://www.cosmos.esa.int/web/spice

Figure 4: Ground tracks for the MEX-TGO BSR measurements, own work

Phase 3: 'Numerical Simulations of the Martian Subsurface'

The MEX-TGO BSR link (Figure 5) starts at the MEX lander relay antenna transmitting a signal (in conventional attitude: nadir-pointing), which travels over a free-space distance to its boresight and surrounding Martian surface, is partially absorbed and dispersed, and reflects to the TGO antenna (also nadir-pointing). The received power P_R is modelled as the sum of the direct signal ($P_{R,dir}$) and power reflected from the subsurface ($P_{R,ss}$), the latter computed using the bistatic radar equation [57, 114, 133]. Here, P_T is the transmitted power, G_T and G_R are the gains computed using Gaussian approximations of the antenna patterns, λ is the wavelength (~70 cm at 437.1 MHz) and R_T and R_R are the distances from the S/C to the specular point. By integrating the BSR equation over the mutual footprint S, Equation 1 is found where

Figure 5: MEX-TGO BSR measurement geometry (not to scale), own work

σ_0 is the specific Radar Cross Section (RCS) per unit surface area. The RCS is a measure of how detectable an object is by radar [57, 114]. To determine σ with attention to coherent and incoherent signal scattering effects, it is conventionally defined by the method of Hagfors [58, 141], included in Equation 1 [20, 133, 146]. It is dependent on [20, 133]: Composition (Fresnel reflectivity ρ), roughness (Width parameter C) and slope (Required specular tilt angle γ). MOLA topography data is taken from NASA's Planetary Data System[2].

$$P_{R,ss} = \int_S \frac{P_T \cdot G_T}{4\pi \cdot R_T^2} \cdot \sigma_0 \cdot \frac{G_R \cdot \lambda^2}{4\pi \cdot R_R^2} dS = \int_S \frac{P_T \cdot G_T}{4\pi \cdot R_T^2} \cdot \rho \cdot C \cdot (cos^4(\gamma) + C \cdot sin^2(\gamma))^{-3/2} \cdot \frac{G_R \cdot \lambda^2}{4\pi \cdot R_R^2} dS \quad (1)$$

The Fresnel reflectivity connects received signal power to the subsurface composition through the dielectric constant ϵ. For non-colocated transmitters and receivers, as with MEX-TGO BSR, the signal is at non-normal incidence and ρ becomes a function of ϵ and the incidence angle θ_i (Equation 2). The Maxwell-Garnett (Equation 3) method is conventionally applied for the relation between composition and ϵ [145]. Herein, the host medium is low-porosity Martian regolith ($\epsilon_h=4.0$) for low to mid-latitudes and non-porous CO_2 ice ($\epsilon_h=2.1$) for near-polar regions ($\geq 60°$) [28]. For water ice, ϵ_{ice} is taken as 3.1 [4, 28, 80] and ν_{ice} describes the volume fraction of water (ice) in the host medium.

$$\rho(\theta_i) = \frac{\rho_\perp(\theta_i) + \rho_\parallel(\theta_i)}{2} = \frac{\left(\frac{cos(\theta_i) - \sqrt{\epsilon - sin^2(\theta_i)}}{cos(\theta_i) + \sqrt{\epsilon - sin^2(\theta_i)}}\right)^2 + \frac{\epsilon cos(\theta_i) - \sqrt{\epsilon - sin^2(\theta_i)}}{\epsilon cos(\theta_i) + \sqrt{\epsilon - sin^2(\theta_i)}}}{2} \quad (2) \qquad \epsilon_{eff} = \epsilon_h \cdot \frac{\epsilon_h + \frac{1 + 2\nu_{ice}}{3}(\epsilon_{ice} - \epsilon_h)}{\epsilon_h + \frac{1 - \nu_{ice}}{3}(\epsilon_{ice} - \epsilon_h)} \quad (3)$$

The MEX-TGO BSR numerical model simulates the received power spectrum using the bistatic radar equation and dielectric constant inferred from GRS and/or FREND data, which is in turn compared with the measured power spectrum, retrieved from the Automatic Gain Control (AGC) data. The current match is limited, reflecting the method's novelty, and surface composition is yet to show a strong signature. However, after calibration, resolution increase and improving direct signal, seasonal and polarization effects modelling, reliable detections appear possible and this model is deemed a good first iteration.

---

[2]https://ode.rsl.wustl.edu/mars/index.aspx

Contents

List of Figures

List of Tables

Nomenclature

Abbreviations

Abbreviation	Definition
ADS	Astrophysics Data System
AGC	Automatic Gain Control
BCE	Before Common Era
BSR	Bi-Static Radar
CEP	Central Elysium Planitia
CK	Spacraft rotations Kernels
CRISM	Compact Reconnaissance Imaging Spectrometer for Mars
CTX	Context Camera
DBK	Database Kernels
DEM	Digital Elevation Model
DoF	Degree of Freedom
DPS	Division for Planetary Sciences
DSK	Digital Shape Kernels
EK	Experiment explanation/Experimenter's notebook Kernels
ESA	European Space Agency
ESAC	European Space Astronomy Centre
ESTEC	European Space Research and Technology Centre
ET	Ephemeris Time
FK	Frames Kernels
FMCW	Frequency Modulated Continuous Wave
FWHW	Full Width Half Maximum
FM2	Flight Model 2
FoV	Field of View
FREND	Fine Resolution Epithermal Neutron Detector
GCR	Galactic Cosmic Rays
GNSS-R	Global Navigation Satellite System - Reflectometry
GPR	Ground Penetrating Radar
GRS	Gamma-Ray Spectrometer
GSS	Gamma Subsystem
HEND	High Energy Neutron Detector
HiRISE	High Resolution Imaging Experiment
HRSC	High Resolution Stereo Camera
IAU	International Astronomical Union
IK	Instruments Kernels
I-MIM	International Mars Ice Mapper
InSight	Interior Exploration using Seismic Investigations, Geodesy and Heat Transport
IQ	In-phase / Quadrature
IR	Infra-Red
ISAD	Icy Soil Acquisition Device
JPL	Jet Propulsion Laboratory
J2000	Astronomical Epoch (January 1st, 2000)
LHCP	Left Hand Circular Polarization
LOI	Location of Interest
↳ LOI-C-x	Location of Interest - Calibration
↳ LOI-S-x	Location of Interest - Science
Ls	Solar longitude
LSK	Leapseconds Kernels
MARCI	Mars Color Imager
MaRS	Mars Express Radio Science Experiment

Abbreviation	Definition
MARSIS	Mars Advanced Radar for Subsurface and Ionosphere Sounding
MDT	Measurement Definition Team
meas_op	Measurement Opportunity
MEGDR	Mission Experiment Gridded Data Records
MelaCom	Mars Express Lander Communications
MEX	Mars Express
MFF	Medusae Fossae Formation
MK	Meta-Kernel
MO	Mars Odyssey
MOLA	Mars Orbiter Laser Altimeter
MOSIR	Mars Orbiter Subsurface Investigation Radar
MRO	Mars Reconnaissance Orbiter
MSc	Master of Science
MSL	Mars Science Laboratory
MTP	Medium Term Plan
MY	Mars Year
NAIF	Navigation and Ancillary Information Facility
NASA	National Aeronautics and Space Administration
NPLD	North Polar Layered Deposit
NS	Neutron Spectrometer
PCK	Planetary Constants Kernels
PDS	Planetary Data System
PLD	Polar Layered Deposit
RA	Robotic Arm
RAC	Robotic Arm Camera
RCS	Radar Cross Section
REQ	Requirement
↳ REQ-MSR	Requirement for Measurement planning
↳ REQ-MSR-GEO	Requirement for Measurement planning on Geometry
↳ REQ-MSR-LOI	Requirement for Measurement planning on Location of Interest coverage
↳ REQ-MSR-SIM	Requirement for Measurement planning on Simulation parameters
↳ REQ-TAR	Requirement for Target locations
RHCP	Right Hand Circular Polarization
RIMFAX	Radar Imager for Mars' subsurface experiment
RMS	Root Mean Square
RoPeR	Mars Rover Penetrating Radar
RoSPR	Rover Subsurface Penetrating Radar
RQ	Research Question
SAR	Synthetic Aperture Radar
S/C	Spacecraft
SCLK	Spacecraft Clock Kernels
SHARAD	Mars SHAllow RADar sounder
SNR	Signal-to-Noise Ratio
SPICE	Spacecraft, Planet, Instrument, C-matrix, Events observation geometry information system
SPK	Spacecraft Kernels
SPLD	South Polar Layered Deposit
spoint	Specular point
STL	Scientific Target Location
↳ STL-C	Scientific Target Location - Calibration
↳ STL-C-Mx	Scientific Target Location - Calibration - Main
↳ STL-C-Bx	Scientific Target Location - Calibration - Backup
↳ STL-S	Scientific Target Location - Science
↳ STL-S-Mx	Scientific Target Location - Science - Main
↳ STL-S-Bx	Scientific Target Location - Science - Backup
TECP	Thermal and Electrical Conductivity Probe
TGO	ExoMars Trace Gas Orbiter

Abbreviation	Definition
TU Delft	Delft University of Technology
UHF	Ultra High Frequency
USGS	United States Geological Survey
UTC	Coordinated Universal Time
VBF	Vastitas Borealis Formation
VHF	Very High Frequency
VSCode	Visual Studio Code
V&V	Verification and Validation
WEH	Water Equivalent Hydrogen
WISDOM	Water Ice and Subsurface Deposit Observation on Mars

Symbols

Symbol	Definition	Unit
a	Semi-major axis of ellipsoidal Mars	m
B	Bandwidth	Hz
b	Semi-minor axis of ellipsoidal Mars	m
C	Hagfors width parameter	rad^{-2}
c	Speed of light (in vacuum)	ms^{-1}
e	Eccentricity	-
e	Emission angle	°
↳ e_{MEX}	Emission angle of MEX	°
↳ e_{TGO}	Emission angle of TGO	°
f	Frequency	Hz
G	Antenna gain	dB, -
↳ G_{dB}	Antenna gain in deciBels	dB
↳ G_{linear}	Linear antenna gain	-
↳ G_R	Receiver antenna gain	dB, -
↳ G_T	Transmitter antenna gain	dB, -
G	Gravitational constant	$m^3kg^{-1}s^{-2}$
$\hat{g}$	Required local unit surface normal for specular reflection	-
i	Instant	-
k_B	Boltzmann constant	JK^{-1}
M	Mass of a large Solar system body	kg
N	Amount	-
$n_{pix/deg}$	Number of pixels per degree	pix/deg
$\hat{n}$	Local unit surface normal	-
↳ $\hat{n}_{ell}$	Local unit surface normal to ellipsoidal Mars	-
P	Power	W, dB
↳ P_{AGC}	Converted power from AGC value	W, dBm
↳ $P_{noise\,floor}$	Power noise floor	W, dBm
↳ P_R	Received power	W, dBm
↳↳ $P_{R,dir}$	Received power - Direct signal	W, dBm
↳↳ $P_{R,ss}$	Received power - Reflected signal from the subsurface	W, dBm
↳ P_T	Transmitter power	W, dBm
R	Distance	m
↳ R_R	Distance to the transmitter	m
↳ R_{sp}	Distance traversed by the signal, i.e. signal path length	m
↳ R_T	Distance to the receiver	m
R_{Ω}	Rodrigues' rotation matrix	-
$\hat{r_R}$	Unit vector from a surface point to the receiver	−
$\hat{r_T}$	Unit vector from a surface point to the transmitter	−
S	Surface area	m^2
↳ $S_{circular\,segment}$	Surface area of a circular segment	m^2

Symbol	Definition	Unit
↳ $S_{gridpoint}$	Surface area of a gridpoint	m^2
s	Surface slope	°
↳ s_{RMS}	RMS surface slope	°
T_{noise}	System noise temperature	K
t	Time	s
↳ t_i	Time at instant i	s
$\vec{v}_{along\ slope}$	Local slope vector	-
$\vec{v}_{local\ East}$	Local East vector	-
$\vec{v}_{local\ North}$	Local North vector	-
$wt\%$	Weight percent	%
z	Topography value at the point of interest	m
↳ z_E	Topography value East to the point of interest	m
↳ z_N	Topography value North to the point of interest	m
↳ z_S	Topography value South to the point of interest	m
↳ z_W	Topography value West to the point of interest	m
γ	Empirical constant for a three-component mixing model	-
γ	Required tilt angle for specular reflection	°
Δx	Pixel size in longitudinal direction	m
Δy	Pixel size in latitudinal direction	m
ϵ	Dielectric constant / permittivity	-
↳ ϵ_{air}	Effective dielectric constant / permittivity of air	-
↳ ϵ_{eff}	Effective dielectric constant / permittivity of a two-component mixture	-
↳ ϵ_h	Dielectric constant / permittivity of the host material	-
↳ ϵ_{ice}	Dielectric constant / permittivity of water ice	-
↳ ϵ_{rock}	Dielectric constant / permittivity of rock	-
θ_i	Incidence angle	°
λ	Longitude	°
↳ λ_i	Longitude at instant i	°
λ	Wavelength	m
μ	Standard gravitational parameter	$m^3 s^{-2}$
ν	Volume fraction	-
↳ ν_{air}	Volume fraction of air (inclusions)	-
↳ ν_{ice}	Volume fraction of water ice	-
↳ ν_{rock}	Volume fraction of rock (host material)	-
ρ	Fresnel reflectivity	-
↳ $\rho_\perp$	Fresnel reflectivity - Normal component	-
↳ $\rho_\parallel$	Fresnel reflectivity - Parallel component	-
σ	Radar cross section	m^2
↳ σ_0	Specific radar cross section per unit surface area	m^2
σ	Standard deviation	-
ϕ	Latitude	°
↳ ϕ_i	Latitude at instant i	°
↳ ϕ_{max}	Upper latitudinal bound	°
↳ ϕ_{min}	Lower latitudinal bound	°
Ω	Rodrigues' antisymmetric matrix	-

1

Introduction and Relevance of the Project

In the early 70s, Mariner 9 (Figure 1.1) made history as the first spacecraft (S/C) to orbit another planet [162], opening humanities' eyes to Mars: The 'Red Planet' [46]. Among Mars' remarkable geological features, Mariner 9 imaged networks, canyons and valleys, reminiscent to terrestrial river channels [7, 25, 63, 99, 126]: Especially the Valles Marineris, which formed from tectonic fractures into grand canyons by fluvial erosion [99]. Mariner 9 found evidence for atmospheric water vapor, water ice in the Northern polar cap and presence of hydrated minerals, leading scientists to hypothesize over extensive underground river systems and the existence of subsurface permafrost [126].
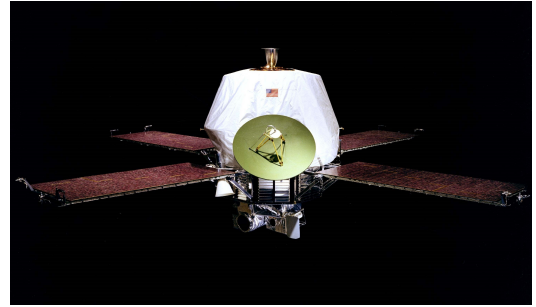
Figure 1.1: Model of Mariner 9, retrieved from Uri [162]

The availability of water is one of the most stringent factors for the existence of extra-terrestrial life [126], a timeless aim of planetary exploration. Thus, historical and modern scientists alike deem Martian research, especially its water supply, of profound scientific implications [7]. Notices of Earth-like life on Mars has been disproven since the Mariner 9 mission, but subsurface water ice can still function as a looking glass into Mars' (biological) past and different potentially hosted lifeforms. It could contain frozen proto-life fragments or complex organic molecules pointing to primitive Martian life forms [96]. Furthermore, Mars will be the first extra-terrestrial planet where humanity will set foot, and shallow subsurface water supplies will play a vital role for means of in-situ resource utilization during sustained presence on the Martian surface, especially at lower risk near equatorial latitudes [165]. Current consensus dictates shallow subsurface water ice to be present from the poles to approximately ±40° latitude, in equilibrium with atmospheric humidity, but presence at mid- to equatorial latitudes is debated [96] and correlation between different measurements, particularly at shallow depths, is poor. Specific geo-morphological conditions must be met for water (in any form) to be stable, only met in the polar regions [64, 140] and the cold Martian conditions lay below the triple point of water [165].

The aim of this MSc thesis is to assess the feasibility of utilizing bi-static radar (BSR) measurements between Mars Express (MEX) and the ExoMars Trace Gas Orbiter (TGO) for Martian subsurface water (ice) research, and in turn use these measurements to correlate knowledge from past and future missions which utilized other approaches. The research builds upon the abstract presented at the 56th Annual Meeting of the Division for Planetary Sciences (DPS 56[1]) by Svedhem et al. [152]. It is performed at the Faculty of Aerospace Engineering of the Delft University of Technology (TU Delft), titled "Probing shallow subsurface water on Mars through bi-static radar measurements at Ultra High Frequency (UHF) Wavelengths" and has the following objective:

Compare current knowledge, particularly the Gamma-Ray Spectrometer (GRS) and Fine Resolution Epithermal Neutron Detector (FREND) maps, on shallow subsurface water ice at mid to equatorial latitudes on Mars

by

planning, performing and processing bi-static radar measurements between the Mars Express (MEX) and the ExoMars Trace Gas Orbiter (TGO) spacecraft, using numerical simulations of the Martian subsurface

Inspiration for the research originates from the MEX-TGO Mutual Occultation experiment. Since 2020, it employs the orbiters' lander UHF communication equipment to study the Martian iono- and atmosphere [24, 112]. Between December 2023 and March 2024, the MEX-TGO coordinated observations were accidentally planned and performed at the incorrect switch-ON time. Due to this, four measurements did not pass through the iono- and atmosphere, but instead probed and reflected back from the subsurface. These were under

---

[1]https://aas.org/meetings/dps56

non-optimal conditions (very high incidence angles and large distances between the S/C), but still a significant signal was received, incentivizing the use of the unmodified setup, with a selection of different times, for BSR.

In MEX-TGO BSR, the setup is as shown in Figure 1.2. MEX transmits a signal at Ultra High Frequency $f = 437.1MHz$ in its conventional attitude (nadir-pointing) and over a nominal duration of 10 minutes. This corresponds to a wavelength of $\lambda = 70cm$, which is consistent with high attenuation and probing of a few metres when it comes in contact with the Martian subsurface. Therefore, the signal is partially absorbed and partially reflected. The echo is dependent on the average permittivity of the shallow subsurface, and thus water ice (and even more so liquid water) have an effect. TGO receives the reflected signal and by pure amplitude analysis, variations in water (ice) content can be determined. MEX-TGO BSR allows almost complete global access, particularly ideal for comparison with the GRS and FREND hydrogen maps. Additionally, by reducing the signal path R_{sp} between the orbiters and Mars tenfold, the Signal-to-Noise Ratio (SNR) is expected to increase by a factor over a hundred (according to $1/R_{sp}^2$) [153]. It should be noted that the MEX transmitter is not a proper radar system and does not allow for pulse compression, meaning no range resolution is possible.
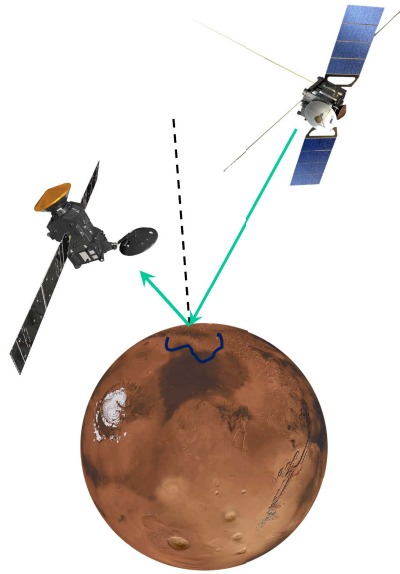
Figure 1.2: MEX-TGO bi-static radar measurement via the Martian surface, own work

To attain the research objective; three high- and six low-level research questions (RQ) are defined:

- RQ1: When can the best bi-static radar measurements be performed between MEX and TGO?
    - RQ1.1: Which regions fit the interest of past and future missions?
    - RQ1.2: What are the relevant selection criteria for quality measurements?
    - RQ1.3: How can MEX-TGO BSR measurements be modelled?
- RQ2: How can bi-static radar measurements be processed to retrieve the amount and form of H_2O?
    - RQ2.1: How does the received signal amplitude depend on the sampled area's dielectric constant?
    - RQ2.2: How does the dielectric constant depend on water and other constituents of the subsurface?
    - RQ2.3: What is the confidence level of the MEX-TGO BSR results?
- RQ3: How do processed MEX-TGO BSR results match the state-of-the-art scientific knowledge?

As follows from the research questions, the research is divided into three main phases: The first is concerned with the background of Martian water research in literature, as well as how MEX-TGO BSR research complements this, the second includes the planning and performing of the MEX-TGO BSR measurements, whilst the third is concerned with the processing of the measurements, including comparison with current knowledge.

Accordingly, the thesis is structured as follows: Chapter 2 gives an overview of Martian history and its hypothesized water presence over time, providing context to the MEX-TGO BSR research. Chapter 3 presents conventional measurement methods employed for Mars water research and relevant results from past and current missions. In Chapter 4, targets locations are defined, such that prior research would be complemented. Chapter 5 discusses the methodology and results of the second phase, including measurement planning (using the SPICE software[2]), submission of the request to the European Space Agency's (ESA) European Space Astronomy Center (ESAC) for performing optimal measurements and the resulting measurements actually (to be) performed. Chapter 6 is concerned with the third phase, i.e. processing of the measurements, and presents the numerical modelling of the Martian subsurface for comparison to the measurement data. Chapter 7 presents the thesis conclusions and recommendations for future work on both MEX-TGO BSR planning and modelling. Lastly, Appendix A contains a list of the used SPICE kernels, Appendix B presents an analysis on the 'midpoint approximation' made for measurement planning and for all measurements: Appendix C presents the mutual signal footprints, Appendix D the AGC data and Appendix E the model results.

All documentation, code and data is saved and organized on a *private GitHub repository*, linked to a remote location through *Visual Studio Code (VSCode)* and backed up frequently. Final versions and model results are available on a *public GitHub repository*[3]. Documentation is written in *LaTeX*, locally in VSCode. For literature research, all papers are saved on a *Mendeley library* and the *Astrophysics Data System (ADS)*[4] is employed.

---

[2] https://www.cosmos.esa.int/web/spice   [4] https://ui.adsabs.harvard.edu/
[3] https://github.com/DJNieuwenhuizen/MSc-thesis/

2

History and Water Presence

Unlike its current cold and dry state, early Mars is believed to have been a warm paradise, with river valleys and a thick atmosphere [67, 128]. Its geological history, dictating these transitions, consists of: The Pre-Noachian period (Section 2.1), Noachian period (Section 2.2), Hesperian period (Section 2.3) and Amazonian period (Section 2.4). Each is characterized by (broadly accepted) differing water presence and habitability potential, as described in the respective sections, providing context to the MEX-TGO BSR research.

2.1. The Pre-Noachian Period

Mars is one of the four terrestrial planets in the inner Solar system, thought to have originated from a gas disc wherein dust grains snowballed into small rocky worlds. Once planet formation was completed, the Martian crust formed and the Pre-Noachian period began, hypothesized to span from **4.5 to 4.1 billion years ago** [45].

In this period, Mars formed a thick atmosphere, resulting from heavy bombardment and mantle outgassing as the planet cooled [45, 128]. It saw the formation of the vast Northern plains (Vastitas Borealis), separated from the rugged Southern highlands by the Martian dichotomy [128, 137], shown in Figure 2.1, and atmospheric water vapour likely condensed into a vast, possibly global, ocean. The water slowly cooled, opening the first possible window for life to emerge and, over time, was absorbed into the subsurface [45].
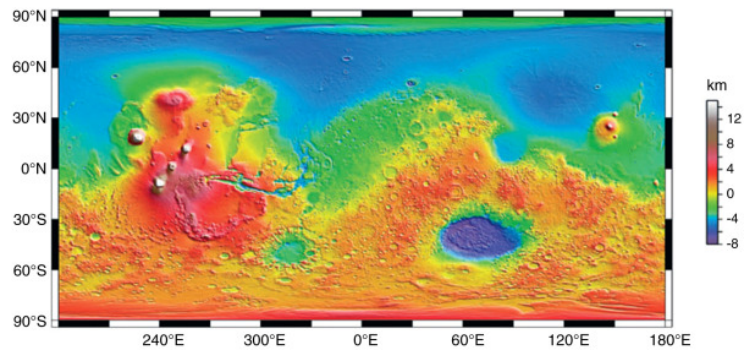
Figure 2.1: The Martian topography as captured by the Mars Orbiter Laser Altimeter (MOLA), retrieved from Smith et al. [137]

2.2. The Noachian Period

The Noachian Period spanned from **4.1 to 3.7 billion years ago** and featured further heavy bombardment, creating much of the Southern cratering and largest still visible impact basins (Hellas, Isidis and Argyre). In parallel, tectonic activity caused widespread fracturing of the surface, most notably: The Valles Marineris. Furthermore, Mars became volcanically active and eruptions thickened the atmosphere, in turn trapping Solar radiation. As temperatures increased, clouds formed and precipitation rain created abundant valley networks and lakes in basins and craters. There may have even been a shallow ocean over the Northern lowlands. [45]
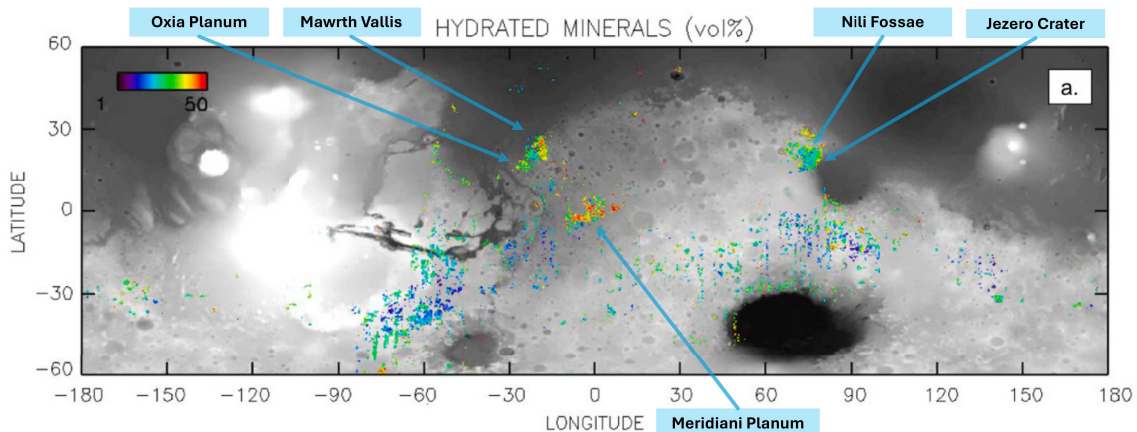
Figure 2.2: Global map of hydrated minerals on Mars, adapted from Riu, Carter, and Poulet [125]

3

Evidence for large-scale Noachian aquatic activity comes from terrestrial runoff channels, enhanced erosion rates and hydrated mineral deposits [67]. The latter are chemically altered rocks which required periodic or prolonged exposure to non-acidic water to form, and are especially abundant in older terrains where the Noachian crust is exposed, as mapped in Figure 2.2 [40, 67, 125]. The global and widespread abundance shows them to be a significant water sink, through which large parts of the surface water percolated into the crust [88].

Throughout the Noachian period, surface conditions remained favorable for possible emergence of life, but habitable regions gradually decreased in size and became more localized [45].

2.3. The Hesperian Period

The Hesperian Period spanned from **3.7 to 2.9 billion years ago**, showing significantly decreased impact cratering and geological activity [45, 65]. However, volcanic plains were widespread over the surface, most abundantly around the Vastitas Borealis, causing over 30% of Northern plain re-surfacing [45, 65, 155]. The peak flux of early-Hesperian eruptions enriched the atmosphere with water vapour and sulfur dioxide, causing it to shortly warm and in turn inducing sulphate precipitation and a transition to sulfur-dominated weathering [1, 65]. Evidence for which has been found in chemically altered rocks by acidic ground water [1, 45, 65].

The warm early-Hesperian atmosphere melted the South polar cap, forming low-latitude paleolakes evident from relatively young aqueous mineral deposits [26, 40, 65]. After the initial volcanic flux, the atmosphere thinned and global dehydration and cooling dominated the remaining Hesperian period [65, 128], leaving habitability to deteriorate rapidly [34]. Episodically, returns to earlier conditions were recorded in sedimentary layers and erosional unconformities, but these can likely be amounted to chaotic variations in Mars' orbit [1].
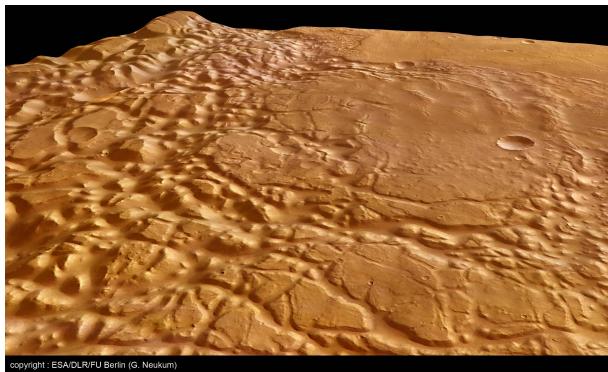
Figure 2.3: Chaotic terrain at Iani Chaos captured by the High Resolution Stereo Camera (HRSC) on Mars Express, retrieved from the European Space Agency [41]
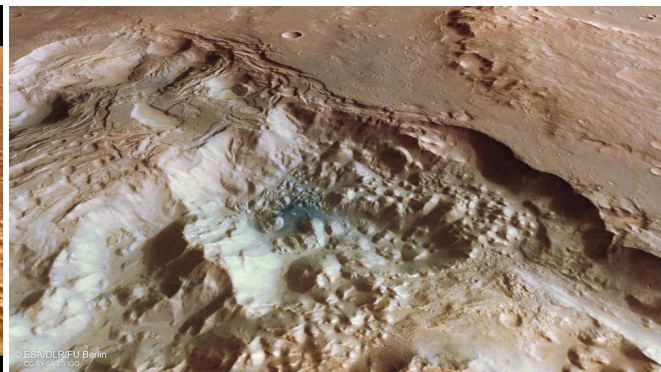
Figure 2.4: Chaotic terrain North of Pyrrhae Chaos captured by the High Resolution Stereo Camera (HRSC) on Mars Express, retrieved from the Deutsches Zentrum für Luft- und Raumfahrt [36]

As the climate cooled down, surface water waned and locked up as permafrost or subsurface ice. Water (ice) pooled underground erupted when heated by impacts or volcanic eruptions, causing catastrophic floods surging across vast stretches of land [36, 61]. Such powerful water releases led to the formation of huge outflow channels and 'chaotic terrain', collapsed landscapes of scattered relief masses and circular depressions [36, 41]. Regions dominated by chaotic terrain include Iani Chaos (Figure 2.3) and Pyrrhae Chaos (Figure 2.4), both in the wider Eastern region of the most notable outflow system: Valles Marineris [36, 45, 61]. Furthermore, floods would form pools in the Northern lowlands, explaining the high water ice content in the North polar cap [88].

2.4. The Amazonian Period

The Amazonian Period spans from **2.9 billion years ago to the present**, covering over half of Mars' geological history [45]. It is absent of large-scale geological and climate activity, and instead characterized by aeolian activity, dehydration and global cooling with limited, primarily glacio-fluvial, aqueous activity [12, 17, 65, 76].

During the Amazonian period, Mars' climate varied periodically. Unlike Earth, it lacks a large moon to act as a gravitational stabilizer, making its orbital parameters, particularly its obliquity, variable over time [76]. During high-obliquity periods, ice was stable at low- to equatorial latitudes, forming extensive glacial land-systems analogous to those on Earth [76]. Orbital data proves these episodic periods of glacio-fluvial activity, even showcasing possible existence of standing bodies of water during the early and perhaps mid-Amazonian period, such as the paleolakes from the Hesperian period [34, 40, 75]. Amazonian-dated rocks show evidence of slow weathering, punctuated only by occasional short-duration erosion in warmer wetter conditions [40, 45]. Furthermore, the North and South pole show layering of surface ice with dust, and their layering and

erosional non-conformities allow for the episodic climate patterns to be retrieved, under the hypothesis that orbital variations controlled the ratio between ice and dust flux toward the poles.

Beside large-scale orbital variations, the Martian climate is also affected seasonally, showcased most notably by the polar ice caps (Figure 2.5). During the cold winters, they extend to latitudes as low as 40° [67]. For Mars Year (MY) 29, Figure 2.6 shows the seasonal variation of the South polar ice cap, as captured by the Mars Color Imager (MARCI) [19]. The top left indicates the Earth date of each compiled image (in YY/MM/DD) and the bottom right shows the Solar longitude (Ls) on that date, whose increase corresponds to a smaller cap.
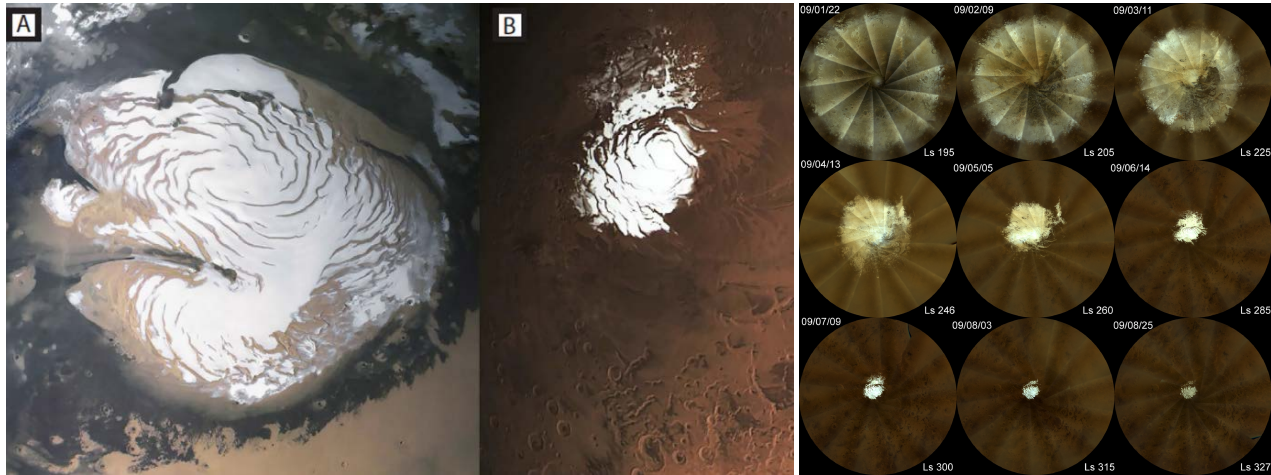
Figure 2.5: The North (A; late spring) and South (B; late summer) polar ice caps as imaged by the HRSC, retrieved from Koutnik et al. [76]

Figure 2.6: MY29 Seasonal variation in the South polar ice cap (up to 55°S) as imaged by MARCI, retrieved from Calvin, Cantor, and James [19]

At present, Mars seems to be coming out of an Ice Age, with evidence of melting polar ice caps and viscous flow features, i.e. extensive mid-latitudinal surface patterns indicating fluvial ice deformation [45, 63, 76]. The thin (primarily CO_2) atmosphere causes water (ice) to instantly vaporize/sublimate at the surface, making it cold, dry and arid [128]. This deteriorated climate has made the Martian surface presently uninhabitable [34], leaving only a water supply under the following conditions:

- **(Non-)polar ice:** Current Mars has abundant amounts of polar and non-polar ice, leftover from recent glacially active periods. These are primarily water ice deposits, but also contain some CO_2 [76].

  - **Subsurface water ice:** The most copious form of water on Mars, especially at high latitudes where hydrogen is abundant in the shallow subsurface, although expected also at lower latitudes as a result from high-obliquity glacial periods [76, 96, 140]. It fills the porosity volume between regolith grains in the subsurface, staying protected from sublimation at the surface [36, 96].
  - **Polar surface water ice:** Mars currently has large layered surface water ice deposits from the poles towards mid-latitudes [76, 140]. Both caps have extreme seasonal effects: During winters, atmospheric CO_2 condenses and adds onto the ice caps, leaving them to reach latitudes as low as 40°. Additionally, the local water vapor condenses onto the cap, to get released again in spring [67].

- **Atmospheric water vapor & adsorbed subsurface water:** The Martian atmosphere is mostly CO_2, but contains some water vapor, mainly supplied by the polar caps [67]. Furthermore, atmospheric H_2O is exchanged with adsorbed subsurface water through 'regolith breathing': Water is driven off the grain and diffuses back into the atmosphere as water vapor during seasonal heating, and is adsorbed back into the subsurface in cooling [67, 165]. The condensed water vapor that diffused onto the regolith grains' surface, is saved as layers of molecules physically, instead of chemically, bonded to the soil grains [67, 96].

- **Hydrated minerals:** Chemically altered rocks with H_2O and/or OH in their mineral structure [67], containing average WEH levels of 10wt% (up to 30wt%) [96] and observed by orbital spectrometers and rovers [40, 45, 96]. Their global abundance shows them to be a significant water sink [88].

3

Humanity's Exploration of Mars

To place MEX-TGO BSR in context of current research, this chapter discusses humanity's exploration of Mars, with a focus on water research. Section 3.1 presents an overall history of Martian exploration, Section 3.2 discusses the orbital and in-situ methods employed for water research and lastly, Section 3.3 and Section 3.4 respectively present relevant orbital and in-situ missions, instruments and experiments to MEX-TGO BSR.

3.1. History of Martian Exploration

Mars is the single most explored planet inside the Solar system (aside from Earth), with first attempts dating back to the ancient Egyptians in the 2nd millennium BCE [123]. Their astronomical studies yielded many practical inventions as well as the discovery of Mars, including tracking of its orbit and retrograde motion [107].

Much later, in 1610, Galileo Galilei made the first telescopic observations of Mars [117], after which astronomers such as Christian Huygens, Giovanni Cassini and William Herschel went on to observe Mars' diameter and most notable features: Shield volcanoes and the seasonally varying polar ice caps [91]. In 1877, Giovanni Schiaparelli observed "cannali": grooves and trenches meandering through the Martian surface. These were mistranslated in English to "canals", a word highly suggestive of water, creating the speculation these were irrigation canals created by an advanced extraterrestrial race [91, 160].
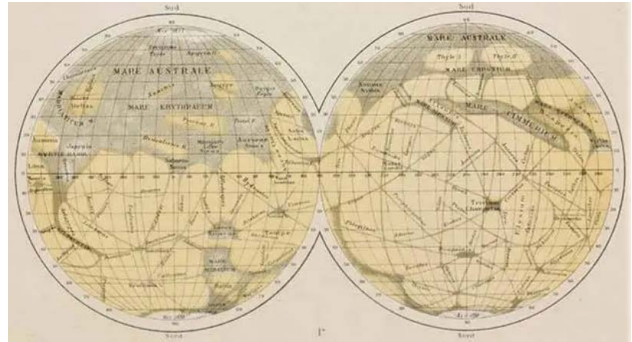
Figure 3.1: Schiaparelli's cannali, retrieved from Uri [160]

The speculation surrounding Mars' water supply and notions of extraterrestrial life fueled humanity's interest in the 'Red Planet'. Although complex alien life was quickly disproven, it was not long after the first missions successfully reached Earth orbit that humanity set its sights on Mars. The Soviet Union was first with their Mars 1960A probe [98]. It aimed to research interplanetary space and perform a flyby returning images of the Martian surface, but it suffered a launch failure in 1960. Four years later NASA launched the first successful Mars mission: the Mariner 4 flyby. It succeeded the failed Mariner 3 under the 'Mariner Program' and returned 21 images of an empty non-living deserted surface in an old highly-cratered southern region. As of yet, the Mars exploration saga includes 48 attempted missions, of which 28 were (partially) successful [172].

3.2. Measurement Methods for Water Research

Throughout the history of Martian exploration, water (ice) research has been of notable interest. This section discusses both orbital (Subsection 3.2.1) and in-situ (Subsection 3.2.2) measurement methods.

3.2.1. Orbital Research

Orbital research is performed by Mars orbiters and flyby's and is most commonly applied to attain a global mapping of the Martian surface and subsurface water volume. It includes methods such as optical imaging, gamma-ray and neutron spectrometry as well as radar sounding, each individually described in this section.

Optical Imaging and Altimetry

Starting with the first successful flyby of Mariner 4 in 1965, optical imaging has been a staple of Martian exploration, allowing identification of ridges and water features in the surface topography. Topography can be further characterized using laser altimeters. These instruments send a signal which is reflected by the surface. Depending on the required return time, the distance to the surface can be calculated. This allows for creating detailed topographic maps which can be used to identify aquatic features, e.g. river valleys and lake beds.

Radar Sounding

Radar sounding is the most conventional orbital measurement method for water (ice) research. Radar instruments always consist of a transmitter and receiver, and come in one of two types:

- **Mono-static radar:** The transmitter and receiver are co-located, and the operational geometry looks as shown in Figure 3.2 for the SHARAD instrument (Subsection 3.3.7).

- **Bi-static radar:** The transmitter and receiver are not co-located, as for MEX-TGO BSR, where MEX hosts the transmitter and TGO the receiver, but also a S/C-based transmitter with an Earth-based receiver (MEX BSR experiment; Subsection 3.3.5). The operational geometry (Figure 3.3) is restrictive in comparison to a dual-S/C setup, as measurements can only be taken for permissive orbital geometry at small Earth-Mars distances [24, 129]. Maximum power reflection follows from the specular point (and surrounding Fresnel zone) as well as the direct contribution from the transmitting antenna's sidelobes [113, 133, 134].
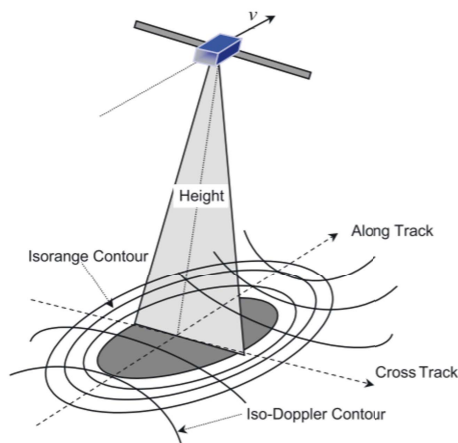
Figure 3.2: SHARAD operational geometry, retrieved from Seu et al. [130]
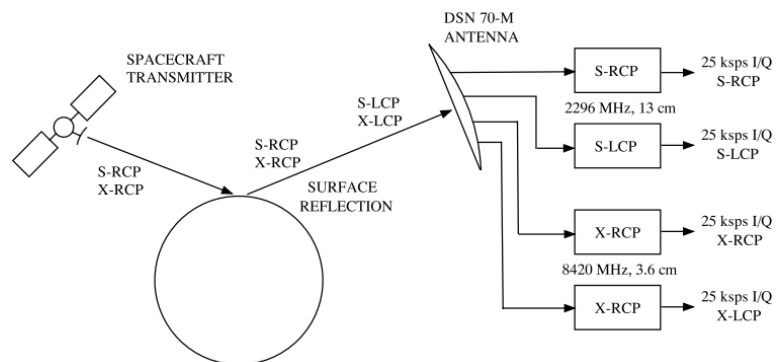
Figure 3.3: MEX BSR operational geometry, retrieved from Simpson et al. [133]

For subsurface sounding, the transmitter transmits radio pulses or a continuous radar signal [73, 108]. Receivers capture these echos after subsurface reflections have taken place, which are used to determine the dielectric and oblique scattering properties of the sampled area [73, 108, 113, 129, 133]. Surface roughness or topographic features causes the incident signal to scatter in non-specular directions, thus producing noise and off-nadir echos (received after the initial specular signal) known as 'clutter' [108, 109, 132]. These are often discriminated from subsurface returns by surface echo simulations [109]. During the subsurface reflection, orthogonal incident Right Hand Circularly Polarized (RHCP) signals (partially) converts into Left Hand Circularly Polarized (LHCP) [113, 129, 133], which depending on the receiving antenna may (not) be registered. Others, like MARSIS (Subsection 3.3.6), use linear polarization instead by employing a dipole antenna [108].

Deposits are reflected in the data by discontinuities in the dielectric constant, resulting from both the compositional as well as structural change inflicted by the hypothesized water (ice) layers [108]. The dielectric constant is a material property, otherwise known as the 'relative permittivity' (or simply 'permittivity'), which describes the material's response to an incoming electric field [56, 158]. A higher dielectric constant corresponds to a higher tendency to reduce an incoming field, instead making it more likely for the signal to reflect off the material [51, 56, 158]. Water-bearing materials have a higher reflection coefficient than pure regolith mixtures due to their higher dielectric constant showing strong subsurface echos in addition to the surface echos [110].

Conventional radars, like MARSIS (Subsection 3.3.6) and SHARAD (Subsection 3.3.7), operate at low frequency. Their long wavelengths correspond to little attenuation in the subsurface, targeting water (ice) deposits at several kilometers deep and even underneath the polar caps [73, 108, 110]. MEX-TGO BSR instead operates at Ultra High Frequency, yielding a penetration of only a few metres and targeting shallow water (ice) deposits.

Gamma-Ray and Neutron Spectrometry

Mars lacks protection from a magnetic field/thick atmosphere and is consistently bombarded by Galactic Cosmic Rays (GCR) [94, 95]. These interact with the constituents of the shallow subsurface (Figure 3.4), causing:

- **Gamma rays:** Cosmic rays impinging on a planetary surface collide with atomic nuclei, causing collisions and excitation. As nuclei get excited, they emit gamma rays, de-exciting at distinct energy levels [95, 127].

- **Fast neutron fluxes:** Collisions of cosmic rays with atomic nuclei produces fast (high-energy) neutrons. These escape or undergo subsurface scattering with a depth dependence similar to gamma rays [15].

- **Thermal and epithermal neutron fluxes:** A collision between a fast neutron and a heavy nucleus causes the neutron to lose energy, i.e. undergo moderation. The resultant excited neutrons are slower and lower

in energy and categorized as (epi)thermal neutrons. They can release as secondary neutrons, or neutron flux, and have a depth dependence two to three times greater than gamma rays [15, 94].

Unlike radar sounding, gamma-ray and neutron spectrometry do not directly measure variations in water ice content, but infer its likelihood based on hydrogen presence. Gamma-ray and neutron spectrometers are statistical instruments, meaning their mapping capabilities are tied to the addition of repeated measurements over single locations [83, 94]. Gamma-ray spectrometers capture emitted gamma rays as sharp emission lines, where energy indicates the element and intensity indicates concentration [102], allowing the derivation of elemental abundance at differing depths [95, 127]. Neutron spectrometers instead directly detect the emitted neutron fluxes, which are sensitive to the presence of different elements, par-

Figure 3.4: Nuclear radiation reactions resulting from a cosmic ray impinging on a planetary surface, retrieved from Mitrofanov [93]

ticularly hydrogen due to their highly similar mass [15, 49, 95]. The neutron flux measured by neutron spectrometers represents those which escaped the surface and are called 'leakage neutrons'. These were likely in vicinity to hydrogen abundances and became moderated down to thermal energies, where high hydrogen content (supposedly as part of H_2O molecules) induces a lesser flux of epithermal neutrons than drier soils. Even for very low amounts, the high-energy (fast) neutron flux is decreased and thermal flux is increased [95].

By mapping neutron emissions, the Water Equivalent Hydrogen (WEH) level is derived, i.e. the weight percent (wt%) of water the subsurface would contain if all detected hydrogen is present as H_2O [96]. First, the Neutron Suppression is defined by taking the ratio of the neutron count rate over a reference rate in the Solis Planum: One of the driest Martian regions with well-estimated 2.78 wt% WEH [14]. Neutron Suppression values are smoothed and converted into WEH by numerically simulating all neutron emission processes [84, 81]. It should be noted that these do not distinguish between different forms of water, i.e. liquid or ice, as neutron emission results are heavily influenced by the unique geomorphological site conditions [86, 96], but an indication is generally accepted to be: Adsorbed water in the range of a few wt%, inside hydrated minerals up to a maximum of ~15-30 wt% [86, 96] and deposits of semi-pure water (ice), characterized by the highest WEH levels.

3.2.2. In-Situ Research

In-situ research is performed by landers and rovers. Ever since the Pathfinder lander, launched by NASA in 1996, deployed the Sojourner rover (Figure 3.5; the first wheeled vehicle to have successfully traversed the Martian surface), wheeled vehicles are a trend seen abundantly in modern Martian exploration [178].

Optical Imaging and In-situ Probing
Similar to orbital optical imaging, landers and rovers can be equipped with cameras to locally image the Martian surface. As such, the Viking 1 lander, launched in 1975 under NASA's 'Viking Program' took and transmitted the first ever picture in the Chryse Plantitia of the Martian surface, shown in Figure 3.6. [183]

Optical imaging is well-equipped for combination with in-situ probing techniques, e.g. digging and drilling. These can uncover ice deposits and image them over time to capture their sublimation.

Figure 3.5: Sojourner rover fully off the ramp and on the Martian soil, retrieved from Williams [178]
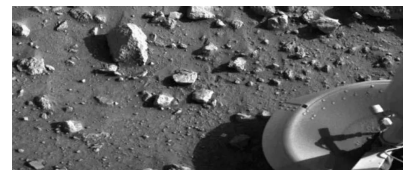
Figure 3.6: First picture taken by Viking 1 on the Martian surface, retrieved from Uri [160]

3.3. Relevant Missions for Orbital Water Research

This section presents orbital missions, instruments and experiments which have or will contribute to water research on Mars. This includes: The Imaging System of the Mariner orbiters (Subsection 3.3.1), Mars Orbiter Laser Altimeter on Mars Global Surveyor (Subsection 3.3.2), High Resolution Imaging Experiment on the Mars Reconnaissance Orbiter (Subsection 3.3.3), Gamma-Ray Spectrometer on 2001 Mars Odyssey (Subsection 3.3.4), the Bi-Static Radar Experiment performed with Earth by Mars Express (Subsection 3.3.5), Mars Advanced Radar for Subsurface and Ionosphere Sounding on Mars Express (Subsection 3.3.6), Mars SHAllow RADar sounder on the Mars Reconnaissance Orbiter (Subsection 3.3.7), Fine Resolution Epithermal Neutron Detector on the ExoMars Trace Gas Orbiter (Subsection 3.3.8), Mars Orbiter Subsurface Investigation Radar on the Tianwen-1 Orbiter (Subsection 3.3.9) and lastly, the International Mars Ice Mapper concept (Subsection 3.3.10).

3.3.1. Imaging System (Mariner 6, 7 and 9)

Mariner 6 and 7 were a dual (identical) spacecraft mission launched by NASA in 1969. During their successful flybys, occurring 5 days apart, they photographed 20% of the planet's diverse surface, including the first images of the south polar ice cap and IR radiometry measurements indicating its largely CO_2 composition [161]. Later in the program, Mariner 9 was the first successful Mars orbiter, launched by NASA in 1971. It encountered one of the largest global dust storms ever observed, after which it started surface mapping, showcasing craters, dried up river beds, volcanoes, the Valles Marineris system and signs of aquatic and aeolian erosion [175].

3.3.2. Mars Orbiter Laser Altimeter (Mars Global Surveyor)

The Mars Global Surveyor, launched by NASA in 1996, was highly successful, demonstrating the first successful use of aerobraking and creating detailed maps of the surface topography with its Mars Orbiter Laser Altimeter (MOLA), such as previously shown in Figure 2.1 [137]. Notable results included substantial proof of fluvial activity [105]. This mainly included the identification of water transportation systems, including outflow channels and paleolake basins through slope and area characterizations on a local and regional scale [137].

3.3.3. High Resolution Imaging Experiment (Mars Reconnaissance Orbiter)

The Mars Reconnaissance Orbiter is a 2005 NASA orbiter with the aim to search for long-term historical aquatic activity [103, 179]. The MRO carried the Context Camera (CTX) and HiRISE (High Resolution Imaging Experiment), which found new impact craters exposing water ice from the subsurface, which would sublimate over time as shown in Figure 3.7.

It also used subsurface radar and spectrometry to study the Martian climate and layered terrains, e.g. CRISM (Compact Reconnaissance Imaging Spectrometer for Mars) used for hydrated mineral mapping and SHARAD (Subsection 3.3.7) [103].
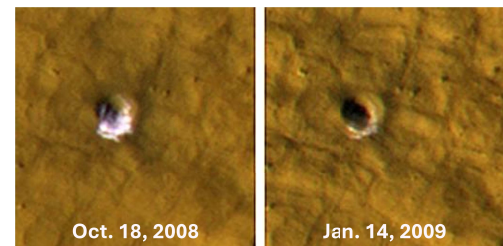
Figure 3.7: Exposed water ice sublimating out of fresh impact craters, as imaged by MRO, adapted from the National Aeronautics and Space Administration [104]

3.3.4. Gamma-Ray Spectrometer (2001 Mars Odyssey)

The 2001 Mars Odyssey (MO) orbiter started scientific operations in 2002 and remains operational to this date, making it the longest operational S/C at Mars. It carries the Gamma-Ray Spectrometer (GRS) [101], consisting of the Gamma Subsystem (GSS), Neutron Spectrometer (NS) and High Energy Neutron Detector (HEND), yielding both gamma-ray and neutron spectrometry capabilities, wherein the NS and HEND complement each other as the NS detects neutrons in lower energy bands and HEND focuses on high-energy fluxes [13, 102, 127].
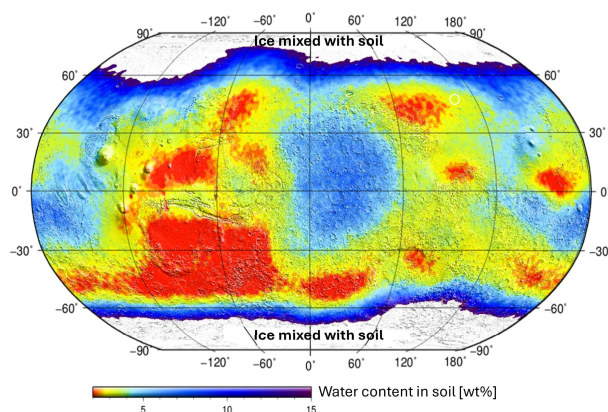
Figure 3.8: Global map of water (ice) in the Martian subsurface based on HEND data, adapted from the Space Research Institute of the Russian Academy of Sciences [138]
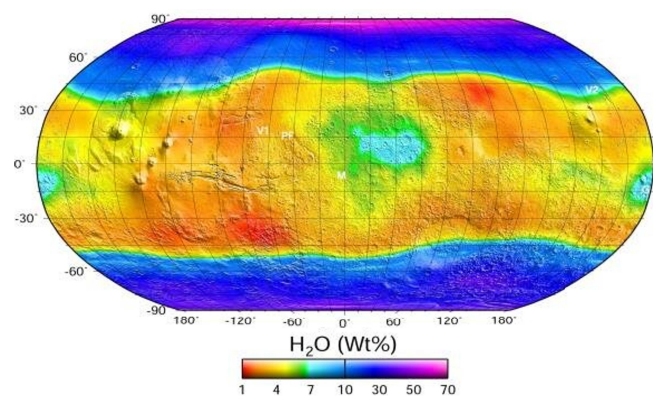
Figure 3.9: Global map of water (ice) in the Martian subsurface based on GSS data, retrieved from Martin [90]

Notable results include:

- **First global hydrogen abundance mapping:** GRS aimed to globally map the elemental composition of the Martian surface and was the first to determine the hydrogen abundance encapsulated in the Martian regolith [15, 127]. The neutron distributions are converted to maps such as shown in Figures 3.8 and 3.9.

- **Large non-polar water ice deposits:** Seen underneath the Arabia Terra between the Elysium and Amazonis Planitia, the Promethei Terra and southern Arcadia Planitia, spreading into the Vastitas Borealis Formation, and scattered widely in the mid-latitudinal to equatorial region, varying in concentration [49, 50, 95]

- **Abundant southern near-polar subsurface water ice:** GRS detected low southern near-polar ($\leq60°$ latitude) epithermal neutron flux, depressed by a minimum factor of two in comparison to near-equatorial regions [127] indicating abundant subsurface water ice. This finding was found to be consistent with numerical models expecting a rich water ice layer underneath a hydrogen-poor regolith layer, some of this ice laying near the surface even having been exposed by Viking observations [49, 127].

3.3.5. Bi-Static Radar Experiment (Mars Express)

Mars Express was the first ESA Mars orbiter and started scientific operations in 2004, staying operational to this day and featuring scientific discoveries such as mapping the complete chemical composition of the atmosphere and tracing the global water supply over time [43, 177]. The Bi-Static Radar (BSR) Experiment is an experiment performed using the Mars Express Radio Science Experiment (MaRS) of Mars Express (MEX) [43, 113].

The BSR experiments are performed in dual-frequency using a distinct S-band ($2.3GHz$; $\lambda = 13.1$ cm), and X-band ($8.4GHz$; $\lambda = 3.6$ cm) [129, 133]. The S-band measurements have higher uncertainty and deeper surface penetration, characterized by weaker echos, and higher compaction yielding ~10-50% higher ϵ values [133]. Other notable MEX BSR results include:

- **Stealth region:** MEX BSR experiments were performed specifically in the Stealth region [113, 134], a region in the Medusae Fossae which extends for approximately 2000 kilometers along the Martian equator, west of the Tharsis Montes, and is characterized by having no distinguishable radar return directly from Earth [39, 134]. The echo powers and retrieved dielectric constants are plotted in Figure 3.10.

- **Polar regions:** MEX BSR surprisingly showcased extremely smooth areas near the poles. These isolated patches extend over several hundred km^2 with RMS surface slopes around 0.17°, shown as narrow spikes in the power spectra [113].
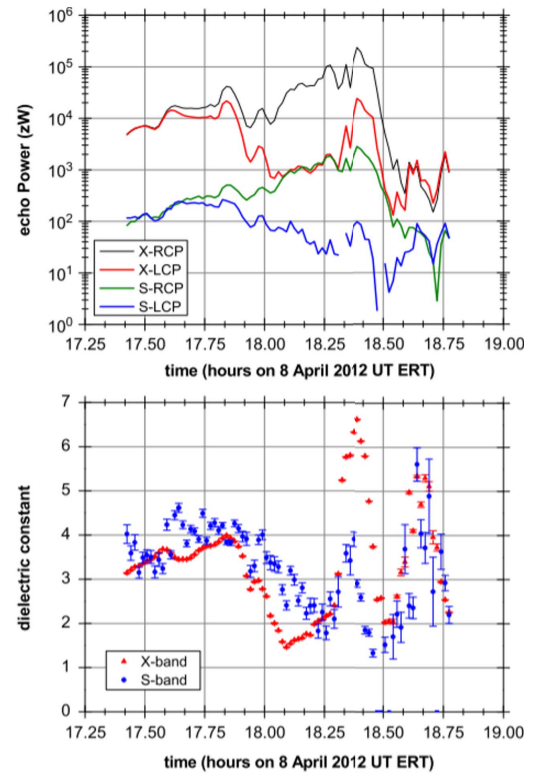
Figure 3.10: Echo powers and dielectric constants over the Stealth region with the MEX BSR experiment, retrieved from Pätzold et al. [113]

3.3.6. Mars Advanced Radar for Subsurface and Ionosphere Sounding (Mars Express)

The Mars Advanced Radar for Subsurface and Ionosphere Sounding (MARSIS) is a dedicated nadir-pointing Synthetic Aperture Radar (SAR) on Mars Express (MEX) with the primary objective to map (ice) water deposits in the upper crust [73, 108, 177]. MARSIS performance was optimized for deep penetration with a 150 m range resolution in free space (or 50-100 m depending on material permittivity) [109, 132]. Notable results include:

- **Medusae Fossae Formation (MFF):** The MFF is a discontinuous set of deposits along the dichotomy, hypothesized to be of pyroclastic origin or an ancient fluvial system [109]. It hosts the Stealth region (studied by MEX BSR as described in Subsection 3.3.5), Lucus Planum and Amazonis Mensa, all analyzed by MARSIS to characterize the MFF regions' ice content [108, 109]. The bulk ϵ was found to be ~2.9±0.4, closely consistent with pure water ice [108, 109, 166]. Expected thickness of MFF ice layers are mapped in Figure 3.11, where the Amazonis Mensa shows the best prospects. According to subsurface echos, it is layered similarly to the polar deposits, covered by a thick dry upper regolith cap [166]. Such layers are not expected in ash, dust or other such sediments [166] and GRS data (Subsection 3.3.4) also notes high WEH, increasing likelihood of a water (ice) deposit [50].

Figure 3.11: Thickness map of the MFF according to MARSIS data, retrieved from Watters et al. [166]

- **Vastitas Borealis Formation (VBF):** The VBF is a vast Hesperian-aged geological unit of the northern lowlands. Due to its smoothness, it is hypothesized to be a sublimation residue in which water (ice) laid from the surrounding outflow channels. Its low permittivity indicates high ground ice contents, where the resultant ϵ values are comparable to a combination of low-density sedimentary deposits and water-ice, creating an ice-rich layer of several tens of meters deep. [108]

- **Athabasca Valles:** The Athabasca Valles is a morphological structure, possibly formed by massive fluvial discharge of melting ground ice or crystallized low-viscosity lava. MARSIS results suggest dielectric characteristics of volcanic origin, but more deeply-buried ice deposits are still deemed likely. [108]

- **Meridiani Planum:** The Meridiani Planum showcases abundant hydrated mineral content hypothesized to have been created through the presence of groundwater [167]. Its bulk ϵ measured by MARSIS varies around 3.6 ±0.6, consistent with a high water (ice) content [167]. However, these values may also be a result of ice-free highly porous, wind-deposited sand, volcanic ash or silicate dust [167].

3.3.7. Mars SHAllow RADar sounder (Mars Reconnaissance Orbiter)

The Mars SHAllow RADar sounder (SHARAD) is a chirped sounding radar on the Mars Reconnaissance Orbiter (MRO) with a frequency centered at 20 MHz, made to complement MARSIS [130, 132]. Due to the higher frequency, SHARAD attains a finer vertical resolution at lesser penetration depth [73, 109, 132]. It maps dielectric interfaces associated with geologic layering in local regions, attaining results on the subsurface composition and water (ice) deposits [130]. It works in targeted mode [122], with scientific targets including stratigraphically relevant regions, volcanic complexes and water (ice) deposits [121, 130] with notable results:

- **North Polar Layered Deposits:** SHARAD spent significant time the North Polar Layered Deposit (NPLD), showcasing a bulk average ϵ consistent with almost pure water ice and only a few percent dust [76].

- **Utopia Planitia:** Utopia Planitia is hypothesized to contain substantial shallow subsurface ice [140], remnant of Hesperian outflow and periglacial activity [165]. SHARAD found significant subsurface ice on its western side, with ice-rich regolith ~10-170 m deep [165] and permittivities around 2.8 ± 0.8 consistent with a mixture of air, dust and 50-85 vol% (volume percent) water [140]. Regretfully, the Viking 2 landing site which also lays in the Utopia Planitia, showed no apparent such subsurface return [122].

- **Central Elysium Planitia (CEP):** The CEP includes interesting regions such as the MFF and Cerberus plains. Like MARSIS, SHARAD investigated the MFF and found bulk dielectric constants of ~2-3 [121]. However, SHARAD only detected ~300 m deep basal reflectors within limited regions of the MFF, where increasing density with depth can be attributed to self-compacting dry material [121]. Overall, the MFF seems a hybrid deposit with sediments placed on something like minimally compacting low-loss ice deposits [121]. The Cerberus plains is a broad low-lying plain within the CEP, with four identified outflow channel systems [184]. Subsurface reflectors were found at 120 m, in combination with $\epsilon \approx 3.12$, consistent with water ice (although it can alternatively fit with ice-poor but porous sediments) [80].

- **Green Valley:** The Green Valley is hypothesized to have layered shallow subsurface water ice to ~10 m depths, evidence of which was found by the Phoenix Robotic Arm (Subsection 3.4.1) [122, 181]. GRS already detected high WEH levels throughout the region [122], and SHARAD found permittivities of ~3.15-8, supporting the dominance of interstitial shallow ground ice surrounded by regolith [122].

3.3.8. Fine Resolution Epithermal Neutron Detector (ExoMars Trace Gas Orbiter)

The ExoMars Trace Gas Orbiter (TGO) is part of the ExoMars 2016 mission, it is currently active in its low 400 km circular orbit where it detects and monitors atmospheric trace gases [100, 173]. It carries the Fine Resolution Epithermal Neutron Detector (FREND) instrument, a neutron telescope, driven by heritage of the GRS neutron emission maps [94]. It aims to map WEH levels in the shallow (first 1-2 m) subsurface at high spatial resolution, 60 to 200 km, through use of a collimation module and limited detector Field of View (FoV) to identify local hydrogen-rich areas, correlate with regional topography and study landing sites [86, 94, 96, 97].
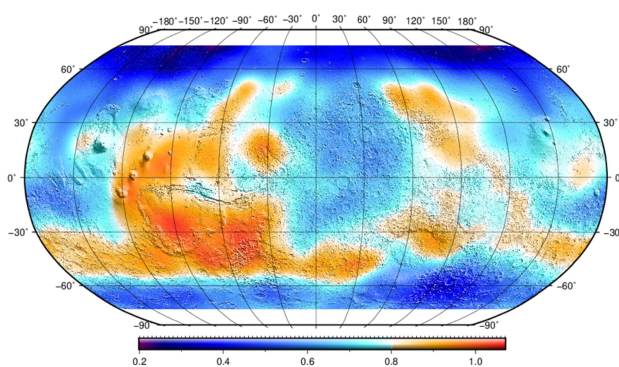
Figure 3.12: Global map of water (ice) in the Martian subsurface based on FREND data, retrieved from Svedhem [144]
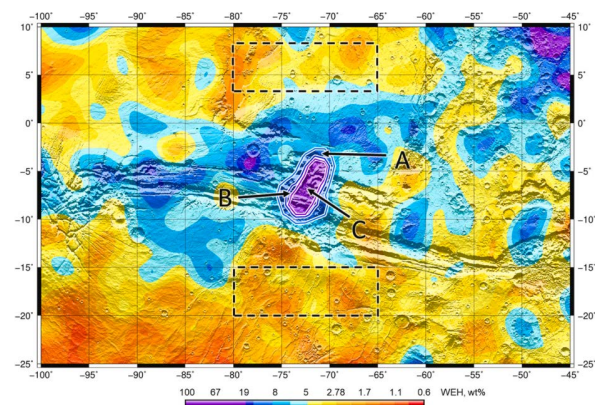
Figure 3.13: Local map of water (ice) in the Valles Marineris based on FREND data, adapted from Mitrofanov et al. [96]

FREND data ranges from 74°S to 74°N latitude, dictated by TGO's orbit inclination [94], but most measurement campaigns thus far aimed at the near-equatorial region from 40°S to 40°N [85, 86]. Figure 3.12 showcases the current status of global processed FREND data and local notable results include:

- **MFF:** A weak epithermal flux was identified in the Medusa Fossae Formation, yielding WEH levels of ~30-82 wt % [86]. Consistent with earlier mission results, this points at semi-pure water ice deposits [86].

- **Xanthe Terra:** The Xanthe Terra lays north-east to the Valles Marineris. FREND data indicates a significant deposit of hydrated minerals and sporadic deposits of semi-pure water ice toward 1 m deep [86]. Water content of these regions was around tens of wt%, including strong statistical certainty (above 3σ) [85].

- **Arabia Terra:** GRS measurements indicated a high WEH content (for near-equatorial cases) in the Arabia Terra regions, reaching values around 10 wt% (likely indicative of hydrated mineral deposits [82]), with which FREND data was in agreement and additionally found regional values of 30-90 wt% [86].

- **Orcus Patera:** The Orcus Patera is a morphological feature of volcanic, tectonic or impact origin. FREND found WEH levels of ~34 to almost 100 wt% indicating definitive water ice presence [86]. It is hypothesized to have formed from an Amazonian lake and is a main contender for primitive biological indicators [86].

- **Valles Marineris:** The Valles Marineris is a prime suspect for subsurface water (ice), with FREND also showcasing highly suppressed neutron emission with WEH values up to 40.3 wt% [96]. Regional data from 2018-2021 is shown in Figure 3.13. Later measurements agreed with the water-rich maxima, but yielded higher average WEH levels of 6.38 wt% [84]. The high variation shows morphological features and topography in the formation, having formed in different geological periods, can coexist [55].

- **Gale crater:** Gale crater has shown conflicting measurements of HEND and the Curiosity rover [87]. HEND measured WEH values around 5 wt% whilst ground measurements were around 1-3 wt% [87]. FREND measurements showed variable WEH levels of 1.79-41.4 wt% averaging at 5.41 wt% [87].

3.3.9. Mars Orbiter Subsurface Investigation Radar (Tianwen-1 Orbiter)

The Tianwen-1 orbiter was part of the first successful Chinese Mars mission with the Zhurong rover (Subsection 3.4.2), arriving in 2021 to study the Martian topography and geology [182]. It carried the Mars Orbiter Subsurface Investigation Radar (MOSIR), a subsurface radar sounder for investigating the composition and structure, including water (ice) and biological marker detections at, e.g., the Zhurong landing site [48, 110, 185].

Unlike MARSIS and SHARAD, MOSIR has two sets of orthogonal dipole antennas that are capable of receiving cross-polarization echoes [48]. The MOSIR operates at dual frequency in three bands: 10-15, 15-20 and 30-50 MHz [48, 110]. This translates in a penetration depth of several hundred metres at vertical resolutions of ~7.5 m (20 MHz bandwidth) or ~30 m (5 MHz bandwidth) in free space [48]. Since limited literature is available on the results of the MOSIR instrument for the near-equatorial region, no notable results can be presented.

3.3.10. International Mars Ice Mapper (Mission Concept)

The International Mars Ice Mapper (I-MIM) is a mission concept in coordinated development between multiple space agencies, preparing for launch in 2031 [6, 163]. I-MIM aims to map and characterize accessible shallow subsurface water ice at mid-to-low latitudes for support of future human exploration [6, 77] through three objectives: map the distribution of water (ice) deposits in the first 10 m depth, characterize accessibility through geotechnical properties and candidate landing site assessment for human exploration [6, 35, 163]. Locations of interest were mapped with potential water (ice) deposit locations for mid-latitudes in Figure 3.14.
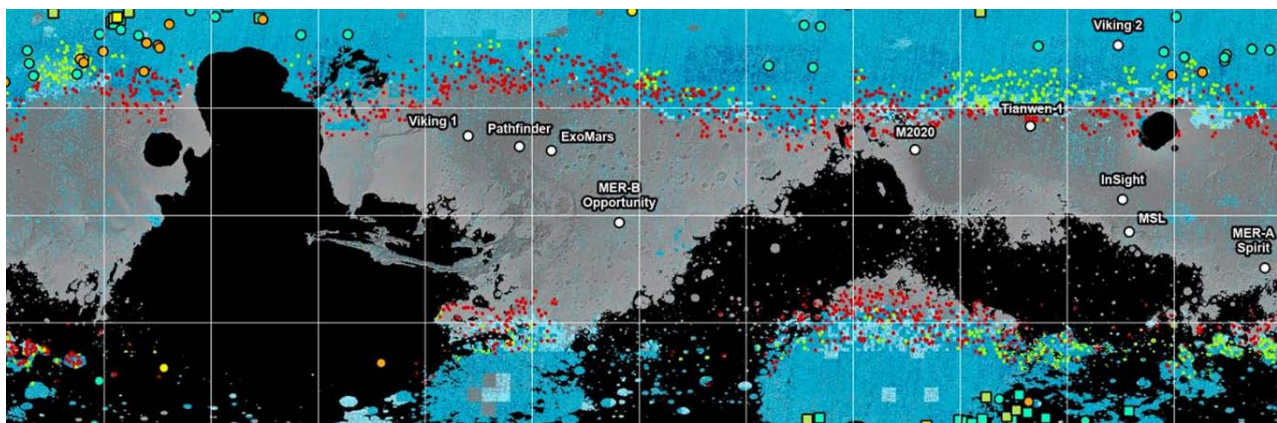
Figure 3.14: Potential mid-latitudinal water (ice) deposits as mapped for I-MIM concept development, retrieved from Lavagna et al. [77]

The main I-MIM payload is an L-band polarimetric SAR operating at 930 MHz, capable of acquiring images in two circular polarizations [5]. It would operate in side- and nadir-oriented SAR sounding with high radiofrequency bandwidth [6], following similar operations strategies to MARSIS and SHARAD [77]. The vertical resolution is expected to be less than one meter, depending on subsurface properties [4]. Supplementary payloads for radar research include a shallow radar sounder at Very High Frequency (VHF) from 100-250 MHz and a submillimeter sounder [5, 3, 164]. Concept development is performed by an international Measurement Definition Team (MDT) [163], which published a final (baseline mission) report in September 2022 [77].

3.4. Relevant Missions for In-Situ Water Research

This section presents in-situ missions, instruments and experiments which have or will contribute to water research on Mars. This includes: The Robotic Arm on the Phoenix Mars Lander (Subsection 3.4.1), Rover Subsurface Penetrating Radar on the Tianwen-1 Rover (Subsection 3.4.2), Radar Imager for Mars' subsurface experiment on the Perseverance rover (Subsection 3.4.3), and lastly, the Water Ice and Subsurface Deposit Observation on Mars instrument planned for the ExoMars rover (Subsection 3.4.4).

3.4.1. Robotic Arm (Phoenix Mars Lander)

The Phoenix lander was a 2007 NASA mission researching polar climate, weather and surface interaction for 90 sols (Mars day; equal to one day and 37 minutes on Earth). It landed in the Green Valley, a relatively homogenous high-latitude part of the VBF dominated by polygonal morphology with high expectancy of shallow subsurface water ice [74, 92, 122, 131, 181]. Its Robotic Arm (RA) has four degrees-of-freedom (DoF) with a reach of 2.4 m [11]. The end effector carries the Icy Soil Acquisition Device (ISAD), Robotic Arm Camera (RAC) and the Thermal and Electrical Conductivity Probe (TECP) [11]. It mapped its landing site [74], yielding:

- **Uncovered ice sublimating away over time:** The RA dug trenches in attempt to to find definitive locations of subsurface water ice. Over its lifetime, it dug twelve trenches, studied its landing thruster pits and took 31 samples within its ~3 m^2 landing site workspace [2, 92], shown partially in Figure 3.15. Eight trenches uncovered subsurface water ice of two types: ~10% bright slab-like (almost) pure water ice (e.g. in the Dodo-Goldilocks trench) and ~90% darker deposits diffused into the soil pores with ~30 ± 20 wt% water ice content (e.g. in the Snow White trench) [33, 92]. The Dodo-Goldilocks trench shown was the first location where ice was uncovered (on sol 7) laying at 3 cm depth under a cloddy soil cover, indicated by the visual appearance and spectral reflectance properties consistent with water ice and 1-2 wt% soil [2]. In sublimation loss studies, centimeters of icy soil disappeared between sols 20 and 24 (Figure 3.16).

- **Materials landing site:** The RA workspace contains three material types: soil, icy soil and semi-pure ice deposits, where soil is any unconsolidated surface material that has undergone soil formation processes [131]. Data is acquired by the ISAD by digging, rasping (high ice content soil is impenetrable for the blades due to ice cementing underneath penetrable soil [131]), dumping and acquiring samples [11].

Figure 3.15: Part of the RA workspace (sol 53), retrieved from Arvidson et al. [2]
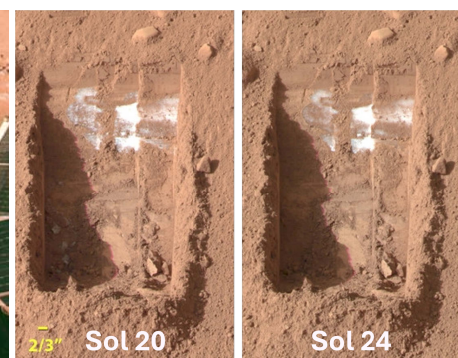
Figure 3.16: Phoenix finding of water ice sublimating away out of dug trenches, adapted from Jet Propulsion Laboratory [70]

3.4.2. Rover Subsurface Penetrating Radar (Tianwen-1 Rover)

The Rover Subsurface Penetrating Radar (RoSPR), or Rover Penetrating Radar (RoPeR) [29, 78, 185], is an instrument on the Tianwen-1 (Zhurong) rover [187]. It is intended to complement the MOSIR (Subsection 3.3.9) with in-situ surveys of its landing site [48], aiming to characterize the upper soil thickness, subsurface water ice deposits and local stratigraphy along its path [79, 185]. This includes soil structure identification and data collection on the soil types, deposition and stratification characteristics and water (ice) content [157]. Zhurong landed in the Utopia Planitia in 2021 [182, 185]; the largest impact basin in the northern hemisphere with an

extensive cover of sedimentary material, characteristic smooth morphology [185] and significant VBF material residual of igneous materials chemically altered by an ancient ocean [29, 71, 78, 188]. Prior morphological analysis and observations all indicate subsurface water (ice) deposits at its upper latitudes [49, 71, 140, 185].

RoSPR findings allow a four-layer division: the first ~10 m has an average ϵ of ~3-4, then ~10-30 m shows an increase to ~4-6 without a sharp interface, indicating rocky blocks of increasing size with depth, ~30-80 m shows similar reflection patterns with ϵ ranging from ~6-7 (more evenly distributed rocks), and the basal layer below 80 m shows the signal has highly attenuated, but is hypothesized to be a continuation of rocky blocks from numerical simulation [78]. Results for the first months of operation (May to September 2021) are shown in Figure 3.17. The average dielectric

Figure 3.17: Variation of the permittivity along the Zhurong rover track, retrieved from Li et al. [78]

constant ranges from 1.6-6.7 at effective high-frequency detection depths of 4.5 m [186]. The low-frequency radar returned up to 80 m depth, eliminating probable existence of a hydrated layer, which would showcase much higher attenuation [78]. However, a multitude of hydrated minerals were found at the landing site, pointing at an active fluvial history and it is not yet possible to rule out saline ice presence [71, 79].

3.4.3. Radar Imager for Mars' subsurface experiment (Perseverance Rover)
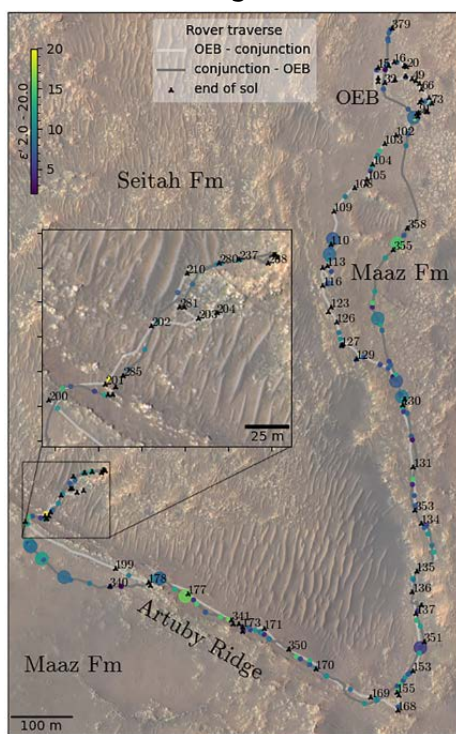
Figure 3.18: Along-track ϵ from RIMFAX data (1.9±1.1 m depth), retrieved from Casademont et al. [27]

The Perseverance rover is part of the NASA Mars 2020 mission and has been conducting mobile in-situ surface studies of Jezero Crater [176]. It carries the Radar Imager for Mars' subsurface experiment (RIMFAX): A ground penetrating Frequency Modulated Continuous Wave (FMCW) radar [60, 188], primarily for detection of near-surface geological structures and water (ice) deposits through study of stratigraphy and dielectric properties, yielding insight into (past) habitability conditions [60, 188].

Operations of RIMFAX are divided in three modes of operation: deep, shallow and surface mode, each with its own radar parameters set to maximize the quality of data collection for the respective subsurface conditions [60]. It aims to investigate the shallow subsurface by transmitting a signal which sweeps through an operational range of 150-1200 MHz (or free-space λ of 2 to 0.25 m [27]), with an effective center frequency of 675 MHz, rather than single pulses [60]. This full bandwidth allows for penetration of only a few meters, and reduced bandwidth at lower frequencies (centered at 375 MHz) is used for deeper structures [60, 188]. RIMFAX found an average permittivity in Jezero Crater of 9.0±2.8 at a mean depth of 1.9±1.1 m, corresponding to a bulk density of 3.2 g/cm^3 and expected origin as igneous deposition or sedimentary layering from fluvial activity [186]. Lower ϵ values of 8.0 are also presented [27], where the upper surface layers are interpreted to be mainly solid bedrock of volcanic origin with along-track ϵ values shown in Figure 3.18.

3.4.4. Water Ice and Subsurface Deposit Observation on Mars (ExoMars Rover)

The ExoMars rover is the second part of the ExoMars 2016 mission, planned to launch in 2028 and search for ancient and present bio-signs in Oxia Planum, on the eastern border of the Chryse Planitia [174]. It will carry the Water Ice and Subsurface Deposit Observation on Mars (WISDOM) instrument, the third rover-mounted Ground Penetrating Radar (GPR), following RoSPR (Subsection 3.4.2) and RIMFAX (Subsection 3.4.3).

WISDOM covers a UHF range of 0.5-3 GHz and possesses over two orthogonal linearly polarized transmitters and two co- and cross-polar receivers [66]. It is a stepped FMCW radar which takes a number of harmonic pulses for each sounding whilst sweeping the instrument bandwidth. The image of the subsurface can be built up according to the varying subsurface permittivity [10, 30]. Its aim is to sound the subsurface to depths of 3-10 m and map the general stratigraphy along its path with a vertical resolution of ~3 cm [10, 30]. Its operations include along-track measurements and targeting areas of scientific interest, where surveys are conducted in parallel profiles to create interpolated three-dimensional maps of the local stratigraphy [30].

4

MEX-TGO Bi-Static Radar Targets

This chapter discusses the targets for the MEX-TGO BSR measurements, as follow from prior Mars research presented in Chapter 3. Section 4.1 re-iterates prior and future landing locations, Section 4.2 lists requirements for the target locations and Section 4.3 discusses the actual locations which are attempted to be studied.

4.1. Landing Locations

Landing locations of all successful prior Mars landers, and the prospective landing site for the ExoMars rover, are shown in Figure 4.1. These locations are automatic Locations of Interest (LOI) for the MEX-TGO BSR, as prior study and characterization by other instruments allows for correlation between different techniques [164].
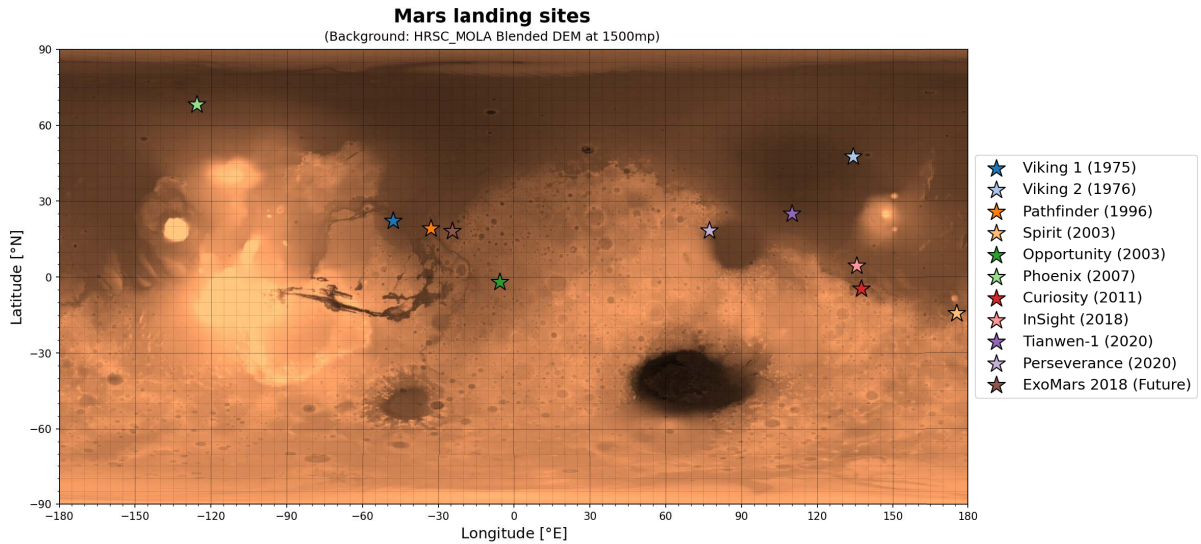
Figure 4.1: Map of previous and future landing sites, own work

4.2. Target Requirements

A cohesive set of main and backup Scientific Target Locations (STLs) is selected from a larger list of LOI, presented in Section 4.3. For this, four requirements are defined, indicated by the 'REQ-TAR' identifier, stating:

- **REQ-TAR-1: All STLs shall be located within the near-equatorial band of 40°S to 40°N latitude.**
  Interest of MEX-TGO BSR is for the near-equatorial region, where likelihood for bio-signatures and relevance to future human exploration is highest. The ±40° band is chosen from literature, e.g. as used by Malakhov et al. [85].

- **REQ-TAR-2: A total of four LOI shall be dictated as the main STLs.**
  It was assumed to have a three-month measurement lead-time and possibility to take measurements once a week [144]. The latter follows from the limit imposed for eight coordinated MEX-TGO measurements per MTP [22], where the other half is put to Mutual Occultation measurements. For the initial thesis planning measurements were expected to take place over the course of eight weeks, from mid-June to mid-August. Therefore, if a measurement is taken once a week and each location is measured twice, the amount of main STLs is limited to four.

- **REQ-TAR-3: One STL shall be a 'calibration location' for definitive subsurface water ice detection.**
  In order to confirm and correlate the measurement data at the STLs, they should be compared to the results at a location of definitive subsurface water (ice) presence, i.e. a 'calibration location'.

- **REQ-TAR-4: Each main STL shall have a corresponding backup STL.**
  It is deemed likely not all main STLs selected will fit with the orbit, time and science planning constraints of MEX and TGO. Therefore, each should have a backup in case the main STL is not feasible.

15

4.3. **Target Locations**

Following research presented in Chapter 3 and prior/future landing locations of Section 4.1, twelve locations are selected as LOIs for scientific purposes (LOI-S), or potential STLs. These include (in no particular order):

- **LOI-S-1: Chryse Planitia**
  The Chryse Planitia was among the first regions imaged by Mariner 9, revealing abundant outflow channels [63]. It has since been studied extensively, with neutron spectrometers showcasing modest potential for water ice, and hosting the landing sites of the Viking 1 (22.24°N 228.01°E) and Pathfinder (19.13°N 213.22°E). It also contains the planned landing site for the ExoMars 2028 rover (18.28°N 204.63°E), which aims to find ancient bio-signatures and water ice deposits in the Oxia Planum, an eastern deposit of water-rich clays [125, 174].

- **LOI-S-2: Utopia Planitia**
  The Utopia Planitia re-surfaced during the Amazonian period [155] and has been proposed as a likely subsurface ice site due to its morphology and significant deposits found by SHARAD on its western side [140, 165], but neutron spectrometers have had limited success in correlating this. It also contains the landing sites of Viking 2 (47.64°N 134.29°E) and Tianwen-1 (25.07°N 109.93°E) [183], but regretfully neither have confirmed water ice presence.

- **LOI-S-3: Elysium Planitia**
  The Elysium Planitia is supported by neutron spectroscopy and radar sounding as a promising region for water ice deposits [49, 80]. It contains the landing sites of InSight (4.50°N 135.62°E), Curiosity (-4.59°N 137.44°E) and Spirit (-14.57°N 175.47°E). However, although in-situ measurements (by Curiosity in Gale Crater) found evidence of an ancient water stream bed and fresh water lake, these indicated lower WEH than orbital data [87, 180].

- **LOI-S-4: Meridiani Planum**
  The Meridiani Planum contains the landing site of Opportunity (-1.95°N 354.47°E), which found extensive hydrated mineral deposits (shown in Figure 2.2) and bedrock altered by aquatic activity [40], consistent with high WEH levels from neutron spectroscopy. Radar sounding revealed dielectric constants consistent with high water ice content, but this is likely attributed to ice-free highly porous wind-deposited materials [122, 171].

- **LOI-S-5: Isidis Planitia**
  The Isidis Planitia contains the landing site of Perseverance (18.44°N 77.45°E), whose RIMFAX instrument found little to no expectancy of subsurface ice in Jezero Crater [27, 142, 186]. Instead, as also revealed by neutron spectroscopy as high WEH levels, the region mainly contains hydrated mineral deposits [87], shown in Figure 2.2.

- **LOI-S-6: Valles Marineris**
  Valles Marineris lies near the equator and is one of the most scientifically exciting regions on Mars [84, 96, 145]. Its origin is deemed likely to be in chaotic fluvial erosion following tectonic fracturing [55, 99]. FREND data indicated local regions of highly suppressed neutron emission, suggesting potential subsurface water ice deposits in addition to the hydrated minerals found in the region (specifically the Aram Chaos impact crater on the eastern side) [40, 96].

- **LOI-S-7: Orcus Patera**
  Orcus Patera is a depression in the Elysium Planitia, hypothesized to have formed through Amazonian lacustrine activity, showcasing promise for biosignature detections. FREND found almost definitive proof for water ice [86].

- **LOI-S-8: Medusae Fossae Formation**
  The MFF is a region of discontinuous deposits laying along the dichotomy, expected to be an ancient fluvial outflow system [109]. Radar sounding has shown potential water ice deposits underneath a dry sediment layer [166]. However, SHARAD found varying properties, causing expectancy of the MFF to be a relatively hybrid deposit, including limited locations of considerable water ice content [121]. GRS also showcased significant WEH, which due to the lack of definitive hydrated mineral content, increases the likelihood of a water (ice) deposit [50].

- **LOI-S-9: Arcadia Planitia**
  The Arcadia Planitia is a region in the northern lowlands, north to the Amazonis Planitia, near the Green Valley and spreading into the VBF [50]. It was found to have significant WEH levels and expected local ice deposits.

- **LOI-S-10: Arabia Terra**
  The Arabia Terra is a hydrated mineral deposit [82], showcasing high WEH levels in neutron spectroscopy [49, 86], with FREND data finding regional values of 30-90 wt% [86]. It represents one of the most enlightening regions on Mars whose water abundance was identified and mapped by gamma-ray/neutron spectrometry [84].

- **LOI-S-11: Xanthe Terra**
  Xanthe Terra is a morphological formation northern to the Valles Marineris, found to contain high WEH levels by FREND [85]. It is seemingly a hydrated mineral deposit, but may contain sporadic shallow water ice [86].

- **LOI-S-12: Promethei Terra**
  Promothei Terra lays along the Hellas Planitia, which contains considerable hydrated mineral deposits. This is reflected in results from neutron spectroscopy, with especially GRS finding significant WEH levels [50].

Additionally, some LOI were identified as guaranteed ice deposits, designated calibration LOI (LOI-C):

- **LOI-C-1: MRO Impact Crater**
  The MRO high resolution camera found impact craters in the northern hemisphere, exposing ice sublimating over time [104]. For example, the crater at 43.28°N 164.22°E (Figure 3.7), on the eastern edge of Utopia Planitia.

- **LOI-C-2: Green Valley**
  The Green Valley contains the landing site of Phoenix (68.22°N 234.25°E), which acquired definitive in-situ proof of water ice presence underneath the top soil [49], shown in Figure 3.16.

- **LOI-C-3: S1094b Crater (Amazonis Planitia)**
  The Amazonis Planitia lies north to the MFF and contains features of likely fluvial origin, e.g. the Mangala Valles expected to have been carved by a catastrophic flood [7]. The S1094b crater (35.1°N 189.8°E) formed in the Amazonis Planitia and is the lowest latitude where a substantial water ice deposit has been exposed [80].

The main calibration (STL-C-Mx) and scientific STLs (STL-S-Mx) and backup calibration (STL-C-Bx) and scientific STLs (STL-S-Bx) are selected according to the requirements of Section 4.2 and water ice expectancy:

- **STL-C-M1: S1094b Crater (LOI-C-3) & STL-C-B1: MRO Impact Crater (LOI-C-1)**
  The S1094b crater lies in the Amazonis Planitia, a well-suited region for calibration studies. The MRO Impact Crater lies just outside 40°N (whereas the Green Valley lays at over 60°N), near the Utopia and Elysium Planitia.

- **STL-S-M1: Utopia Planitia (LOI-S-2)**
  The Utopia Planitia is debated on water ice presence with some indication from neutron spectroscopy, but no definitive proof, making it highly relevant for further study via BSR.

- **STL-S-M2: Elysium Planitia (LOI-S-3)**
  The Elysium Planitia has notable water ice expectancy from neutron spectrometers and orbital radars, but in-situ measurements conflict these results, making it relevant for study via BSR, especially around Orcus Patera (LOI-S-7).

- **STL-S-M3: Valles Marineris (LOI-S-6)**
  The Valles Marineris is one of the most significant regions for Mars' aquatic history. FREND shows considerable local neutron suppression, and only limited hydrated mineral presence, making it highly relevant for study via BSR.

- **STL-S-B1: Medusae Fossae Formation (LOI-S-8)**
  The MFF has been broadly studied and has potential for water ice within its hybrid deposits. However, it is a small region near the Elysium Planitia, limiting measurement potential and making it a backup STL.

- **STL-S-B2: Chryse Planitia (LOI-S-1)**
  The Chryse Planitia has slight expectancy of water ice, less than the main selected regions, but lays near the Valles Marineris. It is therefore selected as a backup STL.

- **STL-S-B3: Xanthe Terra (LOI-S-11)**
  The Xanthe Terra is expected to contain sporadic water ice, but mainly hydrated mineral deposits. It lays near Valles Marineris and would be interesting for further study, it is therefore selected as a backup STL.

These are mapped in Figure 4.2, using the USGS (United States Geological Survey) geologic map of Mars [154].
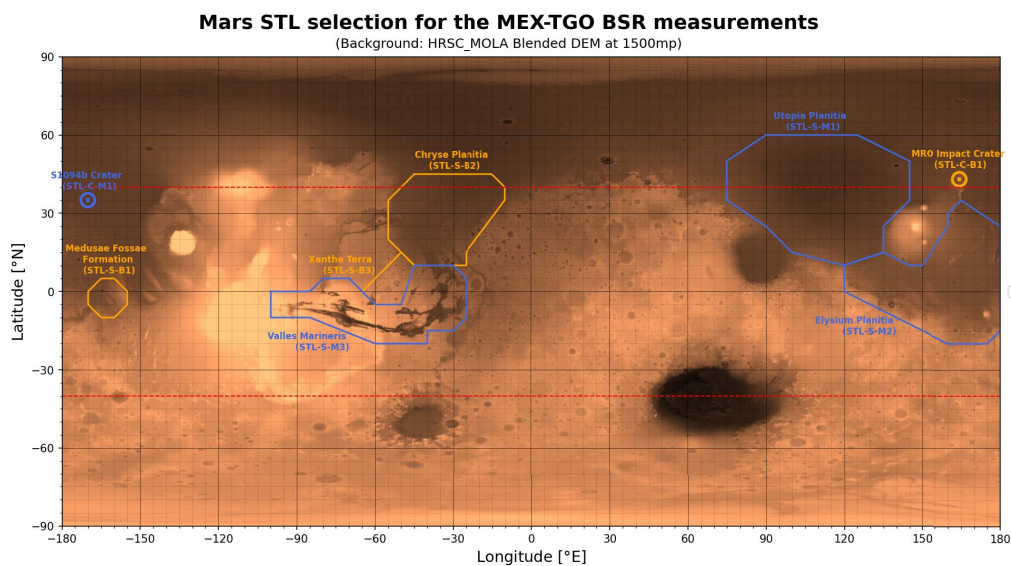
Figure 4.2: Selection of the STL locations for the MEX-TGO BSR measurements, own work

5

Measurement Planning

This chapter discusses the planning phase for the MEX-TGO BSR measurements. Section 5.1 describes the overall methodology and Section 5.2 presents a detailed description of the model used for locating measurement opportunities. Then, Section 5.3 discusses the results of the measurement planning phase, including both those proposed to the European Space Astronomy Centre (ESAC) as well as those actually performed (and to be performed). Lastly, Section 5.4 presents a short discussion on the results and encountered limitations.

5.1. Methodology

This section describes the measurement planning methodology. Subsection 5.1.1 goes into the non-ideal measurements, requested prior to detailed analysis into MEX-TGO BSR planning. Subsection 5.1.2 describes the methodology for finding ideal measurements at locations of interest, which were proposed to ESAC.

5.1.1. Non-ideal Measurements

MEX-TGO BSR follows from the MEX-TGO Mutual Occultation experiment, during which several measurements in MTP257/76 (Medium Term Plan; 257 for MEX and 76 for TGO) were performed at the incorrect switch-ON time and no occultation took place, instead the signal reflected via the surface. These signals were significant enough to detect, but at non-ideal geometries [152]. These measurements are designated BSR campaign 1; relevant parameters are tabulated in Table 5.1 and Figure 5.1 shows the specular point (spoint) tracks.

Table 5.1: BSR campaign 1: January and February 2024 measurement data (MTP257/76)

ID	Timeframe	Observed region		MEX-TGO distance [km]		Equal-emission angle [deg]	
		Name	ID	Minimum	Maximum	Minimum	Maximum
BSR-1.1	2024 January 23rd 03:49:07 - 2024 January 23rd 03:59:07	N/A; Vastitas Borealis	N/A	5260.94	5798.26	1.90	28.52
BSR-1.2	2024 January 30th 10:30:44 - 2024 January 30th 10:40:44	N/A; Vastitas Borealis	N/A	6713.22	8111.79	35.71	69.98
BSR-1.3	2024 February 6th 09:43:22 - 2024 February 6th 09:53:22	N/A; Vastitas Borealis	N/A	4461.97	5921.18	26.17	70.24
BSR-1.4	2024 February 11th 01:53:19 - 2024 February 11th 02:03:19	N/A; Vastitas Borealis	N/A	5560.50	6473.33	12.07	29.06
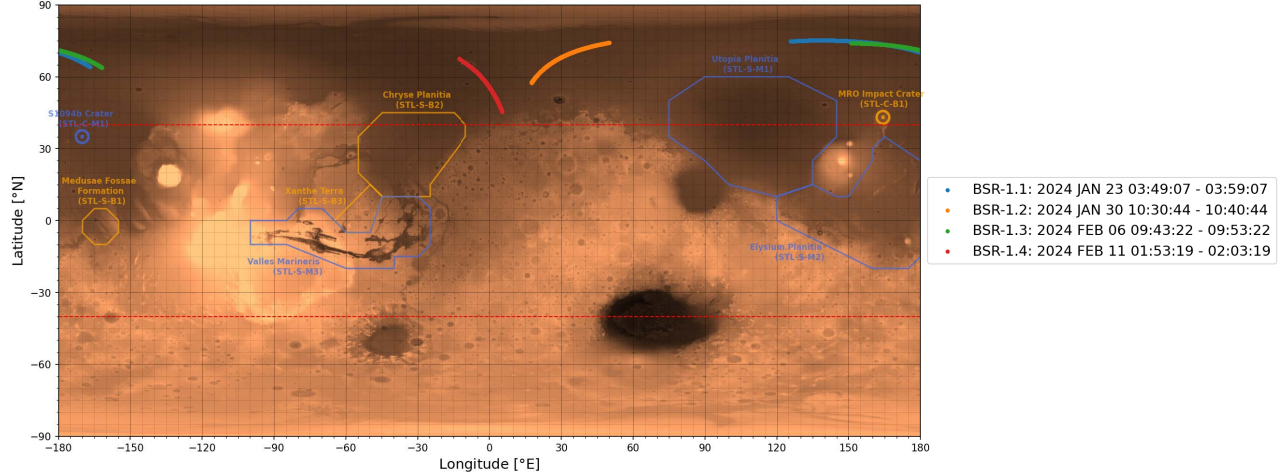
Figure 5.1: BSR campaign 1: Ground tracks for the January and February 2024 measurements (MTP257/76), own work

The specular point is defined as the point on ellipsoidal Mars of equal emission angles with respect to both spacecraft, and at the same time the surface normal vector and vectors to the two S/C all lay in the same plane. It is the expected point of highest reflection and closely resembles a ground track and is therefore used as reference. The implications and validity of this assumption will be discussed in Subsection 6.4.1.

Furthermore, to guarantee data availability for the numerical simulations, two additional measurements were planned in early 2025, MTP272/91, requiring a MEX-TGO distance under 1000 km at the lowest point of the pass. This occurred roughly once every nine orbits in MTP272/91, two of which did not conflict with TGO exclusion or lander visibility periods [23]. For both passes, the specular points move from ~60°N to 80°N latitude [23]. This enters the NPLD, allowing for calibration of well-confirmed water ice with near-equatorial measurements. Relevant measurement data is tabulated in Table 5.2 and Figure 5.2 shows the ground tracks.

Table 5.2: BSR campaign 2: March and April 2025 measurement data (MTP272/91)

ID	Timeframe	Observed region		MEX-TGO distance [km]		Equal-emission angle [deg]	
		Name	ID	Minimum	Maximum	Minimum	Maximum
BSR-2.1	2025 March 20th 23:40:54 - 2025 March 20th 23:50:54	N/A; Vastitas Borealis & NPLD	N/A	557.11	1618.99	31.81	61.13
BSR-2.2	2025 April 5th 16:56:04 - 2025 April 5th 17:06:04	N/A; Vastitas Borealis & NPLD	N/A	502.20	2390.42	22.55	78.54
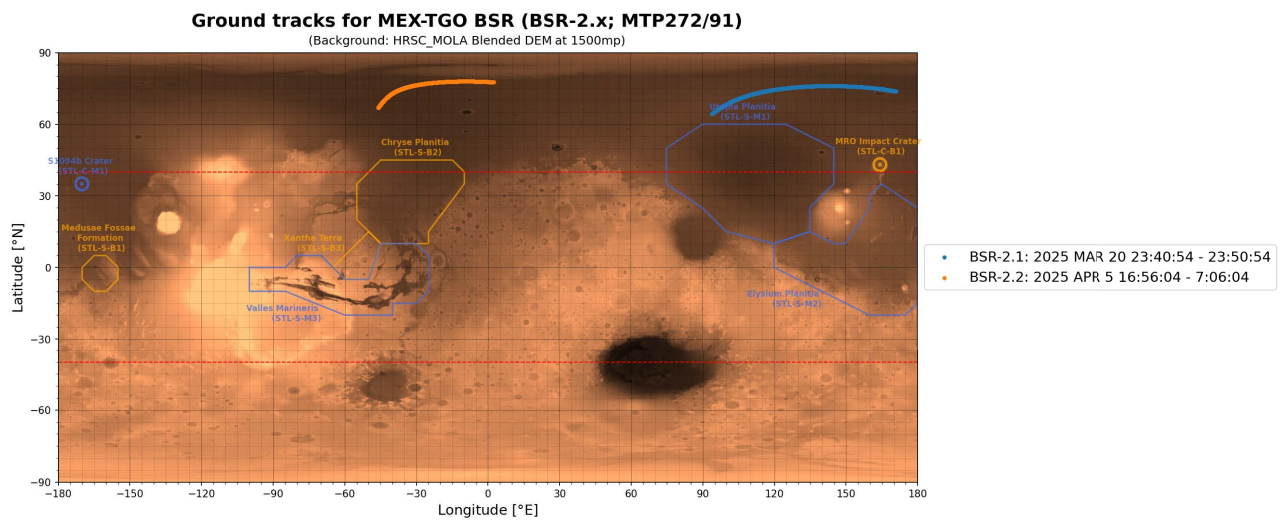
Figure 5.2: BSR campaign 2: Ground tracks for the March and April 2025 measurements (MTP272/91), own work

5.1.2. Ideal Measurements

For the ideal measurements, a numerical model was written in Python to retrieve times at which the specular point track crosses regions of interest, mapped in Figure 4.2 and discussed in Chapter 4. Furthermore, BSR conditions are optimized by restricting the measurement duration and geometry, employing the SPICE information system[1], SpiceyPy interface[2,3] and the MEX and TGO orbits which have the basic orbital parameters as shown in Table 5.3, using SPICE kernels from the Navigation and Ancillary Information Facility's SPICE Data Archive[4] (all of which were used are listed in Appendix A).

Table 5.3: Orbital parameters of MEX and TGO, retrieved from Svedhem et al. [153]

Orbit	Mars Express (MEX)	ExoMars Trace Gas Orbiter (TGO)
Pericenter altitude	$330 km$	$380 km$
Apocenter altitude	$10530 km$	$430 km$
Inclination	$86.9°$	$74°$
Period	$\sim 7 hrs.$	$\sim 2 hrs.$

The methodology for the measurement planning is to run a time frame, specifically a MEX/TGO MTP, through a series of checks. These assess the feasibility of measurements over these time spans in an order decreasing in computational cost, keeping the user updated through terminal print statements and generating a log file. This yields the overarching code architecture in Figure 5.3. The measurement planning model, named 'main_MEXTGOBSR_measurementplanning.py', can be accessed on the thesis GitHub repository[5].

---

[1] https://www.cosmos.esa.int/web/spice
[2] https://github.com/AndrewAnnex/SpiceyPy
[3] https://naif.jpl.nasa.gov/naif/links.html
[4] https://naif.jpl.nasa.gov/naif/data.html
[5] https://github.com/DJNieuwenhuizen/MSc-thesis/
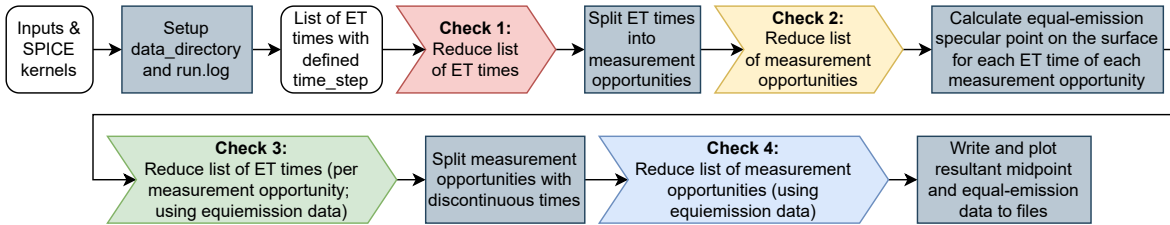
Figure 5.3: High-level code architecture for the measurement planning, own work

The user inputs a Coordinated Universal Time (UTC) frame, which is converted to a list of Ephemeris Time (ET) stamps with a set 'time_step', or interval between two points. This list is run through four checks, differentiated by the nature of how they manipulate the times and measurement opportunities and their computational cost:

- **Check 1: 'Reduce list of ET times'**
  This check is performed on the list of ET times, using loose requirements which have to be adhered during the complete measurement and eliminate large amounts of time stamps with infeasible measurement geometry. It outputs a reduced list of ET times, which can be split into a finite amount of continuous measurement opportunities.

- **Check 2: 'Reduce list of measurement opportunities'**
  This check is performed on the list of measurement opportunities. It inspects whether measurements as a whole adhere to certain requirements. It uses computationally light specular point estimates: 'midpoints', the projection of the middle of the MEX-TGO line of sight at the required Ephemeris Time, onto the surface of ellipsoidal Mars (standard adopted dimensions of 3396.19 km for its semi-major axis and 3376.20 km for its semi-minor axis [38]). The output is a reduced list of feasible measurement opportunities with unchanged lists of ET times per opportunity.

- **Check 3: 'Reduce list of ET times (per measurement opportunity; using equiemission data)'**
  This check is performed on every individual ET time (per measurement opportunity), using requirements to be adhered to at all times. Before starting the check, the specular points and corresponding equal-emission angles are calculated, a computationally intensive step which allows eliminating times on more strict requirements.

- **Check 4: 'Reduce list of measurement opportunities (using equiemission data)'**
  This check takes the equal-emission data for the complete measurement opportunities and checks whether it adheres to the full measurement requirements (similar to step 2, but more strict and elaborate). It outputs the final reduced list of feasible measurement opportunities, including both the midpoint and equal-emission data.

The model outputs a folder containing the following:

- A **run.log** file with the script's logging information
- A **midpoints.txt** file with the names of the midpoint data files
- A **meas_ops.txt** file with the names of the measurement opportunity data files
- A **.csv** file describing the midpoints and measurement opportunity data for each individual opportunity
- Three **.png** plots of the ground tracks, including that of the specular points, midpoints and both combined

5.2. Description of the Model

This section presents the description of the planning model. Subsection 5.2.1 discusses the SPICE kernels, Subsection 5.2.2 the requirements and simulation parameters and Subsection 5.2.3 the detailed architecture.

5.2.1. SPICE Kernels

SPICE kernels are ancillary data files on the Solar system and S/C [32], allowing computations of the measurement geometry at required times. The five main kernel types, described in the SPICE acronym, include:

- **S**PK: Spacecraft kernels
- **P**CK: Planetary ephemeris kernels
- **I**K: Instruments kernels
- **C**K: Spacecraft rotations kernels
- **E**K: Experiment explanation/experimenter's notebook kernels

Furthermore, additional kernels which are not part of the acronym, but frequently used, include:

- FK: Reference frame specification kernels
- SCLK: Spacecraft clock correlation kernels
- LSK: Leapseconds kernels
- MK: Meta-kernels (or 'furnsh' kernels), used to collect and load multiple kernels at once
- DSK: Digital shape kernels
- DBK: Database mechanism kernels

The kernels used for MEX-TGO BSR planning (and processing) are divided over three meta-kernels. Appendix A lists all kernels in Sections A.1, A.2 and A.3 for 'gen_mk.mk' (general Solar system, time and Mars-related), 'MEX_mk.mk' (MEX-specific) and 'TGO_mk.mk' (TGO-specific). For future use of the models, this list should be expanded by loading the additional MEX and TGO SPKs published for data analysis and long-term planning.

5.2.2. Definition of Requirements and Simulation Parameters

Prior to building the planning model, feasible measurement geometries and locations of interest are constrained by requirements. Five of which constrain the geometry, indicated by the 'REQ-MSR-GEO' identifier:

- **REQ-MSR-GEO-1: The line of sight between MEX and TGO shall always be unobstructed.**
  In order for BSR measurements to be feasible, the line of sight between MEX and TGO should be unobstructed. This eliminates times during which Mars is between the two S/C.

- **REQ-MSR-GEO-2: The MEX-TGO distance shall be below 1500 km at the closest pass.**
  To attain sufficient SNR, the signal path length R_{sp} should be minimized. SNR scales by $1/R_{sp}^2$ such that a tenfold decrease in R_{sp} improves SNR by a factor of 100 [144]. This is closely related to the MEX-TGO distance, allowing simpler computations. To increase chances of finding tracks over LOI, the requirement was loosened from 1000 km, as used for BSR-2.x (MTP272/91), whilst still significantly improved from BSR-1.x (MTP257/76). Furthermore, a maximum distance over the entire measurement is set to 3500 km, using an estimate of 6.7 km/s as the maximum relative S/C velocity, i.e. ~2000 km margin on the closest pass in half the measurement duration (five minutes).

- **REQ-MSR-GEO-3: The equal-emission angles shall be below 40° at the closest pass.**
  The emission angles of the S/C with the specular point are assumed equal by the accuracy set in REQ-MSR-SIM-2. Shallow measurement geometry induces undesired signal scattering over the topography and higher direct signal contribution. The maximum was put to 40° at the closest pass to encase the BSR-1.x measurements, but loosened stepwise depending on the results. For low-level assessment, the equal-emission angle is approximated as half the MEX-TGO angular separation from the midpoint. Furthermore, to limit feasible measurement times, a maximum angle over the entire measurement of 60° is set, found to not eliminate otherwise feasible opportunities.

- **REQ-MSR-GEO-4: The measurement duration shall be ten minutes.**
  The measurement duration of MEX-TGO ionospheric BSR, and thus the serendipitous BSR-1.x, was set to ten minutes. Preferably, an ideal measurement duration should be derived for the ideal measurements, which is dependent on data quality as a function of the equal-emission angles and pass length. However, in the interest of time and obtainment of seemingly viable results from the code, it was decided to keep the duration as is.

- **REQ-MSR-GEO-5: The measurements shall take place in the months of July and August 2025.**
  The ESAC measurement request was ready for submission mid-April 2025, a month delay from REQ-TAR-2 discussed in Section 4.2. Considering a three month lead-time on measurement planning and graduation in September 2025, the measurements should take place in July and August 2025, or MTP276/95 and MTP277/96.

Furthermore, two requirements are defined to constrain the ground tracks of measurement opportunities in comparison to the locations of interest, these are indicated by the 'REQ-MSR-LOI' identifier and state:

- **REQ-MSR-LOI-1: Each selected STL shall be sampled twice.**
  To guarantee measurement validity and account for erroneous and/or unexpected signal behavior, each STL should be sampled twice. If measurements differ highly, this indicates a high likelihood of measurement error and the STL may need to be omitted. It also allows for quantifying the consistency of the measurement approach.

- **REQ-MSR-LOI-2: The ground track shall enter the near-equatorial band of 40°S to 40°N latitude.**
  As dictated in REQ-TAR-1 (upon defining the STLs), interest of MEX-TGO BSR is for the near-equatorial region, where likelihood for bio-signatures and relevance to future human exploration is highest. Therefore, in order for a measurement opportunity to be viable, its ground track should enter the ±40° latitudinal band. Furthermore, a limit of ±70° latitude can be imposed over the entire measurement duration. This eliminates equal-emission computations for pure polar ground tracks, without eliminating otherwise feasible measurement opportunities.

Lastly, the data quality for measurement planning is set in the convergence algorithm parameters to balance computational time with accuracy. These are described in the two 'REQ-MSR-SIM' requirements and state:

- **REQ-MSR-SIM-1: The time step between ground track points for planning shall be set to ten seconds.**
  A time step of ten seconds yields continuous ground tracks and little error on the ten-minute measurement duration. For measurement processing, a time step of one second is used, but for planning ten seconds suffices.

- **REQ-MSR-SIM-2: The equal-emission angles shall differ by less than 1E-2°.**
  The equal-emission angle difference is that between the S/C emission angles at the specular point, calculated using an algorithm which iteratively computes the angles until they converge to a set accuracy. To balance errors with computational cost, the criterion was set to 1E-2°, showing non-discernible visual differences in the ground tracks.

5.2.3. Detailed Code Architecture

Figure 5.4 shows the detailed code architecture, expanded from Figure 5.3. It showcases the dataflow and sub-checks of the main four checks, as aligned with the requirements to retrieve feasible opportunities.
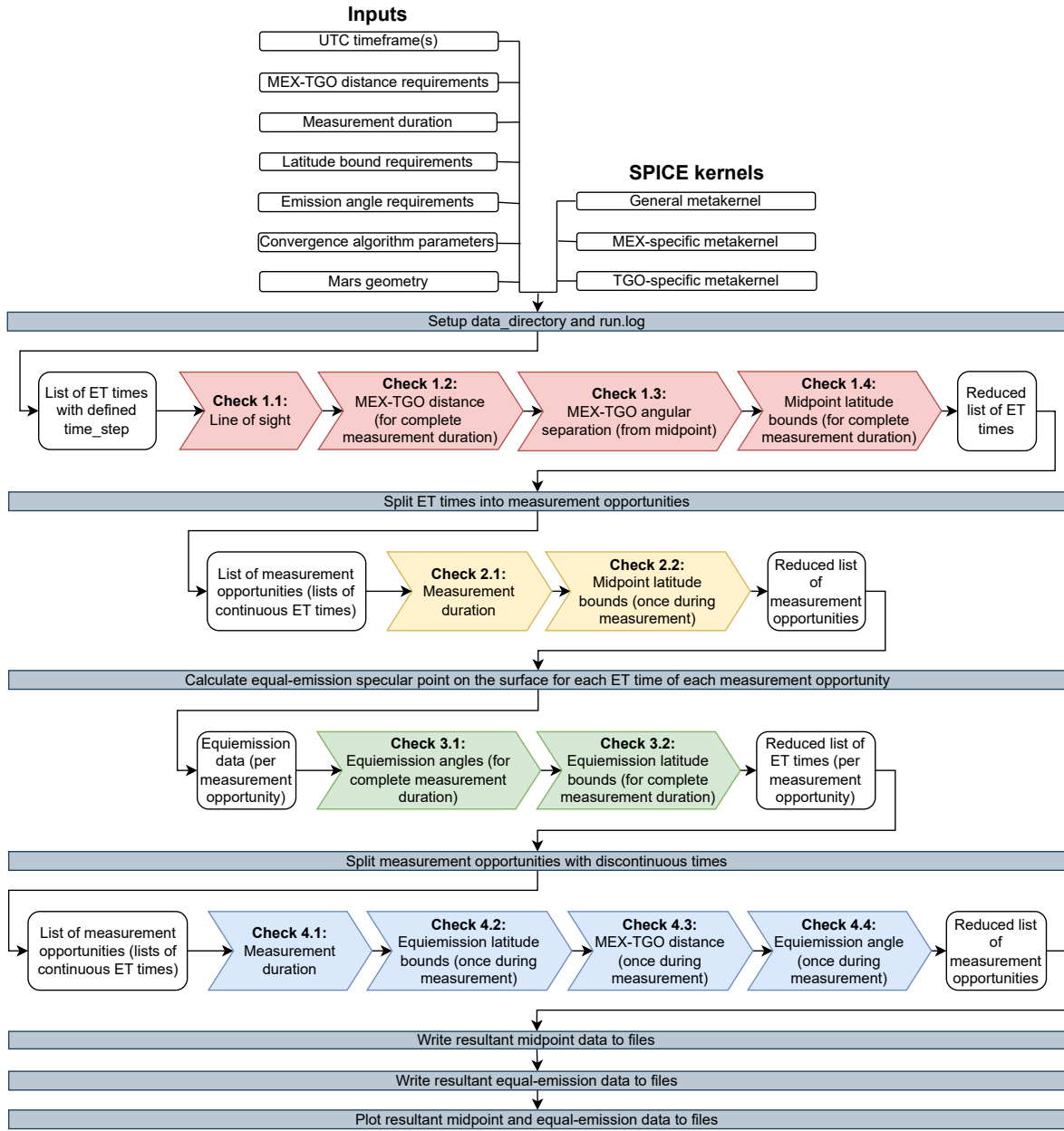
Figure 5.4: Detailed code architecture for the MEX-TGO BSR measurement planning model, own work

5.3. Results

This section presents the results of the BSR measurement planning phase. Subsection 5.3.1 presents the found measurement opportunities, which were requested from ESAC. Subsection 5.3.2 presents those actually (to be) performed (in addition to the non-ideal measurements previously discussed in Subsection 5.1.1).

5.3.1. Requested Measurement Opportunities

The model was ran for July and August 2025 with the aim of retrieving eight viable measurements in either month. A significant difference was identified in the opportunities' adherence to the requirements, presented in Subsection 5.2.2, with July yielding four fully compliant opportunities in LOI and August yielding zero. Therefore, criteria were loosened in a stepwise manner to find the most optimal measurements.

For July 2025, eight measurement opportunities were identified, each in MTP276/95. Relevant measurement data is tabulated in Table 5.4 and Figure 5.5 shows the ground tracks. These are labelled meas_op-3.x, where '3' indicates the third BSR campaign and 'x' indicates each specific opportunity. They cover a well-spread ground

track distribution, including all LOI with the exception of two back-up science STLs (STL-S-B1 'Medusae Fossae Formation' and STL-S-B3' Xanthe Terra) and back-up calibration STL (STL-C-B1 'MRO Impact Crater'). Two opportunities, meas_op-3.6 over STL-S-M3 'Valles Marineris' and meas_op-3.4 over STL-S-M1 'Utopia Planitia' and STL-S-M2 'Elysium Planitia', showcase the best conditions and were proposed to ESAC with priority.

Table 5.4: BSR campaign 3: July 2025 measurement opportunities requested from ESAC (MTP276/95)

| ID | Timeframe | Observed region | | MEX-TGO distance [km] | | Equal-emission angle [deg] | |
		Name	ID	Minimum	Maximum	Minimum	Maximum
meas_op-3.1	2025 July 11th 15:15:07 - 2025 July 11th 15:25:07	Elysium Planitia	STL-S-M2	2232.22	2485.04	54.26	67.91
meas_op-3.2	2025 July 12th 04:59:27 - 2025 July 12th 05:09:27	Valles Marineris & Chryse Planitia	STL-S-M3 & STL-S-B2	1118.50	1203.35	50.37	60.64
meas_op-3.3	2025 July 12th 05:09:27 - 2025 July 12th 05:19:27	Chryse Planitia	STL-S-B2	1157.40	1602.42	40.93	50.16
meas_op-3.4	2025 July 14th 19:53:08 - 2025 July 14th 20:03:08	Elysium Planitia & Utopia Planitia	STL-S-M2 & STL-S-M1	506.44	721.26	28.32	36.55
meas_op-3.5	2025 July 14th 20:03:08 - 2025 July 14th 20:13:08	Utopia Planitia	STL-S-M1	731.19	1490.58	28.15	28.72
meas_op-3.6	2025 July 17th 10:37:50 - 2025 July 17th 10:47:50	Valles Marineris	STL-S-M3	155.05	731.98	9.11	42.78
meas_op-3.7	2025 July 20th 01:49:31 - 2025 July 20th 01:59:31	Utopia Planitia	STL-S-M1	871.29	1564.49	10.83	20.79
meas_op-3.8	2025 July 27th 22:22:06 - 2025 July 27th 22:32:06	S1094b Crater	STL-C-M1	1981.18	2232.38	36.63	64.33
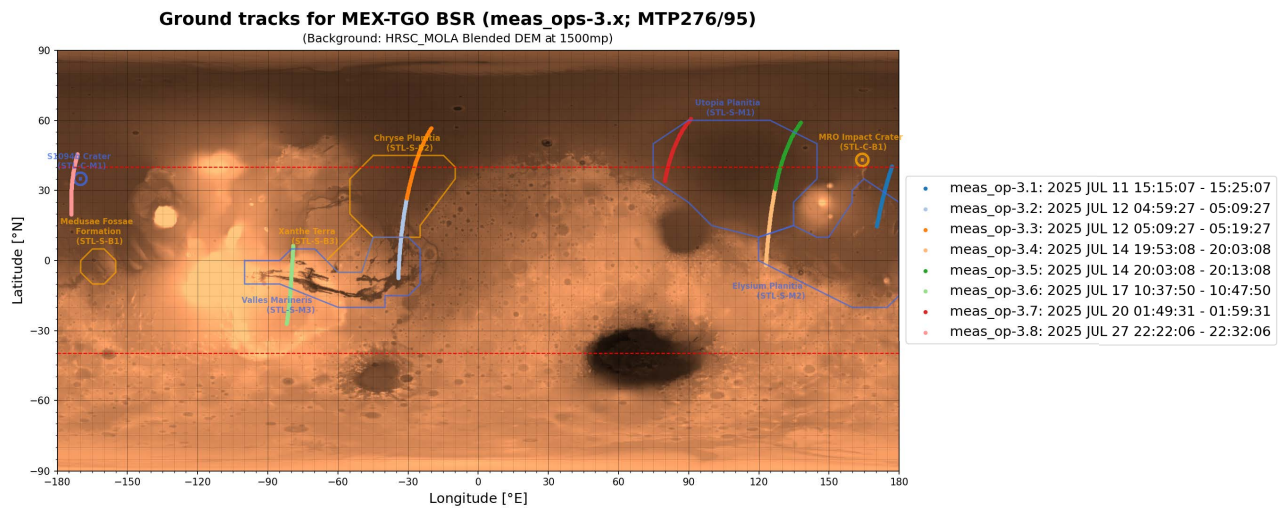
Figure 5.5: BSR campaign 3: Ground tracks for the July 2025 measurement opportunities requested from ESAC (MTP276/95), own work

For August 2025, seven measurement opportunities were identified; two in MTP276/95 and the remainder in MTP277/96. Relevant measurement data is tabulated in Table 5.5 and Figure 5.6 shows the ground tracks. The latter are less well-spread than in July, with a single track over STL-S-B3 'Xanthe Terra' and the rest clustered over STL-S-M2 'Utopia Planitia' and STL-C-B1 'MRO Impact Crater'. Furthermore, the measurement geometry is much less favorable with significantly higher MEX-TGO distances and equal-emission angles. Request of these measurements was therefore seen as a back-up if the July measurements are not sufficiently accepted.

Table 5.5: BSR campaign 4: August 2025 measurement opportunities requested from ESAC (MTP276/95 and MTP277/96)

| ID | Timeframe | Observed region | | MEX-TGO distance [km] | | Equal-emission angle [deg] | |
		Name	ID	Minimum	Maximum	Minimum	Maximum
meas_op-4.1	2025 August 2nd 04:09:47 - 2025 August 2nd 04:19:47	Utopia Planitia	STL-S-M1	2695.75	3198.20	41.57	70.04
meas_op-4.2	2025 August 2nd 17:50:32 - 2025 August 2nd 18:00:32	Xanthe Terra	STL-S-B3	2284.86	2854.13	67.79	85.13
meas_op-4.3	2025 August 5th 08:49:07 - 2025 August 5th 08:59:07	Utopia Planitia	STL-S-M1	2159.69	2912.52	51.18	79.29
meas_op-4.4	2025 August 7th 09:51:03 - 2025 August 7th 10:01:03	Utopia Planitia	STL-S-M1	3768.41	4421.01	63.43	84.61
meas_op-4.5	2025 August 16th 10:14:16 - 2025 August 16th 10:24:16	MRO Impact crater	STL-C-B1	2896.83	4081.15	60.71	88.12
meas_op-4.6	2025 August 18th 11:16:13 - 2025 August 18th 11:26:13	Between MRO Impact crater & Utopia Planitia	STL-C-B1 & STL-S-M1	3529.92	4735.80	55.65	84.83
meas_op-4.7	2025 August 28th 01:42:36 - 2025 August 28th 01:52:36	Utopia Planitia	STL-S-M1	3422.44	4648.75	67.72	72.86

Ground tracks for MEX-TGO BSR (meas_ops-4.x; MTP276/95 and MTP277/96)
(Background: HRSC_MOLA Blended DEM at 1500mp)

- meas_op-4.1: 2025 AUG 02 04:09:47 - 04:19:47
- meas_op-4.2: 2025 AUG 02 17:50:32 - 18:00:32
- meas_op-4.3: 2025 AUG 05 08:49:07 - 08:59:07
- meas_op-4.4: 2025 AUG 07 09:51:03 - 10:01:03
- meas_op-4.5: 2025 AUG 16 10:14:16 - 10:24:16
- meas_op-4.6: 2025 AUG 18 11:16:13 - 11:26:13
- meas_op-4.7: 2025 AUG 28 01:42:36 - 01:52:36
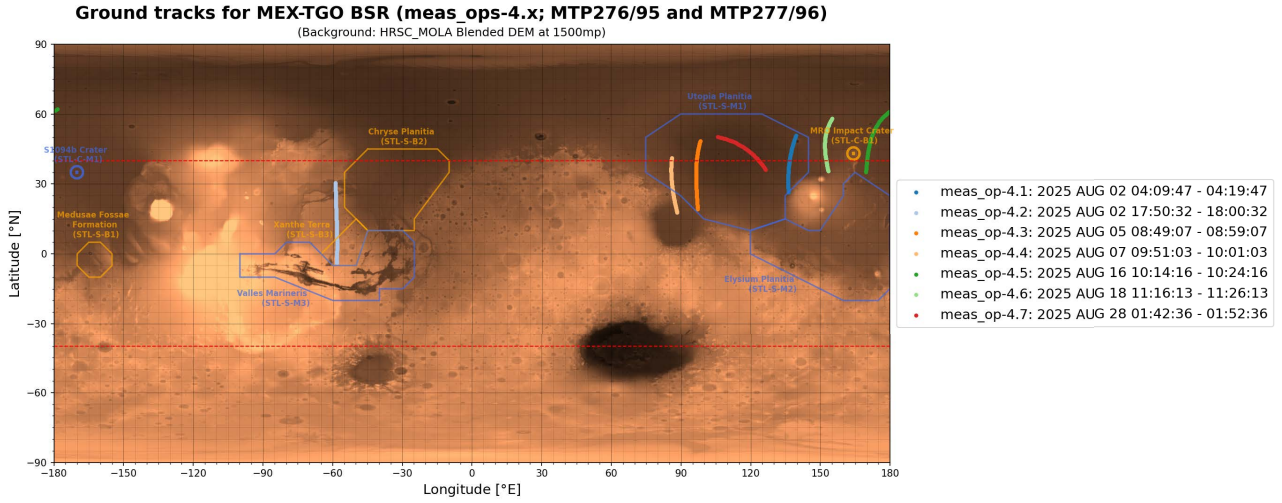
Figure 5.6: BSR campaign 4: Ground tracks for the August 2025 measurement opportunities requested from ESAC (MTP276/95 and MTP277/96), own work

5.3.2. Performed and Future Measurements

The measurement opportunities, documented in Subsection 5.3.1, were requested from the ESA European Space Astronomy Centre (ESAC) for MTP276/95 and MTP277/96. Ultimately, one opportunity was accepted: meas_op-3.6 (in MTP276/95). Other opportunities were in conflict with lander visibility periods [21, 22]. The relevant measurement data is tabulated in Table 5.6 and Figure 5.7 shows the corresponding ground track.

Table 5.6: BSR campaign 3: July 2025 measurement data (MTP276/95)

ID	Timeframe	Observed region		MEX-TGO distance [km]		Equal-emission angle [deg]	
		Name	ID	Minimum	Maximum	Minimum	Maximum
BSR-3.1	2025 July 17th 10:38:31 - 2025 July 17th 10:48:31	Valles Marineris	STL-S-M3	142.31	700.99	6.92	41.96

Ground tracks for MEX-TGO BSR (BSR-3.x; MTP276/95)
(Background: HRSC_MOLA Blended DEM at 1500mp)

- BSR-3.1: 2025 JUL 17 10:38:31 - 10:48:31
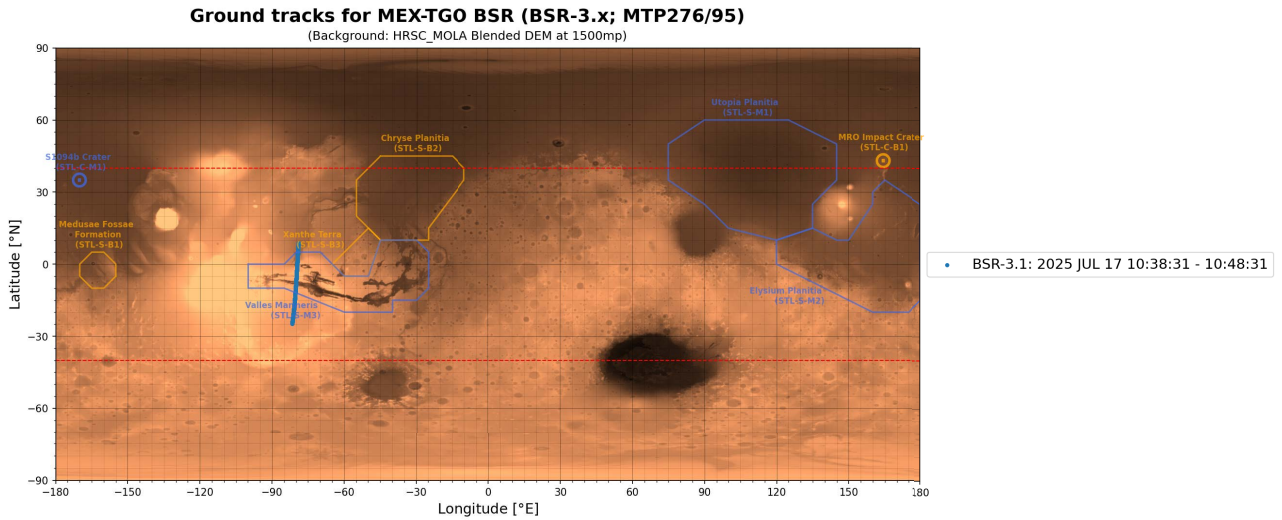
Figure 5.7: BSR campaign 3: Ground track for the July 2025 measurement (MTP276/95), own work

Preparation of the measurement data for processing is done with a different model, named 'main_MEXTGOBSR_ measurementtracks.py', which can be accessed on the thesis GitHub repository[6]. It contains the same functionalities as the measurement planning model, but is adapted to omit the feasibility checks and only output the midpoint and specular point data at increased temporal resolution (time step of 1 second), achieving increased local accuracy on-ground and better insight in the temporal signal variation.

Due to the lander visibility conflict in all MTP277/96 opportunities, an alternative non-ideal measurement was included [22]. It moves over the South Polar region and combines a Mutual Occultation measurement with BSR. It runs for 20 minutes, from 19:39:12 to 19:59:12, but has to be shortened to 19 minutes for BSR processing, from 19:39:12 to 19:58:12. The last minute was found to result in no mutual surface footprint of the two S/C. The measurement data is tabulated in Table 5.7 and Figure 5.8 shows the ground track.

---
[6]https://github.com/DJNieuwenhuizen/MSc-thesis/

Table 5.7: BSR campaign 4: August 2025 measurement data (MTP277/96)

ID	Timeframe	Observed region		MEX-TGO distance [km]		Equal-emission angle [deg]	
		Name	ID	Minimum	Maximum	Minimum	Maximum
BSR-4.1	2025 August 15th 19:39:12 - 2025 August 15th 19:58:12	N/A; SPLD	N/A	1194.06	3465.76	23.22	89.88
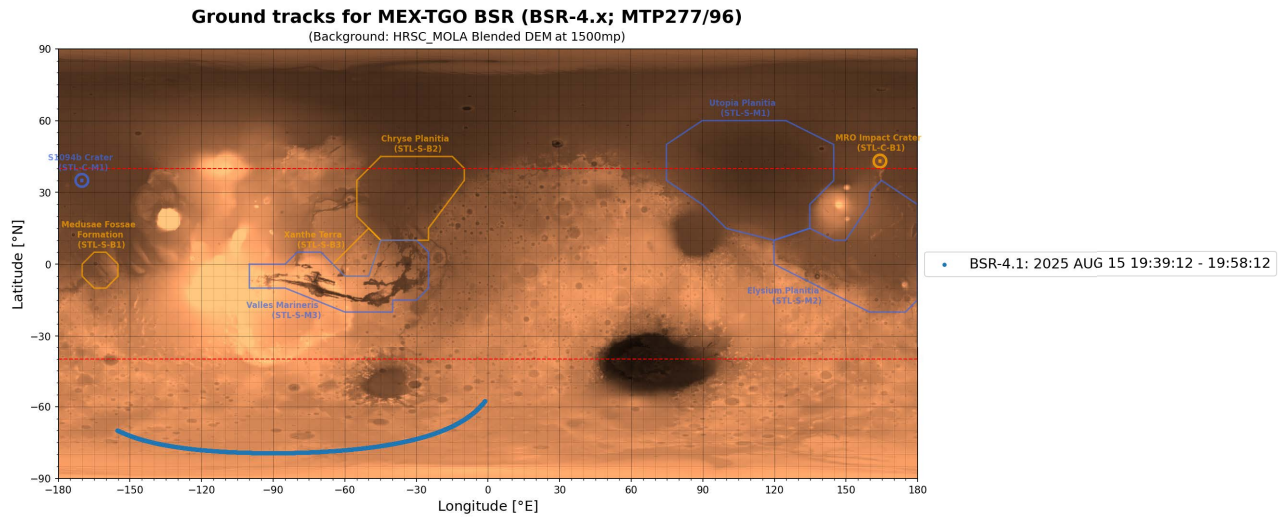
Figure 5.8: BSR campaign 4: Ground track for the August 2025 measurement (MTP277/96), own work

For future work, fourteen measurements are planned in September, October, November and December of 2025, which were not processed nor checked for feasibility within the scope of this thesis.

Table 5.8: BSR campaign 5: September 2025 measurement data (MTP278/97)

ID	Timeframe	Observed region		MEX-TGO distance [km]		Equal-emission angle [deg]	
		Name	ID	Minimum	Maximum	Minimum	Maximum
BSR-5.1	2025 September 22nd 22:56:40 - 2025 September 22nd 23:06:40	N/A; Meridiani Planum	N/A	1088.67	3448.40	45.84	90.78
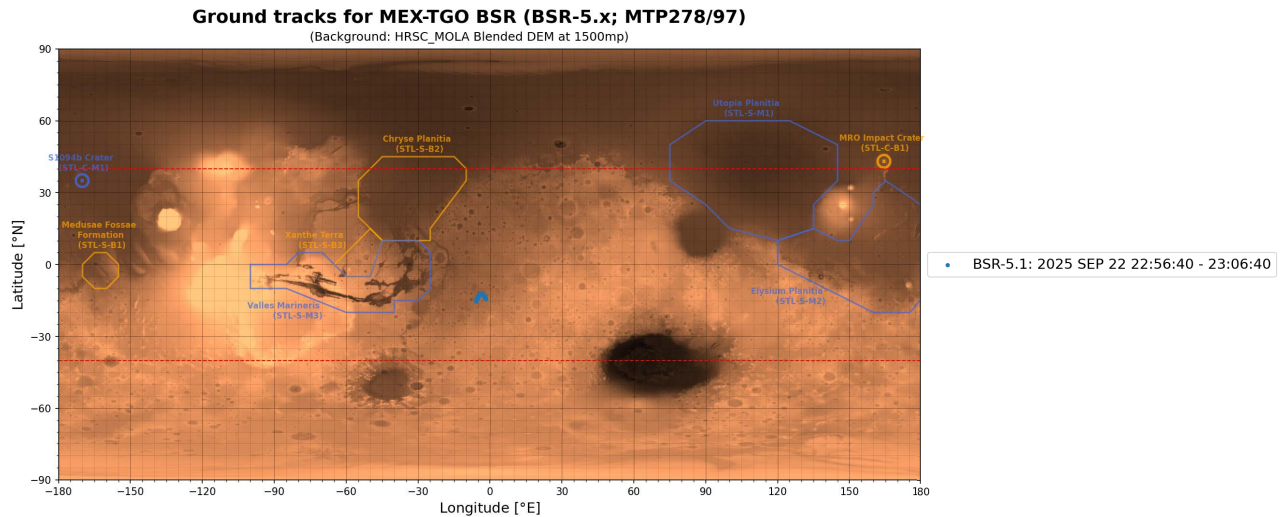
Figure 5.9: BSR campaign 5: Ground track for the September 2025 measurement (MTP278/97), own work

For MTP278/97 (BSR-5.x; September 2025), measurement data is tabulated in Table 5.8 and Figure 5.9 shows the ground track. For MTP279/98 (BSR-6.x; September and October 2025), measurement data is tabulated in Table 5.9 and Figure 5.10 shows the ground tracks. For MTP280/99 (BSR-7.x; November 2025), measurement data is tabulated in Table 5.10 and Figure 5.11 shows the ground tracks. Lastly MTP281/100 (BSR-8.x; November and December 2025) measurement data is tabulated in Table 5.11 and Figure 5.12 shows the ground tracks.

Table 5.9: BSR campaign 6: September and October 2025 measurement data (MTP279/98)

ID	Timeframe	Observed region		MEX-TGO distance [km]		Equal-emission angle [deg]	
		Name	ID	Minimum	Maximum	Minimum	Maximum
BSR-6.1	2025 September 30th 19:33:20 - 2025 September 30th 19:43:20	N/A; Hesperia Planum	N/A	680.15	3496.89	16.40	89.65
BSR-6.2	2025 October 7th 05:02:15 - 2025 October 7th 05:10:15	N/A; Noachis Terra	N/A	399.27	3536.40	26.03	91.55
BSR-6.3	2025 October 13th 00:38:36 - 2025 October 13th 00:57:36	N/A; Promethei & Cimmeria Terra	N/A	325.46	4104.91	23.47	90.96
BSR-6.4	2025 October 15th 15:30:52 - 2025 October 15th 15:40:52	N/A; Aonia Terra	N/A	671.10	3706.34	42.04	91.48
BSR-6.5	2025 October 16th 05:21:53 - 2025 October 16th 05:41:53	N/A; SPLD	N/A	440.95	4235.12	30.34	91.63
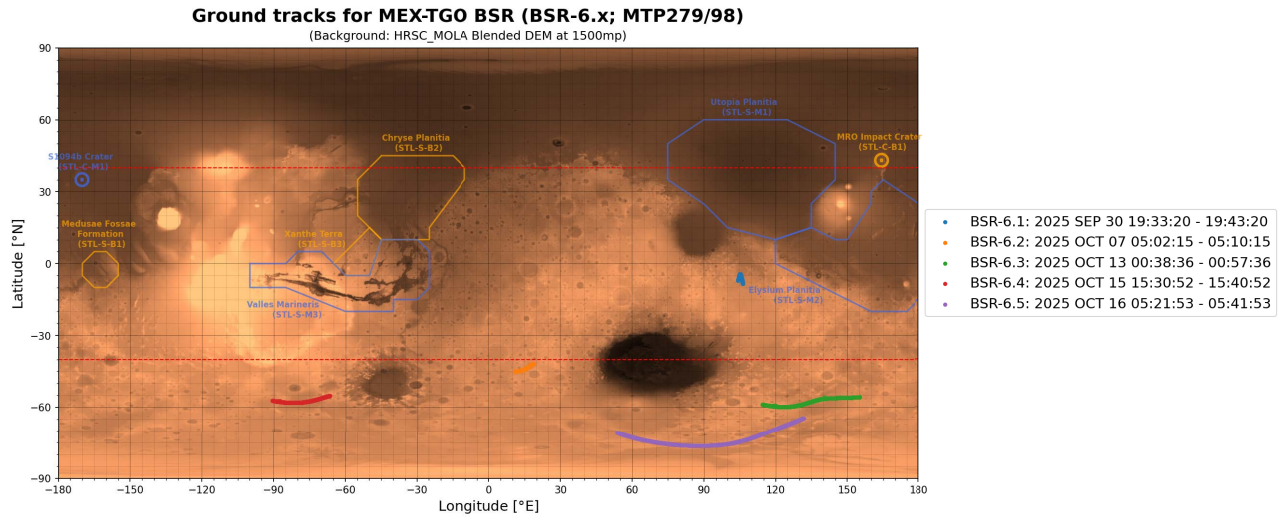
Figure 5.10: BSR campaign 6: Ground tracks for the September and October 2025 measurements (MTP279/98), own work

Table 5.10: BSR campaign 7: November 2025 measurement data (MTP280/99)

ID	Timeframe	Observed region		MEX-TGO distance [km]		Equal-emission angle [deg]	
		Name	ID	Minimum	Maximum	Minimum	Maximum
BSR-7.1	2025 November 1st 12:33:54 - 2025 November 1st 12:43:54	N/A; SPLD	N/A	386.78	1755.84	27.57	69.71
BSR-7.2	2025 November 4th 03:21:58 - 2025 November 4th 03:31:58	N/A; SPLD	N/A	115.83	2921.84	8.76	81.65
BSR-7.3	2025 November 9th 09:10:58 - 2025 November 9th 09:20:58	N/A; SPLD	N/A	526.90	1551.98	35.23	68.31
BSR-7.4	2025 November 15th 04:49:32 - 2025 November 15th 04:59:32	N/A; SPLD	N/A	1131.83	1714.30	59.64	69.83
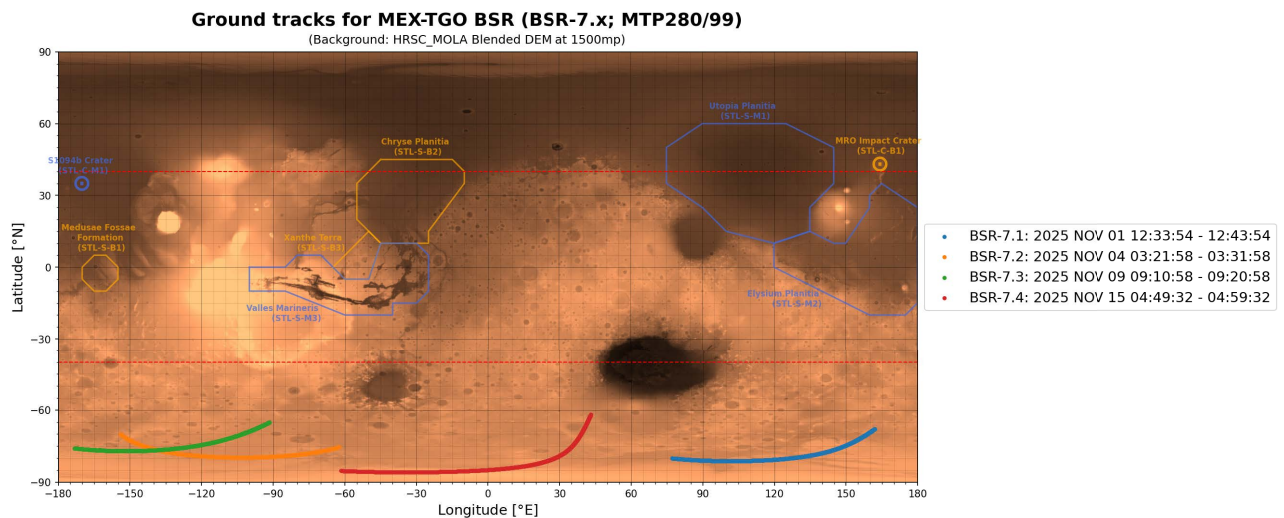
Figure 5.11: BSR campaign 7: Ground tracks for the November 2025 measurements (MTP280/99), own work

Table 5.11: BSR campaign 8: November and December 2025 measurement data (MTP281/100)

ID	Timeframe	Observed region		MEX-TGO distance [km]		Equal-emission angle [deg]	
		Name	ID	Minimum	Maximum	Minimum	Maximum
BSR-7.1	2025 November 25th 16:19:48 - 2025 November 25th 16:29:48	N/A; SPLD	N/A	255.80	804.62	14.50	48.68
BSR-7.2	2025 November 30th 22:04:33 - 2025 November 30th 22:14:33	N/A; SPLD	N/A	950.66	1104.91	44.00	56.02
BSR-7.3	2025 December 11th 23:25:54 - 2025 December 11th 23:35:54	N/A; SPLD	N/A	920.28	1056.65	41.88	57.38
BSR-7.4	2025 December 14th 14:12:14 - 2025 December 14th 14:22:14	N/A; SPLD	N/A	788.71	880.94	46.16	48.76
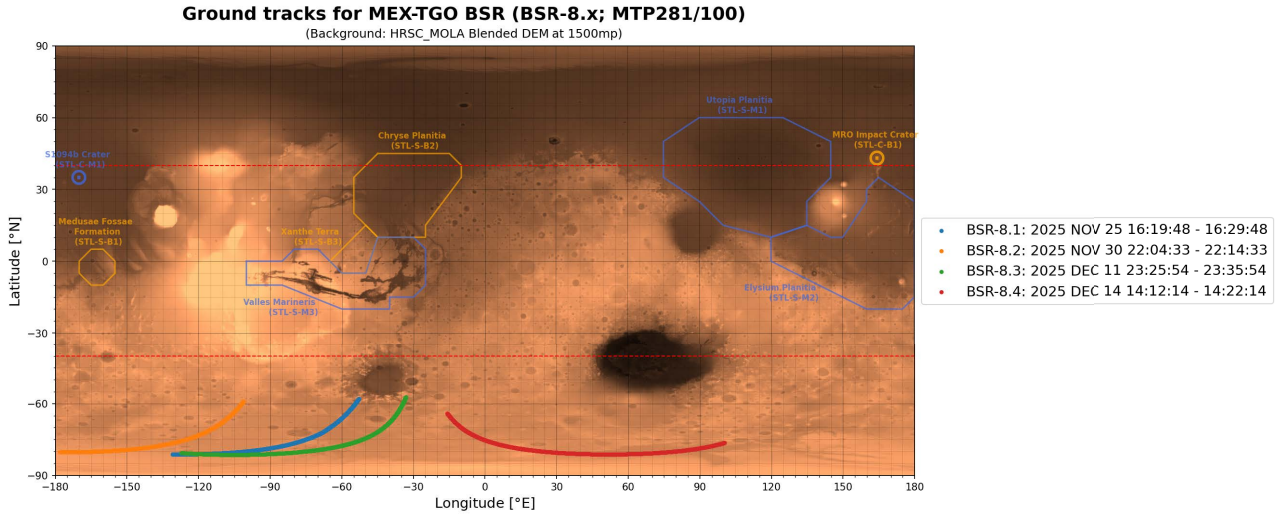
Figure 5.12: BSR campaign 8: Ground tracks for the November and December 2025 measurements (MTP281/100), own work

5.4. Discussion

This section presents a discussion on the measurement planning phase, and specifically, the model. Subsection 5.4.1 presents verification and validation of the model, while Subsection 5.4.2 discusses its limitations.

5.4.1. Verification and Validation

Only limited verification and validation was performed on the measurement planning model, as focus laid on the processing in Chapter 6. The main steps taken to verify and validate the model are presented below.

Result Comparison with the 'compute_equiemission_point.py' Code

Results of the measurement planning model were compared with those generated by the 'compute_ equiemission_point.py' code. This file was provided by ESAC for estimating the specular point under equal-emission conditions. The results of the two models were found to be the same.

Validity of the Midpoint Estimates

For assessing feasibility of measurement (times) in Checks 1 and 2, as presented in Figures 5.3 and 5.4, the midpoint estimates are used. These are the computationally light approximation of the specular point, calculated by projecting the middle of the MEX-TGO line of sight onto the surface of ellipsoidal Mars.

A comparison is given for the performed and requested measurements in Appendix B, and depending on the exact conditions, these can be an almost perfect, or relatively poor, approximation of the specular point. The quality was sufficient for current measurement planning, but seemingly decreases at greater distances of the S/C from the surface. Reason for this is that the midpoint estimates are driven both by the angular positions as well as distance to the S/C (if MEX is at much higher altitude than TGO, the vector pointing towards the middle of the line of sight will be at a smaller angle with the one pointing to MEX than to TGO), whilst the specular points are only driven by the angular positions. Hence, at greater distances, the distance component of the midpoint estimates becomes more significant, leading to a poorer approximation of the specular points.

Cosmographia Visualizations

One of the methods used to validate results generated by the code, specifically measurement times, is visualizing them in Cosmographia[7]. Cosmographia is a 3D visualization tool which can be used in combination with

---

[7]https://www.cosmos.esa.int/web/spice/cosmographia

SPICE kernels to visualize S/C and planetary positions [44]. Such comparisons can look as shown in Figures 5.15 and 5.14 for the start and Figures 5.13 and 5.16 for the end of measurement BSR-2.1. This check would be performed for the complete measurement duration, using the .gif files generated by the model.
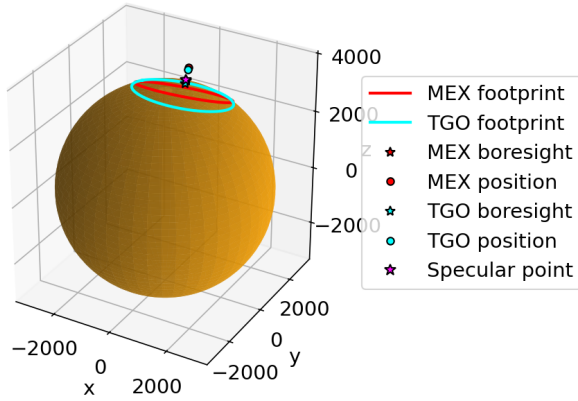
Figure 5.13: 3D Mutual footprint for BSR-2.1 at start of measurement: 20th of March 2025 23:40:54, own work
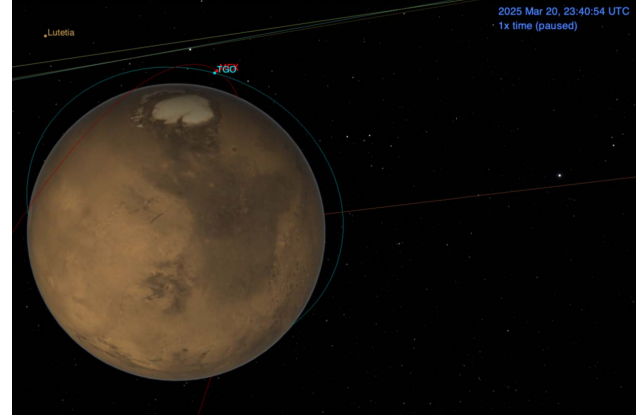
Figure 5.14: 3D Cosmographia visualization for BSR-2.1 at start of measurement: 20th of March 2025 23:40:54, own work
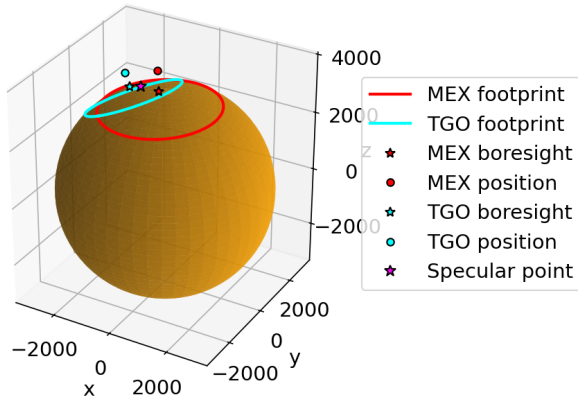
Figure 5.15: 3D Mutual footprint for BSR-2.1 at end of measurement: 20th of March 2025 23:50:54, own work
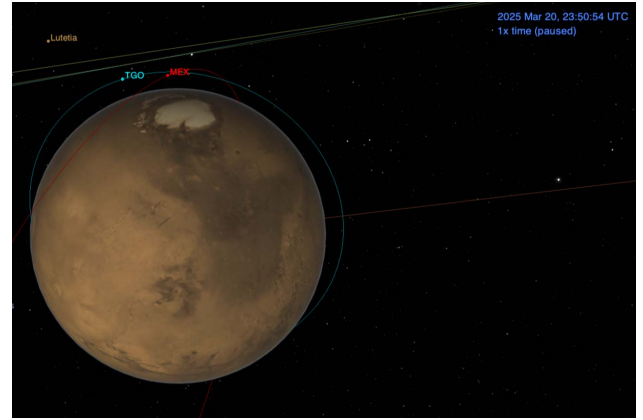
Figure 5.16: 3D Cosmographia visualization for BSR-2.1 at end of measurement: 20th of March 2025 23:50:54, own work

5.4.2. Limitations

There are a number of limitations to the measurement planning model, partially discovered only after starting to analyze the BSR data with the model described in Chapter 6. The most significant limitations include:

- **Lander visibility periods:**
  The most significant limitation encountered with obtaining approval for the ESAC measurement proposal was conflict with lander visibility periods, noted in Subsection 5.3.2. For future iterations of the model, these should be included as a Check. Furthermore, it is expected for the lander visibility periods to be relaxed in the future, as in most cases these are unnecessarily conservative [22].

- **Time input:**
  The model takes UTC time ranges as input, which is suboptimal for planning. Instead, it should always take the MEX-TGO coordinated planning MTPs at input, in accordance with the ESAC planning standards.

- **Optimal measurement duration:**
  The BSR measurement duration was kept to ten minutes, as for the Mutual Occultation measurements. However, it it likely this is not optimal for BSR measurements. No optimal duration was researched, but doing so could be beneficial for future MEX-TGO BSR campaigns.

- **Re-quantification and automatic loosening of requirements:**
  The measurement planning model was created before starting data analysis, hence does not take into account findings from analysis with regard to properly quantifying requirements. For example, REQ-MSR-GEO-3 only states the equal-emission angle shall be below 40° at the closest pass, whilst from analysis it is expected that RHCP-LHCP polarization effects render the AGC measurements unusable at

small emission angles, as only the RHCP signal can be registered (refer to Subsection 6.4.1).
Furthermore, the model makes use of the S/C distance to limit opportunities, whilst the actual parameter driving the SNR is the signal path length. This is more costly to calculate, but would be a better metric to use, especially if an approximation could be used of lesser computational intensity.
Lastly, the model is unable to automatically loosen requirements. Instead these need to be manually updated, making the process inefficient for finding the optimal measurements in lesser conditions.

- **Computational cost:**
  Running the model, especially the equal-emission calculations, is computationally expensive. Further limiting the opportunities going into this step would be beneficial. This could include finding a better approximation for the specular point track to be used instead of the midpoint estimates (at least for when MEX is at high altitudes), or otherwise optimizing the equal-emission computation itself.

- **Target search capability:**
  The model currently lacks the ability to search for measurements in specific target areas, with the exemption of searching inside the near-equatorial band, i.e. certain latitudinal bounds. It would be beneficial to include search capability in specific regions, e.g. request a measurement over Valles Marineris and have the model recognize when it can be performed.

- **Dedicated pointing:**
  As will be presented in Section 7.2, MEX-TGO BSR might eventually attempt measurement campaigns with dedicated pointing. The current model assumes conventional nadir pointing, thus if a pointing campaign is initiated, the model will need to include the capability to assess such measurements.

Overall the model is a good first iteration, but requires further development to be fully functional, efficient and well-matched to analysis findings and requirements. It is expected for many BSR opportunities (small S/C distances) to arise in the near future [22]. For this the main limiting factor of lander visibility periods should be included and an updated measurement planning and preference strategy should be set.

6

Numerical Simulations of the Subsurface

This chapter presents the numerical simulations of the subsurface, written for analysis of the MEX-TGO BSR measurements. Section 6.1 discusses the methodology, Section 6.2 presents a detailed description of the different elements of the model, Section 6.3 presents the application to measurement data and corresponding results and lastly, Section 6.4 presents a short discussion on the (confidence level of the) results.

6.1. Methodology

This section discusses the methodology and theory behind the model. First, Subsection 6.1.1 presents the measurement geometry for MEX-TGO BSR. Then Subsection 6.1.2 presents the radar equations, employed to model the received signal and lastly, Subsection 6.1.3 discusses the connection between water ice content in subsurface, its dielectric constant and the resultant attenuation in the signal power.

6.1.1. BSR Link Geometry

The MEX-TGO BSR link, shown in Figure 6.1, starts at the lander relay antenna of MEX (transmitter). It transmits a signal (in its conventional attitude: nadir-pointing), which travels over a free-space distance to its boresight and surrounding area on the Martian surface, is partially absorbed and dispersed, and reflects over a free-space distance to the TGO antenna (receiver; also in its conventional nadir-pointing attitude).
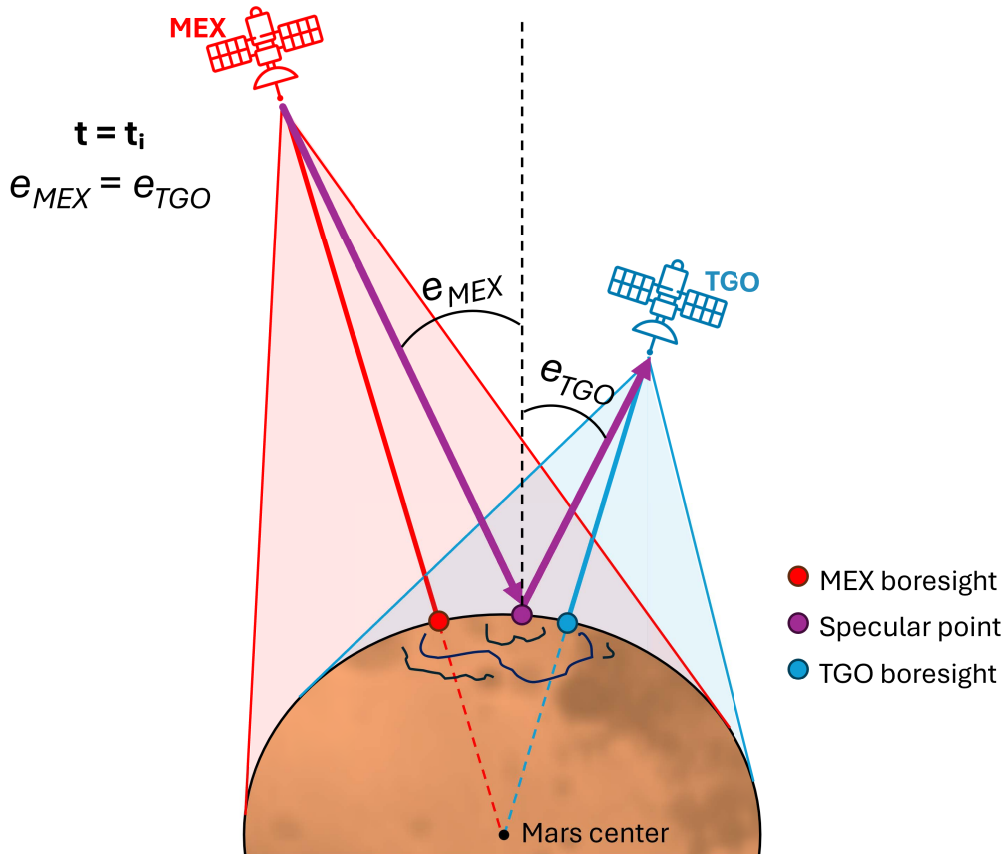
Figure 6.1: MEX-TGO BSR measurement geometry (not to scale), own work

The point of highest reflection on the surface is assumed to be the specular point (implication of this assumption will be discussed in Section 6.4). It is defined as the point on the mean Martian surface where the incidence and reflection angles are equal, and at the same time the surface normal vector and vectors to the two S/C all lay in the same plane [134]. For MEX-TGO BSR, the angle of incidence is the emission angle of MEX with the specular point e_{MEX} and the reflection angle is the emission angle of TGO with the specular point e_{TGO}, denoting the specular point also as the equal-emission point. At an instant i during a MEX-TGO BSR measurement, the specular point lays at planetocentric coordinate (ϕ_i, λ_i), determined through numerically propagating the signal with SPICE[1] (and SpiceyPy[2,3]) and running a convergence algorithm until the emission angles with respect to the point are equal (to a set accuracy) and the vectors remain in-plane with the surface normal.
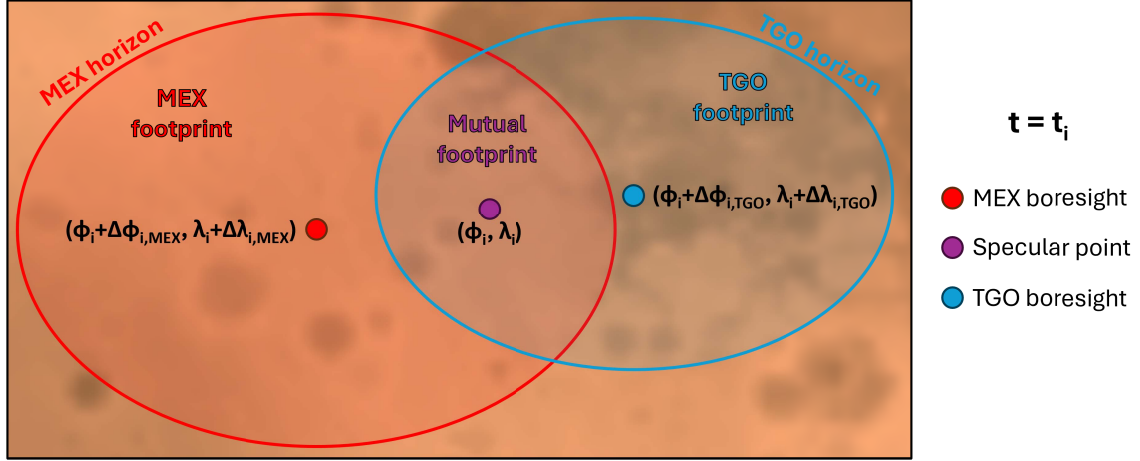
Figure 6.2: BSR signal footprint (not to scale), own work

As can be seen in Figure 6.2, the specular point lays offset from the peak signal, or boresight, of both spacecraft. The nominal S/C attitude is nadir pointing, meaning the boresights lay along the vector of either S/C to the center of Mars. Their coordinates are defined as $(\phi_i + \Delta\phi_{i,MEX}, \lambda_i + \Delta\lambda_{i,MEX})$ and $(\phi_i + \Delta\phi_{i,TGO}, \lambda_i + \Delta\lambda_{i,TGO})$ and limits of the mutual signal footprint are bound by the field of view, or Martian horizon, of either S/C. However, TGO is in a low-altitude near-circular orbit whilst MEX is in a highly elliptical orbit, as presented in Table 5.3. Since TGO is generally at a lower altitude, it thus also creates a smaller antenna footprint.

6.1.2. Radar Equations

The received power P_R is modelled in Equation 6.1 as the sum of the power reflected from the subsurface ($P_{R,ss}$) and the direct signal ($P_{R,dir}$). The latter entails remnants of the signal directly picked up by TGO, which is expected to be insignificant in most, but not all, measurement geometries. It can be computed using Friis' transmission formula shown in Equation 6.2, where P_T is the transmitted power (5 W for the MEX MelaCom transmitter [139]), G_T and G_R are the antenna gains of MEX and TGO respectively, λ is the wavelength and R is the distance between the S/C [8]. The wavelength λ is ~70 cm for MEX-TGO BSR at UHF, which follows from Equation 6.3, with f being the frequency (437.1 MHz) and c the speed of light in vacuum (~$3 \cdot 10^8$ m/s) [109].

$$P_R = P_{R,ss} + P_{R,dir} \quad (6.1) \qquad P_{R,dir} = P_T \cdot \frac{G_T \cdot G_R \cdot \lambda^2}{(4\pi \cdot R)^2} \quad (6.2) \qquad \lambda = \frac{c}{f} \quad (6.3)$$

The reflected signal can be computed using Equation 6.4: The bistatic radar equation [57, 114, 133]. Here, R_T and R_R are the distances from the S/C to the specular point and σ is the radar cross section (RCS) of the surface. By integrating Equation 6.4 over the sampled area S, i.e. mutual footprint visible to the transmitter and receiver as shown conceptually in Figure 6.2, Equation 6.5 is found where σ_0 is the specific RCS per unit surface area.

$$P_{R,ss} = \frac{P_T \cdot G_T}{4\pi \cdot R_T^2} \cdot \sigma \cdot \frac{G_R \cdot \lambda^2}{4\pi \cdot R_R^2} \quad (6.4) \qquad P_{R,ss} = \int_S \frac{P_T \cdot G_T}{4\pi \cdot R_T^2} \cdot \sigma_0 \cdot \frac{G_R \cdot \lambda^2}{4\pi \cdot R_R^2} dS \quad (6.5)$$

Radar scattering arises from two main mechanisms: Coherent and incoherent [20]. Coherent scattering is caused when surfaces inside the sampled area are smooth to a fraction of the signal wavelength. Incoherent scattering follows from tilted facets, i.e. topography on a comparable or larger scale than the signal wavelength, which cause mirror-like behavior in off-nadir directions. The RCS is a measure of how detectable an object, with specific surface properties, is by radar [57, 114]. To determine σ with attention to both coherent and

---

[1] https://www.cosmos.esa.int/web/spice [3] https://naif.jpl.nasa.gov/naif/links.html
[2] https://github.com/AndrewAnnex/SpiceyPy

incoherent signal scattering effects, it is conventionally defined by the method of Hagfors [58, 141] shown in Equation 6.6 [20, 133, 146]. This method is derived from empirical data and thus not a theoretical method.

$$\sigma_0 = \rho \cdot C \cdot (cos^4(\gamma) + C \cdot sin^2(\gamma))^{-3/2} \quad (6.6) \qquad\qquad C^{-1/2} = s_{RMS} \quad (6.7)$$

As shown in Equation 6.6, the RCS is dependent on three properties of the subsurface [20, 133]:

- **Subsurface composition:** Encompassed in the 'Fresnel reflectivity' ρ, which ranges between 0 and 1 and can be related to the dielectric constant ϵ, as will be discussed in Subsection 6.1.3. The RCS (and thus received power) scales linearly with this property, where a higher reflectivity yields a stronger signal.

- **Surface roughness:** Encompassed in the 'Width parameter' C, expressed in radians. There is no definite relationship of C to the surface roughness, but as higher surface roughness causes incoherent signal scattering and enlarged spectrum width (weaker received echo) proportional to the RMS (Root Mean Square) slope s_{RMS}, it is conventionally related to s_{RMS} via Equation 6.7 [59, 135, 141]. The s_{RMS} is defined as the effective variance in the slopes, i.e. their standard angular deviation [72, 135].

- **Surface slope/inclination:** Encompassed in the 'Required tilt angle for specular reflection' γ. It relates local surface alignment to the required geometry for ideal specular reflection [57]. It is measured from the local mean surface normal and defined in Equation 6.8, where, $\hat{n}$ is the unit normal to the surface at the point of relevance and $\hat{g}$ is the required unit normal to the surface at the point of relevance for a perfect specular reflection, which follows from Equation 6.9. Here, $\hat{r_T}$ and $\hat{r_T}$ are the respective unit vectors from the relevant point to MEX, the transmitter, and TGO, the receiver. The geometry is shown in Figure 6.3.

$$\begin{aligned} \gamma &= \arccos(\hat{n} \cdot \hat{g}) \\ &= \arccos(|\hat{n}| \cdot |\hat{g}| \cdot \cos(\gamma)) \quad (6.8) \\ &= \arccos(\cos(\gamma)) \end{aligned}$$

$$\hat{g} = \frac{\hat{r_T} + \hat{r_R}}{|\hat{r_T} + \hat{r_R}|} \quad (6.9)$$

A detailed description of the computation will be given in Subsection 6.2.4, where the required topography data is taken from NASA's Planetary Data System[4]. MOLA data is expected to be sufficient, as it also was for modelling scattering effects in BSR observations between the Earth and Mars Odyssey with a wavelength of 75 cm [57], which is comparable to the 70 cm used for MEX-TGO BSR, as well as for the radar sounding of the Lucas Planum [109].
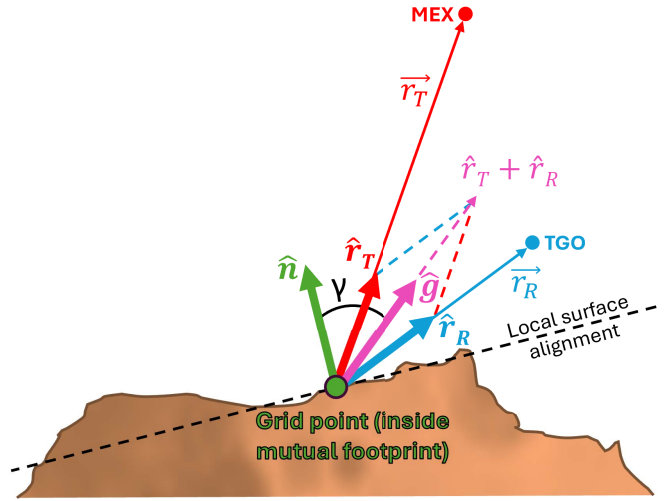
Figure 6.3: Geometry behind the tilt angle γ (not to scale), own work

6.1.3. Determination of the Dielectric Constant

The Fresnel reflectivity ρ connects received signal power to the subsurface composition through its relation to the dielectric constant ϵ. As previously discussed in Subsection 3.2.1, the dielectric constant is a material property, otherwise known as the 'relative permittivity' (or simply the 'permittivity'), which describes the material's response to an incoming electric field [56, 132, 158]. For non-colocated transmitters and receivers, as with MEX-TGO BSR, the signal is a non-normal incidence and the Fresnel reflectivity becomes a function of both ϵ as well as the incidence angle θ_i. Equations 6.10 and 6.11 are used for the case where the signal is normal to the plane of incidence ($\rho_\perp(\theta_i)$) or inside the plane of incidence ($\rho_\parallel(\theta_i)$) respectively [47].

$$\rho_\perp(\theta_i) = \left(\frac{cos(\theta_i) - \sqrt{\epsilon - sin^2(\theta_i)}}{cos(\theta_i) + \sqrt{\epsilon - sin^2(\theta_i)}}\right)^2 \quad (6.10) \qquad \rho_\parallel(\theta_i) = \frac{\epsilon cos(\theta_i) - \sqrt{\epsilon - sin^2(\theta_i)}}{\epsilon cos(\theta_i) + \sqrt{\epsilon - sin^2(\theta_i)}} \quad (6.11)$$

However, MEX-TGO BSR is unable to measure polarization of the signal after reflection. Therefore, the Fresnel reflectivity $\rho(\theta_i)$ is found by averaging both cases (normal $\rho_\perp(\theta_i)$ and parallel $\rho_\parallel(\theta_i)$) as shown in Equation 6.12.

$$\rho(\theta_i) = \frac{\rho_\perp(\theta_i) + \rho_\parallel(\theta_i)}{2} \quad (6.12)$$

---

[4]https://ode.rsl.wustl.edu/mars/index.aspx

Relation between composition and ϵ follows from the density and porosity of the medium in which the signal attenuates [121]. Ices are non-porous, but showcase lower ϵ as they have low density in comparison to rocks. When little to no ice is present sedimentary deposits tend to self-compact, resulting in high bulk density [167].

Different surface constituents, especially water ice, can present both as inclusions and distinct layers. In either case, non-polar water-rich soil will always be buried underneath water-poor regolith due to the instability at the surface [49]. Burial depth varies, where e.g. regions of high aeolian activity will have a thin cover of fine-grained weathered dust whilst volcanic regions will have thick layers of igneous unweathered rock. Due to these variations, there are also multiple methods available to determine ϵ over a mix of constituents, such as:

- **Two-component (ice-dust) mixing model by Polder and Santen [119]:**
  Orosei et al. [109] presented a mixing formula for permittivity estimations of an ice-dust mixture, shown in Equation 6.13. This was based upon the model from Polder and Santen [119], where ϵ_h is the permittivity of the host material (regolith), ϵ_i is the permittivity of the inclusion material (water ice) and ϵ_{eff} is the effective combined permittivity [109]. This model balances the two components with respect to the total unknown medium by weighting according to the volume fraction v_{ice} of the ice inclusions [109].

$$(1 - v_{ice}) \cdot \frac{\epsilon_h - \epsilon_{eff}}{\epsilon_h + 2 \cdot \epsilon_{eff}} + v_{ice} \cdot \frac{\epsilon_i - \epsilon_{eff}}{\epsilon_i + 2 \cdot \epsilon_{eff}} = 0 \tag{6.13}$$

- **Three-component mixing model by Baker and Carter [4]:**
  Others, such as Ma et al. [80] and Baker and Carter [4] presented three-component models. Equation 6.14 shows the mixing power law model. Here γ is an empirically derived exponent, equal to 2.7 and v represents the volume fractions of the materials, including a term for air with ϵ_{air} equal to 1.0 [4].

$$\epsilon_{eff}^{1/\gamma} = v_{rock} \cdot \epsilon_{rock}^{1/\gamma} + v_{ice} \cdot \epsilon_{ice}^{1/\gamma} + v_{air} \cdot \epsilon_{air}^{1/\gamma} \tag{6.14}$$

- **Maxwell Garnett method:**
  As described by Markel [89], the Maxwell Garnett is based upon spherical inclusions of permittivity ϵ_{ice} and volume fraction v_{ice} in a host medium with permittivity ϵ_h, shown in Equation 6.15.

$$\epsilon_{eff} = \epsilon_h \cdot \frac{\epsilon_h + \frac{1 + 2v_{ice}}{3} \cdot (\epsilon_{ice} - \epsilon_h)}{\epsilon_h + \frac{1 - v_{ice}}{3} \cdot (\epsilon_{ice} - \epsilon_h)} \tag{6.15}$$

The Maxwell-Garnett method is most conventional and applied for the MEX-TGO BSR model [145]. Herein, the host medium is low-porosity Martian regolith (ϵ_h=4.0), i.e. a mix of basaltic rock and dust, for low to mid-latitudes or non-porous CO_2 ice (ϵ_h=2.1) for near-polar regions ($\geq 60°$) [28]. For water ice, ϵ_{ice} is taken as 3.1 [4, 28, 80]. It is important to note that ϵ values can overlap between different materials and the permittivity of water is well-defined, but it is much more complex to define for regolith which can range from 4-10 (highly igneous regions) [4, 28, 80]. Geo-morphological conditions, models and results from other technologies need to be compared with BSR results to take definitive conclusions on water (ice) presence [50, 140].

6.2. Description of the Model

This section describes the numerical model of the subsurface for MEX-TGO BSR. First, Subsection 6.2.1 lays down the modelling approach and high-level architecture. Secondly, detailed computations inside the high-level model elements are discussed, including: The measurement geometry computations for the mutual signal footprint (Subsection 6.2.2), simulated MEX and TGO antenna patterns (Subsection 6.2.3), processing of the MOLA data (Subsection 6.2.4), processing of the GRS and FREND data (Subsection 6.2.5) and processing of the Automatic Gain Control (AGC) data retrieved from the MEX-TGO BSR measurements (Subsection 6.2.6). Lastly, Subsection 6.2.7 presents the resultant low-level model architecture, including all sub-computations.

6.2.1. Definition of Modelling Approach and High-Level Architecture

To process the MEX-TGO BSR measurements, the numerical model should simulate the received power spectrum using the bistatic radar equation, as presented in Subsection 6.1.2, and dielectric constant inferred from GRS and/or FREND data. This allows for comparison of the modelled power spectrum with the measured power spectrum, which is retrieved from the Automatic Gain Control (AGC) data, and thus conclude on the subsurface composition as expected through the different measurement methods [57, 133]. This yields the MEX-TGO BSR model architecture, for 'main_MEXTGOBSR_model.py', of Figure 6.4. Beforehand,

the footprints are derived with 'main_MEXTGOBSR_footprint.py' and slopes with 'infer_slope_MOLA.py'. Afterward, 'main_MEXTGOBSR_visualizeresults.py' is used for visualizing results. All code is on GitHub [5].
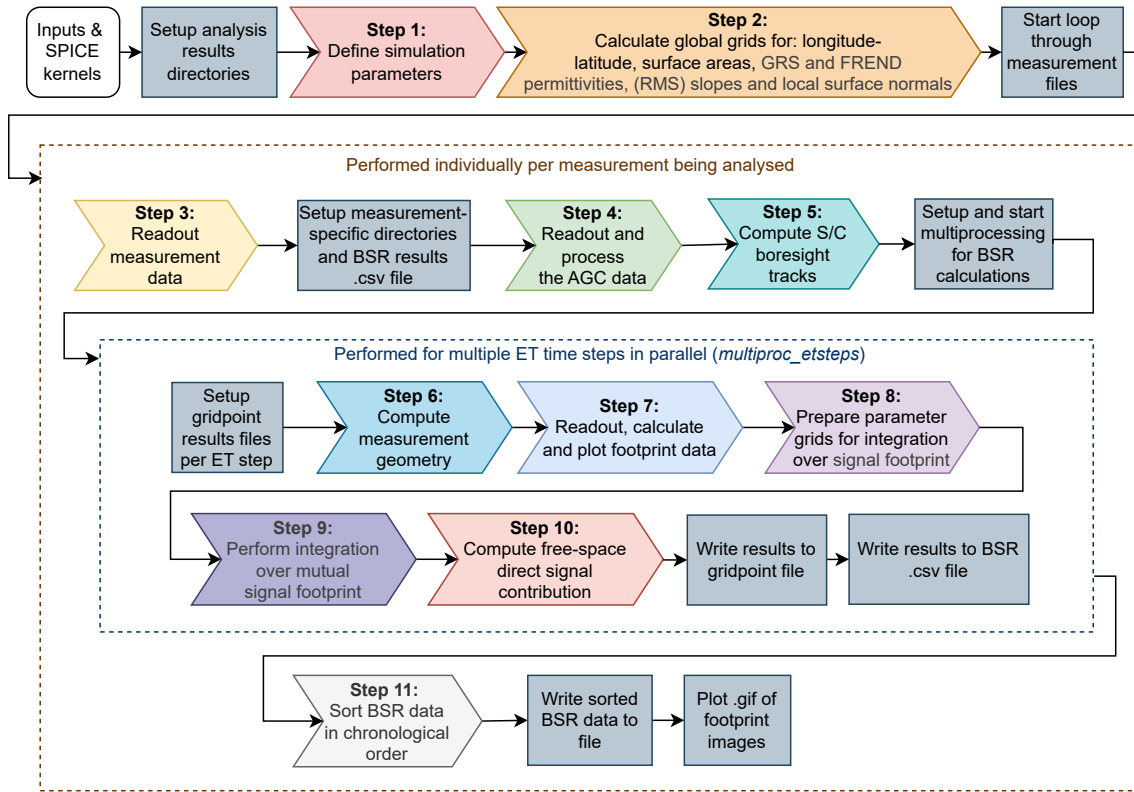
Figure 6.4: High-level code architecture for the MEX-TGO BSR model, own work

The model parameters are processed as grids, i.e. 2D arrays, wherin the grid cells are bound and defined by longitude-latitude bands. The spatial resolution is dictated by the MOLA data and set to 4x4 pixels (equivalent to 0.25°) to limit computational cost. However, it was increased to 16x16 pixels (equivalent to 0.0625°) for one measurement (BSR-2.1) to showcase the effect of higher resolution, discussed in Subsection 6.4.1.

6.2.2. Measurement Geometry and Determination of the Mutual Footprint

The mutual footprint is computed separately from the main model using 'main_MEXTGOBSR_footprint.py'. At every time step in a measurement, it calculates the illuminated area by characterizing the horizon as an ellipse on ellipsoidal Mars as seen from either S/C. A list of 360 points is generated around the borders of the footprint and written to .csv files, to be imported in the main model. Grid points inside the footprint are given a value of 1, and those outside a value of 0, to create a mask for which the integration is to be performed. For illustrative purposes, .gif files are created of each measurement to showcase the progression of the footprint in both 2D and 3D. These are not included in the report, but can be accessed on the thesis GitHub repository[6]. Figures 6.5 and 6.6 show the resultant footprint of the BSR-2.1 measurement at its start and end respectively. Figures 6.7 and 6.8 illustrate it in 3D. Similar figures for BSR campaigns 1 through 4 can be found in Appendix C.
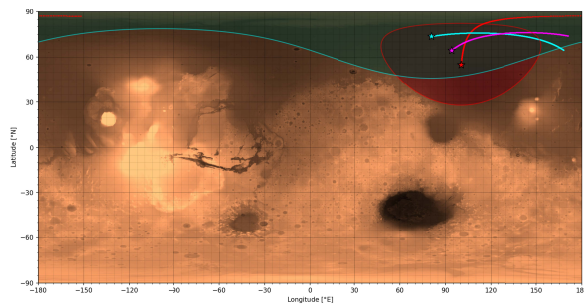
Figure 6.5: Mutual signal footprint for BSR-2.1 at start of measurement (20th of March 2025 23:40:54; using 4 pixel/degree resolution), own work
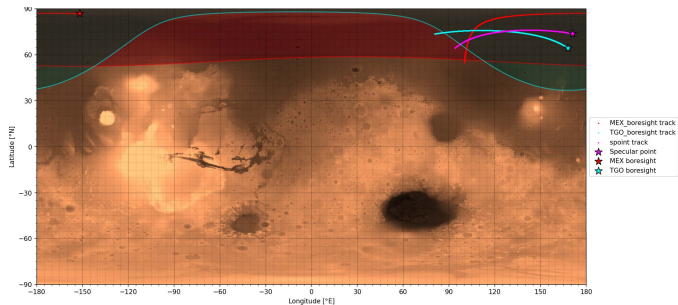
Figure 6.6: Mutual signal footprint for BSR-2.1 at end of measurement (20th of March 2025 23:50:54; using 4 pixel/degree resolution), own work

---

[5]https://github.com/DJNieuwenhuizen/MSc-thesis/

[6]https://github.com/DJNieuwenhuizen/MSc-thesis/
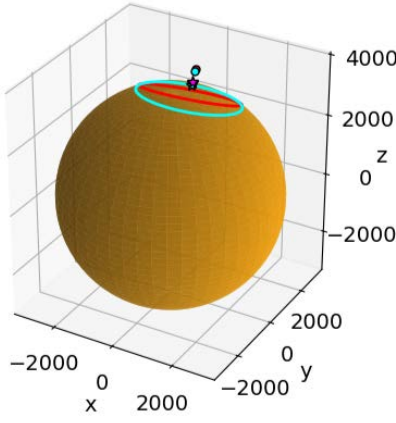
Figure 6.7: 3D Mutual footprint for BSR-2.1 at start of measurement (20th of March 2025 23:40:54), own work
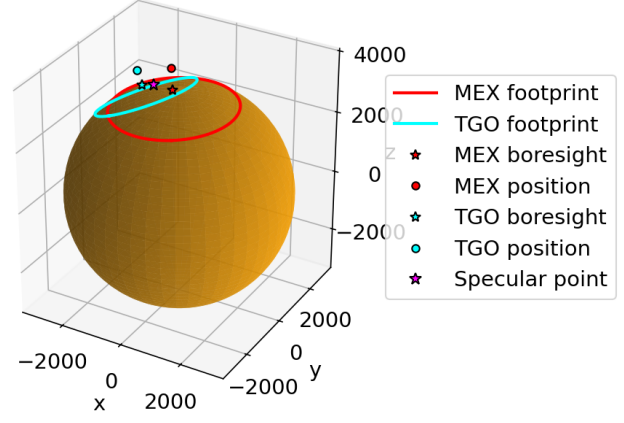
Figure 6.8: 3D Mutual footprint for BSR-2.1 at end of measurement (20th of March 2025 23:50:54), own work

For determining the surface area within the footprint, a circular segment on ellipsoidal Mars between ϕ_{min} and ϕ_{max} (the lower and upper latitudinal bounds) is integrated according to Equation 6.16 [170]. The gridpoint surface area is then calculated by dividing the segment by the amount of pixels along the longitudinal direction.

$$S_{gridpoint} = \frac{1}{360 \cdot n_{pix/deg}} \cdot S_{circular\ segment} \tag{6.16}$$

$$= \frac{1}{360 \cdot n_{pix/deg}} \cdot \left(\frac{2\pi \cdot a}{\sqrt{2}} \cdot \int_{\phi_{min}}^{\phi_{max}} \sqrt{(a^2 + b^2 + (a^2 - b^2) \cdot cos(2 \cdot v))} \cdot sin(v) dv \right)$$

Furthermore, time steps are processed in sets of four (16 pixel/degree resolution) or ten (4 pixel/degree resolution) in parallel to decrease required run time (at maximum available computational capacity).

6.2.3. Antenna Patterns

As shortly noted in Subsection 6.2.2, radar signal strength decreases further away from the boresight. This is characterized in the antenna gain, determined at each location in the footprint by the S/C antenna gain patterns. For MEX, the MelaCom antenna system has forward link off-boresight gains as tabulated in Table 6.1, which when fit to a Gaussian curve (the standard shape for radar signals [106, 147]) results in the antenna pattern shown in Figure 6.9. As the MEX gain data does not contain values beyond 65° (and TGO beyond 90°), it is dangerous to extrapolate to higher off-boresight angles, the implication of which is discussed in Section 6.4.

Table 6.1: MEX MelaCom antenna gain pattern values (forward link; 437.1 MHz), retrieved from Svedhem [147] and Stanton, Bavin, and Cassidy [139]

Off-boresight angle [deg]	Antenna gain [dB]	Loss compared to boresight [dB]
0	+6.0	0.0
10	+5.5	-0.5
35	+3.0	-3.0
50	-2.0	-8.0
65	-10.0	-16.0
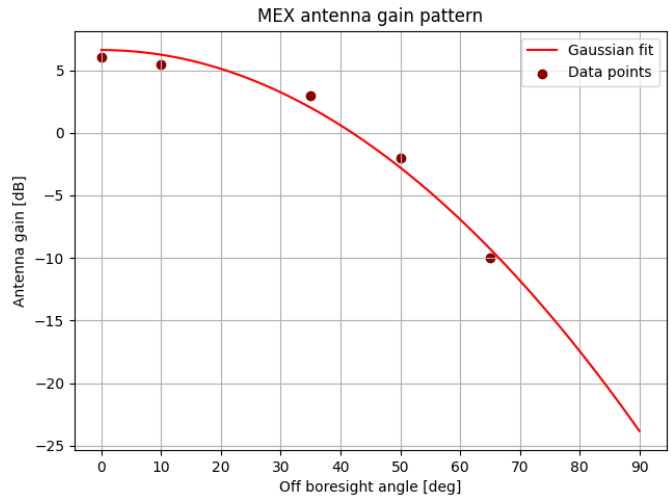
Figure 6.9: MEX MelaCom antenna gain pattern with Gaussian inter-/extrapolation (forward link; 437.1 MHz), own work

For TGO, the forward link pattern (437.1 MHz) is used for its Flight Model 2 (FM2) antenna, as the return link is only valid for 401 MHz. Data for the mockup was retrieved for every ten degrees, as shown in Table 6.2. It was also fit to a Gaussian curve, resulting in the antenna pattern shown in Figure 6.10. This shows overall better gain performance than MEX. However due to the lower orbit of TGO, it will also often be at a larger incidence angle with grid points in the mutual surface footprint than MEX, which is generally at a higher altitude.

Table 6.2: TGO FM2 antenna gain pattern values (forward link; 437.1 MHz), retrieved from Svedhem [147, 148]

Off-boresight angle [deg]	Antenna gain [dB]	Loss compared to boresight [dB]
0	+6.1	0.0
10	+5.9	-0.2
20	+5.1	-1.0
30	+4.4	-1.7
40	+3.1	-3.0
50	+0.9	-5.2
60	-1.6	-7.7
70	-4.9	-11.0
80	-9.2	-15.3
90	-16.8	-22.9
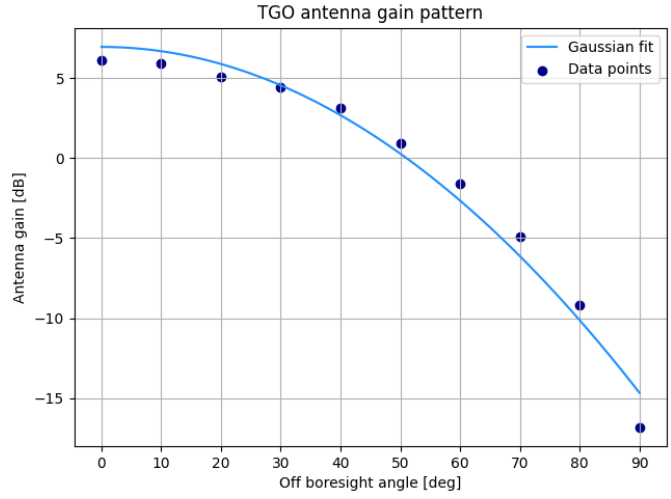
Figure 6.10: TGO FM2 antenna gain pattern with Gaussian interpolation (forward link; 437.1 MHz), own work

In order to use the antenna gains in the BSR equation (Equation 6.5), they must be converted from deciBels to a linear scale using Equation 6.17. Here, G_{dB} is the antenna gain in deciBels and G_{linear} is the linear counterpart.

$$G_{linear} = 10^{\frac{G_{dB}}{10}}$$

(6.17)

6.2.4. Processing of MOLA Data for Topography Scaling Factor

The topography scaling factor $C \cdot (cos^4(\gamma) + C \cdot sin^2(\gamma))^{-3/2}$ characterizes the sampled area topography in the RCS according to the Hagfors model (Equation 6.6) through C, dependent on the RMS slope s_{RMS} (Equation 6.7), and γ, on the local surface normal $\hat{n}$ and measurement geometry $\hat{g}$ (Equations 6.8 and 6.9). To retrieve s_{RMS} and $\hat{n}$, MOLA data (Subsection 3.3.2) is taken from NASA's Planetary Data System[7]. There are different raw and derived products available [115], but the selected ones are the Mission Experiment Gridded Data Records (MEGDRs) [116, 136]. These are global topography data sets accumulated by binning altimetry over the entire mission, available in resolutions of 4, 16, 32, 64 and 128 pixels per degree [116]. To limit computational cost, 4 pixel per degree was used, with the number of observations ('counts') per bin shown in Figure 6.11. However, as will be discussed in Subsection 6.4.1, this induces aberrations in the results and thus the 16 pixel/degree resolution was also used for one of the measurements, with counts shown in Figure 6.12. The polar regions were not sampled routinely, as they laid off-nadir from the MGS orbit, thus empty bins were interpolated [137].
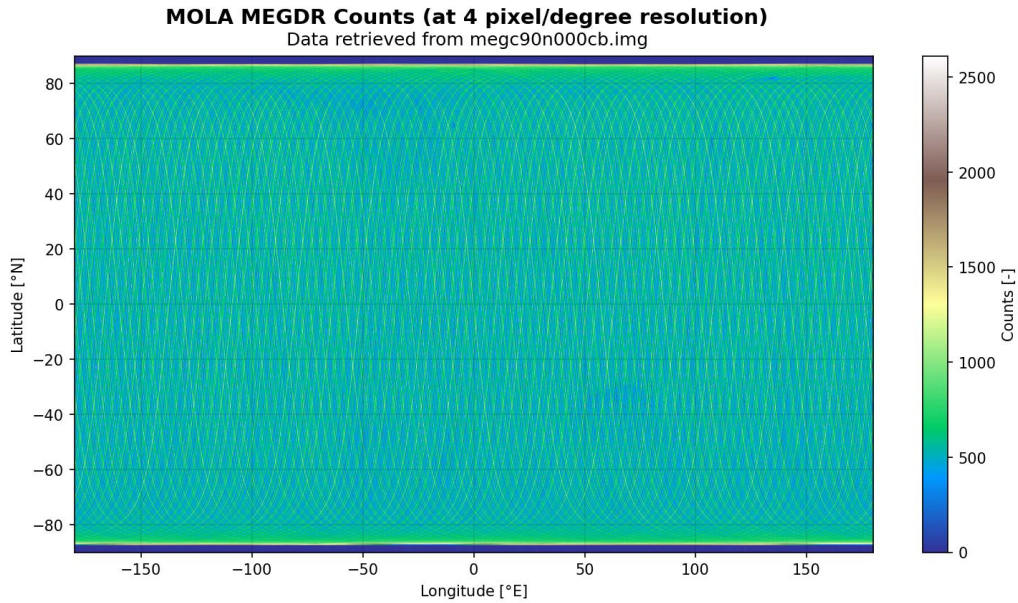
Figure 6.11: Counts inferred from MOLA MEGDRs in 4 pixel per degree resolution (from *megc90n000cb.img* [116, 136]), own work

The topography data in 4 pixel per degree resolution for the MOLA MEGDRs is shown in Figure 6.13 and for the 16 pixel per degree resolution in Figure 6.14. These results were validated by comparing the resultant elevation range (-8068 to 21134 m) to the expected elevation range from literature (-8206 to 21181 m) [20].

---

[7]https://ode.rsl.wustl.edu/mars/index.aspx

MOLA MEGDR Counts (at 16 pixel/degree resolution)
Data retrieved from megc90n000eb.img
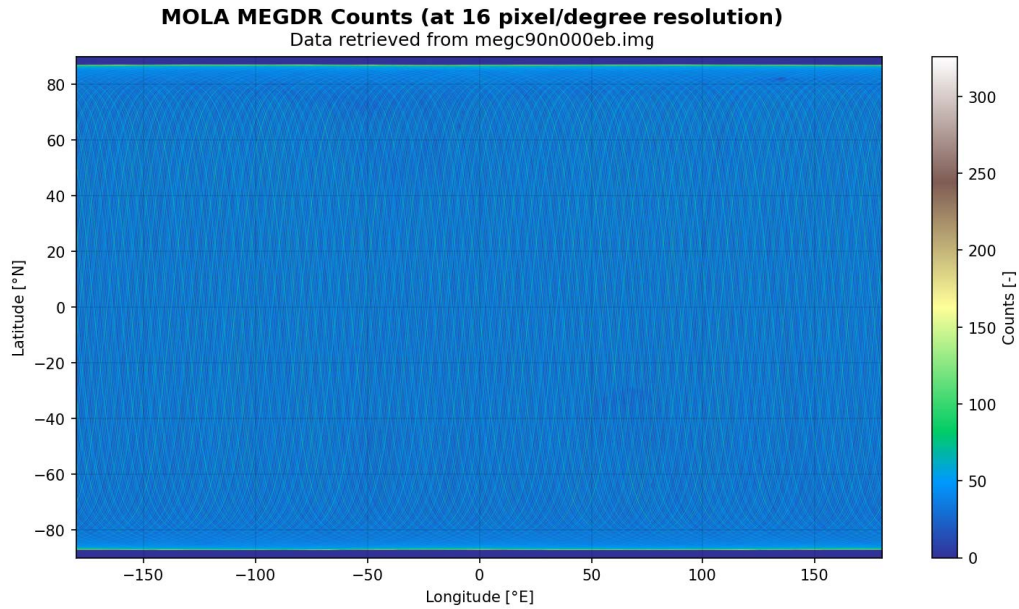
Figure 6.12: Counts inferred from MOLA MEGDRs in 16 pixel per degree resolution (from *megc90n000eb.img* [116, 136]), own work

MOLA MEGDR Topography (at 4 pixel/degree resolution)
Data retrieved from megt90n000cb.img
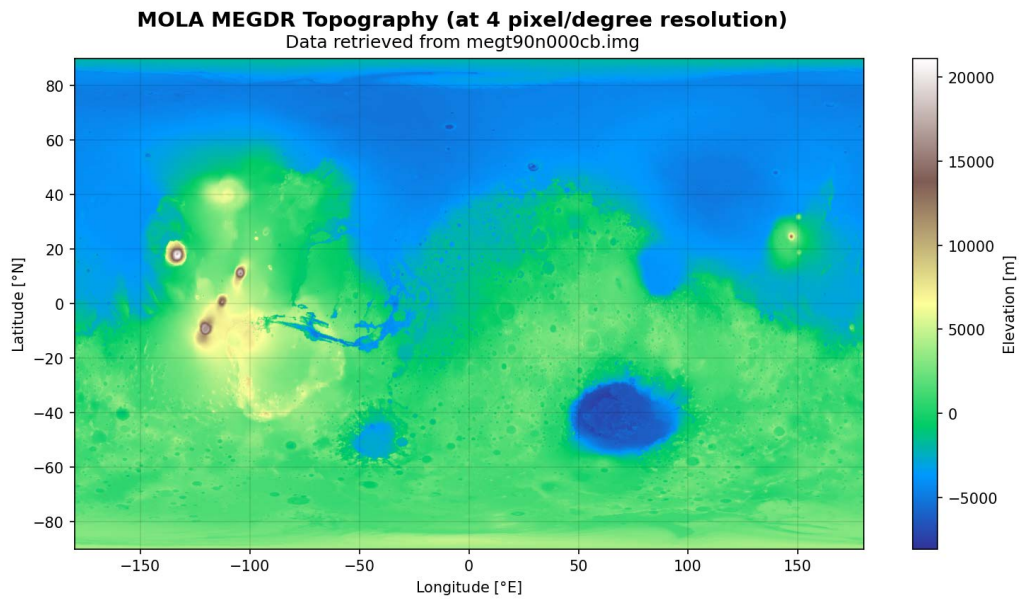
Figure 6.13: Topography inferred from MOLA MEGDRs in 4 pixel per degree resolution (from *megt90n000cb.img* [116, 136]), own work

MOLA MEGDR Topography (at 16 pixel/degree resolution)
Data retrieved from megt90n000eb.img
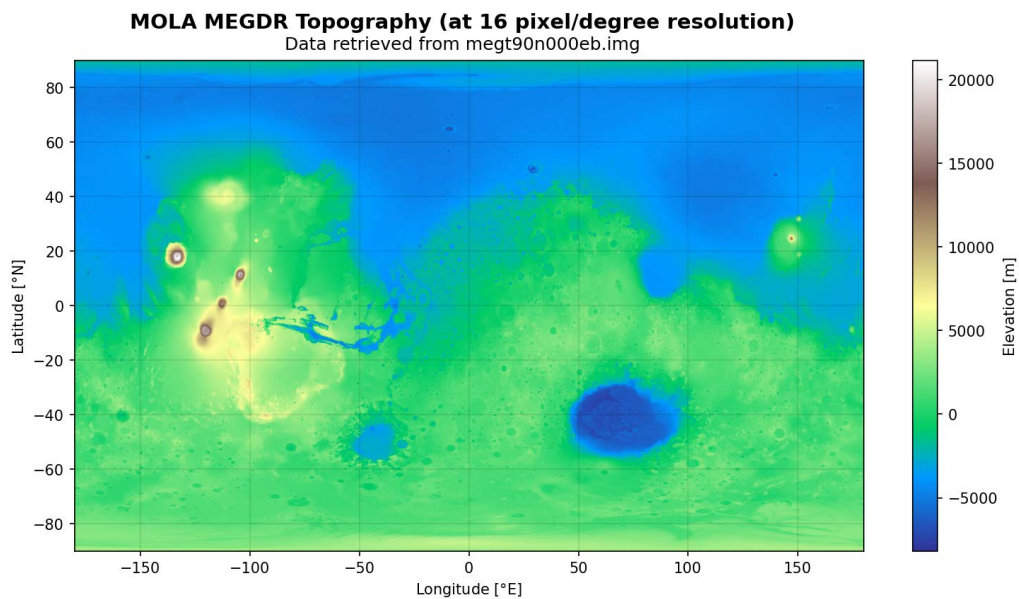
Figure 6.14: Topography inferred from MOLA MEGDRs in 16 pixel per degree resolution (from *megt90n000eb.img* [116, 136]), own work

To derive the slope for a gridpoint, a four-point raster is implemented around the pixel, as shown in Figure 6.15 [53]. The slope s is then calculated using Equation 6.18, where z is the topography value at the point of interest, and z_N, z_E, z_S and z_W are the neighboring values in Northern, Eastern, Southern and Western direction [52]. Furthermore, the parameters Δx and Δy represent the pixel size in longitudinal (x) and latitudinal (y) direction.

$$s = \sqrt{(\frac{z_E - z_W}{2 \cdot \Delta x})^2 + (\frac{z_N - z_S}{2 \cdot \Delta y})^2} \qquad (6.18)$$

Figure 6.15: Standard four-point raster for slope calculation, own work
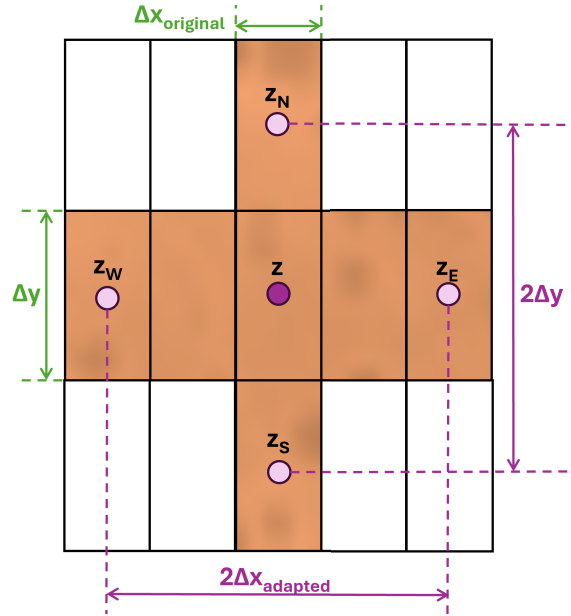
Figure 6.16: Adapted four-point raster for slope calculation, own work

The MOLA data is binned by longitude and latitude, meaning the latitudinal distance (Δy) stays relatively constant regardless of pixel location, whilst the longitudinal distance (Δx) decreases rapidly toward the poles. This induces a strong directional bias and incorrect slope values in the polar regions. Therefore, an adapted version of the raster (Figure 6.16) was implemented. Instead of using the neighboring pixels along x, the Δx is matched to approximately the same value as Δy, and the corresponding pixels are used for z_E and z_W (in case of the example in Figure 6.16, this entails using the second neighboring pixel instead of the first). This makes the slope resolution spatially consistent at ~29.6 km per two pixels (where slopes are calculated over 2 times Δx and 2 times Δy) for 4 pixel/degree resolution, or ~7.4 km per two pixels for 16 pixel/degree resolution.

$$\Delta x = \frac{2\pi \cdot R}{360 \cdot n_{pix/deg}} \qquad (6.19) \qquad \Delta y = a \cdot \int_{\phi - 1/n_{pix/deg}}^{\phi + 1/n_{pix/deg}} \sqrt{1 - e^2 \cdot sin^2(\theta)} d\theta \qquad (6.20)$$

$$e = \sqrt{1 - \frac{b^2}{a^2}} \qquad (6.21)$$

Furthermore, Δx and Δy themselves are calculated with Equations 6.19 and 6.20. Δx is relatively simple to calculate by dividing the local circumference (which is circular with radius R) by the amount of pixels, where $n_{pix/deg}$ is equal to the number of pixels per degree, i.e. resolution. Δy is more complicated, as the circumference of an ellipse cannot be expressed elementarily, instead it has to be retrieved for every latitude ϕ through the elliptic integral of the second kind [169], shown adapted in Equation 6.20. Here e is the eccentricity, or 'elliptic modulus', defined in Equation 6.21 where a is the semi-major axis and b the semi-minor axis of the Martian ellipsoid [168, 124], values for which are again taken as 3396.19 km and 3376.20 km respectively [38].

Resulting slopes are shown in Figures 6.17 and 6.19 for the 4 and 16 pixel per degree resolutions respectively. These are validated using slope values found in literature, such as shown in Figure 6.18, which were published by the Jet Propulsion Laboratory [69] and derived from MOLA data on 30 km spatial resolution, i.e. corresponding to the 4 pixel per degree resolution, and showcasing good agreement with the model results.
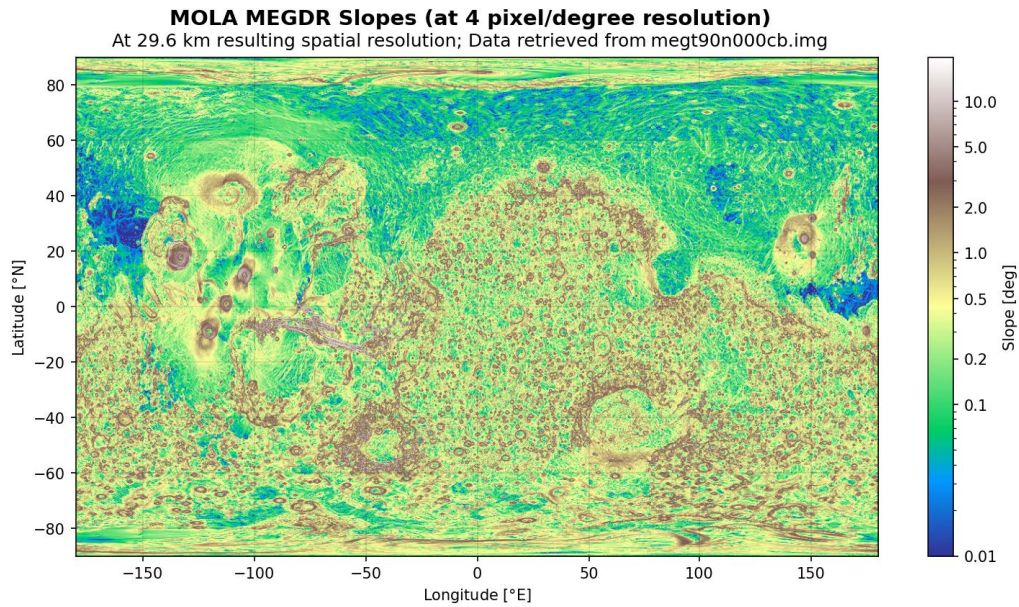
Figure 6.17: Slopes inferred from MOLA MEGDRs in 4 pixel per degree angular resolution (~29.6 km spatial resolution), own work
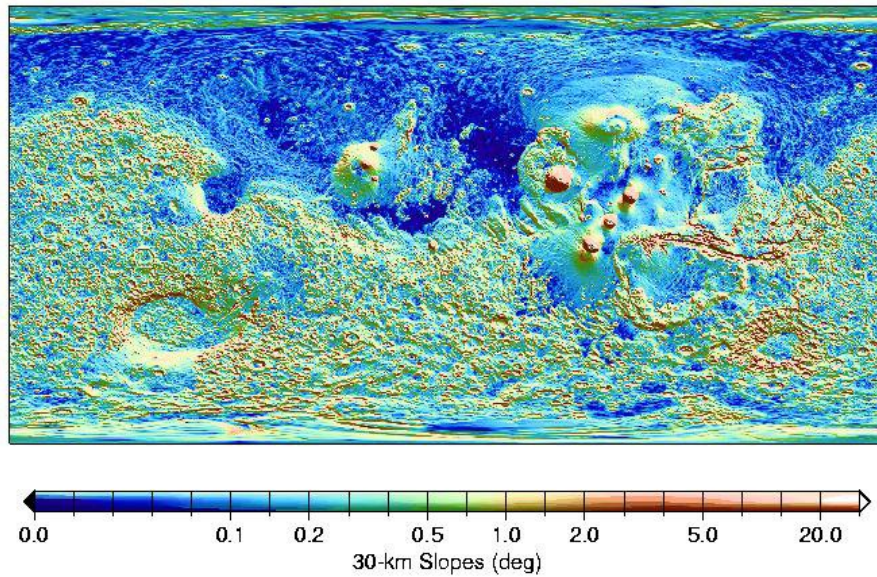
Figure 6.18: Slopes inferred from MOLA data in literature (30.0 km baselines), retrieved from the Jet Propulsion Laboratory [69]
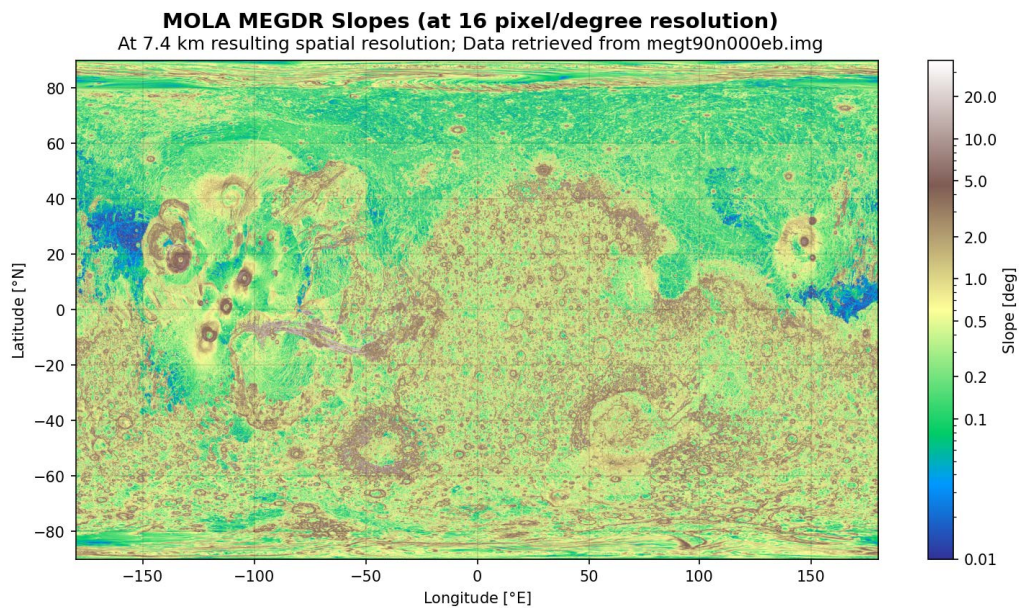
Figure 6.19: Slopes inferred from MOLA MEGDRs in 16 pixel per degree angular resolution (~7.4 km spatial resolution), own work

An additional step is needed for $\hat{n}$, as not only the absolute value, but also the directionality of the slope is necessary. For this, the local tangent plane to the slope is defined by the local Northern and Eastern direction at gridpoint (ϕ_i, λ_i), calculated with Equations 6.22 and 6.23 respectively [18]. The local North is tangent to constant longitude, pointing to increasing latitude, whilst the local East is tangent to constant latitude and points to increasing longitude. The vector along the slope is then defined by Equation 6.24.

$$\vec{v}_{local\,North} = \begin{bmatrix} -sin(\lambda_i) \\ cos(\lambda_i) \\ 0 \end{bmatrix} \quad (6.22) \qquad \vec{v}_{local\,East} = \begin{bmatrix} -cos(\lambda_i) \cdot sin(\phi_i) \\ -sin(\lambda_i) \cdot sin(\phi_i) \\ cos(\phi_i) \end{bmatrix} \quad (6.23)$$

$$\vec{v}_{\substack{along \\ slope}} = x_{component} \cdot \vec{v}_{local\,East} + y_{component} \cdot \vec{v}_{local\,North} \quad (6.24)$$

$$= (\frac{z_E - z_W}{2 \cdot \Delta x}) \cdot \vec{v}_{local\,East} + (\frac{z_N - z_S}{2 \cdot \Delta y}) \cdot \vec{v}_{local\,North}$$

Taking the local unit surface normal on ellipsoidal Mars $\hat{n}_{ell}$ (ignoring topography effects) and rotating it around the local unit along-slope vector $\hat{v}_{along\,slope}$ by the absolute slope value s (using rotation matrix $R_\Omega(s)$) yields $\hat{n}$. This is expressed in Equation 6.25, wherein I is the identity matrix and Ω is the antisymmetric matrix, made up of the unit slope vector components according to Rodrigues' Rotation Formula [9]. Furthermore, $\hat{g}$ can be derived elementarily from the measurement geometry, which allows for computing the tilt angle γ.

$$\hat{n} = R_\Omega(s) \cdot \hat{n}_{ell} \quad (6.25)$$

$$= (I + \Omega \cdot sin(s) + \Omega^2 \cdot (1 - cos(s))) \cdot \hat{n}_{ell}$$

$$= (\begin{bmatrix} 1 & 0 & 0 \\ 0 & 1 & 0 \\ 0 & 0 & 1 \end{bmatrix} + \begin{bmatrix} 0 & -\omega_z & \omega_y \\ \omega_z & 0 & -\omega_x \\ -\omega_y & \omega_x & 0 \end{bmatrix} \cdot sin(s) + \begin{bmatrix} 0 & -\omega_z & \omega_y \\ \omega_z & 0 & -\omega_x \\ -\omega_y & \omega_x & 0 \end{bmatrix}^2 \cdot (1 - cos(s))) \cdot \hat{n}_{ell}$$

$$= (\begin{bmatrix} 1 & 0 & 0 \\ 0 & 1 & 0 \\ 0 & 0 & 1 \end{bmatrix} + \begin{bmatrix} 0 & -\hat{v}_{along\,slope,z} & \hat{v}_{along\,slope,y} \\ \hat{v}_{along\,slope,z} & 0 & -\hat{v}_{along\,slope,x} \\ -\hat{v}_{along\,slope,y} & \hat{v}_{along\,slope,x} & 0 \end{bmatrix} \cdot sin(s) + \begin{bmatrix} 0 & -\hat{v}_{along\,slope,z} & \hat{v}_{along\,slope,y} \\ \hat{v}_{along\,slope,z} & 0 & -\hat{v}_{along\,slope,x} \\ -\hat{v}_{along\,slope,y} & \hat{v}_{along\,slope,x} & 0 \end{bmatrix}^2 \cdot (1 - cos(s))) \cdot \hat{n}_{ell}$$

For the absolute slopes s, effectively a plane is fitted over the raster with a two-pixel width component in Northern and Eastern direction. As C is not dependent on the absolute slope, but RMS slope s_{RMS}, a different method is implemented: For the RMS slopes, the derivation follows from the slope variation, thus four values in Northern, Eastern, Southern and Western direction of one-pixel width are calculated. The used raster is shown in Figure 6.20 for the ideal/standard situation, and adapted for consistent spatial resolution in Figure 6.21.
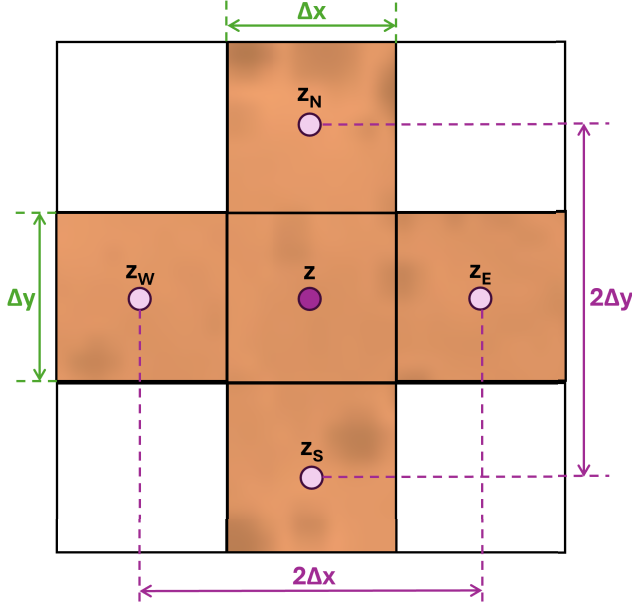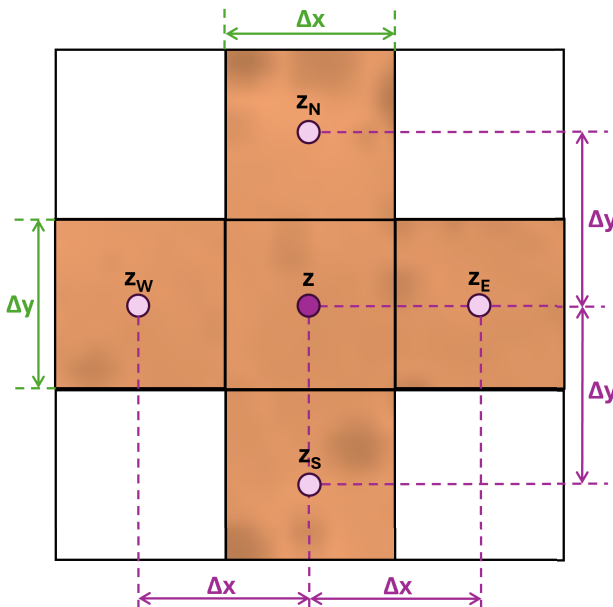

Figure 6.20: Standard four-point raster for RMS slope calculation, own work
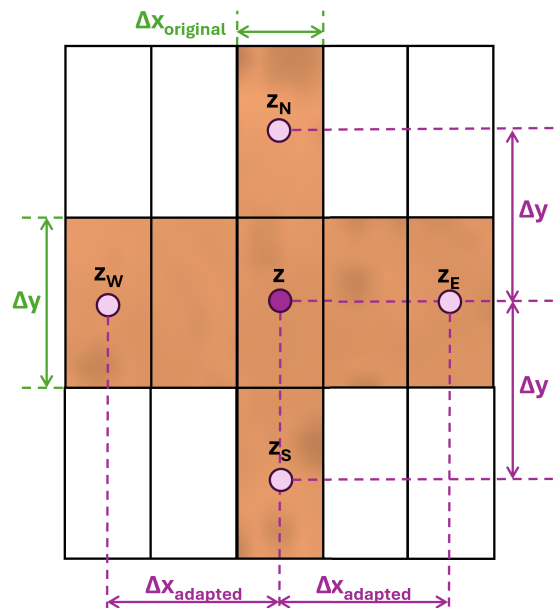
Figure 6.21: Adapted four-point raster for RMS slope calculation, own work

The RMS slope at each pixel is calculated using the standard definition of RMS (Equation 6.26) resulting in Equation 6.27. This yields the RMS slopes imaged in Figure 6.22 with a spatial resolution of ~14.8 km per pixel for the 4 pixels/degree, and in Figure 6.23 with a spatial resolution of ~3.7 km per pixel for 16 pixels/degree.

$$RMS = \sqrt{\frac{1}{N} \cdot \Sigma_i x_i^2} \tag{6.26}$$

$$s_{RMS} = \sqrt{\frac{1}{4} \cdot \left(\left(\frac{|z - z_N|}{\Delta y}\right)^2 + \left(\frac{|z - z_E|}{\Delta x}\right)^2 + \left(\frac{|z - z_S|}{\Delta y}\right)^2 + \left(\frac{|z - z_W|}{\Delta x}\right)^2\right)} \tag{6.27}$$
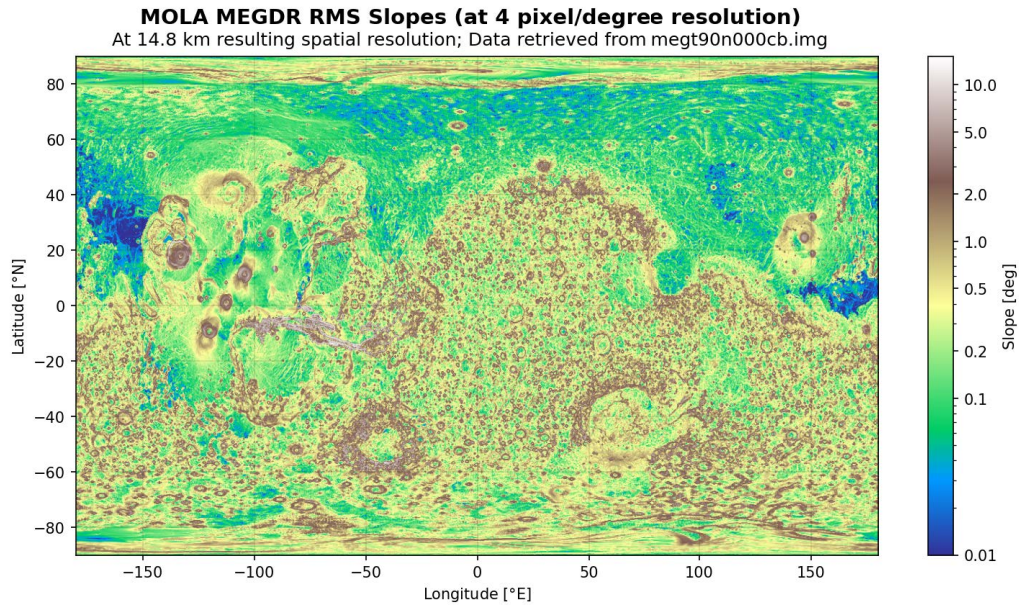
Figure 6.22: RMS slopes inferred from MOLA MEGDRs in 4 pixel per degree angular resolution (~14.8 km spatial resolution), own work
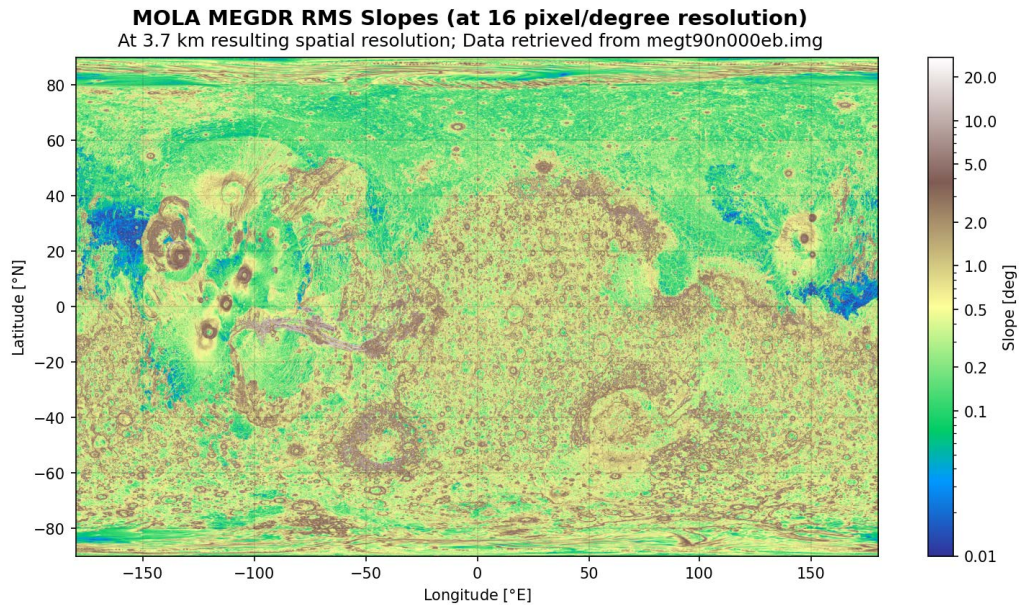
Figure 6.23: RMS slopes inferred from MOLA MEGDRs in 16 pixel per degree angular resolution (~3.7 km spatial resolution), own work

6.2.5. Processing of GRS and FREND Data

In the Maxwell-Garnett method (Equation 6.15), the permittivities are scaled with the volume fraction of water ice v_{ice}, as derived from GRS and FREND neutron spectrometry data. The GRS data was retrieved from the PDS Geosciences Node [116] and the FREND data from Golovin [54], plotted in Figures 6.24 and 6.25. The FREND data set used contains the processed results accumulated over five years and has not yet been published, but one can refer to Malakhov et al. [81] to access the prior version containing ~three years of data.
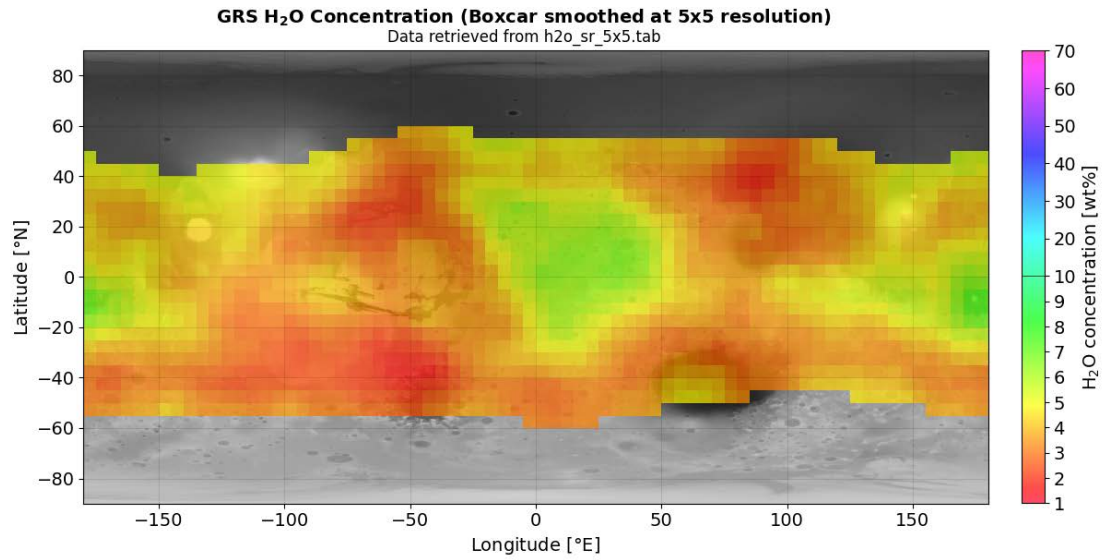
Figure 6.24: Direct plot of GRS data (derived H_2O concentration in 5x5° longitude-latitude bins, smoothed using a Boxcar filter; from '*h2o_sr_5x5.tab*' [116]), own work
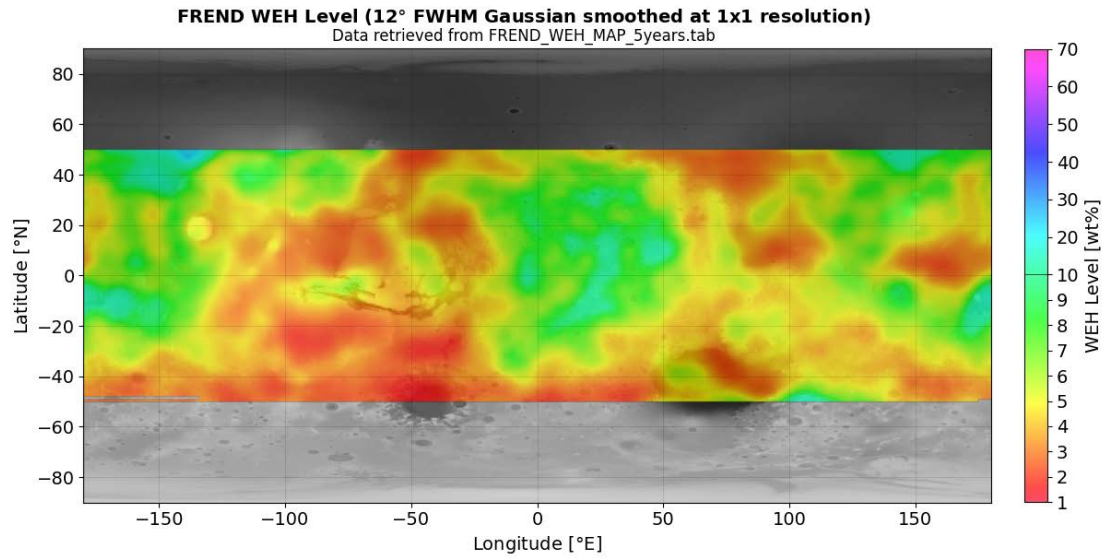
Figure 6.25: Direct plot of FREND data (derived H_2O concentration in 1x1° longitude-latitude bins, smoothed using a 12° FWHW Gaussian filter; from '*FREND_WEH_MAP_5years.txt*' [54]), own work
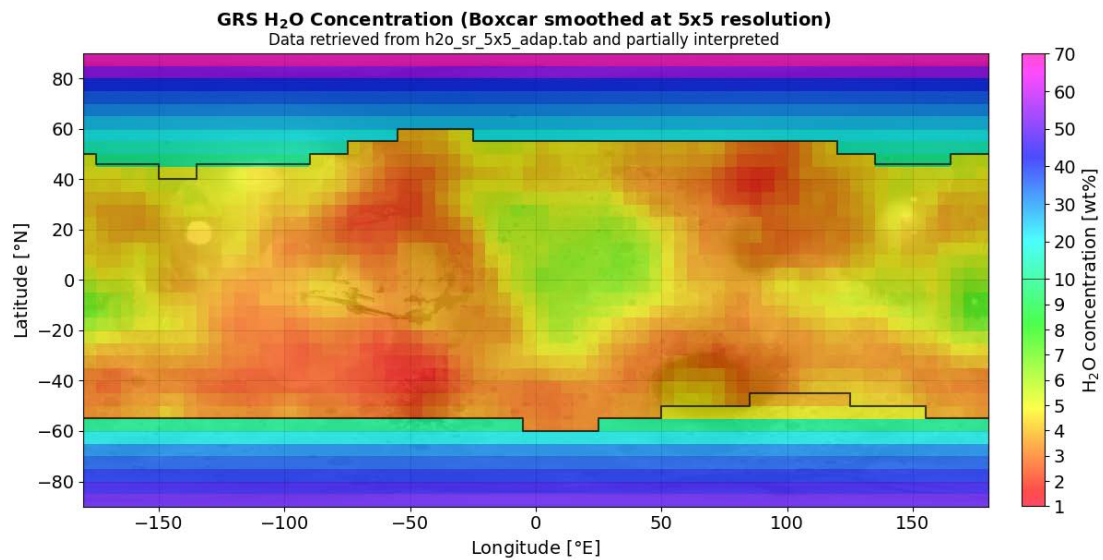
Figure 6.26: Partially interpreted plot of GRS data (derived H_2O concentration in 5x5° longitude-latitude bins, smoothed using a Boxcar filter; from '*h2o_sr_5x5.tab*' [116]), own work

The FREND resolution is much higher than GRS and showcases more extreme local values. However, both datasets lack polar coverage, even though the instruments collected data there (as shown in Figures 3.9 and 3.12, discussed in Section 3.3). Reason for this is the high seasonal dependence of WEH levels in these regions [84], where the warmer seasons sublimate away the H_2O and especially the CO_2. Thus, global derived H_2O concentration sets are not public [149] and it was decided to interpret additional GRS data from Figure 3.9, constant over 5° latitude bands, giving a baseline for MEX-TGO BSR modelling [149], shown in Figure 6.26.

For most measurements, only this partially interpreted GRS data is used, as the ground tracks run largely over high-latitudinal regions outside the bounds of the derived data of either instrument. This is with the exception of BSR-3.1 which runs over the Valles Marineris, shown previously in Figure 5.7, thus allowing comparison with both the GRS and FREND datasets. The effective dielectric constant can then be computed according to the methodology in Subsection 6.1.3, which yields the map shown in Figure 6.27 for GRS, and partial FREND map in Figure 6.28. For the MEX-TGO BSR modelling, both the GRS and FREND inferred permittivities are linearly interpolated to achieve the required resolution, i.e. 4 or 16 pixel per degree.
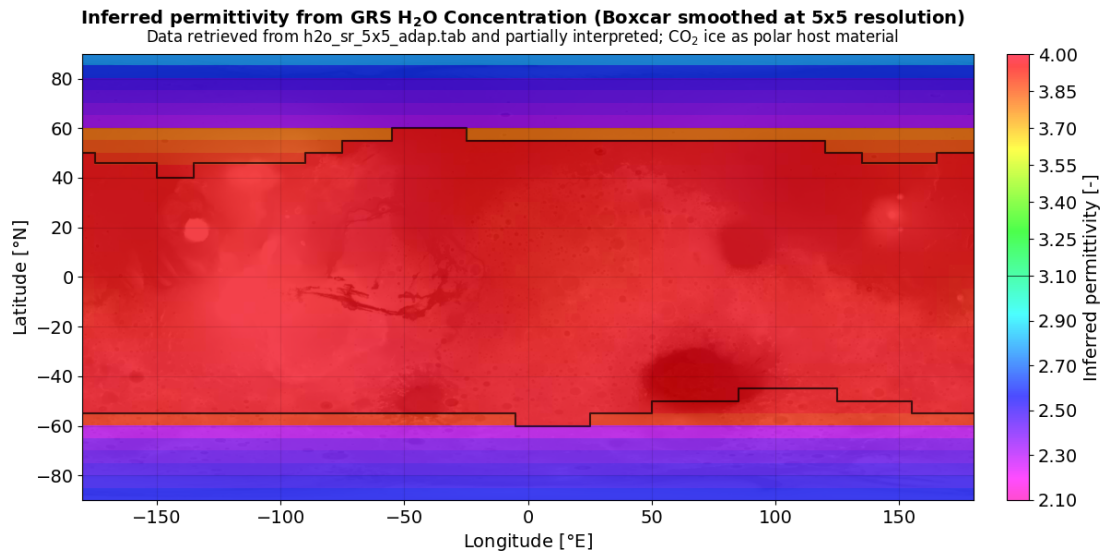
Figure 6.27: Inferred dielectric constant plot from the partially interpreted GRS data (derived H_2O concentration in 5x5° longitude-latitude bins, smoothed using a Boxcar filter; from *'h2o_sr_5x5.tab'* [116]), own work
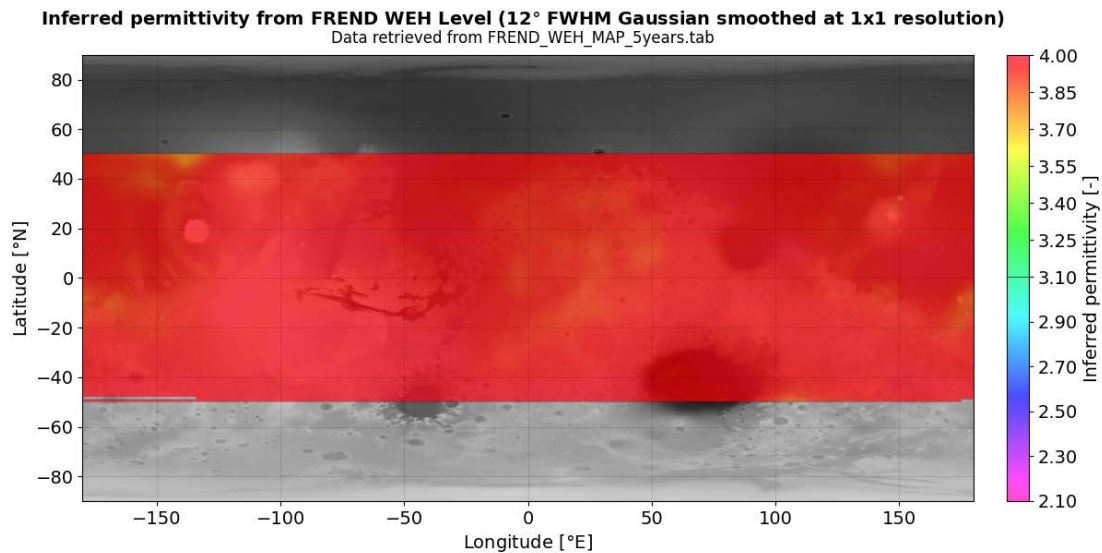
Figure 6.28: Inferred dielectric constant plot from the FREND data (derived H_2O concentration in 1x1° longitude-latitude bins, smoothed using a 12° FWHW Gaussian filter; from *'FREND_WEH_MAP_5years.txt'* [54]), own work

6.2.6. Processing of AGC Data

The MEX-TGO BSR data is collected as Automatic Gain Control (AGC) data, which is directly representative of the received signal power [149, 156]. It has to be read out from the IQ (In-phase / Quadrature) sample records downlinked by TGO, which are tabulated in Table 6.3. The IQ files starts with a number of time-coded records (96 bits long) and is followed by all non-time-coded records (32 bits long) [68, 148], the latter of which are relevant for the AGC measurements and whose 32-bit representation divided according to Table 6.4.

Table 6.3: IQ file names for the MEX-TGO BSR measurements

BSR Measurement ID	IQ file name
BSR-1.1	IQ___DMEX__05376B74_2024-023T03-48-39_8F540240230137_00001.EXM
BSR-1.2	IQ___DMEX__05376BCD_2024-030T10-30-15_8F540240300137_00001.EXM
BSR-1.3	IQ___DMEX__05376C22_2024-037T09-42-58_8F540240370137_00001.EXM
BSR-1.4	IQ___DMEX__05376C5B_2024-042T01-53-04_8F540240420137_00001.EXM
BSR-2.1	IQ___DMEX__05377FA0_2025-079T23-40-39_8F540250790137_00001.EXM
BSR-2.2	IQ___DMEX__05378060_2025-095T16-55-49_8F540250950137_00001.EXM
BSR-3.1	IQ___DMEX__05378500_2025-192T16-16-12_8F540251920137_00001.EXM
BSR-4.1	IQ___DMEX__053786AD_2025-227T19-38-57_8F540252270137_00001.EXM

Table 6.4: 32-bit representation of the IQ file non-time coded records, retrieved from Svedhem [148]

Field name	Description	Bits	Width	Note
Header	Type of Sample	<31:28>	<4>	'1000' (0x8) - I & Q non-time-coded sample
I Sample	I Amplitude	<27:20>	<8>	Amplitude of I data sample
Q Sample	Q Amplitude	<19:12>	<8>	Amplitude of Q data sample
AGC	AGC Measurement	<11:4>	<8>	Amplitude of AGC sample
Trailer	Type of Sample	<3:0>	<4>	'0111' (0x7) - I & Q non-time-coded sample

The direct readout AGC data shows a sampling rate of 32 kHz and, once decoded from binary, ranges from 0 to 255. For BSR-2.1, the AGC data (both complete and as downsampled to 1 second time resolution for MEX-TGO BSR analysis) is shown in in Figure 6.29. The same graphs for all measurements are shown in Appendix D.
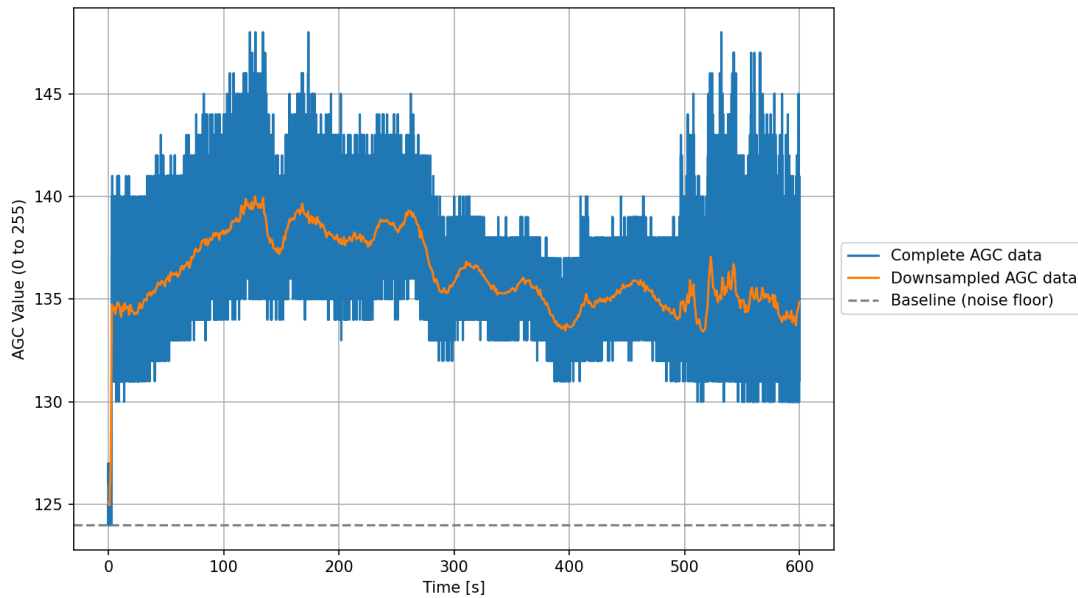
Figure 6.29: AGC data for BSR-2.1 (direct readout from IQ file), own work

The AGC data has to be converted to Watts, for which the following assumptions and calculations are made:

- The power noise floor $P_{noise\ floor}$ has to be computed through Equations 6.28 and 6.29 [37, 120]. Here k_B is the Boltzmann constant ($1.380649 \cdot 10^{-23}$), T_{noise} is the noise temperature and B is the signal bandwidth. T_{noise} was retrieved from Parrott et al. [111] to be 500 K and B is 1 MHz, as retrieved from Svedhem [150]. This noise floor is expected to serve as a conservative estimate, and actually lay lower in reality according

to a lower system noise temperature (~290 K) (and modelling) [151, 156], but such change lays inside the uncertainty margins of the uncalibrated AGC data.

$$P_{noise\,floor}[W] = k_B \cdot T_{noise} \cdot B \tag{6.28}$$

$$P_{noise\,floor}[dB] = 10 \cdot \log_{10}(P_{noise\,floor}[W] \cdot 10^3) \tag{6.29}$$

- The AGC baseline is assumed to be 124, as corresponds approximately with no signal present in the AGC data (most notably for BSR-2.1, 2.2 and 3.1 in Figures D.9, D.11 and D.13 of Appendix D).
- Every step in AGC count corresponds to a dB stepsize of 1, i.e. an increase of 1 in the AGC value corresponds to +1 dB in the received signal strength. This is applied as shown in Equation 6.30.

$$P_{AGC}[dB] = P_{noise\,floor}[dB] + (AGC_{count} - AGC_{baseline}) \cdot dB_{stepsize} \tag{6.30}$$

- The dB is not elementarily connected to the power in Watts, this transfer function is not known by definition but approximated in a way which yields realistic expected values, as shown in Equation 6.31, according to the conversion nominally used for dBm. Results of the conversion are shown in Figure 6.30 for BSR-2.1. AGC and converted power data for the remainder of measurements are plotted in Appendix D.

$$P_{AGC}[W] = 10^{\frac{P_{AGC}[dB]}{10}} \cdot 10^{-3} \tag{6.31}$$
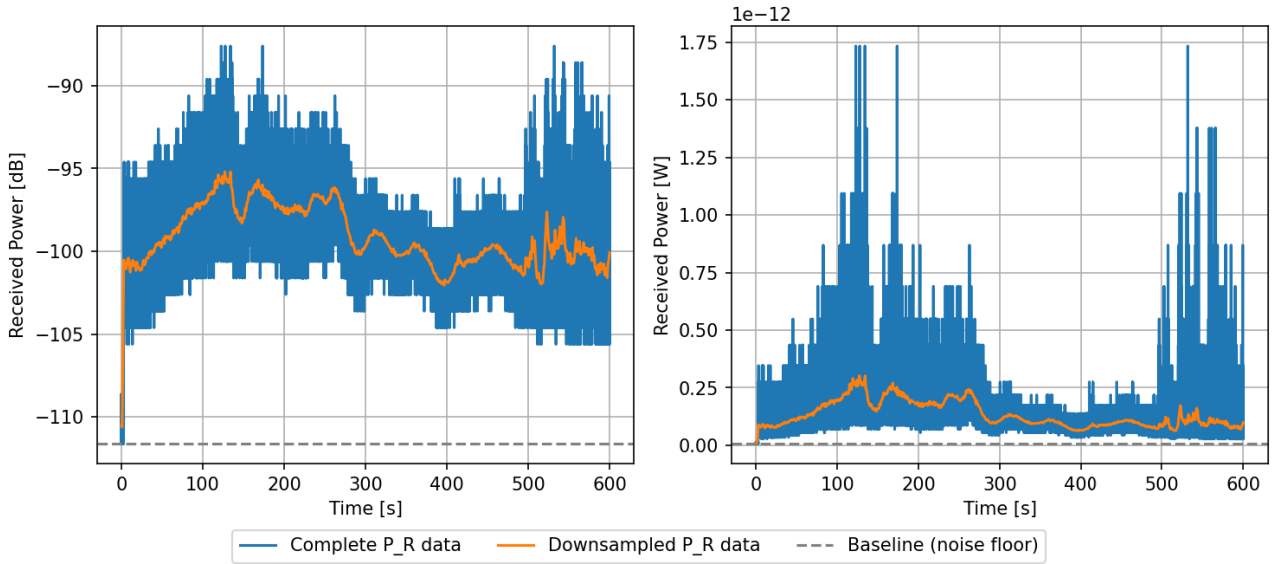
Figure 6.30: Converted received power data for BSR-2.1, own work

6.2.7. Detailed Code Architecture

Before running the main model, two steps have to be taken:

- The (RMS) slopes and local surface normals are computed with 'infer_slope_MOLA.py', with a breakdown of the detailed code architecture shown in Figure 6.31.
- The footprint borders are computed with 'main_MEXTGOBSR_footprint.py', with a breakdown of the detailed code architecture shown in Figure 6.32.

Finally, the detailed code architecture, expanded from Figure 6.4, is shown (split) in Figures 6.33 and 6.34.

Inputs

Plotting background

MOLA MEGDR data resolution

Mars geometry

SPICE kernels

General metakernel

Setup required paths for MEGDR data and directories for writing results

Readout MOLA MEGDR data

Slope-step 1.1:
Readout MEGDR data
as big-endian 2-byte
signed integers

Slope-step 1.2:
Flip data along
latitude axis

Slope-step 1.3:
Shift data longitudes
from [0°, 360°]
to [-180°, 180°]

megdr_data

Setup required paths and files for slope results for use in model ('4pixel_slopes.csv')

Calculate slopes

Slope-step 2.1:
Set up empty (RMS)
slopes and surface
normal grids

Slope-step 2.2:
Integrate over
latitudes to
calculate Delta y

Slope-step 2.3:
Loop over
latitudes to
calculate Delta x

Slope-step 2.4:
Loop over latitudes to calculate
the required Delta x multiplier
for spatial consistence

Slope-step 2.5:
Calculate (RMS)
slope with adapted
four-point grid

slope_deg,
slope_RMS_deg

Calculate local surface normals

Slope-step 3.1:
Calculate the local
surface normal on perfect
ellipsoidal Mars

Slope-step 3.2:
Calculate the
local North and
East direction

Slope-step 3.3:
Calculate the
local vector
along the slope

Slope-step 3.4:
Rotate the local perfect ellipsoid
surface normal around the local
slope vector to retrieve n_hat

n_hat

Write results to .csv data files

Make plots of the direct topography (2D and 3D), data counts and derived (RMS) slopes

Figure 6.31: Detailed architecture for inferring the (RMS) slopes and local surface normals prior to the MEX-TGO BSR measurement processing model, own work

Inputs

Functions: create_gif

BSR titles

Plotting settings and background

Mars geometry

SPICE kernels

General metakernel

MEX-specific metakernel

TGO-specific metakernel

Setup paths for reading out measurement tracks and results directory

Preparation for footprint calculations

Footprint-step 1.1:
Readout
measurement
tracks file

planning_data

Footprint-step 1.2:
Set et_steps to
planning_data['et']

Footprint-step 1.3:
Create empty lists for the specular points,
midpoints, S/C boresights, footprint border
coordinates ('intpoint_track') and 3D S/C locations

Setup data file per footprint (ET time)

Measurement geometry

Footprint-step 2.1:
Readout
measurement
tracks file

Footprint-step 2.2:
Calculate S/C
positions in
IAU$_{Mars}$

Footprint-step 2.3:
Calculate S/C
boresight coordinates
in IAU$_{Mars}$

Footprint-step 2.4:
Append calculated
values to
parameter lists

r_MEX_track, r_TGO_track,
spoint_track, midpoint_track,
MEXbs_track, TGObs_track

Calculate illuminated area

Footprint-step 3.1:
Calculate the limb of the triaxial
ellipsoid on Mars (illuminated
area) as viewed from either S/C

Footprint-step 3.2:
Generate a SPICE
ellipse from the
limb vectors

Footprint-step 3.3:
Calculate the planetocentric
coordinates of the ellipse
(over 360 steps)

Footprint-step 3.4:
Append calculated
values to
inpoint_tracks

MEX_intpoint_track,
TGO_intpoint_track

Save footprint data to file

Make plots of the calculated footprints (horizon border, boresights and specular points) in 2D and 3D

Generate gifs 'animation_2D.gif' and 'animation_3D.gif' of the 2D and 3D footprint images

Figure 6.32: Detailed architecture for inferring the footprint boundary coordinates prior to the MEX-TGO BSR measurement processing model, own work

Figure 6.33: Detailed architecture for the MEX-TGO BSR measurement processing model (part 1), own work

Figure 6.34: Detailed architecture for the MEX-TGO BSR measurement processing model (part 2), own work

6.3. Results

Results from the BSR model are visualized with 'main_MEXTGOBSR_visualizeresults.py'. For analysis within the scope of the thesis, results for BSR campaign 1 (BSR-1.1, BSR-1.2, BSR-1.3 and BSR-1.4; Subsection 6.3.1), BSR campaign 2 (BSR-2.1 and BSR-2.2; Subsection 6.3.2), BSR campaign 3 (BSR-3.1; Subsection 6.3.3) and BSR campaign 4 (BSR-4.1; Subsection 6.3.4) are taken under consideration and presented respectively in this section.

6.3.1. BSR Campaign 1 (MTP257/76)

BSR campaign 1 contains the four serendipitous measurements which took place over January and February 2024, each of which will be shortly presented in this section. For BSR campaign 1 there is a direct signal expected to tune the AGC. It could be taken out with frequency analysis [150], but this is left for future work.

BSR-1.1 (January 23rd 2024)

Figure 6.35 shows the 'Comparison of Model vs. Data' of the BSR-1.1 measurement. It compares the converted AGC data 'Data (MEX-TGO BSR)' with the modelled received power as follows from summing the contribution of reflection using inferred permittivities from GRS, and the direct free-space element 'Model (GRS + freespace)', also both shown individually as 'Model (GRS)' and 'Model (freespace)' respectively. Additionally, the received power noisefloor is shown 'Noisefloor', calculated with Equation 6.28 presented previously.

Figure 6.35: Model results 'Comparison of Model vs. Data' for BSR-1.1 (using 4 pixel/degree resolution, GRS data and CO_2 ice as the polar host material), own work
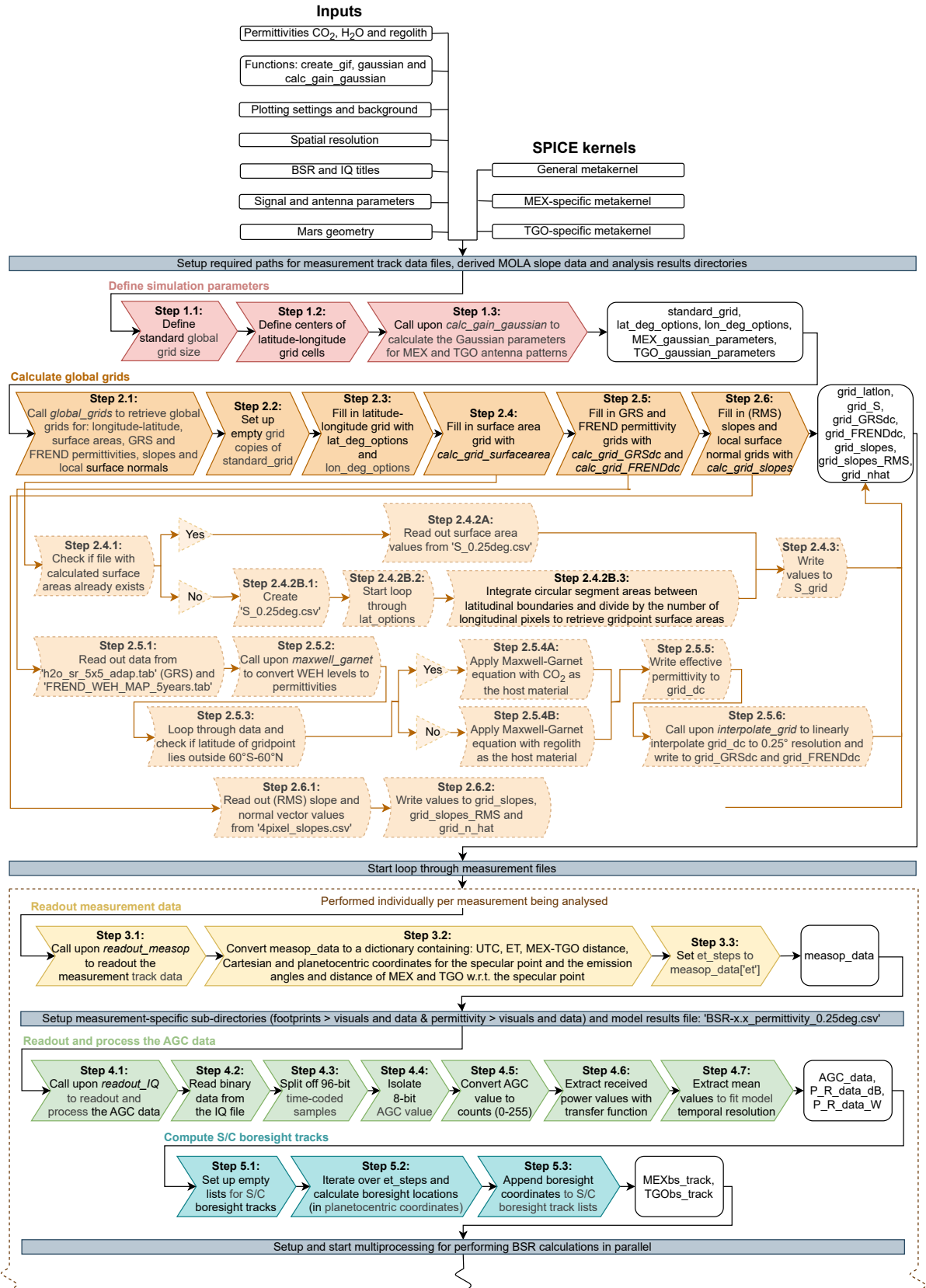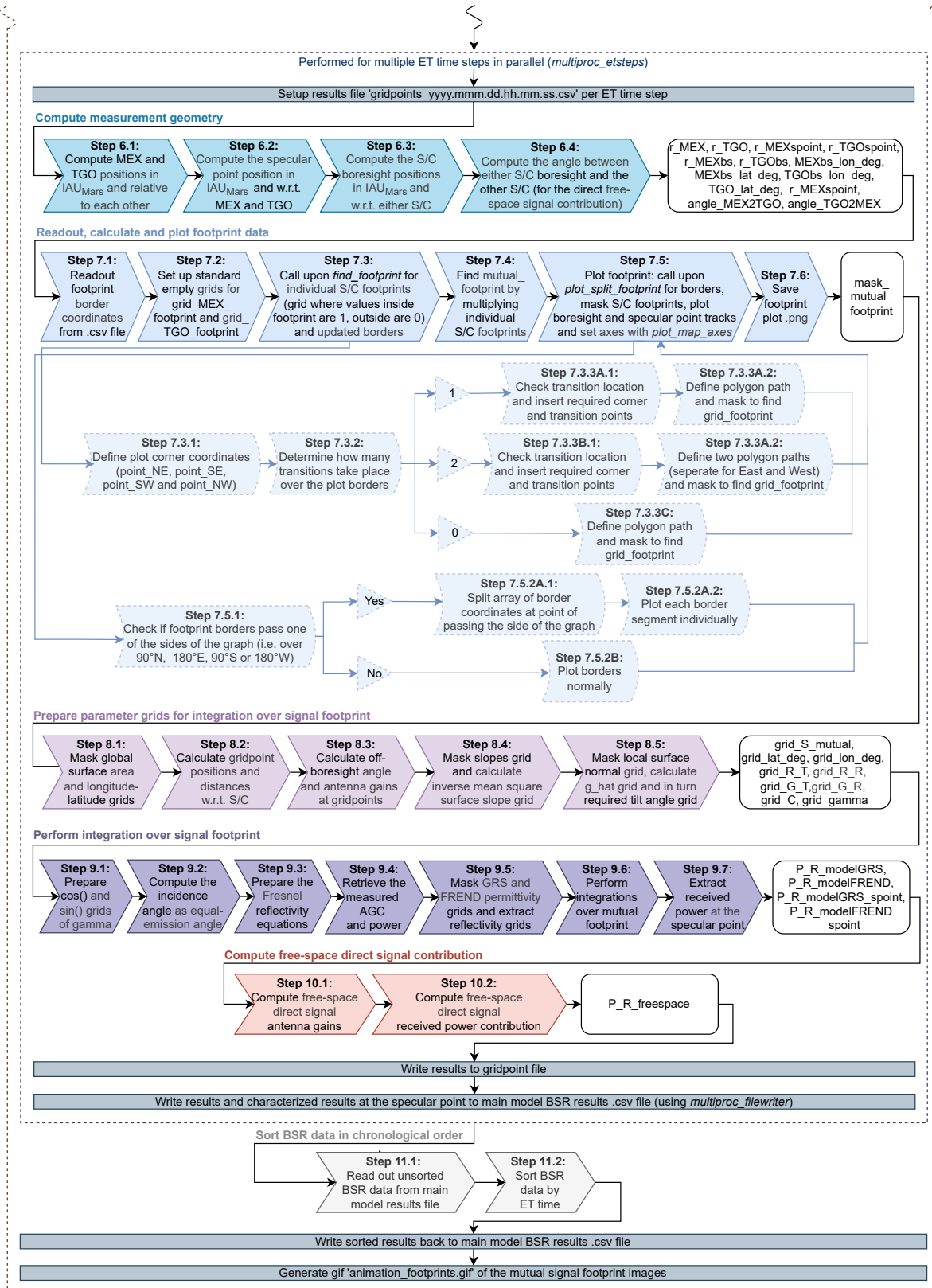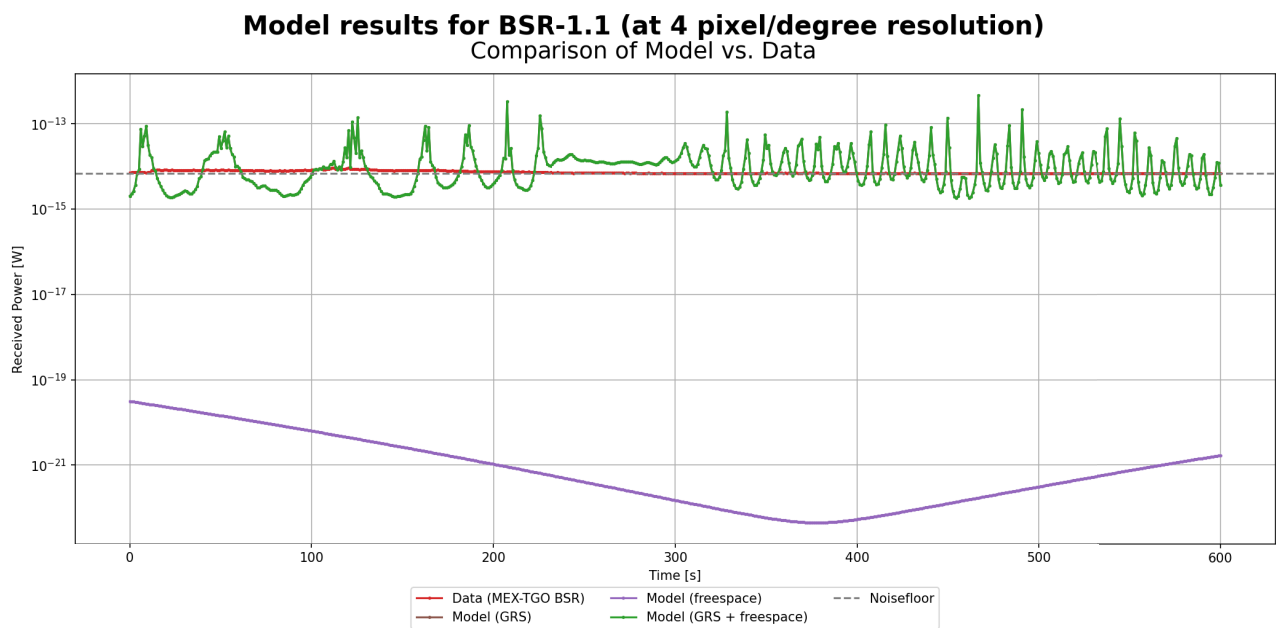
Notable deductions for BSR-1.1 include:

- **Freespace contribution:** The direct signal contribution is significantly lower than the reflected signal, showcasing a difference of over four to eight orders of magnitude. This makes it such that the freespace contribution is negligible for the combined 'Model (GRS + freespace)'.

- **Magnitude combined model and periodicity effect:** Although starting below the noise floor, the combined model oscillates around both the noise floor and AGC data, showcasing an especially high frequency periodicity effect from ~320 s onwards.

- **Signal mirroring effect:** At ~85 s the modelled signal seemingly exhibits a mirroring effect, with similar sized peaks on either side progressing to a higher frequency ripple.

BSR-1.2 (January 30th 2024)

Figure 6.36 shows the 'Comparison of Model vs. Data' of the BSR-1.2 measurement, notably it can be seen:

- **Freespace contribution:** The direct signal contribution is significantly lower than the reflected signal, showcasing a difference of over two to four orders of magnitude. This makes it such that the freespace contribution is negligible for the combined 'Model (GRS + freespace)'. However, the shape better matches that of the data than is the case for the pure model, which corresponds to the expectation of the direct signal tuning the AGC, wherein there is an issue in the computation of the direct signal in the model.

- **Noise floor:** All model lines are generally below the noise floor, with the exception of a number of peaks.
- **Periodicity/Ripple effect:** The model exhibits a high-frequency and amplitude ripple effect after ~200 s.

Figure 6.36: Model results 'Comparison of Model vs. Data' for BSR-1.2 (using 4 pixel/degree resolution, GRS data and CO_2 ice as the polar host material), own work

BSR-1.3 (February 6th 2024)

Figure 6.37 shows the 'Comparison of Model vs. Data' of the BSR-1.3 measurement, notably it can be seen:

- **Periodicity/Ripple effect:** The model exhibits a periodic ripple effect. Firstly from ~60-80 s in a single peak, then consistently and at high frequency after passing ~200 s.
- **Freespace contribution:** The direct signal contribution decreases linearly and is negligible for most of the combined 'Model (GRS + freespace)'. However, the shape better matches that of the data than is the case for the pure model, which corresponds to the expectation of the direct signal tuning the AGC, wherein there is an issue in the computation of the direct signal in the model.

Figure 6.37: Model results 'Comparison of Model vs. Data' for BSR-1.3 (using 4 pixel/degree resolution, GRS data and CO_2 ice as the polar host material), own work
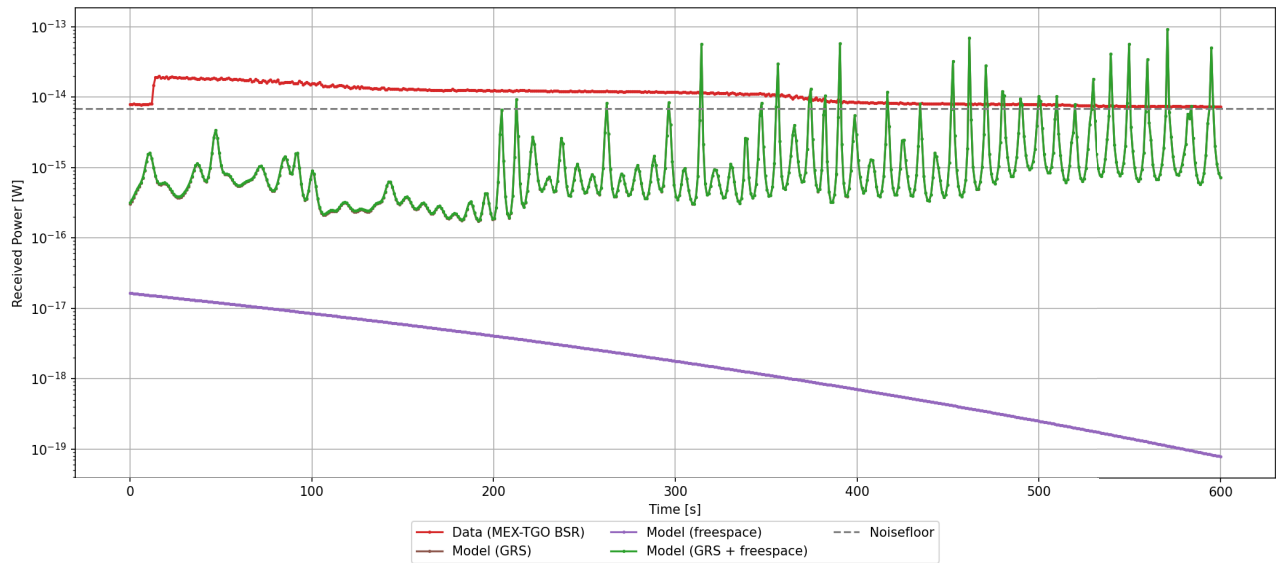
BSR-1.4 (February 11th 2024)

Figure 6.38 shows the 'Comparison of Model vs. Data' of the BSR-1.4 measurement, notably it can be seen:

- **Freespace contribution:** The direct signal contribution is significantly lower than the reflected signal, showcasing a difference of over six to eight orders of magnitude. This makes it such that the freespace contribution is negligible for the combined 'Model (GRS + freespace)'.

- **Periodicity/Ripple effect:** The model exhibits a ripple effect with changing period and amplitude, oscillating around the both the data and the noisefloor.

- **Signal mirroring effect:** At ~76 s the modelled signal seemingly exhibits a mirroring effect, with similar sized peaks and dips on either side, before moving to a higher frequency periodicity effect.

Figure 6.38: Model results 'Comparison of Model vs. Data' for BSR-1.4 (using 4 pixel/degree resolution, GRS data and CO_2 ice as the polar host material), own work

6.3.2. BSR Campaign 2 (MTP272/91)

BSR campaign 2 contains the two non-ideal measurements which took place over March and April 2025.

BSR-2.1 (March 20th 2025)

Figure 6.39 shows the 'Comparison of Model vs. Data' of the BSR-2.1 measurement.
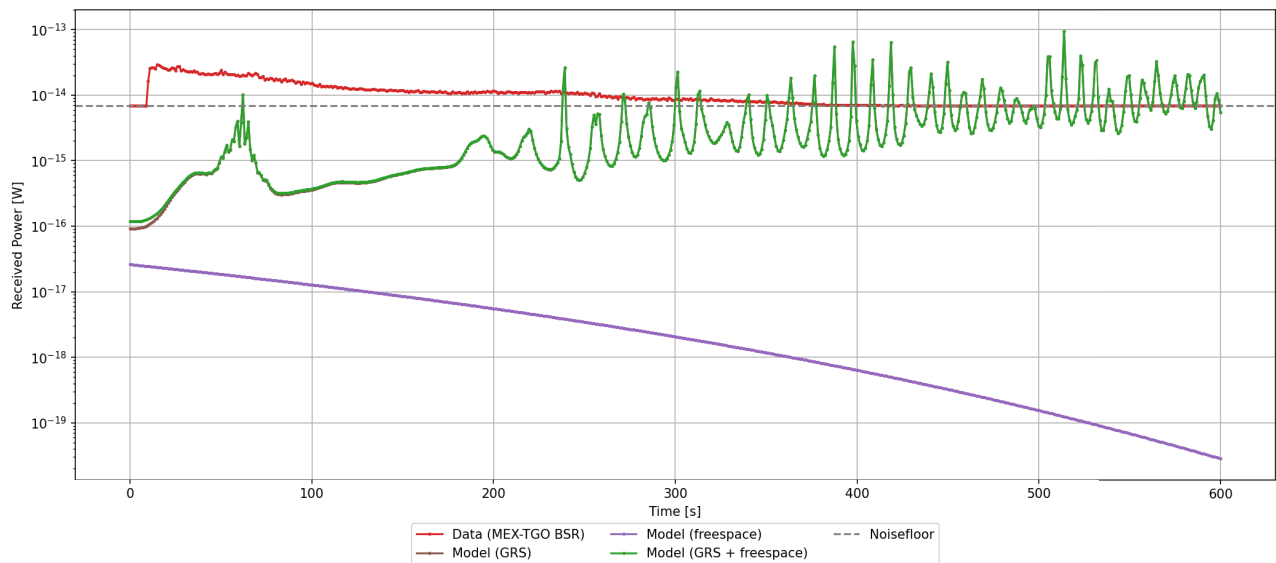

Figure 6.39: Model results 'Comparison of Model vs. Data' for BSR-2.1 (using 4 pixel/degree resolution, GRS data and CO_2 ice as the polar host material), own work

Notable deductions for BSR-2.1 include:

- **Freespace contribution:** The direct signal contribution is significantly lower than the reflected signal, showcasing a difference from two to six orders of magnitude. This makes it such that the freespace contribution is practically negligible for the combined 'Model (GRS + freespace)'.

- **Louth crater:** Both the model and data show a dip in the received power between ~130-150 s, consistent with the exception that the models exhibits a slight raise inside the dip, which is not observed in the data. This dip occurs right as the specular point track passes over 'Louth crater' [16, 31], a ~36 km diameter crater located at 70°N 103.2°E, shown in Figure 6.40. It contains a ~10-15 km diameter water ice cap which is know to go through seasonal diffusive cycles of sublimation and condensation [16, 31].

Figure 6.40: Louth crater as imaged by the MRO Context Camera (CTX), retrieved from Collet et al. [31]

- **Periodicity/Ripple effect:** Throughout the measurement, the modelled signal changes from very high frequency (short periods) to lower frequency (larger periods), and back to higher frequency.

- **Signal mirroring effect:** At ~433 s the modelled signal seemingly exhibits a mirroring effect, a relatively flat region on either side with periodic peaks of higher frequency further away from the 'mirror'.

- **Overall behavior:** To assist in assessing the overall model behavior in comparison to the data (not assessing the 'Louth dip'), a smoothing was attempted with a Savgol, Kalman, Lowess and Moving Average filter [118]. The Savgol and Kalman filters induced too many artifacts. The Lowess filter (applied with a data fraction used for each estimation of 0.09) and Moving Average (applied with a window size of 61, i.e. ~10%) results are shown in Figure 6.41, including:

  - **Location A:** The Moving Average of the model shows a good match with the data starting relatively flat up to 'Location A', then progressing mostly linearly up to the 'Louth' dip.

  - **Locations B1 and B2:** Both the Moving Average of the model and data exhibit two bulges located here. For the Lowess of the model, the first bulge seems to correspond somewhat, but overall does not show a good match and behaves relatively linear on a downward trend.

  - **Location C:** Starting at this location, the data exhibits an obvious dip. The Moving Average of the model showcases a similar start, whilst the Lowess of the model seems to showcases a bulge instead.

  - **Location D:** Both the models and data showcase the start of a semi-linear decrease in received power.

Figure 6.41: Model results 'Comparison of Model vs. Data (with smoothing)' for BSR-2.1 (using 4 pixel/degree resolution, GRS data and CO_2 ice as the polar host material), own work

BSR-2.2 (April 5th 2025)

Figure 6.42 shows the 'Comparison of Model vs. Data' of the BSR-2.2 measurement.
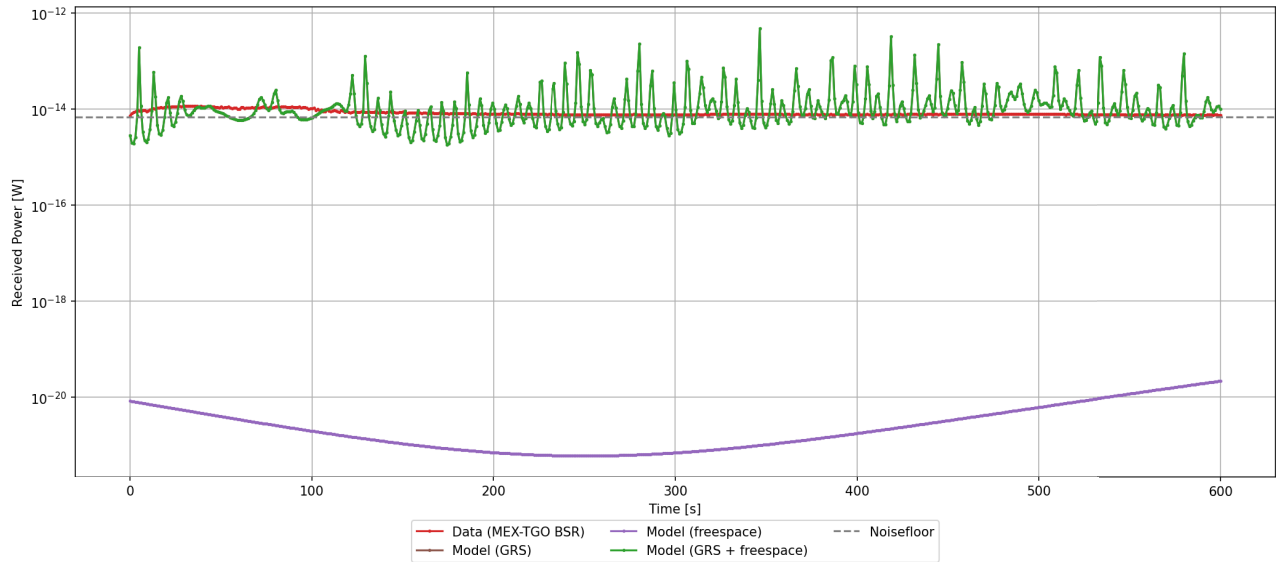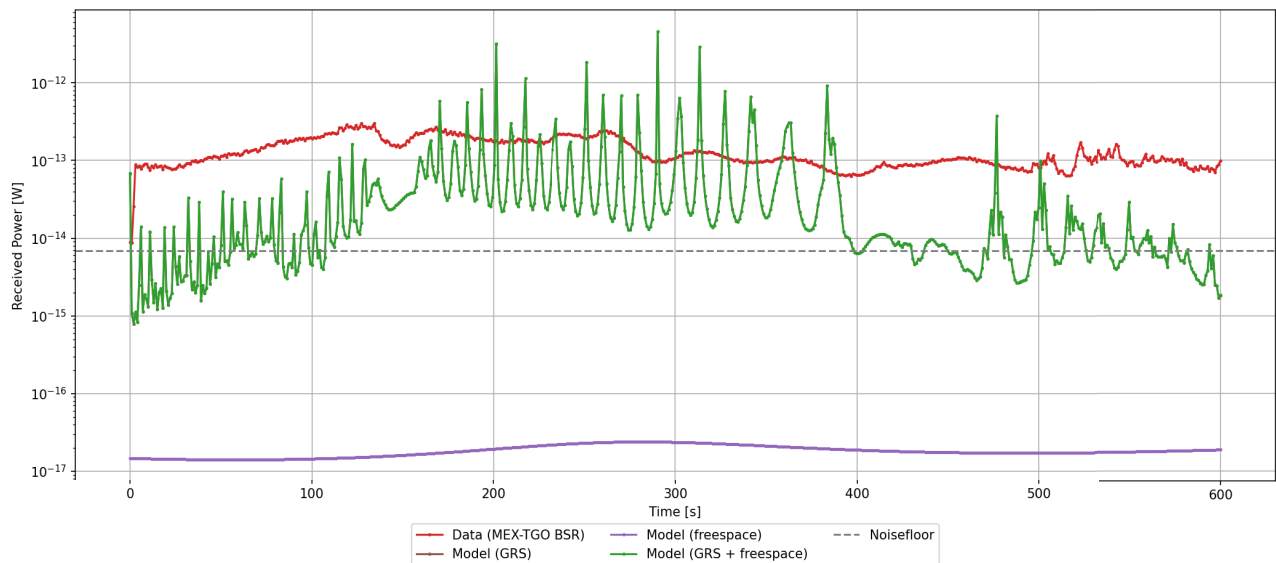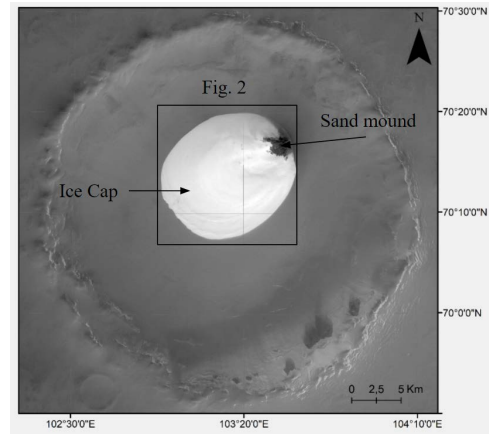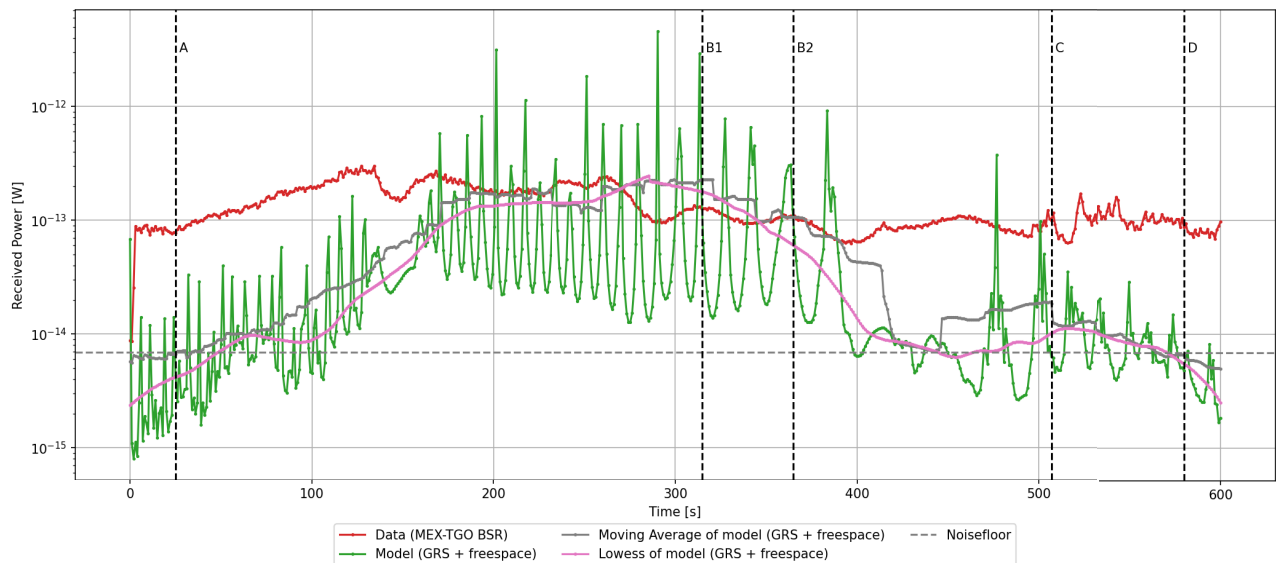

Figure 6.42: Model results 'Comparison of Model vs. Data' for BSR-2.2 (using 4 pixel/degree resolution, GRS data and CO_2 ice as the polar host material), own work

Notable deductions for BSR-2.2 include:

- **Freespace contribution:** The direct signal contribution is initially significant enough to raise the combined 'Model (GRS + freespace)' magnitude closer to the data. After ~100 s, the reflections drive the modelled signal, increasing to a maximum of six orders of magnitude higher than the freespace contribution.

- **Periodicity and signal mirroring effect:** The model exhibits a ripple with constant period up to ~350 s, after which it quickly increases and starts showcasing non-periodic chaotic behavior. Around ~517 s a mirroring effect can be recognized inside a relatively flat region surrounding by two similar peaks.

- **Overall behavior:** The overall model shape matches well to the data, seen better in the smoothed plots (created with the same set Lowess and Moving Average filters as BSR-2.1) shown in Figure 6.43.

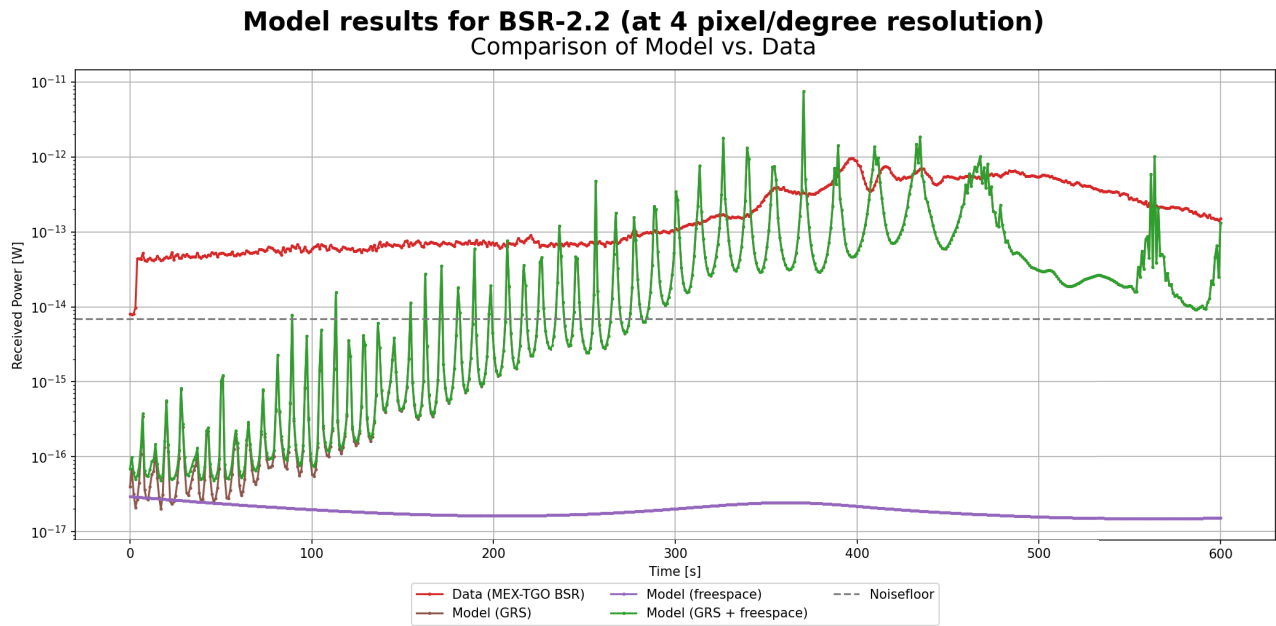
Figure 6.43: Model results 'Comparison of Model vs. Data (with smoothing)' for BSR-2.2 (using 4 pixel/degree resolution, GRS data and CO_2 ice as the polar host material), own work
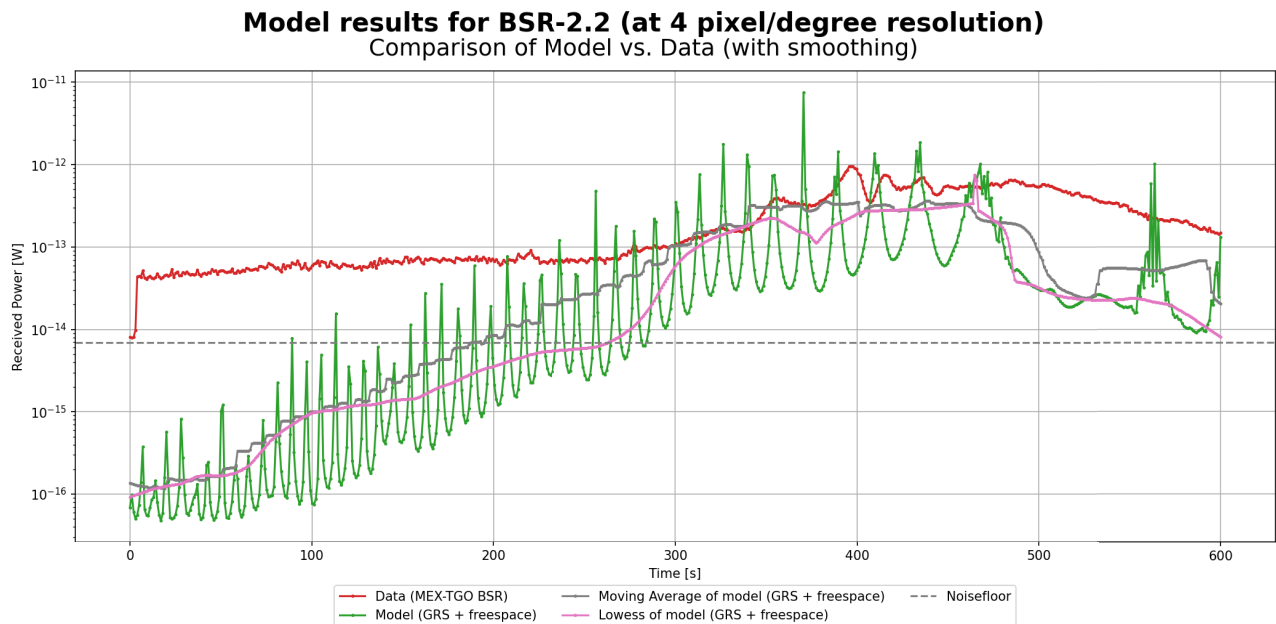
6.3.3. BSR Campaign 3 (MTP276/95)

BSR campaign 3 only contains the July 2025 measurement, planned after requesting the ideal measurement results of the measurement planning model from ESAC.

BSR-3.1 (July 17th 2025)

Figure 6.44 shows the 'Comparison of Model vs. Data' of the BSR-3.1 measurement, notable deductions include:

- **Freespace contribution:** The direct signal contribution is significantly lower than the reflected signal, showcasing a difference of over three to five orders of magnitude. This makes it such that the freespace contribution is practically negligible for the combined 'Model (GRS + freespace)'.

- **Low (consistent) received signal data:** Unlike most other measurements, BSR-3.1 yields a significantly higher modelled received power than is seen in the data. The AGC data shows a variation within 2 counts, i.e. 2 dB, in a bathtub shape, equal to 130 at the sides and stagnating at 129 between ~100 and ~500 s (refer to Figure D.11 in Appendix D). Due to the low distance and equal-emission angles, a strong signal is expected to be received, but it is deemed likely that this is not captured by TGO due to the polarisation switch from RHCP to LHCP at the surface, the latter of which cannot be measured by TGO's antenna. This will be discussed further in Subsection 6.4.1, but seemingly makes the BSR-3.1 data inconclusive.

- **High frequency ripple:** The entirety of the BSR-3.1 shows a very high frequency ripple with varying amplitude. As the Valles Marineris over which the track passes is very topographically diverse, it is deemed likely for the switches between smoothed and rippled modelled signal to be linked to topography.
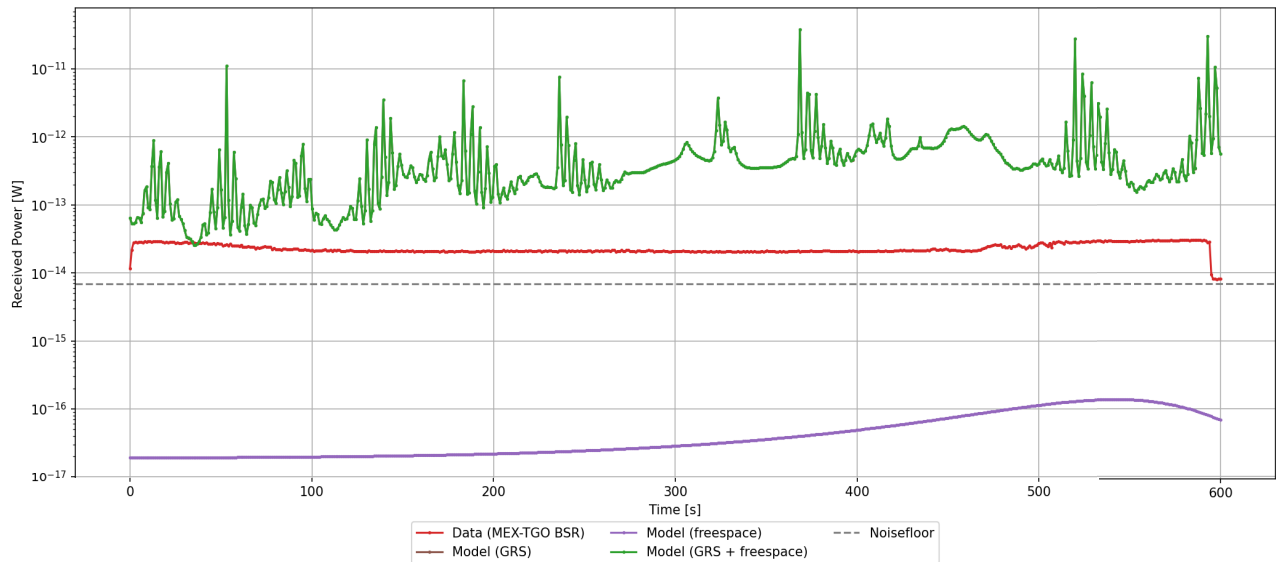
Figure 6.44: Model results 'Comparison of Model vs. Data' for BSR-3.1 (using 4 pixel/degree resolution and GRS data), own work

6.3.4. BSR Campaign 4 (MTP277/96)

BSR campaign 4 only contains the August 2025 measurement, a longer duration measurement planned after the MTP277/96 measurements requested from ESAC all conflicted with lander visibility periods.

BSR-4.1 (August 15th 2025)

Figure 6.45 shows the 'Comparison of Model vs. Data' of BSR-4.1, with notable deductions including:

- **Entry into occultation and free-space contribution:** The part of the BSR-4.1 measurement that goes into BSR analysis is shortened from 20 to 19 minutes as for the final minute there is no mutual signal footprint. However, at ~1100s the data already shows effectively no signal (AGC equal to the noise floor), signifying the start of the MEX-TGO mutual occultation. Accordingly, the model showcases highly decreased signal, already starting linearly at ~500s and switching to the free-space contribution driving the model at ~900s.

- **Low amplitude periodicity:** As with most prior measurements, BSR-4.1 also showcases a ripple/high periodicity effect. This is with seemingly smaller amplitude variations, but this can mainly be amounted to the plot's scale, with amplitude variations between one to two orders of magnitude.

Figure 6.45: Model results 'Comparison of Model vs. Data' for BSR-4.1 (using 4 pixel/degree resolution, GRS data and CO_2 ice as the polar host material), own work
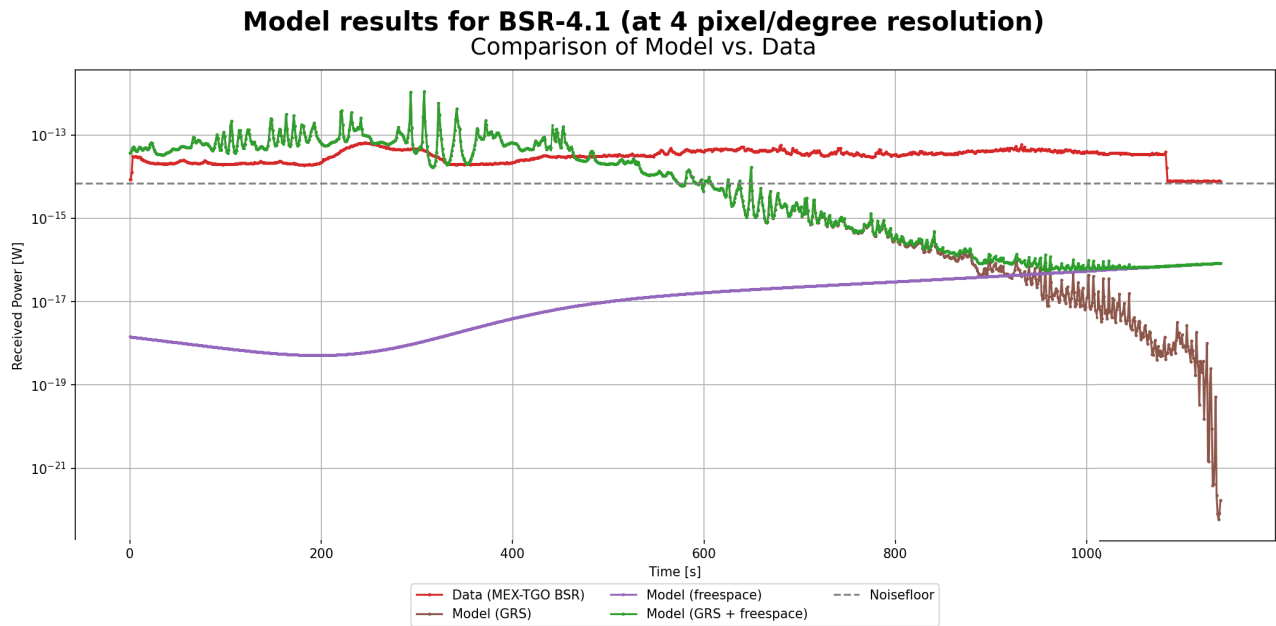
6.4. Discussion

This section presents a discussion on the measurement processing phase, and specifically, the model. Overall the BSR model shows a relatively poor fit to the measurements. This is not a surprising result as MEX-TGO BSR is a novel measurement method and this is the first modelling attempt, and the AGC data is yet to be calibrated (for which tests are planned between December 2025 and February 2026), thus inducing further uncertainty. Subsection 6.4.1 presents a discussion on the model results and verification and validation, while Subsection 6.4.2 presents insights on the model sensitivity, limitations and uncertainties.

6.4.1. Model Results, Verification and Validation

This section presents a discussion on the model results as well as some verification and validation performed. The BSR parameters and identified peculiarities noted in Section 5.3 are discussed in further detail below.

Effects of the BSR Model Parameters

All BSR parameters (for the subsurface signal reflection) are plotted and included in Section E.1 of Appendix E to assess the 'Effects of the BSR Model Parameters'. Comparing these with the measurement results in Section 5.3 provides the following preliminary insights:

- **Signal path and S/C distances:** For BSR campaigns 1 and 3, the signal path and spacecraft distances were found to be relatively constant across all measurements, thus having little to no effect on the model results. For BSR campaign 2, the distances varied more significantly (~1000-2500 km) and their progression matches the inverse shape of the modelled data, where shorter paths correspond to higher signals.

- **Surface composition (reflectivity and permittivity):** The surface composition seemingly has little effect on the received power, but further analysis is required to characterize the relation, as will follow.

- **Topography and equal-emission angles:** The equal-emission angles correspond strongly to the shape of the free-space contribution, especially BSR campaign 1. The topography on the other hand, is driving for the received signal power magnitude and shape through the high influence in the reflected signal, matching the topography scaling factor of the point of highest return closely. A more detailed analysis is required on the periodicity effects, which will be presented later in this section.

- **Mutual surface footprint:** The mutual surface footprint seemingly has no effect on the returned signal magnitude, this can likely be amounted by the power return being driven by a small Fresnel zone of a (few) pixel(s), but further analysis has to be performed characterizing this behavior.
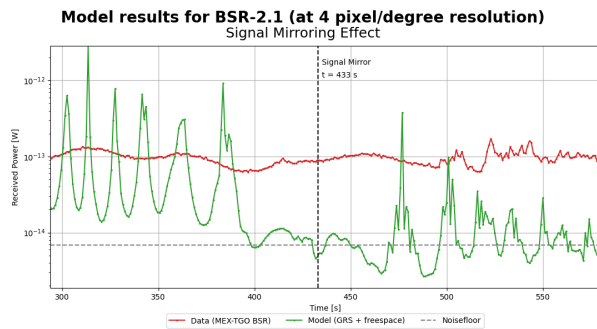
Signal Mirroring Effects

In measurements BSR-1.1, BSR-1.4, BSR-2.1 and BSR-2.2, a signal mirroring effect can be identified, shown zoomed in in Figures 6.46, 6.47, 6.48 and 6.49. Each shows a 'mirror' point inside a relatively flat region of the modelled signal, surrounding by differing transitions into a ripple effect.
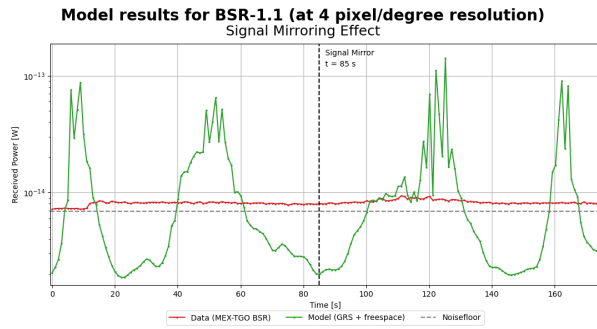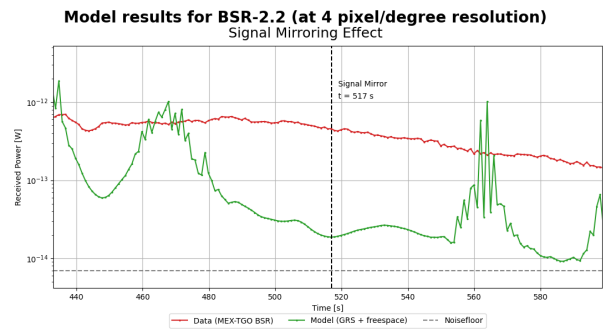
Figure 6.46: Zoomed in model results 'Signal Mirroring Effect' for BSR-1.1 (using 4 pixel/degree resolution, GRS data and CO_2 ice as the polar host material), own work
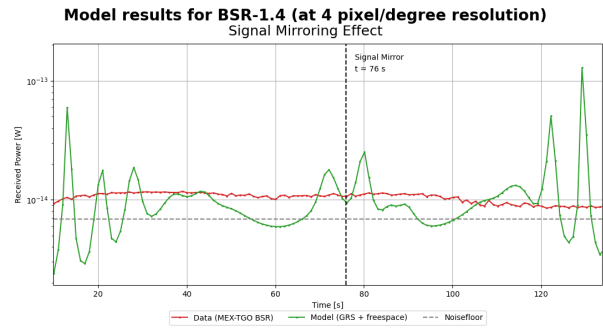
Figure 6.47: Zoomed in model results 'Signal Mirroring Effect' for BSR-1.4 (using 4 pixel/degree resolution, GRS data and CO_2 ice as the polar host material), own work

Figure 6.48: Zoomed in model results 'Signal Mirroring Effect' for BSR-2.1 (using 4 pixel/degree resolution, GRS data and CO_2 ice as the polar host material), own work
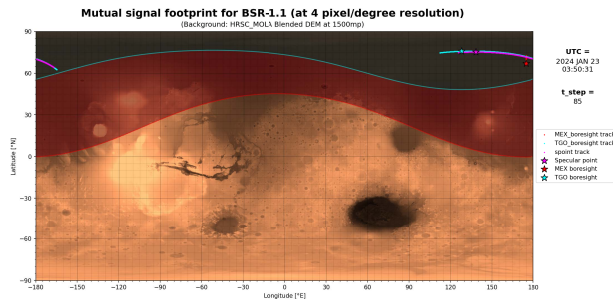

Figure 6.49: Zoomed in model results 'Signal Mirroring Effect' for BSR-2.2 (using 4 pixel/degree resolution, GRS data and CO_2 ice as the polar host material), own work

The time stamps of the specular point tracks and corresponding footprints for the middle of the signal mirroring effect are shown in Figures 6.50, 6.51, 6.52 and 6.53. Interestingly, for all but BSR-4.1, these correspond with the moment at which the specular point track direction changes from east-northeastern-bound to east-southeastern-bound, indicating a dependence on S/C movement which should be explored in future work.

Figure 6.50: Footprints corresponding to model results 'Signal Mirroring Effect' for BSR-1.1 (using 4 pixel/degree resolution, GRS data and CO_2 ice as the polar host material), own work
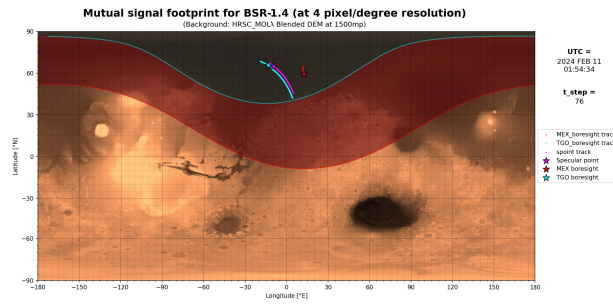
Figure 6.51: Footprints corresponding to model results 'Signal Mirroring Effect' for BSR-1.4 (using 4 pixel/degree resolution, GRS data and CO_2 ice as the polar host material), own work

Figure 6.52: Footprints corresponding to model results 'Signal Mirroring Effect' for BSR-2.1 (using 4 pixel/degree resolution, GRS data and CO_2 ice as the polar host material), own work

Figure 6.53: Footprints corresponding to model results 'Signal Mirroring Effect' for BSR-2.1 (using 4 pixel/degree resolution, GRS data and CO_2 ice as the polar host material), own work
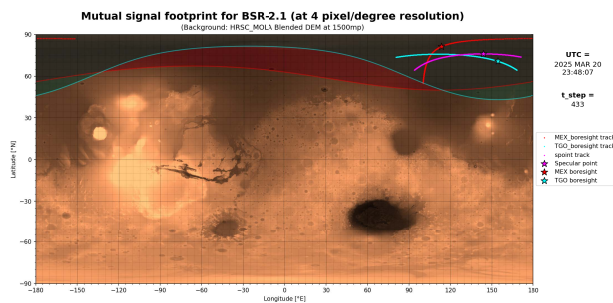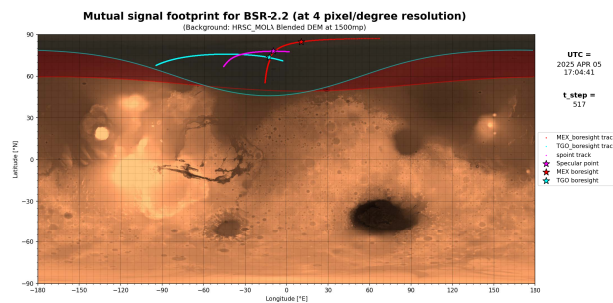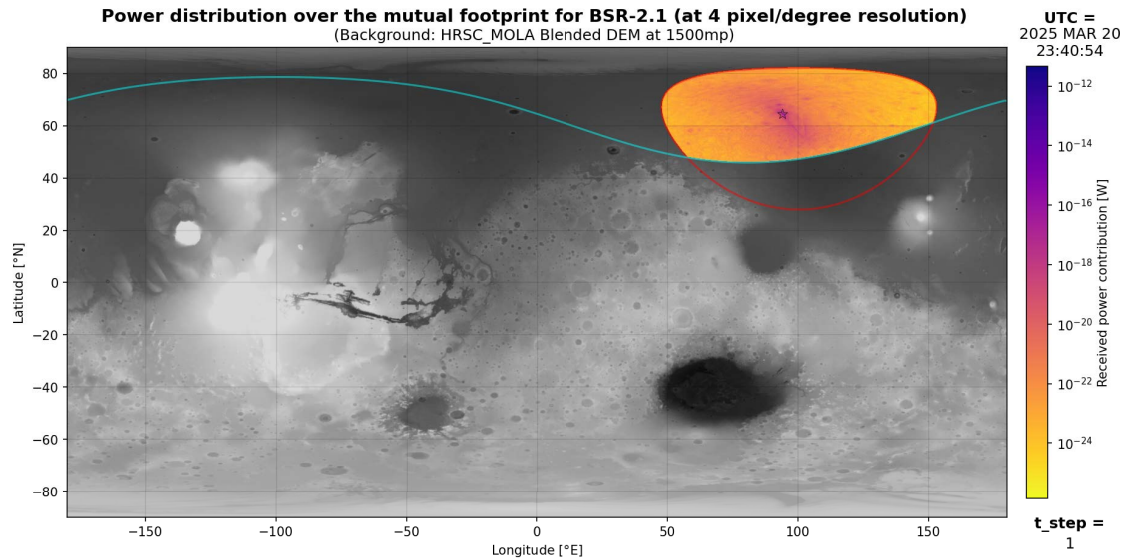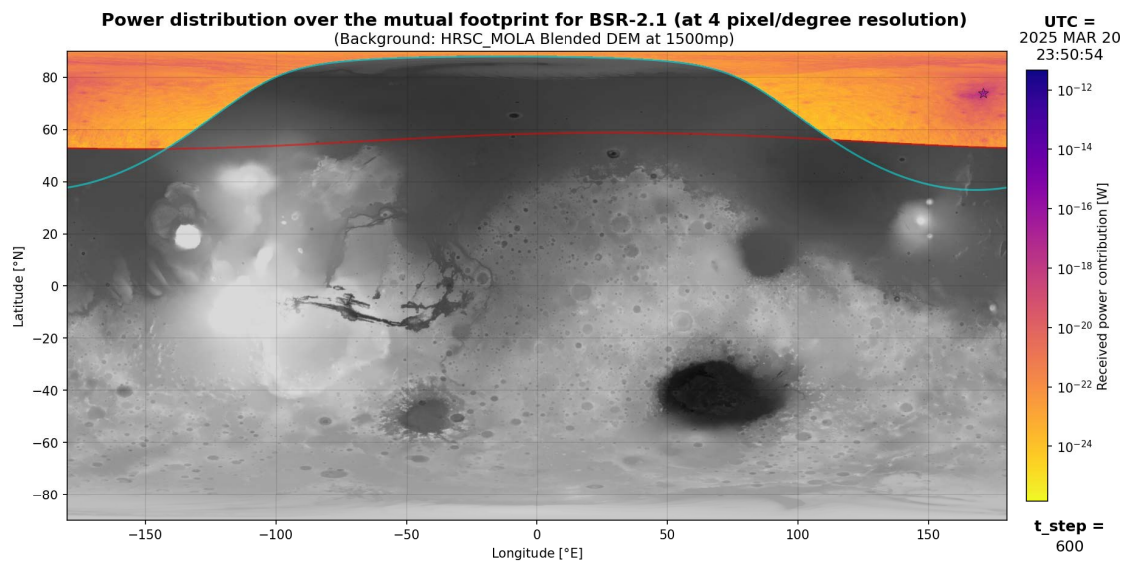
Power Distribution over the Mutual Footprint

In modelling the subsurface reflection, the bi-static radar equation is integrated over the mutual surface footprint. For this, each pixel is defined as a gridpoint, bound by its planetocentric coordinates. The received power is then calculated per gridpoint, values of which give insight to the degree in which local changes affect measurement behavior. For this, the first step in characterizing the model is made by plotting this contribution over the footprint. For BSR-2.1, this yields the footprints shown in Figures 6.54 and 6.55 for the start and end of the signal respectively. The plots for all measurements are included in Subsection E.2.1 of Appendix E.

Figure 6.54: Model results 'Power distribution over the mutual footprint' for BSR-2.1 at start of measurement (20th of March 2025 23:40:54; using 4 pixel/degree resolution, GRS data and CO_2 ice as the polar host material), own work

Figure 6.55: Model results 'Power distribution over the mutual footprint' for BSR-2.1 at end of measurement (20th of March 2025 23:50:54; using 4 pixel/degree resolution, GRS data and CO_2 ice as the polar host material), own work

These logarithmically scaled color plots show a highly centered driving power contribution in vicinity to the specular point, shown in close-up by Figures 6.56 and 6.57. Especially in Figure 6.56, it can be seen that a single darker pixel fully drives the total modelled power return from reflection. This pixel and surrounding region is the Fresnel zone of the MEX-TGO BSR measurements. As it gets closer to the poles, it becomes more elongated due to the map projection, around the equator it is more circular, e.g. for BSR-3.1 shown in Figures 6.58 and 6.59. Furthermore, a significant effect can be identified in addition to the Fresnel zone, coming from the surrounding topography giving higher surface returns. This was verified by putting the color map to full opacity, thus allowing no influence from the background image on the display of the power contributions.

Figures 6.60 and 6.61 show the zoomed in footprints for BSR-2.1 at 16 pixel/degree resolution. Here a slightly smoother Fresnel zone can be identified, driving the total power return, and clearer topographical features.

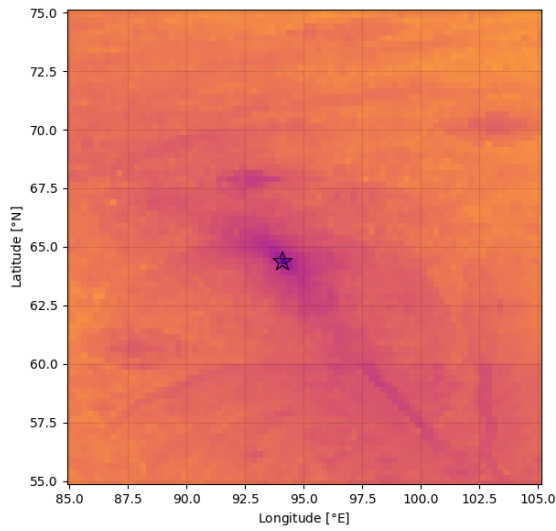**Figure 6.56:** Zoomed in model results 'Power distribution over the mutual footprint' for BSR-2.1 at start of measurement (20th of March 2025 23:40:54; using 4 pixel/degree resolution, GRS data and CO_2 ice as the polar host material), own work

Figure 6.57: Zoomed in model results 'Power distribution over the mutual footprint' for BSR-2.1 at end of measurement (20th of March 2025 23:50:54; using 4 pixel/degree resolution, GRS data and CO_2 ice as the polar host material), own work
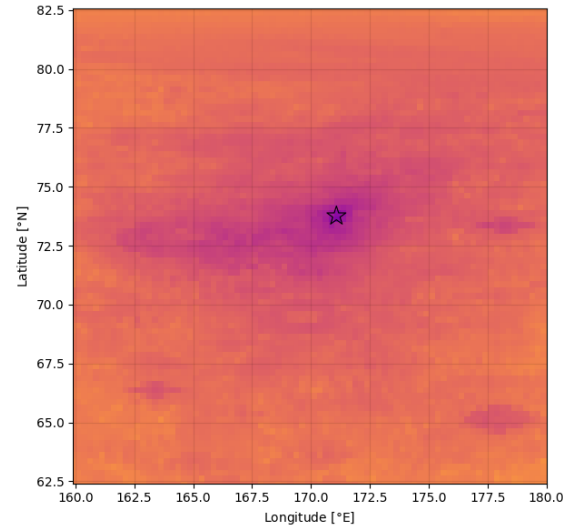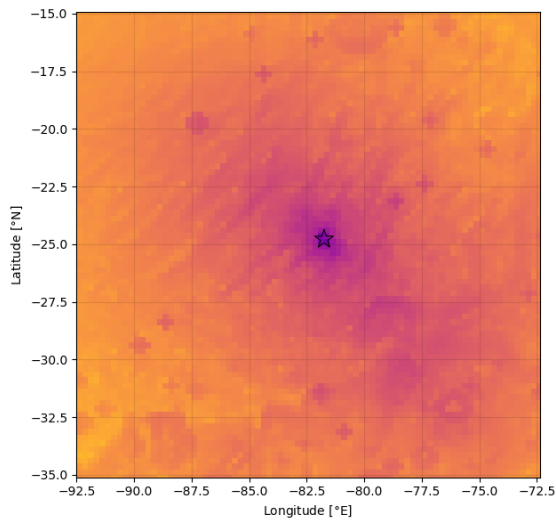

Figure 6.58: Zoomed in model results 'Power distribution over the mutual footprint' for BSR-3.1 at start of measurement (17th of July 2025 10:38:31; using 4 pixel/degree resolution and GRS data), own work

Figure 6.59: Zoomed in model results 'Power distribution over the mutual footprint' for BSR-3.1 at end of measurement (17th of July 2025 10:48:31; using 4 pixel/degree resolution and GRS data), own work

Figure 6.60: Zoomed in model results 'Power distribution over the mutual footprint' for BSR-2.1 at start of measurement (20th of March 2025 23:40:54; using 16 pixel/degree resolution, GRS data and CO_2 ice as the polar host material), own work

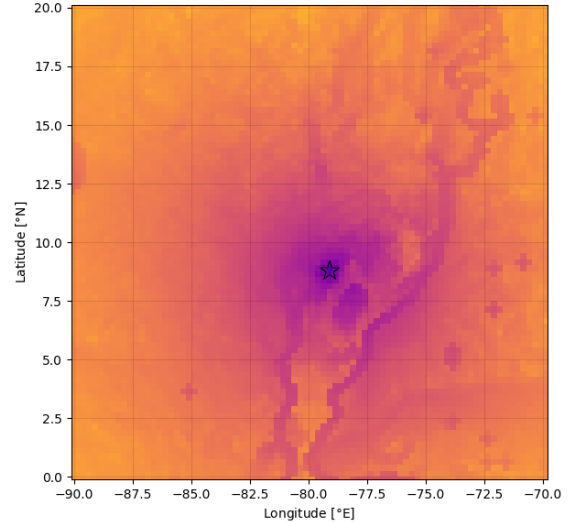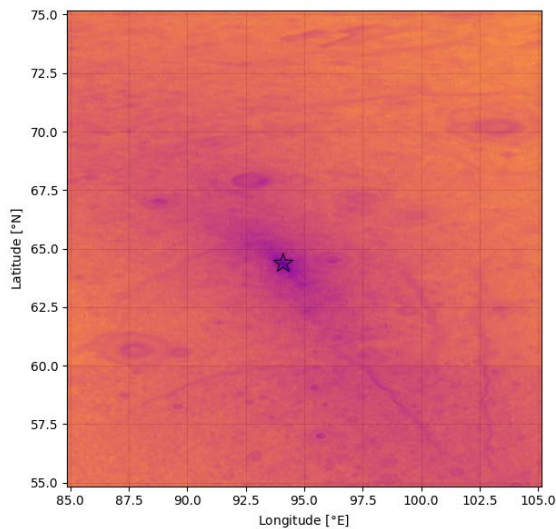**Figure 6.61:** Zoomed in model results 'Power distribution over the mutual footprint' for BSR-2.1 at end of measurement (20th of March 2025 23:50:54; using 16 pixel/degree resolution, GRS data and CO_2 ice as the polar host material), own work
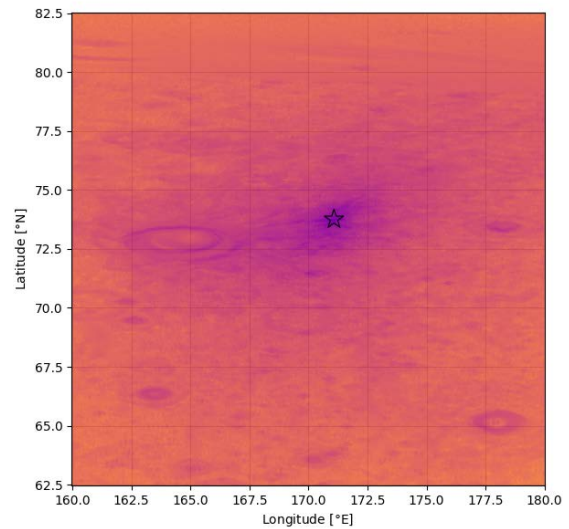
Figure 6.62 shows the implication of the Fresnel zone represented by the 'Point of max. P_R', i.e. the gridpoint showcasing the highest contribution to the total reflected power. Furthermore, the power return of the gridpoint containing the theoretical specular point is also indicated. As expected from the power distribution visuals, this shows a very significant dependence of the total power on only the individual gridpoint of highest return, including its extreme periodicity. The same plots are provided for all other measurements in Subsection E.2.2 of Appendix E and Figure 6.63 shows the BSR-2.1 results for the increased 16 pixel/degree resolution.
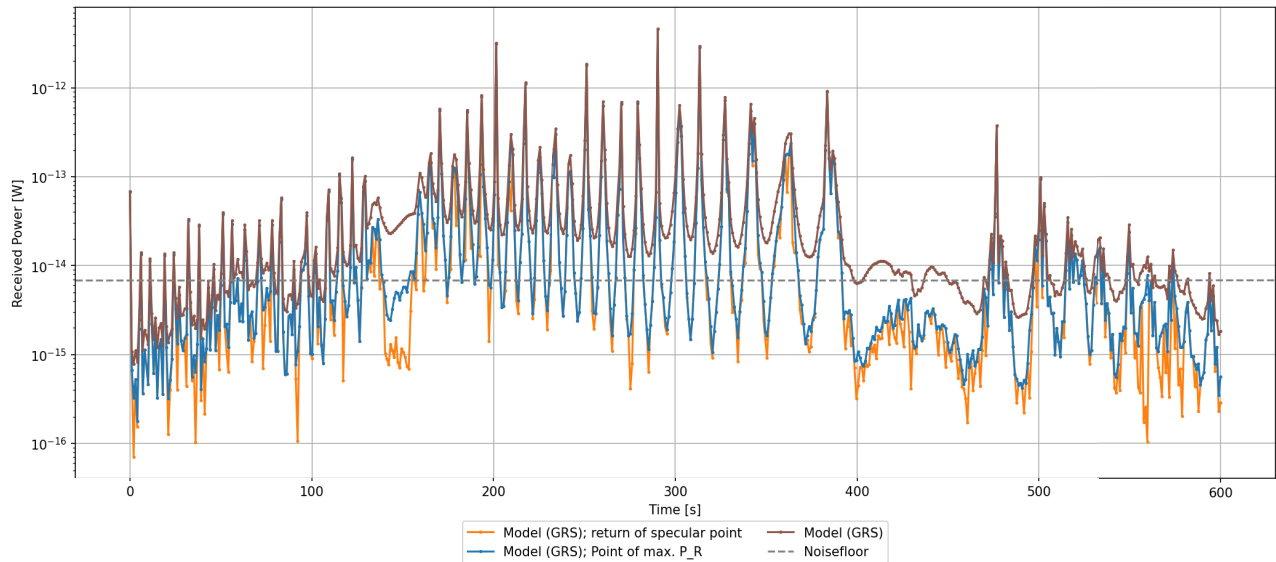
Figure 6.62: Model results 'Power distribution over the mutual footprint' via comparison of the power contributions over time for BSR-2.1 (using 4 pixel/degree resolution, GRS data and CO_2 ice as the polar host material), own work
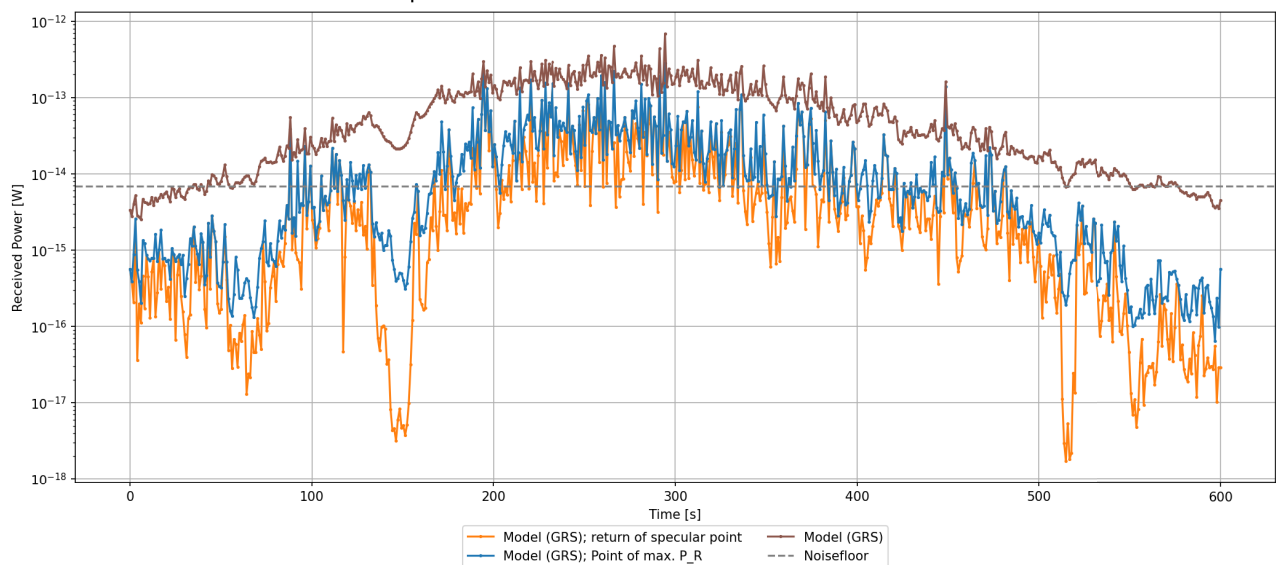
Figure 6.63: Model results 'Power distribution over the mutual footprint' via comparison of the power contributions over time for BSR-2.1 (using 16 pixel/degree resolution, GRS data and CO_2 ice as the polar host material), own work

For BSR-2.1, it can be noted that the specular point is mostly valid approximation of the point of maximum return, but deviates up to around two orders of magnitude in the model dips (most notably between ~130-150 s for the 'Louth' crater). To further analyze this effect, Figure 6.64 shows the ground track of the point of maximum power return along the theoretical tracks of the specular point, midpoint approximation and the MEX and TGO boresights. These same plots are also given for all measurements in Subsection E.2.3 of Appendix E and Figure 6.65 shows it for BSR-2.1 at the increased 16 pixel per degree resolution.
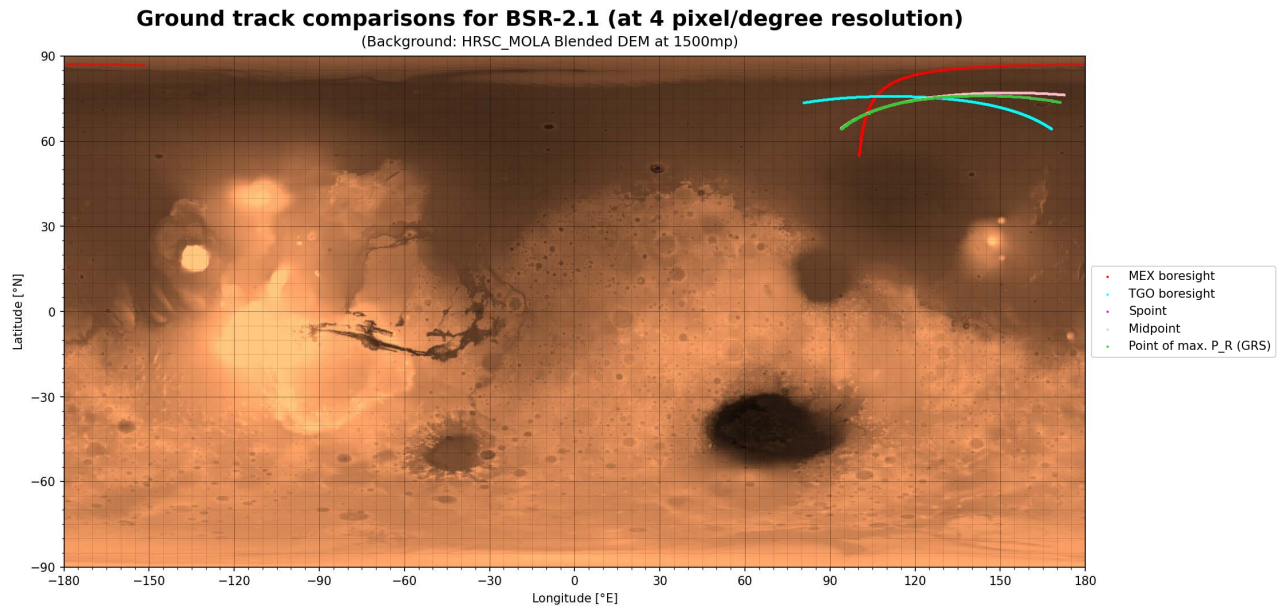
Figure 6.64: Model results 'Power distribution over the mutual footprint' via comparison of the ground tracks of maximum return for BSR-2.1 (using 4 pixel/degree resolution, GRS data and CO_2 ice as the polar host material), own work

Figure 6.65: Model results 'Power distribution over the mutual footprint' via comparison of the ground tracks of maximum return for BSR-2.1 (using 16 pixel/degree resolution, GRS data and CO_2 ice as the polar host material), own work
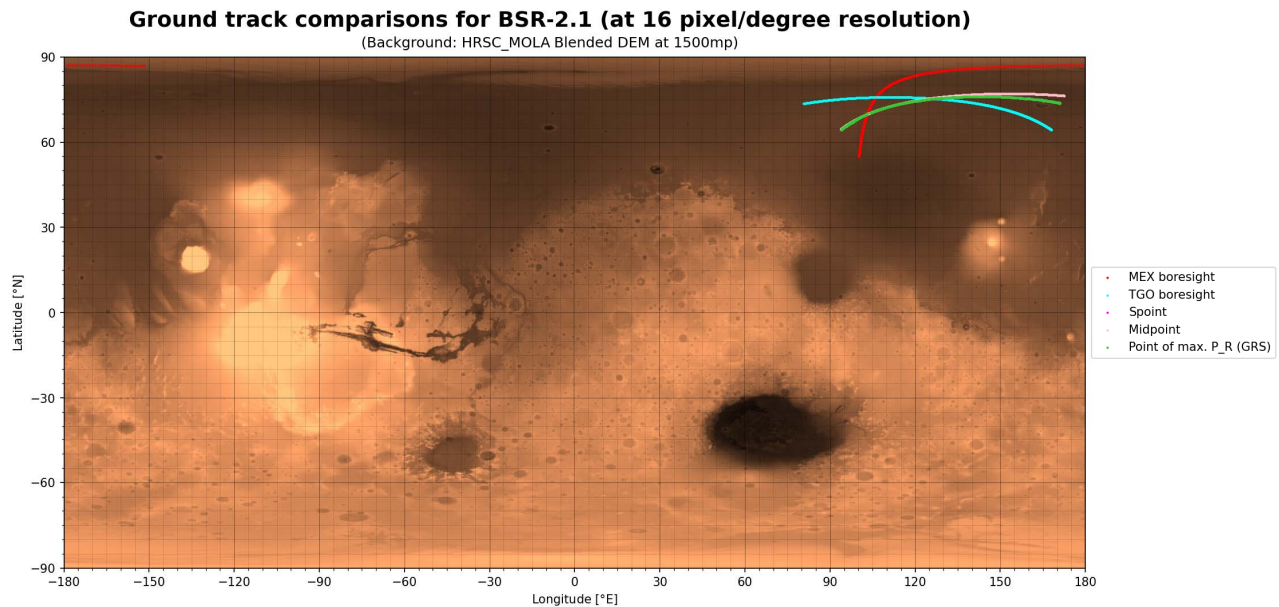
The mutual surface footprint calculation was validated by computing the complete surface area of ellipsoidal Mars by summing all gridpoint surface areas. This yielded a value of ~144 373 441 km^2 for the 4-pixel resolution (ignoring topographical effects), thus closely corresponding to the expected value of ~145 000 000 km^2 [42].

Signal Polarisation at Reflection

When a perfectly RHCP signal hits a smooth flat surface at zero incidence, only an LHCP signal is reflected. In practice, this geometry does not occur and the reflection process converts the RHCP signal into a combination of RHCP and LHCP [133]. However, if a pure (or mostly) LHCP signal is intercepted by an antenna designed only for RHCP, it is not registered (at least not if it is a perfect antenna, which does not exist in practice).

For MEX-TGO BSR, the FM2 antenna on TGO only measures RHCP, meaning small incidence angles on the surface may lead to difficult to detect signals. This is expected to be the case for the BSR-3.1 measurement over Valles Marineris, thus causing the insignificant and stable measured AGC (refer to Figure D.13).

Free-space Direct Signal Contribution and Antenna Pattern Extrapolation

All free-space direct signal contribution parameter plots are included in Section E.3 of Appendix E. Overall, these contributions are unexpectedly negligible in comparison to the complete modelled signal following from reflection. As expected, the power scales up with decreasing MEX-TGO distance. However, the free-space calculation is driven by the low antenna gains. The gains are calculated w.r.t. to the off-boresight angles of the S/C in comparison to each other. However, in most measurement geometries, this surpasses the antenna pattern limits for extrapolation (65° for MEX and 90° for TGO), as shown conclusively in Figure 6.66. It is likely, the antenna sidelobes at over these angles are still significant and have a higher return in the complete modelled signal, creating a signal floor such as seen in BSR-4.1 as the geometry passes into MEX-TGO mutual occultation (Figure 6.45), but antenna data for performing these updated computations is unavailable.
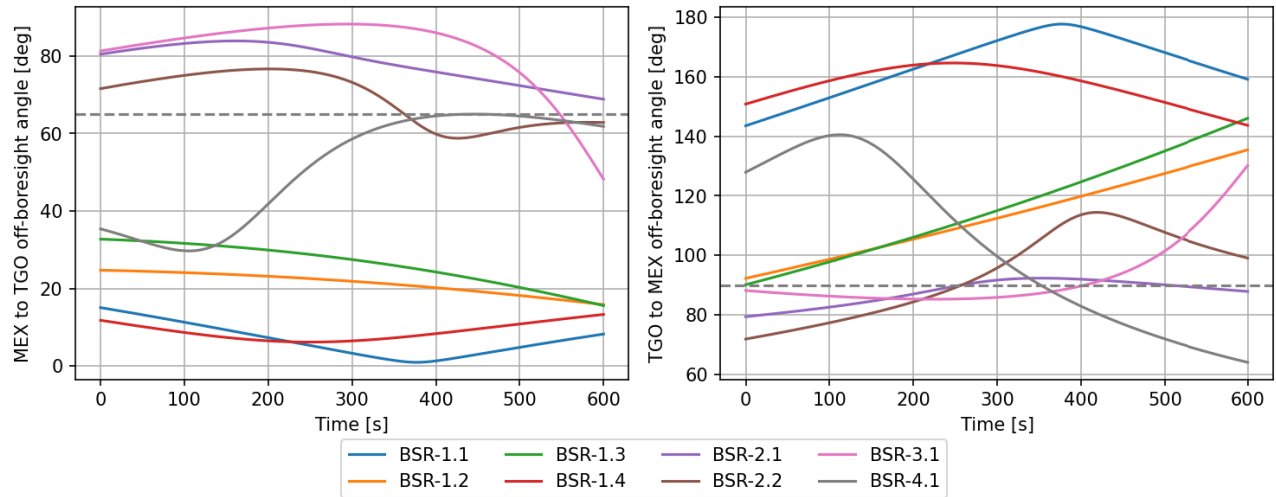

Figure 6.66: Maximum free-space S/C off-boresight angles for all measurements, own work

For verification purposes, the S/C off-boresight angles were also checked with respect to the outer edges of their footprints. As shown in Figure 6.67, the maximum S/C horizon angles do not pass the extrapolation limits (65° for MEX and 90° for TGO) at any point during any of the measurements, making the results valid.
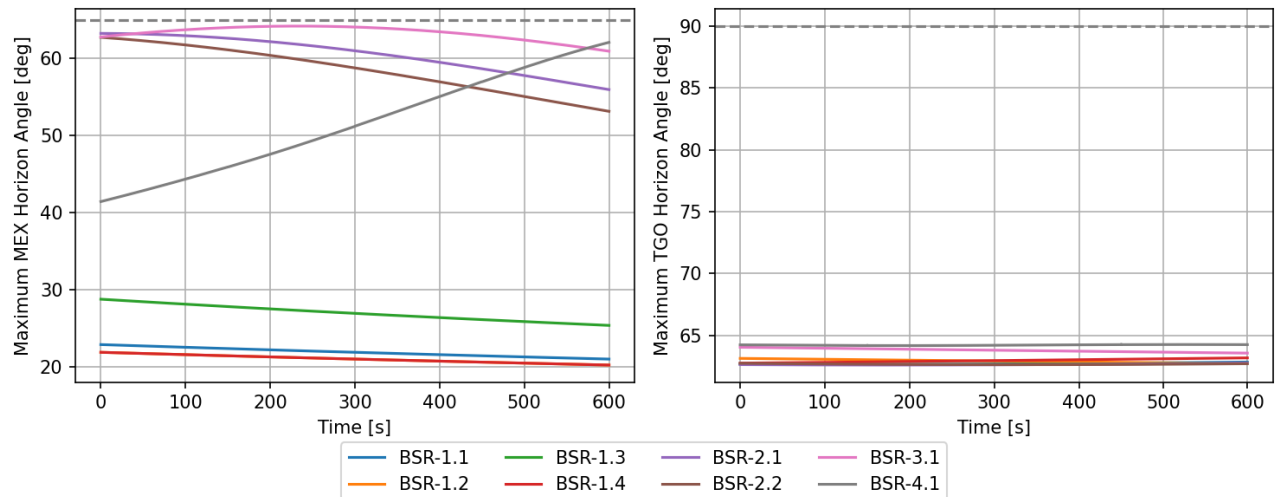
Figure 6.67: Maximum horizon angles, i.e. S/C off-boresight angles, for all measurements, own work

Effect of the Surface Composition

Overall the surface composition seems of little effect to the model. However, as described in Subsection 6.2.5, the model switches the H_2O host material from regolith to CO_2 ice when passing 60°N, abruptly and significantly lowering the dielectric constant (Figure 6.27). The inferred permittivity map if the host material was kept as regolith for all latitudes is shown in Figure 6.68. To thus get insight on the effect of the surface composition, a comparison can be run between using CO_2 or regolith as the polar host material. The result is shown in Figures 6.69 (for 4 pixel per degree resolution) and 6.70 (for 16 pixel per degree resolution) for BSR-2.1 and in Section E.4 of Appendix E for all measurements. It can be noted that although regolith (higher dielectric constant) yields a slightly higher received power, the difference cannot yield conclusive results as of yet as accuracy of the modelled received power is still too low, but does indicate potential for future iterations.
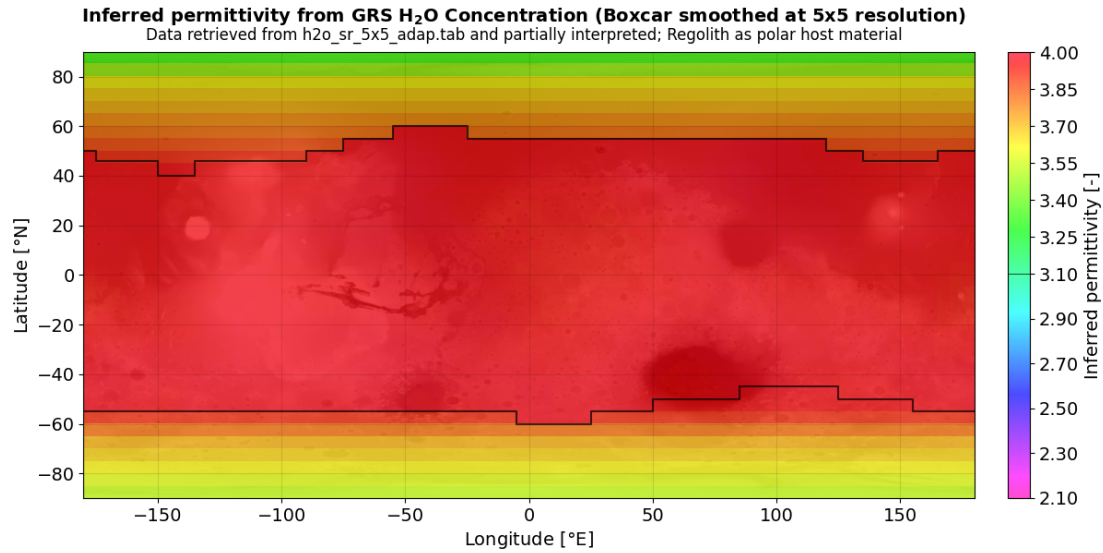
Figure 6.68: Inferred dielectric constant plot from the partially interpreted GRS data (derived H$_2$O concentration in 5x5° longitude-latitude bins, smoothed using a Boxcar filter; from *'h2o_sr_5x5.tab'* [116]), own work
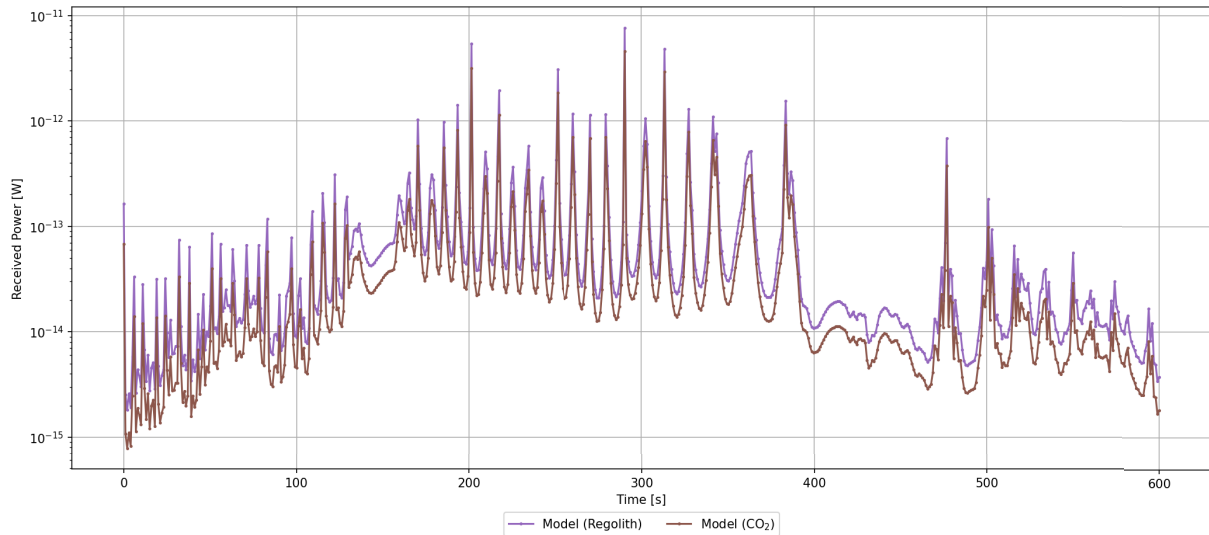
Figure 6.69: Model results 'Effect of the Surface Composition: Regolith vs. CO$_2$ host comparison' for BSR-2.1 (using 4 pixel/degree resolution and GRS data), own work
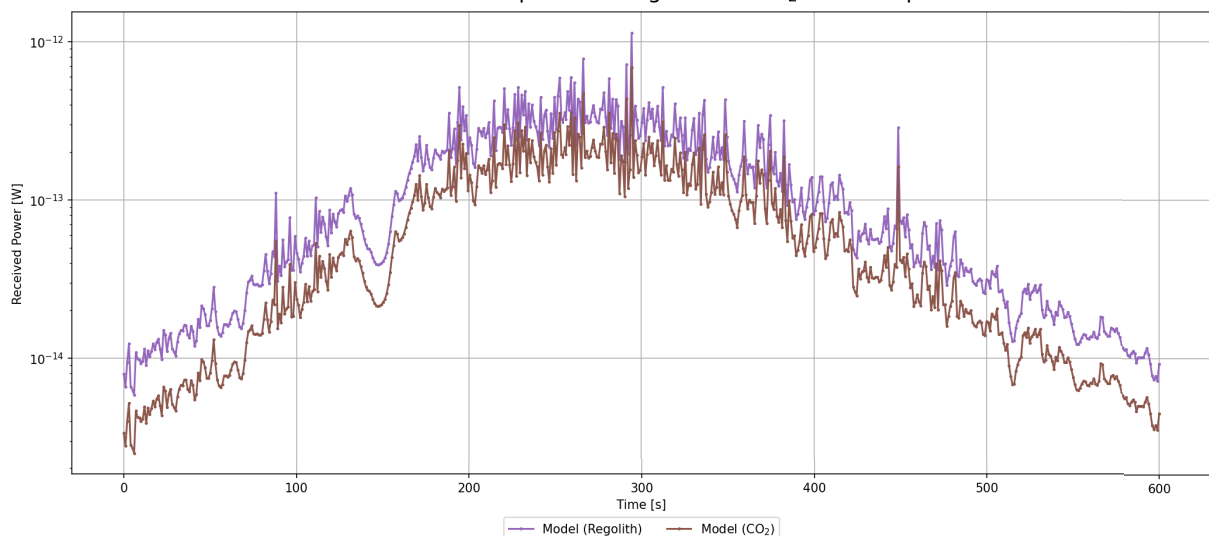
Figure 6.70: Model results 'Effect of the Surface Composition: Regolith vs. CO$_2$ host comparison' for BSR-2.1 (using 16 pixel/degree resolution and GRS data), own work

Furthermore, a comparison between the results for GRS and those for FREND can be made for (only) BSR-3.1, which falls inside the available data range for both instruments. The relevant power distribution plots over the footprint are shown for GRS in Figures E.25 and E.26, and for FREND in Figures E.27 and E.28. Furthermore, those for the temporal variation in the modelled power can be found in Figures E.38 (GRS) and E.39 (FREND).

At this level there is no distinguishable difference between using data from either instrument. Therefore, Figure 6.71 shows a compiled plot with the final reflection model and difference between the instrument results. Here, the lines for either instrument overlap and are not visually distinguishable. The difference between the GRS and FREND models ('Absolute difference'; light-blue line) is always approximately two orders of magnitude smaller than the actual received power. This indicates the choice of instrument has a negligible effect on the first iteration of the MEX-TGO BSR measurement processing model.

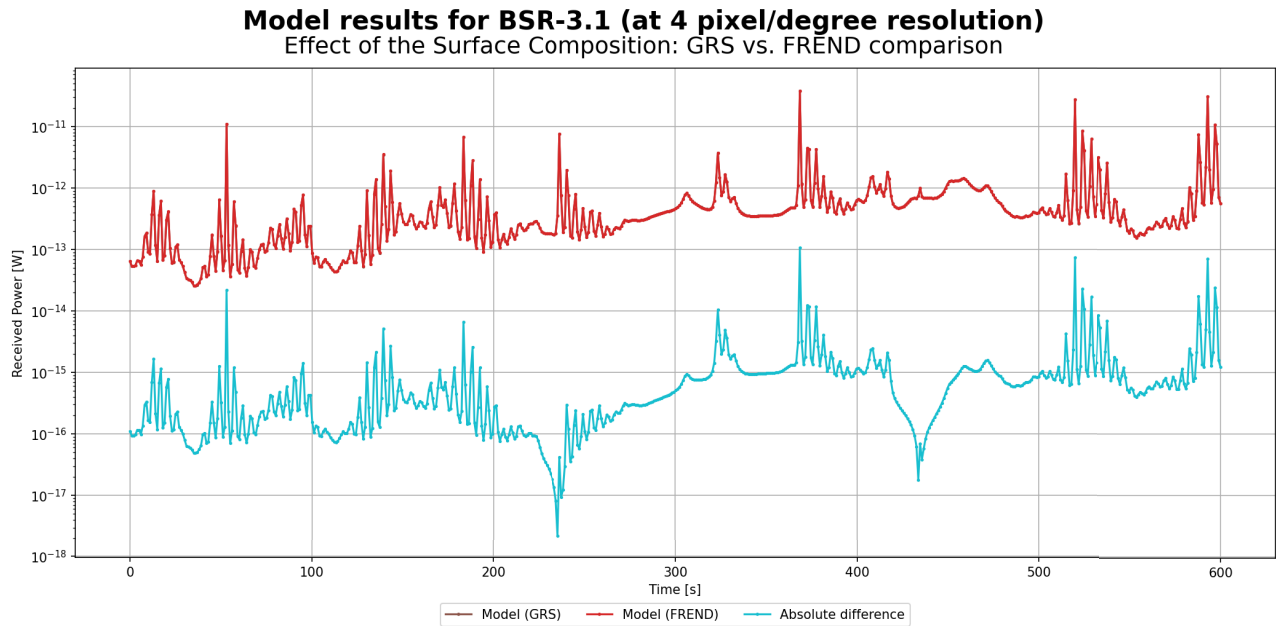**Figure 6.71:** Model results 'Effect of the Surface Composition: GRS vs. FREND comparison' for BSR-3.1 (using 4 pixel/degree resolution), own work
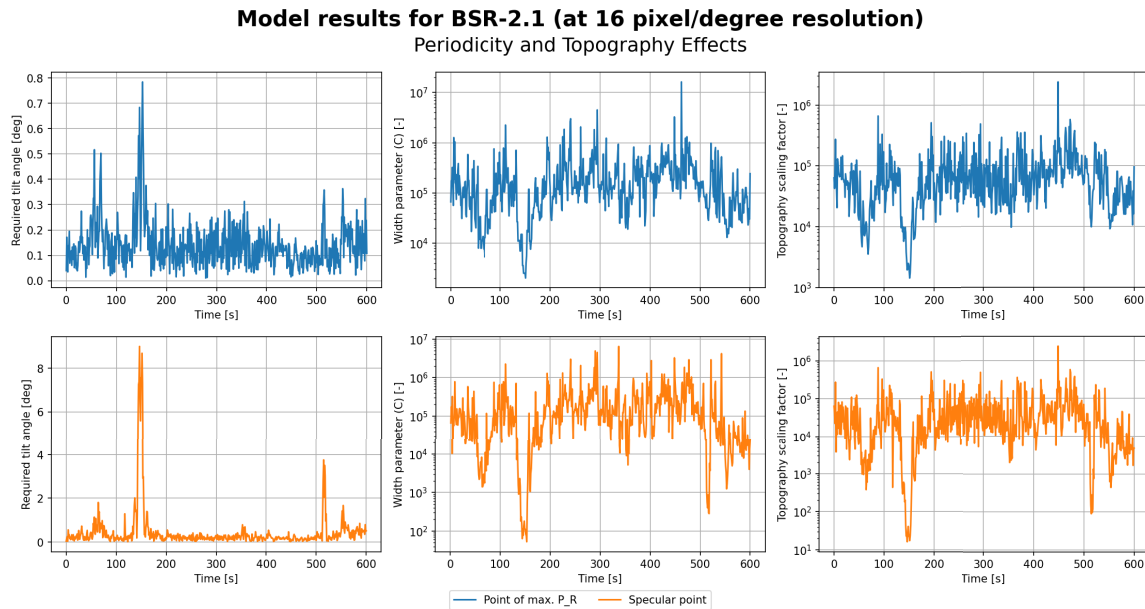
Periodicity and Topography Effects

The modelled power return showcases a periodicity effect, which roots in topography and spatial resolution effects effects. Topography effects consist of the required tilt angle γ and width parameter C, shown isolated from the other BSR parameters in Figures 6.72 and 6.73 for BSR-2.1 (all others are presented in Section E.5 of Appendix E). As can be seen in the scaling factor (right column; linearly related to the received power), the periodicity and amplitude variations follow from both the required tilt angle and the width parameter.

Considering the high periodicity in the parameters, especially the required tilt angle, the hypothesis lies in the roughness of the spatial resolution of the simulations ($\sim$29.6 km) causing large changes as the pixels change and the S/C moves from one to the next. The resolution was selected as it is the lowest available resolution MOLA data (4 pixels per degree). This was expected to be sufficient, and higher resolutions were not possible due to the increased computational cost. However, as the scattering model is very sharp and the MOLA data is very rough, the model was adapted such that it could run once for one of the measurements at higher spatial resolution (16 pixels per degree), already shown for a number of the previous points of discussion.

The model results for BSR-2.1 using this higher resolution topography yields the results of Figure 6.74. This shows the periodicity is highly decreased in amplitude variations, but shows much more frequent peaks. This corresponds nicely to what would be expected for a smoother resolution (i.e. more pixel transitions at lesser differences). Furthermore, when assessing the final 100 seconds (from $\sim$500-600 s) in Figure 6.74, the shapes of the data and modelled power return shown a high correspondence, although differing by approximately one order of magnitude in their absolute values. Overall, it shows good incentive for adapting the model to run with even further increased (e.g. 32 pixel per degree) resolution MOLA data to better match the data.

Model results for BSR-2.1 (at 4 pixel/degree resolution)
Periodicity and Topography Effects
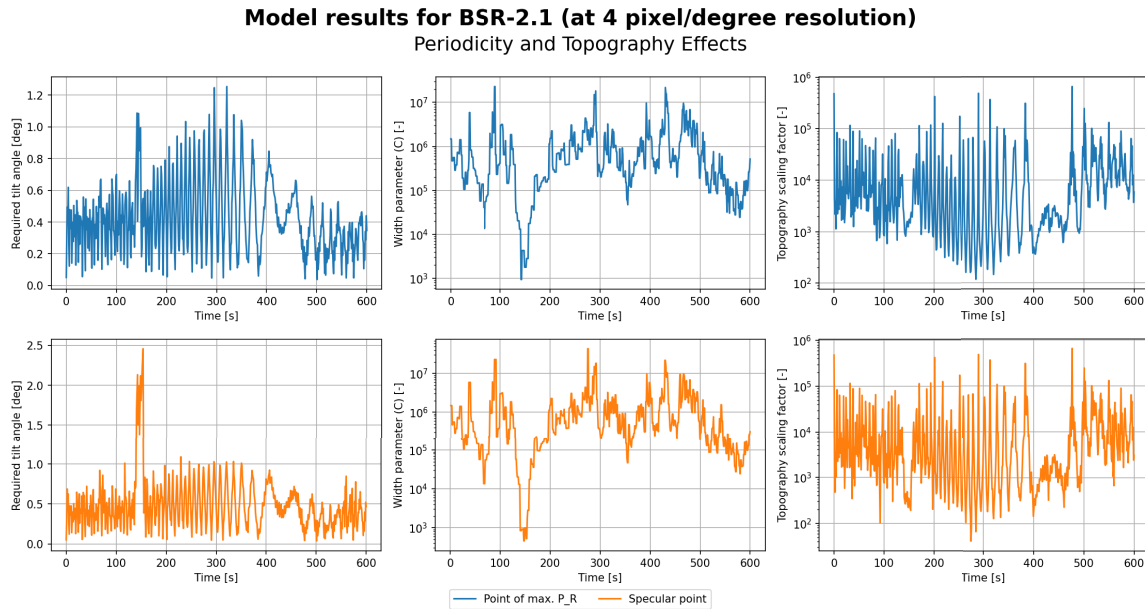
Figure 6.72: Model results 'Periodicity and Topography Effects' for BSR-2.1 (using 4 pixel/degree resolution), own work

Model results for BSR-2.1 (at 16 pixel/degree resolution)
Periodicity and Topography Effects

Figure 6.73: Model results 'Periodicity and Topography Effects' for BSR-2.1 (using 16 pixel/degree resolution), own work

Model results for BSR-2.1 (at 16 pixel/degree resolution)
Comparison of Model vs. Data
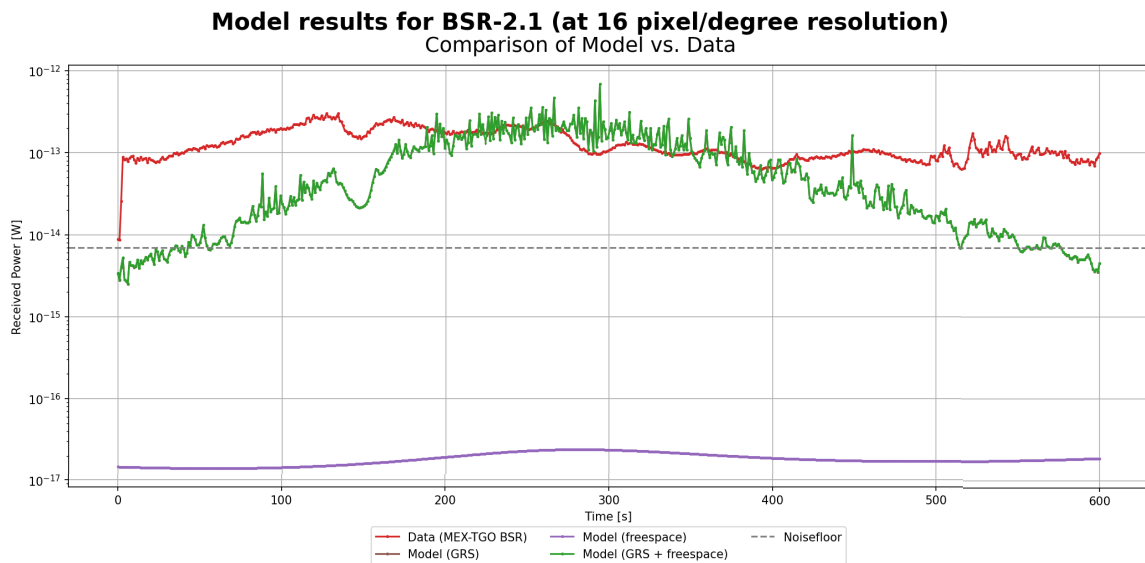
Figure 6.74: Model results 'Comparison of Model vs. Data' for BSR-2.1 (using 16 pixel/degree resolution, GRS data and CO_2 ice as the polar host material), own work

In addition to adapting the MOLA resolution, it may yield better results to also redefine the interpretation of the width parameter C, which as previously noted, has no definite relation to surface topography and is only defined according to Equation 6.7 due to its simplicity and often having good agreement with results [72, 141]. This can be done in two ways, most simply by redefining the RMS slope calculation [141], e.g. taking a larger grid at higher MOLA resolution over which the RMS computation is performed. Alternatively, a different scattering model could be employed to redefine the RCS completely. Roughness is more conventionally defined in terms of metres, but required in radians for the Hagfors model, making it somewhat of an abstract interpretation whereas more representative results may be reached by making the model explicitly dependent on spatial, instead of angular, roughness. Furthermore, increased surface roughness increases the width of the echo spectrum [135]. Thus performing a frequency analysis on the BSR data may yield input on the definition of the width parameter and the bandwidth could be used to infer values for C which in turn can be used for modelling. For continued research, different interpretations for C should be compared.

6.4.2. Sensitivity, Limitations and Uncertainties

To characterize model behavior and dependency on the different parameters, the most influential parameters should be identified. A number of uncertainties and limitations were identified in a qualitative manner. These points (and other identified limitations) require further research and/or data for next iterations of the MEX-TGO BSR processing model to reach higher certainty in the results:

- **Rough spatial resolution & Computational cost:**
  The first step to be taken for improved model results is increasing the spatial resolution, possibly by use of a supercomputer, by using higher resolution MOLA data (ideally at least 32 pixels per degree). Within the scope of the thesis, this was not feasible for reasons of the associated computational cost. In addition it would also be recommended to increase the temporal resolution, i.e. decreasing the time step of the measurements, to better capture regional effects.

- **Antenna extrapolation limits & Freespace contributions:**
  Antenna extrapolation beyond 65° for MEX and 90° for TGO is both not currently feasible as the data is not available. For both antenna patterns, the gain data has to be extrapolated to larger angles than data is available for to calculate the freespace direct signal contribution. This causes a large underestimation of the total modelled signal strength, complicating comparisons with the data. Additionally, the available gain data represents an average of all azimuths, inducing further uncertainty in the model.

- **Permittivity variation with frequency:**
  Measured dielectric constants drop with increasing frequency [159], meaning there is a dependence of the permittivity on frequency variations. This was left outside the scope of the thesis and is expected to lay in the error margins for the first model iteration, but should be considered in further research.

- **Polar region H_2O concentrations and seasonal dependence:**
  For current modelling in the polar regions, no already processed WEH levels from neutron spectrometry data were available and no seasonal variation was taken into account. Simultaneously measurement planning in the near-equatorial region is highly limited by lander visibility periods, making polar measurements more likely to occur. Thus, for future research, seasonal dependence and actual processed H_2O concentrations in the polar regions should be determined.

- **Polarization effects:**
  The TGO FM2 antenna can only measure RHCP signals, meaning that if the reflected signal is mostly LHCP, it will not be detected. To account for this, polarization effects should be included in the model wherin only RHCP signals contribute to the total received power.

- **AGC calibration:**
  The AGC data is uncalibrated. Tests are planned between December 2025 and February 2026 which should yield calibrated data and transfer function for further research.

- **Definition of the width parameter C:**
  There is no definite relation of the width parameter C to surface topography, causing high expectancy of erroneous behavior in the model. For future research, different interpretations for C should be compared, e.g. by redefining the RMS slope calculation or by employing a different scattering model to redefine the RCS completely.

Quantitative characterization follows from the sensitivity and error bar analysis, which was not performed, but is also recommended for future research.

7

Conclusions and Recommendations

The objective of this thesis' research was to: "Compare current knowledge, particularly the Gamma-Ray Spectrometer (GRS) and Fine Resolution Epithermal Neutron Detector (FREND) maps, on shallow subsurface water ice at mid to equatorial latitudes on Mars by planning, performing and processing bi-static radar measurements between the Mars Express (MEX) and the ExoMars Trace Gas Orbiter (TGO) spacecraft, using numerical simulations of the Martian subsurface". Conclusions to the research are presented in Section 7.1 and recommendations for future work are in Section 7.2, including those for the measurement planning and analysis phase respectively, as well as next steps overall for the continuation of MEX-TGO BSR.

7.1. Conclusions

In order to organize the main conclusions, one can look back at the research questions (RQs) from Chapter 1:

RQ1: When can the best bi-static radar measurements be performed between MEX and TGO?
The timing for the best bi-static radar measurements is driven by a combination of phases 1 and 2 of the MSc thesis research, namely the determination of regions of interest as well as orbital modelling and measurement planning to probe these regions. The involved sub-questions state:

- RQ1.1: Which regions fit the interest of past and future missions?
  For the thesis literature study, extensive research was performed on Mars' geological past and exploration history, documented in Chapters 2 and 3. As discussed in Chapter 4, this yielded a list of twelve locations of scientific interest (LOI-S) and three locations of interest for calibration (LOI-C). Through a set of requirements, including the initially expected limit for eight measurements taken within the thesis duration, regions of highest interest were prioritized as Scientific Target Locations (STLs). The selection includes three regions of scientific interest (STL-S) and one region with interest for calibration (STL-C). Furthermore, for each STL a backup region was selected to allow some flexibility in the measurement planning, yielding Figure 7.1.
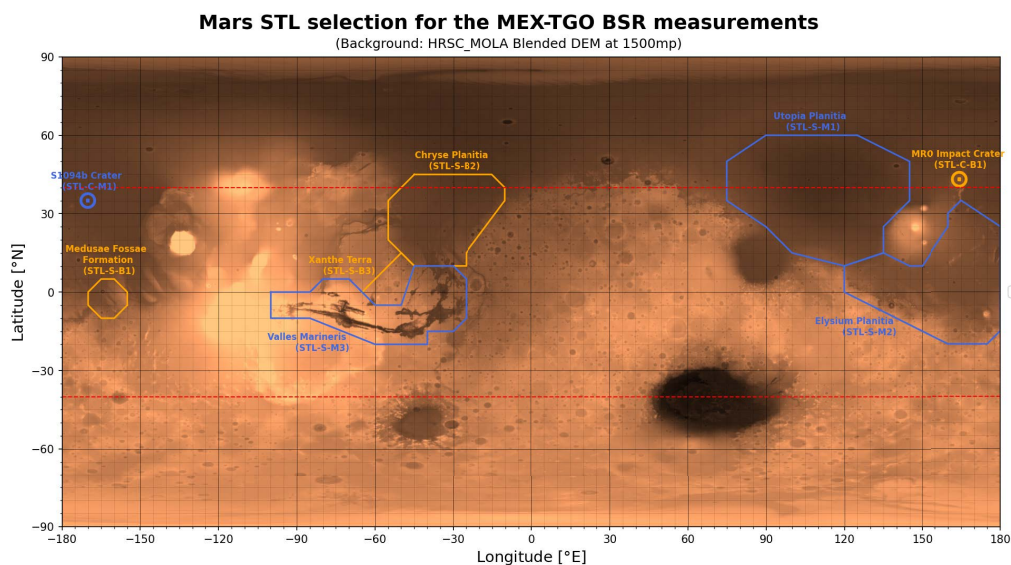
Figure 7.1: Selection of the STL locations for the MEX-TGO BSR measurements, own work

- RQ1.2: What are the relevant selection criteria for quality measurements?
  For the measurement planning phase (Chapter 5), the main selection criteria were defined in the model checks, including a maximum MEX-TGO distance at the closest pass, maximum equal-emission angles, ten-minute

66

minimum measurement duration and requirement for the specular point ground track to probe into the near-equatorial region. However it was concluded to be a significant limitation of the model to not take into account lander visibility periods, which drive the MEX-TGO BSR measurement feasibility. Furthermore, due to the novelty of the research, focus should switch from target-based to measurement-quality based planning.

During the measurement analysis phase (Chapter 6), it was additionally concluded that measurements with low equal-emission angles (such as BSR-3.1) are at risk of yielding insignificant power return due to polarization effects. This should be studied in further detail for future iterations of measurement planning, and included as a check for feasible measurement geometry.

- RQ1.3: How can MEX-TGO BSR measurements be modelled?
  A numerical model can be written in Python, employing the SPICE information system[1], SpiceyPy interface[2,3] and SPICE kernels from the Navigation and Ancillary Information Facility's SPICE Data Archive [4] (containing ancillary S/C and Solar System information). Detailed modelling steps and architecture are presented in Figure 5.4 (measurement planning) and Figures 6.33 and 6.34.

RQ2: How can bi-static radar measurements be processed to retrieve the amount and form of H_2O?

The processing of BSR measurements is closely linked to phase 3, i.e. the numerical modelling of the MEX-TGO BSR signal propagation and subsurface interaction. The involved sub-questions state:

- RQ2.1: How does the received signal amplitude depend on the sampled area's dielectric constant?
  The received signal amplitude can be connected to the dielectric constant of the sampled area with the Bi-Static Radar Equation (Equation 7.1) and Hagfors Model (Equation 7.2), described in Subsection 6.1.2. The Fresnel reflectivity ρ is directly dependent on the dielectric constant ϵ through Equation 7.3 [20, 133].

$$P_{R,ss} = \int_S \frac{P_T \cdot G_T}{4\pi \cdot R_T^2} \cdot \sigma_0 \cdot \frac{G_R \cdot \lambda^2}{4\pi \cdot R_R^2} dS \quad (7.1) \qquad \sigma_0 = \rho \cdot C \cdot (cos^4(\gamma) + C \cdot sin^2(\gamma))^{-3/2} \quad (7.2)$$

$$\rho(\theta_i) = \frac{\rho_\perp(\theta_i) + \rho_\parallel(\theta_i)}{2} = \frac{\left(\frac{cos(\theta_i) - \sqrt{\epsilon - sin^2(\theta_i)}}{cos(\theta_i) + \sqrt{\epsilon - sin^2(\theta_i)}}\right)^2 + \left(\frac{\epsilon cos(\theta_i) - \sqrt{\epsilon - sin^2(\theta_i)}}{\epsilon cos(\theta_i) + \sqrt{\epsilon - sin^2(\theta_i)}}\right)}{2} \quad (7.3)$$

Overall it was found for the dielectric constant to be near-negligible in final model results, showcasing only a slight dependency in the magnitude of the total modelled received power. This entails the surface composition is yet to show a strong signature. However, after calibration, resolution increase and improving direct signal, seasonal and polarization effects modelling, reliable detections through MEX-TGO BSR do appear to be possible.

- RQ2.2: How does the dielectric constant depend on water and other constituents of the subsurface?
  The dielectric constant is a function of the subsurface constituents, which can be modelled through a mixing model. The chosen model is the one by Maxwell Garnett (Equation 7.4) described in Subsection 6.1.3.

$$\epsilon_{eff} = \epsilon_h \cdot \frac{\epsilon_h + \frac{1 + 2v_{ice}}{3} \cdot (\epsilon_{ice} - \epsilon_h)}{\epsilon_h + \frac{1 - v_{ice}}{3} \cdot (\epsilon_{ice} - \epsilon_h)} \quad (7.4)$$

The volume fraction of water ice (v_{ice}) can be taken from gamma-ray/neutron spectrometry data (GRS and FREND). Furthermore, the host medium is set to low-porosity Martian regolith (ϵ_h=4.0) for low to mid-latitudes or non-porous CO_2 ice (ϵ_h=2.1) for near-polar regions ($\geq 60°$) [28]. For water ice, ϵ_{ice} is taken as 3.1 [4, 28, 80]. The effective dielectric constant (ϵ_{eff}) can then be translated into the Fresnel reflectivity for use in the bi-static radar equation.

- RQ2.3: What is the confidence level of the MEX-TGO BSR results?
  The confidence level in the numerical model has to be quantitatively estimated through a sensitivity analysis and estimation of the error bars, but qualitative insights include: High dependence on spatial resolution, and driving uncertainties from antenna pattern extrapolation for the free-space direct signal contribution, polarization effects and uncalibrated AGC data, and lack of polar coverage and seasonal dependence in neutron spectrometry data.

RQ3: How do processed MEX-TGO BSR results match the state-of-the-art scientific knowledge?

Current match of the modelled results does not match the state-of-the-art scientific knowledge on Martian water (ice). However, this is deemed an effect of the novelty of the model, being the first iteration of MEX-TGO BSR application for this research. A better match may come out of future iterations.

---

[1] https://www.cosmos.esa.int/web/spice
[2] https://github.com/AndrewAnnex/SpiceyPy
[3] https://naif.jpl.nasa.gov/naif/links.html
[4] https://naif.jpl.nasa.gov/naif/data.html

7.2. Recommendations and Future Work

From the conclusions to the thesis and first iteration of MEX-TGO BSR application to Martian subsurface water (ice) research, a number of recommendations can be drawn with regard to measurement planning and measurement analysis. Furthermore, work is already being put towards the next steps of the research.

Recommendations on 'Measurement Planning' include:

- Increase the computational speed by only considering the Fresnel zone, or designing a less computationally intensive algorithm for deriving the equal-emission conditions at the specular points. Additionally, it would be beneficial to research and implement a better non-computationally intensive specular point approximation, as the midpoints highly decrease in accuracy with increasing MEX altitude.

- Loosen the target-related constraints to allow for a transition from target-based to measurement-quality based planning. The ±40° near-equatorial band is highly limiting. Instead of attempting to plan measurements purely in the water (ice) STLs, a more diverse data set of BSR measurements in different regions yield better chances of improving the technique before attempting further water (ice) research. Sampling different regions, especially igneous, to compare with icy regions should showcase exceedingly higher ϵ values around ~7-10 [121].

- Re-quantify and re-define measurement observation geometry requirements, and validate these with actual resultant measurement quality.

- Research an optimal MEX-TGO BSR measurement duration.

Recommendations on 'Measurement Analysis' include:

- Conduct a more detailed analysis on the 'Louth crater'.

- Characterize the underlying behavior of the signal mirroring effect, including a possible dependence on S/C movement and specular ground tracks.

- Increase the spatial resolution (by using higher resolution MOLA data). At minimum it should be increased to 16 pixels per degree for all measurements, but if computational resources, i.e. use of a supercomputer, permit it, it is possible run at 32, 64 or 128 pixels per degree.

- Increase the temporal resolution (after assessing the impact of running on higher spatial resolution).

- Implement seasonal dependence. Global GRS sums are available for different seasons [62], but these are not processed to H_2O concentrations. Processing these and then comparing them with BSR measurements in the same seasons could improve the definitiveness of dielectric constant variation findings.

- Assess the difference in results when opting for a tri-axial ellipsoid instead of a bi-axial ellipsoid, e.g. with the parameters as presented by Smith et al. [137] (Table 4). The South pole is known to have a higher elevation than the North pole and significant rise exists in the Tharsis region.

- Include modelling of polarization effects, i.e. when the originally RHCP signal transmitted by MEX hits the surface at small incidence, it is partially converted to LHCP, which cannot be received by TGO. This should be implemented as un-received signal in the modelling.

- Perform a quantitative characterization of the driving parameters by sensitivity and error bar analysis.

- Compare different (re-)definitions for the width parameter C in the Hagfors model.

Next steps, already put into progress, include:

- Fourteen measurements are already planned in upcoming MTPs. Furthermore, many BSR opportunities with small S/C distances are still expected in the near future [22]. For this the main limiting factor of lander visibility periods should be included and updated measurement planning and preference strategy should be set. It may also be considered to relax the margins for the lander visibility periods, as these are currently highly conservative [22].

- Follow-up work is to be performed on employing GNSS-R techniques for improving BSR measurements [143]. This includes deviating from the conventional nadir-pointing setup, requiring a longer time scale to assess measurement planning potential, but greatly increasing the amount of taken measurements.

- Calibration of the AGC data is required by having the S/C look at each other. The calibration test is happening between December 2025 to February 2026 with at least four positions, and will allow for characterization of the transfer function.

References

[1] J.C. Andrews-Hanna and K.W. Lewis. "Early Mars hydrology: 2. Hydrological evolution in the Noachian and Hesperian epochs". In: *Journal of Geophysical Research* 116 (2011). DOI: 10.1029/2010JE003709.

[2] R.E. Arvidson et al. "Results from the Mars Phoenix Lander Robotic Arm experiment". In: *Journal of Geophysical Research* 114.E00E02 (2009). DOI: 10.1029/2009JE003408.

[3] D.H. Baker et al. *International Mars Ice Mapper Mission: Investigating Subsurface Ice on Mars for Science and Human Exploration*. In: 55th Geological Society of America Connects; Pittsburgh, Pennsylvania. [Conference abstract]. Oct. 2023. DOI: 10.1130/abs/2023AM-395187.

[4] D.M.H. Baker and L.M. Carter. "Ice Content of Mantling Materials in Deuteronilus Mensae, Mars". In: *Journal of Geophysical Research* 128 (2023). DOI: 10.1029/2022JE007549.

[5] D.M.H. Baker et al. *International Mars Ice Mapper Mission Concept Phase Two: Cross-cutting Science and Reconnaissance Objectives*. In: 55th Lunar and Planetary Science Conference; The Woodlands, Texas. [Conference paper]. Mar. 2024.

[6] D.M.H. Baker et al. *International Mars Ice Mapper Mission: Reconnaissance for the Human Exploration of Mars and Decadal-level Science*. In: 54th Lunar and Planetary Science Conference; The Woodlands, Texas. [Conference paper]. Mar. 2023.

[7] V.R. Baker and D.J. Milton. "Erosion by Catastrophic Floods on Mars and Earth". In: *Icarus* 23 (1974), pp. 27–41. DOI: 10.1016/0019-1035(74)90101-8.

[8] C. A. Balanis. *Antenna Theory: Analysis and Design*. Hoboken, New Jersey, United States of America: John Wiley & Sons, 2016.

[9] S. Belongie. *Rodrigues' Rotation Formula*. From MathWorld - A Wolfram Resource. 2025. URL: https://mathworld.wolfram.com/RodriguesRotationFormula.html (visited on Aug. 9, 2025).

[10] W. Benedix et al. "The ExoMars 2028 WISDOM antenna assembly: Description and characterization". In: *Planetary and Space Science* 253.105995 (2024). DOI: 10.1016/j.pss.2024.105995.

[11] R.G. Bonitz et al. "NASA Mars 2007 Phoenix Lander Robotic Arm and Icy Soil Acquisition Device". In: *Journal of Geophysical Research* 113.E00A01 (2008). DOI: 10.1029/2007JE003030.

[12] M.C. Bourke et al. "Extraterrestrial dunes: An introduction to the special issue on planetary dune systems". In: *Geomorphology* 121 (2010), pp. 1–14. DOI: 10.1016/j.geomorph.2010.04.007.

[13] W. V. Boynton et al. "The Mars Odyssey Gamma-Ray Spectrometer Instrument Suite". In: *Space Science Reviews* 110 (2004), pp. 37–83. DOI: 10.1023/B:SPAC.0000021007.76126.15.

[14] W.V. Boynton et al. "Concentration of H, Si, Cl, K, Fe, and Th in the low- and mid-latitude regions of Mars". In: *Journal of Geophysical Research* 112.E12S99 (2007). DOI: 10.1029/2007JE002887.

[15] W.V. Boynton et al. "Distribution of Hydrogen in the Near Surface of Mars: Evidence for Subsurface Ice Deposits". In: *Science* 297.5578 (2002), pp. 81–85. DOI: 10.1126/science.1073722.

[16] A.J. Brown et al. "Louth crater: Evolution of a layered water ice mound". In: *Icarus* 196 (2008), pp. 433–445. DOI: 10.1016/j.icarus.2007.11.023.

[17] D.M. Burr and J.A. Finch. "Seeking sand origins on Mars: Towards testing the volcaniclastic hypothesis globally". In: *Icarus* 420 (2024), p. 116194. DOI: 10.1016/j.icarus.2024.116194.

[18] G. Cai, B.M. Chen, and T.H. Lee. *Advances in Industrial Control - Unmanned Rotorcraft Systems*. London, United Kingdom: Springer, 2011.

[19] W.M. Calvin, B.A. Cantor, and P.B. James. "Interannual and seasonal changes in the south seasonal polar cap of Mars: Observations from MY 28-31 using MARCI". In: *Journal of Geophysical Research* 292 (2017), pp. 144–153. DOI: 10.1016/j.icarus.2017.01.010.

[20] B.A. Campbell et al. "Roughness and near-surface density of Mars from SHARAD radar echoes". In: *Journal of Geophysical Research* 118 (2013), pp. 436–450. DOI: 10.1002/jgre.20050.

[21] A. Cardesin-Moinelo. "Personal communication". [Email: 'MTP276/095: MEX-TGO 8 passes (including 1 BSR)']. May 2025.

[22] A. Cardesin-Moinelo. "Personal communication". [Email: 'MTP277/096: MEX-TGO passes (+long BSR)']. June 2025.

[23] A. Cardesin-Moinelo. "Personal communication". [Email: 'Added 2 MEX-TGO BSR Opportunities in MTP272/91']. Jan. 2025.

[24] A. Cardesin-Moinelo et al. "Mars Express: 20 Years of Mission, Science Operations and Data Archiving". In: *Space Science Reviews* 220.25 (2024). DOI: 10.1007/s11214-024-01059-0.

[25] M.H. Carr. *The Surface of Mars*. Cambridge, United Kingdom: Cambridge University Press, 2007.

[26] J. Carter et al. "A Mars orbital catalog of aqueous alteration signatures (MOCAAS)". In: *Icarus* 389 (2023), p. 115164. DOI: 10.1016/j.icarus.2022.115164.

[27] T.M. Casademont et al. "RIMFAX Ground Penetrating Radar Reveals Dielectric Permittivity and Rock Density of Shallow Martian Subsurface". In: *Journal of Geophysical Research* 128.E2022JE007598 (2023). DOI: 10.1029/2022JE007598.

[28] L. Castaldo et al. "Global permittivity mapping of the Martian surface from SHARAD". In: *Earth and Planetary Science Letters* 462 (2017), pp. 55–65. DOI: 10.1016/j.epsl.2017.01.012.

[29] R. Chen et al. "Martian soil as revealed by ground-penetrating radar at the Tianwen-1 landing site". In: *Geology* 51.3 (2023), pp. 315–319. DOI: doi.org/10.1130/G50632.1.

[30] V. Ciarletti et al. "Astrobiology". In: *The WISDOM Radar: Unveiling the Subsurface Beneath the ExoMars Rover and Identifying the Best Locations for Drilling* 17.6 (2017), pp. 565–584. DOI: 10.1089/ast.2016.1532.

[31] A. Collet et al. *Aeolian bedforms formed by ice sublimation and vapor condensation on Louth crater ice, Mars*. In: 16th Europlanet Science Congress; Granada, Spain. [Conference abstract]. Sept. 2022. DOI: 10.5194/epsc2022-471.

[32] M. Costa-Sitja. "SPICE for ESA Planetary Missions: geometry and visualization support to studies, operations and data analysis within your reach". In: *SpaceOps Conference* 2553 (2018). DOI: 10.2514/6.2018-2553.

[33] S. Cull et al. "Compositions of Subsurface Ices at the Mars Phoenix Landing Site". In: *Geophysical Research Letters* 37.L24203 (2010). DOI: 10.1029/2010GL045372.

[34] A.F. Davila, K. Warren-Rhodes, and J. DiRuggiero. "Mars Geological Enigmas (From the Late Noachian Epoch to the Present Day)". In: ed. by R.J. Soare et al. 1st ed. Elsevier Inc., 2021. Chap. 12 - The Atacama Desert: a window into late Mars surface habitability?, pp. 333–355. DOI: 10.1016/C2019-0-01457-4.

[35] R.M. Davis et al. *International Mars Ice Mapper Mission: A Reconnaissance Mission for the Human Exploration of Mars*. In: Low-Cost Science Mission Concepts for Mars Exploration; Pasadena, Canada. [Conference paper]. Mar. 2022.

[36] Deutsches Zentrum für Luft- und Raumfahrt. *Chaos on Mars*. 2020. URL: https://www.dlr.de/en/latest/news/2020/04/20201119_chaos-on-mars (visited on Dec. 11, 2024).

[37] DRex Electronics. *Converting dBm to Watts: A Practical Guide*. 2024. URL: https://www.icdrex.com/converting-dbm-to-watts-a-practical-guide/ (visited on Aug. 10, 2025).

[38] T.C. Duxbury et al. *Mars Geodesy/Cartography Working Group recommendations on Mars cartographic constants and coordinate systems*. In: 4th Symposium on Geospatial Theory, Processing and Applications; Ottawa, Canada. [Conference paper]. July 2002.

[39] K.S. Edgett et al. "Geologic context of the Mars radar 'Stealth' region in southwestern Tharsis". In: *Journal of Geophysical Research* 102.9 (1997), pp. 21, 545–21, 567. DOI: 10.1029/97JE01685.

[40] B.L. Ehlmann and C.S. Edwards. "Mineralogy of the Martian Surface". In: *Annual Review of Earth and Planetary Sciences* 42 (2014), pp. 291–315. DOI: 10.1146/annurev-earth-060313-055024.

[41] European Space Agency. *Chaotic terrain in Iani Chaos*. 2006. URL: https://www.esa.int/Science_Exploration/Space_Science/Mars_Express/Chaotic_terrain_in_Iani_Chaos (visited on Dec. 11, 2024).

[42] European Space Agency. *Facts about Mars*. 2025. URL: https://www.esa.int/Science_Exploration/Space_Science/Mars_Express/Facts_about_Mars (visited on Aug. 12, 2025).

[43] European Space Agency. *Mars Express*. 2024. URL: https://www.esa.int/Science_Exploration/Space_Science/Mars_Express (visited on Dec. 19, 2024).

[44] European Space Agency. *SPICE-Enhanced Cosmographia Visualization Tool*. 2025. URL: https://www.cosmos.esa.int/web/spice/cosmographia (visited on Aug. 22, 2025).

[45] European Space Agency. *The Ages of Mars*. 2019. URL: https://sci.esa.int/web/mars-express/-/55481-the-ages-of-mars (visited on Nov. 22, 2024).

[46] European Space Agency. *The Red Planet*. 2024. URL: https://www.esa.int/Science_Exploration/Human_and_Robotic_Exploration/Exploration/The_Red_Planet (visited on Nov. 22, 2024).

[47] J.V. Evans. "Radar Studies of Planetary Surfaces". In: *Annual Reviews* 7 (1969), pp. 201–248. DOI: 10.1146/annurev.aa.07.090169.001221.

[48] M. Fan et al. "The Mars Orbiter Subsurface Investigation Radar (MOSIR) on China's Tianwen-1 Mission". In: *Space Science Reviews* 217.8 (2021). DOI: 10.1007/s11214-020-00786-4.

[49] W.C. Feldman et al. "Global Distribution of Neutrons from Mars: Results from Mars Odyssey". In: *Science* 297.5578 (2002), pp. 75–78. DOI: 10.1126/science.1073541.

[50] W.C. Feldman et al. "Mars Odyssey neutron data: 2. Search for buried excess water ice deposits at nonpolar latitudes on Mars". In: *Journal of Geophysical Research* 116.E11009 (2011). DOI: 10.1029/2011JE003806.

[51] Gems Sensors. *What is Dielectric Constant and How it Affects Radar*. 2025. URL: https://article.gemssensors.com/knowledge/dielectric-constant-and-how-it-affects-radar (visited on Aug. 11, 2025).

[52] Geospatial Analysis Online. *Gradient, slope and aspect*. 2025. URL: https://spatialanalysisonline.com/HTML/gradient__slope_and_aspect.htm (visited on Aug. 8, 2025).

[53] Geospatial Analysis Online. *Raster models*. 2025. URL: https://spatialanalysisonline.com/HTML/raster_models.htm (visited on Aug. 8, 2025).

[54] D. Golovin. "Personal communication". [Email: 'FREND water map']. Feb. 2025.

[55] D.V. Golovin et al. *Local Areas of High Water Content in the Central Part of Valles Marineris by FREND Neutron Telescope Data*. In: 55th Lunar and Planetary Science Conference; The Woodlands, Texas. [Conference abstract]. Mar. 2024.

[56] M.A. Gottlieb and R. Pfeiffer. *Dielectrics*. California Institute of Technology. 2013. URL: https://www.feynmanlectures.caltech.edu/II_10.html (visited on Aug. 7, 2025).

[57] H.M. Gunnarsdottir et al. "Root-mean-square surface slopes of Phoenix landing sites with 75-cm bistatic radar received by Mars Odyssey". In: *Journal of Geophysical Research* 113.E00A02 (2007). DOI: 10.1029/2007JE003040.

[58] T. Hagfors. "Backscatter from an undulating surface with applications to radar returns from the Moon". In: *Journal of Geophysical Research* 69.18 (1964), pp. 3779–3784. DOI: 10.1029/JZ069i018p03779.

[59] T. Hagfors. "Remote Probing of the Moon by Infrared and Microwave Emissions and by Radar". In: *Radio Science* 5.2 (1970), pp. 189–227. DOI: 10.1029/RS005i002p00189.

[60] S. Hamran et al. "Radar Imager for Mars' Subsurface Experiment—RIMFAX". In: *Space Science Reviews* 216.128 (2020). DOI: 10.1007/s11214-020-00740-4.

[61] K.P. Harrison and M.G. Chapman. "Evidence for ponding and catastrophic floods in central Valles Marineris, Mars". In: *Icarus* 198 (2008), pp. 351–364. DOI: 10.1016/j.icarus.2008.08.003.

[62] K. Harshman. "Personal communication". [Email: 'RE: GRS H2O concentration data for MSc thesis - Global coverage?'] Aug. 2025.

[63] W.K. Hartmann and O. Raper. *The new Mars: The discoveries of Mariner 9*. Special Publication. Washington, D.C.: National Aeronautics and Space Administration, Jan. 1974. URL: https://ntrs.nasa.gov/citations/19750005657.

[64] J.W. Head and D.K. Weiss. "Preservation of ancient ice at Pavonis and Arsia Mons: Tropical mountain glacier deposits on Mars". In: *Planetary and Space Science* 103 (2014), pp. 331–338. DOI: 10.1016/j.pss.2014.09.004.

[65] J.W. Head and L. Wilson. *The Noachian-Hesperian Transition on Mars: Geological Evidence for a Punctuated Phase of Global Volcanism as a Key Driver in Climate and Atmospheric Evolution*. In: 42nd Lunar and Planetary Science Conference; The Woodlands, Texas. [Conference paper]. Mar. 2011.

[66] Y. Hervé et al. "The WISDOM radar on board the ExoMars 2022 Rover: Characterization and calibration of the flight model". In: *Planetary and Space Science* 189.104939 (2020). DOI: 10.1016/j.pss.2020.104939.

[67] B.M. Jakosky. "Atmospheric Loss to Space and the History of Water on Mars". In: *Annual Review of Earth and Planetary Sciences* 49 (2021), pp. 71–93. DOI: 10.1146/annurev-earth-062420-052845.

[68] N. James and S. Phillipo. *IFMS Open Loop Processor Tool - User manual WO 12*. GSY/140070/116848. Issue 1.2. Essex, United Kingdom: BAE Systems, Aug. 2014.

[69] Jet Propulsion Laboratory. *MOLA Global Map of Surface Gradients on Mars*. California Institute of Technology. 2000. URL: https://www.jpl.nasa.gov/images/pia02809-mola-global-map-of-surface-gradients-on-mars/ (visited on Sept. 11, 2025).

[70] Jet Propulsion Laboratory. *NASA Phoenix Mars Lander Confirms Frozen Water*. 2008. URL: https://www.jpl.nasa.gov/news/nasa-phoenix-mars-lander-confirms-frozen-water/ (visited on Dec. 19, 2024).

[71] C. Jiang et al. "Water Ice and Possible Habitability in the Landing Area of Tianwen-1 Mission". In: *Space Science Reviews* 220.35 (2024). DOI: 10.1007/s11214-024-01068-z.

[72] J.T. Johnson, K.F. Warnick, and P. Xu. "On the Geometrical Optics (Hagfors' Law) and Physical Optics Approximations for Scattering From Exponentially Correlated Surfaces". In: *IEEE Transactions on Geoscience and Remote Sensing* 45.8 (2007), pp. 2619–2629. DOI: 10.1109/TGRS.2007.900682.

[73] R. Jordan et al. "The Mars express MARSIS sounder instrument". In: *Planetary and Space Science* 57 (2009), pp. 1975–1986. DOI: 10.1016/j.pss.2009.09.016.

[74] H.U. Keller et al. "Phoenix Robotic Arm Camera". In: *Journal of Geophysical Research* 113.E00A17 (2008). DOI: 10.1029/2007JE003044.

[75] E.S. Kite et al. "Persistent or repeated surface habitability on Mars during the late Hesperian - Amazonian". In: *Geophysical Research Letters* 44 (2017). DOI: 10.1002/2017GL072660.

[76] Michelle Koutnik et al. "Ices in the Solar System: A Volatile-Driven Journey from the Inner Solar System to its Far Reaches". In: ed. by R.J. Soare et al. Elsevier Inc., 2024. Chap. 4: Glacial deposits, remnants, and landscapes on Amazonian Mars: Using setting, structure, and stratigraphy to understand ice evolution and climate history, pp. 101–142. DOI: 10.1016/C2021-0-01783-1.

[77] M. Lavagna et al. *International Mars Ice Mapper Mission - Reconnaissance/Science Measurement Definition Team Final Report*. Aug. 2022. URL: https://smd-cms.nasa.gov/wp-content/uploads/2023/04/I_MIM_MDT_Final_Report_24_Aug_2022_exec_sum2.pdf.

[78] C. Li et al. "Layered subsurface in Utopia Basin of Mars revealed by Zhurong rover radar". In: *Nature* 610 (2022), pp. 308–323. DOI: 10.1038/s41586-022-05147-5.

[79] S. Liu et al. "Data Pre-Processing and Signal Analysis of Tianwen-1 Rover Penetrating Radar". In: *Remote Sensing* 15.966 (2023). DOI: 10.3390/rs15040966.

[80] Y. Ma et al. "SHARAD observations for layered ejecta deposits formed by late-Amazonian-aged impact craters at low latitudes of Mars". In: *Icarus* 404.115689 (2023). DOI: 10.1016/j.icarus.2023.115689.

[81] A. Malakhov et al. *Water content in the upper 1 meter of the Martian regolith, estimated from FREND experiment data*. In: Zenodo. [Dataset WEHMaps.txt Version 1]. 2022. DOI: 10.5281/zenodo.6282971.

[82] A.V. Malakhov et al. *Areas with Enhanced Water Content Observed in Equatorial Areas of Mars Through TGO's FREND Neutron Telescope*. In: 52nd Lunar and Planetary Science Conference; Virtual. [Conference abstract]. Mar. 2021.

[83] A.V. Malakhov et al. *Global Water Distribution Maps in the Upper Martian Subsurface by FREND Neutron Telescope Onboard ExoMars TGO*. In: 53rd Lunar and Planetary Science Conference; The Woodlands, Texas. [Conference abstract]. Mar. 2022.

[84] A.V. Malakhov et al. "High Resolution Map of Water in the Martian Regolith Observed by FREND Neutron Telescope Onboard ExoMars TGO". In: *Journal of Geophysical Research* 127.e2022JE007258 (2022). DOI: 10.1029/2022JE007258.

[85] A.V. Malakhov et al. *High Water Content Areas Identified In Equatorial Band of Mars by FREND Neutron Telescope Onboard ExoMars TGO*. In: 2021 General Assembly of the European Geosciences Union; Virtual. [Conference abstract]. Apr. 2021. DOI: doi.org/10.5194/egusphere-egu21-8797.

[86] A.V. Malakhov et al. "Ice Permafrost "Oases" Close to Martian Equator: Planet Neutron Mapping Based on Data of FREND Instrument Onboard TGO Orbiter of Russian-European ExoMars Mission". In: *Astronomy Letters* 46.6 (2020), pp. 407–421. DOI: 10.1134/S1063773720060079.

[87] A.V. Malakhov et al. *Regional Water Variations on Mars: New Data from TGO's FREND*. In: 51st Lunar and Planetary Science Conference; The Woodlands, Texas. [Conference abstract]. Mar. 2020.

[88] M. Manga. "Martian floods at Cerberus Fossae can be produced by groundwater discharge". In: *Geophysical Research Letters* 31 (2004). DOI: 10.1029/2003GL018958.

[89] V.A. Markel. "Introduction to the Maxwell Garnett approximation: tutorial". In: *Journal of the Optical Society of America* 33.7 (2016), pp. 1244–1256. DOI: 10.1364/JOSAA.33.001244.

[90] A. Martin. *Misión Mars Odyssey*. In: Máster en Ciencia y Tecnología desde el Espacio; Universidad de Alcalá, Spain. [Research proposal]. Jan. 2022. DOI: 10.13140/RG.2.2.15000.32005.

[91] P. Masson. *The History of Mars Exploration*. In: 1st Mars Express Science Conference; Noordwijk, The Netherlands. [Conference presentation]. Feb. 2005.

[92] M.T. Mellon et al. "Ground ice at the Phoenix Landing Site: Stability state and origin". In: *Journal of Geophysical Research* 114.E00E07 (2009). DOI: 10.1029/2009JE003417.

[93] I. Mitrofanov. *Hydrogen/Water on the Moon*. In: 2009 Annual Meeting of the Lunar Exploration Analysis Group; Houston, Texas. [Conference presentation]. Nov. 2009.

[94] I. Mitrofanov et al. "Fine Resolution Epithermal Neutron Detector (FREND) Onboard the ExoMars Trace Gas Orbiter". In: *Space Science Reviews* 214.86 (2018). DOI: 10.1007/s11214-018-0522-5.

[95] I. Mitrofanov et al. "Maps of Subsurface Hydrogen from the High Energy Neutron Detector, Mars Odyssey". In: *Science* 297.5578 (2002), pp. 78–81. DOI: 10.1126/science.1073616.

[96] I. Mitrofanov et al. "The evidence for unusually high hydrogen abundances in the central part of Valles Marineris on Mars". In: *Icarus* 374 (2022), p. 114805. DOI: 10.1016/j.icarus.2021.114805.

[97] M.I. Mokrousov et al. "Promising Neutron Detector with Anticoincidence Protection". In: *Physics of Particles and Nuclei Letters* 16.2 (2019), pp. 93–99. DOI: 10.1134/S1547477119020080.

[98] B.C. Murray and M.E. Davies. "A Comparison of U.S. and Soviet Efforts to Explore Mars". In: *Science* 151.3713 (1966), pp. 945–954. DOI: 10.1126/science.151.3713.94.

[99] T.A. Mutch and J.W. Head. "The Geology of Mars: A Brief Review of Some Recent Results". In: *Reviews of Geophysics and Space Physics* 13.3 (1975). DOI: 10.1029/RG013i003p00411.

[100] National Aeronautics and Space Administration. *ExoMars Program*. 2024. URL: https://science.nasa.gov/mission/tgo/ (visited on Dec. 19, 2024).

[101] National Aeronautics and Space Administration. *Mars Odyssey*. 2024. URL: https://science.nasa.gov/mission/odyssey/ (visited on Dec. 20, 2024).

[102] National Aeronautics and Space Administration. *Mars Odyssey Science Instruments*. 2024. URL: https://science.nasa.gov/mission/odyssey/science-instruments/ (visited on Dec. 23, 2024).

[103] National Aeronautics and Space Administration. *Mars Reconnaissance Orbiter - Science Instruments*. 2025. URL: https://science.nasa.gov/mission/mars-reconnaissance-orbiter/science-instruments/ (visited on Aug. 11, 2025).

[104] National Aeronautics and Space Administration. *PIA12217: Underground Ice on Mars Exposed by Impact Cratering*. 2009. URL: https://www.jpl.nasa.gov/images/pia12217-underground-ice-on-mars-exposed-by-impact-cratering/ (visited on Dec. 19, 2024).

[105] G. Neumann. *The Whole MOLA Catalog*. From Goddard Space Flight Center - Planetary Geology, Geophysics and Geochemistry Laboratory. 2025. URL: https://pgda.gsfc.nasa.gov/products/62 (visited on Aug. 11, 2025).

[106] G.A. Neumann et al. "Mars Orbiter Laser Altimeter pulse width measurements and footprint-scale roughness". In: *Geophysical Research Letters* 30.11 (2003), pp. 1561–1564. DOI: 10.1029/2003GL017048.

[107] B. Novakovic. "Senenmut: An Ancient Egyptian Astronomer". In: *Publication of Astronomical Observatory of Belgrade* (2008). DOI: 10.48550/arXiv.0801.1331.

[108] R. Orosei et al. "Mars Advanced Radar for Subsurface and Ionospheric Sounding (MARSIS) after nine years of operation: A summary". In: *Planetary and Space Science* 112 (2015), pp. 98–114. DOI: 10.1016/j.pss.2014.07.010.

[109] R. Orosei et al. "Radar sounding of Lucus Planum, Mars, by MARSIS". In: *Journal of Geophysical Research* 122 (2017), pp. 1405–1418. DOI: 10.1002/2016JE005232.

[110] R. Orosei et al. "The Global Search for Liquid Water on Mars from Orbit: Current and Future Perspectives". In: *Life* 10.120 (2020). DOI: 10.3390/life10080120.

[111] J. Parrott et al. "First Results of Mars Express - ExoMars Trace Gas Orbiter Mutual Radio Occultation". In: *ESS Open Archive* (2023). DOI: `10.22541/essoar.169603561.10488051/v1`.

[112] J. Parrott et al. "Ionospheric Analysis with Martian Mutual Radio Occultation". In: *Journal of Geophysical Research* 130.6 (2025). DOI: `10.1029/2024JE008854`.

[113] M. Pätzold et al. "Mars Express 10 years at Mars: Observations by the Mars Express Radio Science Experiment (MaRS)". In: *Planetary and Space Science* 127 (2016), pp. 44–90. DOI: `10.1016/j.pss.2016.02.013`.

[114] M. Pätzold et al. "MaRS: Mars Express Radio Science Experiment". In: *European Space Agency* (2006). Retrieved from `https://sci.esa.int/documents/33745/35957/1567258041276-MaRS.pdf`.

[115] PDS Geosciences Node. *Mars Global Surveyor: MOLA*. Washington University in St. Louis. 2025. URL: `https://pds-geosciences.wustl.edu/missions/mgs/mola.html` (visited on Aug. 8, 2025).

[116] PDS Geosciences Node. *Mars Global Surveyor: MOLA MEGDRs*. Washington University in St. Louis. 2025. URL: `https://pds-geosciences.wustl.edu/missions/odyssey/grs_elements.html` (visited on Aug. 9, 2025).

[117] W.T. Peters. "The Appearance of Venus and Mars in 1610". In: *Journal for the History of Astronomy* 15.3 (1984). DOI: `10.1177/002182868401500306`.

[118] Pierian Training. *Python Smoothing Data: A Comprehensive Guide*. 2023. URL: `https://pieriantraining.com/python-smoothing-data-a-comprehensive-guide/` (visited on Aug. 12, 2025).

[119] D. Polder and J.H. van Santen. "The Effective Permeability of Mixtures of Solids". In: *Physica* 12.5 (1946), pp. 257–271. DOI: `10.1016/S0031-8914(46)80066-1`.

[120] I. Poole. *What is Noise Floor for radio receivers*. From 'Electronics Notes'. 2025. URL: `https://www.electronics-notes.com/articles/radio/radio-receiver-sensitivity/what-is-noise-floor.php` (visited on Aug. 10, 2025).

[121] N.E. Putzig et al. "Science results from sixteen years of MRO SHARAD operations". In: *Icarus* 419.115715 (2024). DOI: `10.1016/j.icarus.2023.115715`.

[122] N.E. Putzig et al. "SHARAD soundings and surface roughness at past, present, and proposed landing sites on Mars: Reflections at Phoenix may be attributable to deep ground ice". In: *Journal of Geophysical Research* 119 (2014), pp. 1936–1949. DOI: `10.1002/2014JE004646`.

[123] J.F. Quack. "The Planets in Ancient Egypt". In: *Oxford Research Encyclopedia of Planetary Science* (2019). DOI: `10.1093/acrefore/9780190647926.013.61`.

[124] A. Ram. *Elliptic Functions sn, cn, dn, as Trigonometry*. University of Melbourne, Australia. 2014. URL: `http://math.soimeme.org/~arunram/Resources/EllipticFunctionsAsTrigonometry.html` (visited on Aug. 9, 2025).

[125] L. Riu, J. Carter, and F. Poulet. "The M3 project: 3 – Global abundance distribution of hydrated silicates at Mars". In: *Icarus* 374 (2022), p. 114809. DOI: `10.1016/j.icarus.2021.114809`.

[126] C. Sagan and J. Lederberg. "The Prospects for Life on Mars: A Pre-Viking Assessment". In: *Icarus* 28 (1976), pp. 291–300. DOI: `10.1016/0019-1035(76)90039-7`.

[127] R.S. Saunders et al. "2001 Mars Odyssey Mission Summary". In: *Space Science Reviews* 110 (2004), pp. 1–36. DOI: `10.1023/B:SPAC.0000021006.84299.18`.

[128] M. Scherf and H. Lammer. "Did Mars Possess a Dense Atmosphere During the First 400 Million Years?" In: *Space Science Reviews* 217.2 (2021). DOI: `10.1007/s11214-020-00779-3`.

[129] D. Scholl et al. *Bistatic Radar Observations in 2022 with Mars Express*. In: 17th Europlanet Science Congress; Berlin, Germany. [Conference abstract]. Sept. 2024. DOI: `10.5194/epsc2024-487`.

[130] R. Seu et al. "SHARAD sounding radar on the Mars Reconnaissance Orbiter". In: *Journal of Geophysical Research* 112.E05S05 (2007). DOI: `10.1029/2006JE002745`.

[131] A. Shaw et al. "Phoenix soil physical properties investigation". In: *Journal of Geophysical Research* 114.E00E05 (2009). DOI: `10.1029/2009JE003455`.

[132] E.S. Shoemaker et al. "New Insights Into Subsurface Stratigraphy Northwest of Ascraeus Mons, Mars, Using the SHARAD and MARSIS Radar Sounders". In: *Journal of Geophysical Research* 127 (2022). DOI: `10.1029/2022JE007210`.

[133] R.A. Simpson et al. "Determination of local surface properties using Mars Express bistatic radar". In: *Journal of Geophysical Research* 111.6 (2006). DOI: `10.1029/2005JE002580`.

[134] R.A. Simpson et al. "Polarization in Bistatic Radar Probing of Planetary Surfaces: Application to Mars Express Data". In: *Proceedings of the IEEE* 99.5 (2011), pp. 858–874. DOI: `10.1109/JPROC.2011.2106190`.

[135] R.A. Simpson et al. "Viking Bistatic Radar Observations of the Hellas Basin on Mars: Preliminary Results". In: *Science* 203.4375 (1979), pp. 45–46. DOI: `10.1126/science.203.4375.45`.

[136] D.E. Smith et al. *Mars Global Surveyor Laser Altimeter Mission Experiment Gridded Data Record*. In: NASA Planetary Data System. [Dataset MGS-M-MOLA-5-MEGDR-L3-V1.0]. 2003. DOI: `10.17189/1519460`.

[137] D.E. Smith et al. "Mars Orbiter Laser Altimeter: Experiment summary after the first year of global mapping of Mars". In: *Journal of Geophysical Research* 106.E10 (2001), pp. 23689–23722. DOI: `10.1029/2000JE001364`.

[138] Space Research Institute of the Russian Academy of Sciences. *HEND*. 2023. URL: `https://iki.cosmos.ru/en/research/missions/hend` (visited on Dec. 23, 2024).

[139] D. Stanton, R. Bavin, and M. Cassidy. *MelaCom UHF Transponder for Mars Express - User Manual*. MEX-DER-TN-205. Farnborough, United Kingdom: QinetiQ ltd, Jan. 2002.

[140] C.M. Stuurman et al. "SHARAD detection and characterization of subsurface water ice deposits in Utopia Planitia, Mars". In: *Geophysical Research Letters* 43 (2016), pp. 9484–9491. DOI: 10.1002/2016GL070138.

[141] A.K. Sultan-Salem and G.L. Tyler. "Hagfors' law revisited". In: *Journal of Geophysical Research* 111.E06S07 (2006). DOI: 10.1029/2005JE002489.

[142] J. Sun et al. "Exploring the dielectric loss of Martian regolith in the frequency domain using Zhurong radar data". In: *Icarus* 425.116315 (2025). DOI: 10.1016/j.icarus.2024.116315.

[143] L.H. Svedhem. "Applying GNSS-R techniques to improve the analysis of Bi-Static radar measurements between Mars Express and ExoMars TGO in order to search for sub-surface water". [Project Description: 'Master project in Aerospace Engineering (2025-1)']. May 2025.

[144] L.H. Svedhem. "Personal communication". [Supervisor Meeting #1]. Nov. 2024.

[145] L.H. Svedhem. "Personal communication". [Supervisor Meeting #3]. Dec. 2024.

[146] L.H. Svedhem. "Personal communication". [Supervisor Meeting #8]. Apr. 2025.

[147] L.H. Svedhem. "Personal communication". [Supervisor Meeting #13]. June 2025.

[148] L.H. Svedhem. "Personal communication". [Email: 'Emailing: IQ_AGC_bit_description.docx']. July 2025.

[149] L.H. Svedhem. "Personal communication". [Supervisor Meeting #18]. July 2025.

[150] L.H. Svedhem. "Personal communication". [Supervisor Meeting #20]. July 2025.

[151] L.H. Svedhem. "Personal communication". [Supervisor Meeting #23]. Sept. 2025.

[152] L.H. Svedhem et al. *Probing shallow subsurface water on Mars at UHF wavelengths*. In: 56th Annual Division for Planetary Sciences meeting; Boise, Idaho. [Conference abstract]. Oct. 2024.

[153] L.H. Svedhem et al. *Probing shallow subsurface water on Mars at UHF wavelengths*. In: 56th Annual Division for Planetary Sciences meeting; Boise, Idaho. [Conference presentation]. Oct. 2024.

[154] K.L. Tanaka et al. "Geologic map of Mars". In: *Geological Survey Scientific Investigations* Map 3292 (2014). Pamphlet prepared for the National Aeronautics and Space; Scale 1:20.000.000. DOI: 10.3133/sim3292.

[155] K.L. Tanaka et al. "Resurfacing history of the northern plains of Mars based on geologic mapping of Mars Global Surveyor data". In: *Journal of Geophysical Research* 108.4 (2003), p. 8043. DOI: 10.1029/2002JE001908.

[156] Thales Alenia Space. *ExoMars User Manual*. EXM-MS-MAN-AI-0005. 2015.

[157] H. Tian et al. "Zhurong: Features and mission of China's first Mars rover". In: *The Innovation* 2.3 (2021). DOI: 10.1016/j.xinn.2021.100121.

[158] University of Cambridge. *The dielectric constant*. Dissemination of IT for the Promotion of Materials Science (DoITPoMS). 2025. URL: https://www.doitpoms.ac.uk/tlplib/dielectrics/dielectric_constant.php (visited on Aug. 7, 2025).

[159] University of Cambridge. *Variation of the dielectric constant in alternating fields*. Dissemination of IT for the Promotion of Materials Science (DoITPoMS). 2025. URL: https://www.doitpoms.ac.uk/tlplib/dielectrics/variation.php (visited on Aug. 12, 2025).

[160] J. Uri. *45 Years Ago: Viking 1 and 2 off to Mars*. National Aeronautics and Space Administration. 2020. URL: https://www.nasa.gov/history/45-years-ago-viking-1-and-2-off-to-mars/ (visited on Dec. 17, 2024).

[161] J. Uri. *50 Years Ago: Mariner 6 and 7 Explore Mars*. National Aeronautics and Space Administration. 2019. URL: https://www.nasa.gov/history/50-years-ago-mariner-6-and-7-explore-mars/ (visited on July 16, 2025).

[162] J. Uri. *50 Years Ago: Mariner 9 Enters Mars Orbit*. National Aeronautics and Space Administration. 2021. URL: https://www.nasa.gov/history/50-years-ago-mariner-9-enters-mars-orbit/ (visited on Nov. 25, 2024).

[163] T. Usui et al. *An Overview of the International Mars Ice Mapper Mission*. In: 86th Annual Meeting of the Meteoritical Society; Brussels, Belgium. [Conference paper]. Aug. 2023.

[164] M.A. Viotti et al. *The International Mars Ice Mapper (I-IM) Mission: A Concept Advancing Climatology, Geology, Habitability, and Science for Human Exploration*. In: 8th International Conference on Mars Polar Science and Exploration; Yukon, Canada. [Conference paper]. July 2024.

[165] T.G. Wasilewski. "Evaluation of drilling-based water extraction methods for Martian ISRU from mid-latitude ice resources". In: *Planetary and Space Science* 158 (2018), pp. 16–24. DOI: 10.1016/j.pss.2018.05.012.

[166] T.R. Watters et al. "Evidence of Ice-Rich Layered Deposits in the Medusae Fossae Formation of Mars". In: *Geophysical Research Letters* 51 (2024). DOI: 10.1029/2023GL105490.

[167] T.R. Watters et al. "Radar sounder evidence of thick, porous sediments in Meridiani Planum and implications for ice-filled deposits on Mars". In: *Geophysical Research Letters* 44 (2017), pp. 9208–9215. DOI: 10.1002/2017GL074431.

[168] E.W. Weisstein. *Elliptic Integral*. From MathWorld - A Wolfram Resource. 2025. URL: https://mathworld.wolfram.com/EllipticIntegral.html (visited on Aug. 9, 2025).

[169] E.W. Weisstein. *Elliptic Integral of the Second Kind*. From MathWorld - A Wolfram Resource. 2025. URL: https://mathworld.wolfram.com/EllipticIntegraloftheSecondKind.html (visited on Aug. 9, 2025).

[170] E.W. Weisstein. *Oblate Spheroid*. From MathWorld - A Wolfram Resource. 2025. URL: https://mathworld.wolfram.com/OblateSpheroid.html (visited on Aug. 10, 2025).

[171] D.R. Williams. *2001 Mars Odyssey*. NASA Space Science Data Coordinated Archive. 2022. URL: https://nssdc.gsfc.nasa.gov/nmc/spacecraft/display.action?id=2001-013A (visited on Dec. 19, 2024).

[172] D.R. Williams. *Chronology of Mars Exploration*. NASA Space Science Data Coordinated Archive. 2024. URL: https://nssdc.gsfc.nasa.gov/planetary/chronology_mars.html (visited on Dec. 18, 2024).

[173] D.R. Williams. *ExoMars 2016*. NASA Space Science Data Coordinated Archive. 2022. URL: https://nssdc.gsfc.nasa.gov/nmc/spacecraft/display.action?id=2016-017A (visited on Dec. 19, 2024).

[174] D.R. Williams. *ExoMars Rover*. NASA Space Science Data Coordinated Archive. 2022. URL: https://nssdc.gsfc.nasa.gov/nmc/spacecraft/display.action?id=EXOMARS22 (visited on Dec. 19, 2024).

[175] D.R. Williams. *Mariner 9*. NASA Space Science Data Coordinated Archive. 2022. URL: https://nssdc.gsfc.nasa.gov/nmc/spacecraft/display.action?id=1971-051A (visited on Dec. 19, 2024).

[176] D.R. Williams. *Mars 2020*. NASA Space Science Data Coordinated Archive. 2022. URL: https://nssdc.gsfc.nasa.gov/nmc/spacecraft/display.action?id=2020-052A (visited on Dec. 19, 2024).

[177] D.R. Williams. *Mars Express*. NASA Space Science Data Coordinated Archive. 2022. URL: https://nssdc.gsfc.nasa.gov/nmc/spacecraft/display.action?id=2003-022A (visited on Dec. 19, 2024).

[178] D.R. Williams. *Mars Pathfinder Project Information*. NASA Space Science Data Coordinated Archive. 2022. URL: https://nssdc.gsfc.nasa.gov/planetary/mesur.html (visited on Dec. 19, 2024).

[179] D.R. Williams. *Mars Reconnaissance Orbiter*. NASA Space Science Data Coordinated Archive. 2022. URL: https://nssdc.gsfc.nasa.gov/nmc/spacecraft/display.action?id=2005-029A (visited on Dec. 19, 2024).

[180] D.R. Williams. *Mars Science Laboratory (MSL)*. NASA Space Science Data Coordinated Archive. 2022. URL: https://nssdc.gsfc.nasa.gov/nmc/spacecraft/display.action?id=2011-070A (visited on Dec. 19, 2024).

[181] D.R. Williams. *Phoenix Mars Lander*. NASA Space Science Data Coordinated Archive. 2022. URL: https://nssdc.gsfc.nasa.gov/nmc/spacecraft/display.action?id=2007-034A (visited on Dec. 19, 2024).

[182] D.R. Williams. *Tianwen 1*. NASA Space Science Data Coordinated Archive. 2022. URL: https://nssdc.gsfc.nasa.gov/nmc/spacecraft/display.action?id=2020-049A (visited on Dec. 19, 2024).

[183] D.R. Williams. *Viking Mission to Mars*. NASA Space Science Data Coordinated Archive. 2018. URL: https://nssdc.gsfc.nasa.gov/planetary/viking.html (visited on Dec. 19, 2024).

[184] S. Xiong et al. "Subsurface Reflectors Detected by SHARAD Reveal Stratigraphy and Buried Channels Over Central Elysium Planitia, Mars". In: *Earth and Space Science* 8 (2021). DOI: 10.1029/2019EA000968.

[185] Z. Yongliao et al. "Scientific objectives and payloads of Tianwen-1, China's first Mars exploration mission". In: *Advances in Space Research* 67 (2021), pp. 812–823. DOI: 10.1016/j.asr.2020.11.005.

[186] L. Zhang et al. "The Dielectric Properties of Martian Regolith at the Tianwen-1 Landing Site". In: *Geophysical Research Letters* 50.E2022GL102207 (2023). DOI: 10.1029/2022GL102207.

[187] Z. Zhang et al. *Analysis of the Martian subsurface from the observation of the Rover Subsurface Penetrating Radar (RoSPR) onboard Tianwen-1*. In: 17th Europlanet Science Congress; Berlin, Germany. [Conference abstract]. Sept. 2024. DOI: 10.5194/epsc2024-441.

[188] N. Zheng et al. "Water Ice Resources on the Shallow Subsurface of Mars: Indications to Rover-Mounted Radar Observation". In: *Remote Sensing* 16.824 (2024). DOI: 10.3390/rs16050824.

A

SPICE Kernels

This appendix presents the complete list of kernels used for the MEX-TGO BSR measurement planning, processing and modelling, retrieved from the Navigation and Ancillary Information Facility's *SPICE Data Archive* [1]. Sections A.1, A.2 and A.3 list those contained in 'gen_mk.mk' (general Solar system, time and Mars-related kernels), 'MEX_mk.mk' (MEX-specific kernels) and 'TGO_mk.mk' (TGO-specific kernels) respectively.

For future use of the MEX-TGO BSR models, this list of kernels should be expanded to ensure correct results. This entails loading the additional MEX and TGO spacecraft trajectory kernels as published for data analysis, and possible update(s) of the long-term planning kernels in operational Mars-centric ephemeris.

A.1. gen_mk.mk

The 'gen_mk.mk' meta-kernel calls general Solar System, Time and Mars-related kernels which are independent of any specific mission. These are retrieved from the 'Generic Kernels' archive of the NAIF server [2] and include:

- **LSK:**
  - Generic Leapseconds Kernel:
    * *naif0012.tls.pc*
- **PCK:**
  - Standard gravitational parameter μ (gravitational constant G times mass M) values for the Sun, planets and planetary system barycenters:
    * *de-403-masses.tpc*
  - Generic Planetary Constants Kernel:
    * *pck00011.tpc*
- **SPK:**
  - Mars Satellite Ephemeris, required for determination of the location of Mars' Center of Mass (499), which differs by approximately 20 cm from Mars' Barycenter (4). Kernel covers dates from the 4th of January 1900 up to the 3rd of January 2100:
    * *mar097.bsp*
  - Current official planetary ephemeris for the Solar system. Kernel covers dates from the 1st of January 1550 up to the 22nd of January 2650:
    * *de430.bsp*

A.2. MEX_mk.mk

The 'MEX_mk.mk' meta-kernel calls MEX-specific kernels. These are retrieved from the 'Mars Express' archive for operational flight projects of the NAIF server [3] and include:

- **FK:**
  - Frames kernel for the Mars Express spacecraft and Beagle-2 Lander, version 1.6:
    * *MEX_V16.TF*

- **SPK:**

  - Mars Express spacecraft trajectory kernels of type T19, used for long-term planning in operational Mars-centric ephemeris:

    * *ORMF_T19_240614_320101_01863.BSP*

  - Mars Express spacecraft trajectory kernels of type T19, used for data analysis (contains predicted and reconstructed ephemeris after orbit insertion):

    * *ORMM_T19_240101000000_01847.BSP*
    * *ORMM_T19_240201000000_01852.BSP*
    * *ORMM_T19_240301000000_01856.BSP*
    * *ORMM_T19_240401000000_01858.BSP*
    * *ORMM_T19_240501000000_01862.BSP*
    * *ORMM_T19_240601000000_01865.BSP*
    * *ORMM_T19_240701000000_01871.BSP*
    * *ORMM_T19_240801000000_01875.BSP*
    * *ORMM_T19_240901000000_01879.BSP*
    * *ORMM_T19_241001000000_01883.BSP*
    * *ORMM_T19_241101000000_01887.BSP*
    * *ORMM_T19_241201000000_01891.BSP*
    * *ORMM_T19_250101000000_01895.BSP*
    * *ORMM_T19_250201000000_01899.BSP*
    * *ORMM_T19_250301000000_01903.BSP*
    * *ORMM_T19_250401000000_01907.BSP*
    * *ORMM_T19_250501000000_01912.BSP*
    * *ORMM_T19_250601000000_01916.BSP*
    * *ORMM_T19_250701000000_01916.BSP*

A.3. TGO_mk.mk

The 'TGO_mk.mk' meta-kernel calls TGO-specific kernels. These are retrieved from the 'ExoMars 2016' archive for operational flight projects of the NAIF server[4] and include:

- **FK:**

  - Frames kernel for the ExoMars Trace Gas Orbiter spacecraft, version 2.7:

    * *em16_tgo_v27.tf*

- **SPK:**

  - ExoMars Trace Gas Orbiter spacecraft trajectory kernels, used for long-term planning in operational Mars-centric ephemeris (only contains predicted data for the science phase):

    * *em16_tgo_flp_010_01_20220804_20310104_v01.bsp*

  - ExoMars Trace Gas Orbiter spacecraft trajectory kernels, used for data analysis (contains predicted and reconstructed ephemeris for the science phase):

    * *em16_tgo_fsp_332_01_20240101_20240615_v01.bsp*
    * *em16_tgo_fsp_333_01_20240109_20240622_v01.bsp*
    * *em16_tgo_fsp_334_01_20240113_20240706_v01.bsp*
    * *em16_tgo_fsp_335_01_20240113_20240706_v01.bsp*
    * *em16_tgo_fsp_336_01_20240129_20240713_v01.bsp*
    * *em16_tgo_fsp_337_01_20240205_20240720_v01.bsp*
    * *em16_tgo_fsp_338_01_20240212_20240727_v01.bsp*
    * *em16_tgo_fsp_339_01_20240220_20240803_v01.bsp*
    * *em16_tgo_fsp_340_01_20240226_20240810_v01.bsp*
    * *em16_tgo_fsp_341_01_20240304_20240817_v01.bsp*
    * *em16_tgo_fsp_342_01_20240312_20240824_v01.bsp*
    * *em16_tgo_fsp_343_01_20240319_20240831_v01.bsp*
    * *em16_tgo_fsp_344_01_20240325_20240907_v01.bsp*

---

[4] https://naif.jpl.nasa.gov/pub/naif/EXOMARS2016/kernels/

* *em16_tgo_fsp_345_01_20240402_20240914_v01.bsp*
* *em16_tgo_fsp_346_01_20240408_20240921_v01.bsp*
* *em16_tgo_fsp_347_01_20240416_20240928_v01.bsp*
* *em16_tgo_fsp_348_01_20240422_20241005_v01.bsp*
* *em16_tgo_fsp_349_01_20240429_20241012_v01.bsp*
* *em16_tgo_fsp_350_01_20240506_20241019_v01.bsp*
* *em16_tgo_fsp_351_01_20240515_20241026_v01.bsp*
* *em16_tgo_fsp_352_01_20240520_20241102_v01.bsp*
* *em16_tgo_fsp_353_01_20240528_20241109_v01.bsp*
* *em16_tgo_fsp_354_01_20240603_20241116_v01.bsp*
* *em16_tgo_fsp_355_01_20240610_20241123_v01.bsp*
* *em16_tgo_fsp_356_01_20240617_20241130_v01.bsp*
* *em16_tgo_fsp_357_01_20240624_20241207_v01.bsp*
* *em16_tgo_fsp_358_01_20240703_20241214_v01.bsp*
* *em16_tgo_fsp_359_01_20240708_20241221_v01.bsp*
* *em16_tgo_fsp_360_01_20240715_20241228_v01.bsp*
* *em16_tgo_fsp_361_01_20240722_20250104_v01.bsp*
* *em16_tgo_fsp_362_01_20240729_20250111_v01.bsp*
* *em16_tgo_fsp_363_01_20240806_20250201_v01.bsp*
* *em16_tgo_fsp_364_01_20240806_20250201_v01.bsp*
* *em16_tgo_fsp_365_01_20240813_20250201_v01.bsp*
* *em16_tgo_fsp_366_01_20240813_20250201_v01.bsp*
* *em16_tgo_fsp_367_01_20240903_20250215_v01.bsp*
* *em16_tgo_fsp_368_01_20240909_20250222_v01.bsp*
* *em16_tgo_fsp_369_01_20240916_20250301_v01.bsp*
* *em16_tgo_fsp_370_01_20240923_20250308_v01.bsp*
* *em16_tgo_fsp_371_01_20240930_20250315_v01.bsp*
* *em16_tgo_fsp_372_01_20241008_20250322_v01.bsp*
* *em16_tgo_fsp_373_01_20241014_20250329_v01.bsp*
* *em16_tgo_fsp_374_01_20241021_20250405_v01.bsp*
* *em16_tgo_fsp_375_01_20241028_20250412_v01.bsp*
* *em16_tgo_fsp_376_01_20241104_20250419_v01.bsp*
* *em16_tgo_fsp_377_01_20241111_20250426_v01.bsp*
* *em16_tgo_fsp_378_01_20241118_20250503_v01.bsp*
* *em16_tgo_fsp_379_01_20241125_20250510_v01.bsp*
* *em16_tgo_fsp_380_01_20241202_20250517_v01.bsp*
* *em16_tgo_fsp_381_01_20241209_20250524_v01.bsp*
* *em16_tgo_fsp_382_01_20241209_20250524_v01.bsp*
* *em16_tgo_fsp_383_01_20241217_20250621_v01.bsp*
* *em16_tgo_fsp_384_01_20241230_20250621_v01.bsp*
* *em16_tgo_fsp_385_01_20250106_20250621_v01.bsp*
* *em16_tgo_fsp_386_01_20250113_20250628_v01.bsp*
* *em16_tgo_fsp_387_01_20250120_20250705_v01.bsp*
* *em16_tgo_fsp_388_01_20250127_20250712_v01.bsp*
* *em16_tgo_fsp_389_01_20250130_20250802_v01.bsp*
* *em16_tgo_fsp_390_01_20250130_20250802_v01.bsp*
* *em16_tgo_fsp_391_01_20250218_20250802_v01.bsp*
* *em16_tgo_fsp_392_01_20250224_20250809_v01.bsp*
* *em16_tgo_fsp_393_01_20250303_20250816_v01.bsp*
* *em16_tgo_fsp_394_01_20250310_20250823_v01.bsp*
* *em16_tgo_fsp_395_01_20250317_20250830_v01.bsp*

B

Midpoint vs. Specular Point Ground Tracks

This appendix presents the ground tracks for the MEX-TGO BSR measurements, including both the midpoint estimates, used for measurement planning, and the specular points.

The midpoints are calculated by projecting the middle of the MEX-TGO line of sight onto the surface of ellipsoidal Mars. The specular points are calculated using a convergence algorithm to achieve equal-emission angles for both S/C. The specular points are more computationally intensive, but yield a better estimation of the points with largest contribution to the received signal. The different ground tracks are denoted by:

- **'midpoint':** Ground track of midpoints for either measurement opportunities, or the (to be) performed measurements.
- **'meas_op':** Ground track of specular points for measurement opportunities.
- **'BSR':** Ground track of specular points for (to be) performed measurements.

Ground tracks for MEX-TGO BSR (BSR-1.x; MTP257/76)
(Background: HRSC_MOLA Blended DEM at 1500mp)
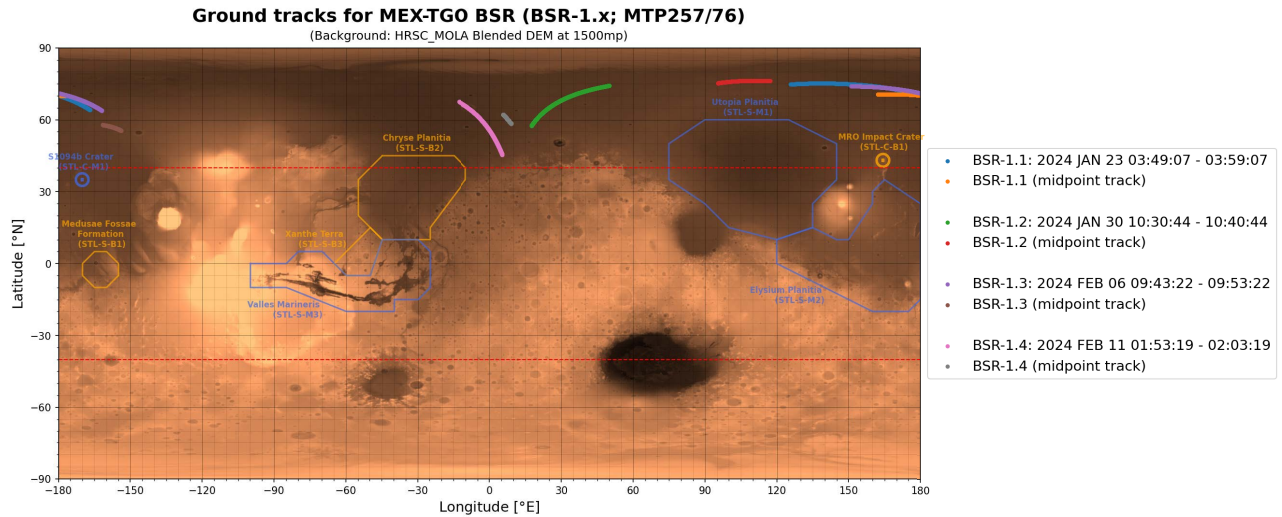
Figure B.1: BSR campaign 1: The midpoint and specular point ground tracks for the January and February 2024 measurements (MTP257/76), own work

Ground tracks for MEX-TGO BSR (BSR-2.x; MTP272/91)
(Background: HRSC_MOLA Blended DEM at 1500mp)
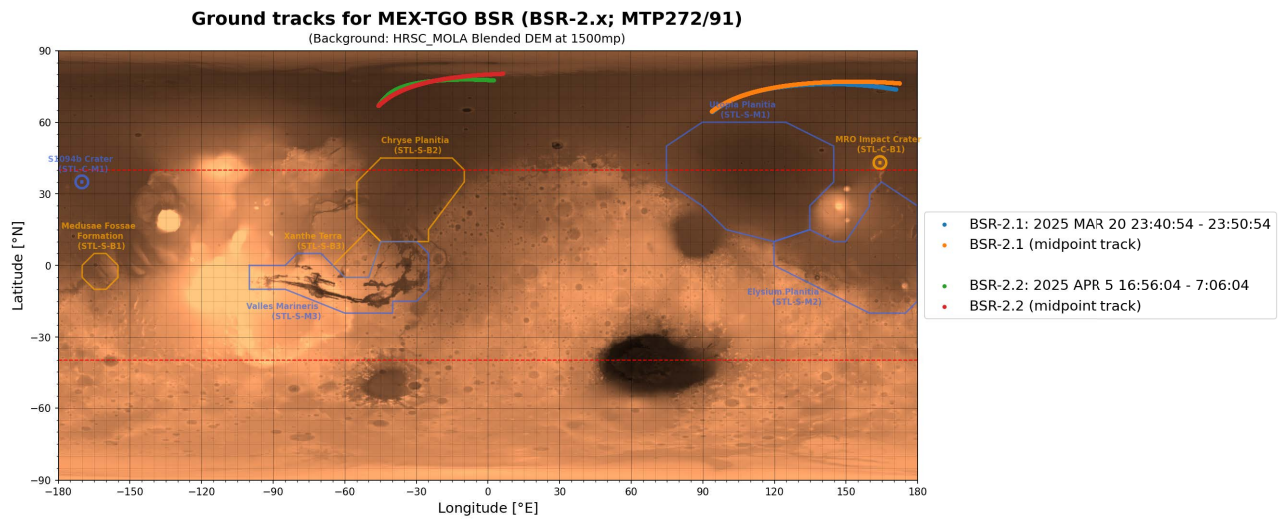
Figure B.2: BSR campaign 2: The midpoint and specular point ground tracks for the March and April 2025 measurements (MTP272/91), own work

Ground tracks for MEX-TGO BSR (meas_ops-3.x; MTP276/95)
(Background: HRSC_MOLA Blended DEM at 1500mp)
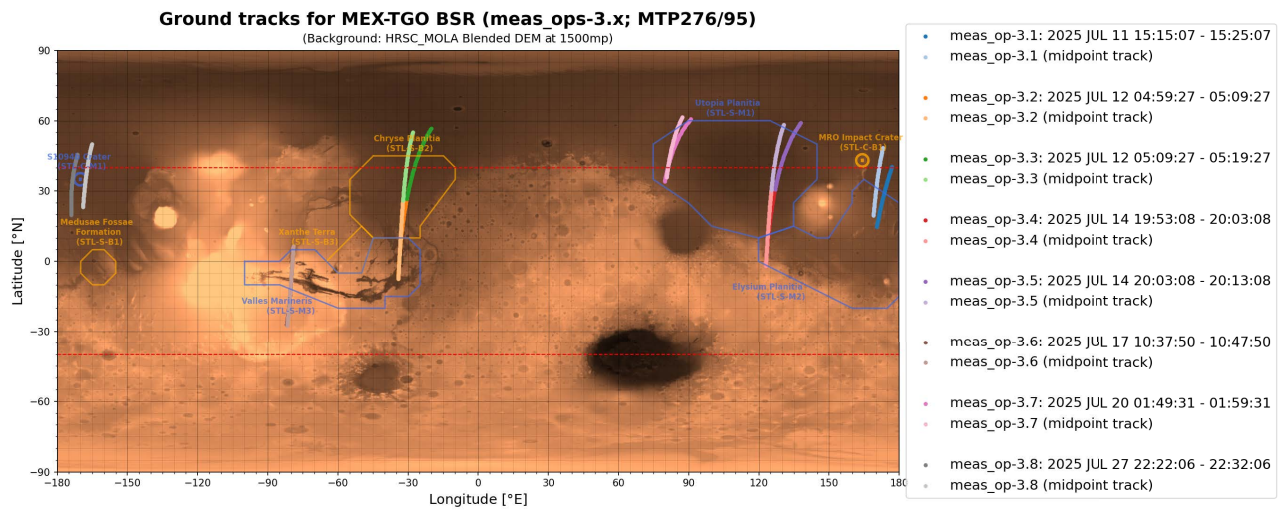
Figure B.3: BSR campaign 3: The midpoint and specular point ground tracks for the July 2025 measurement opportunities requested from ESAC (MTP276/95), own work
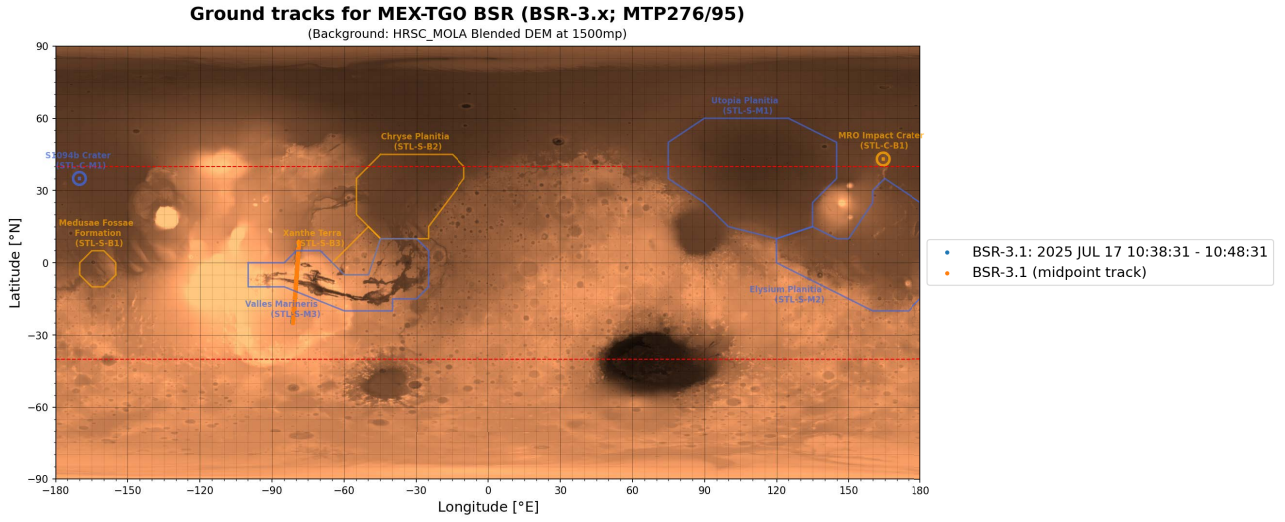
Figure B.4: BSR campaign 3: The midpoint and specular point ground tracks for the July 2025 measurement (MTP276/95), own work
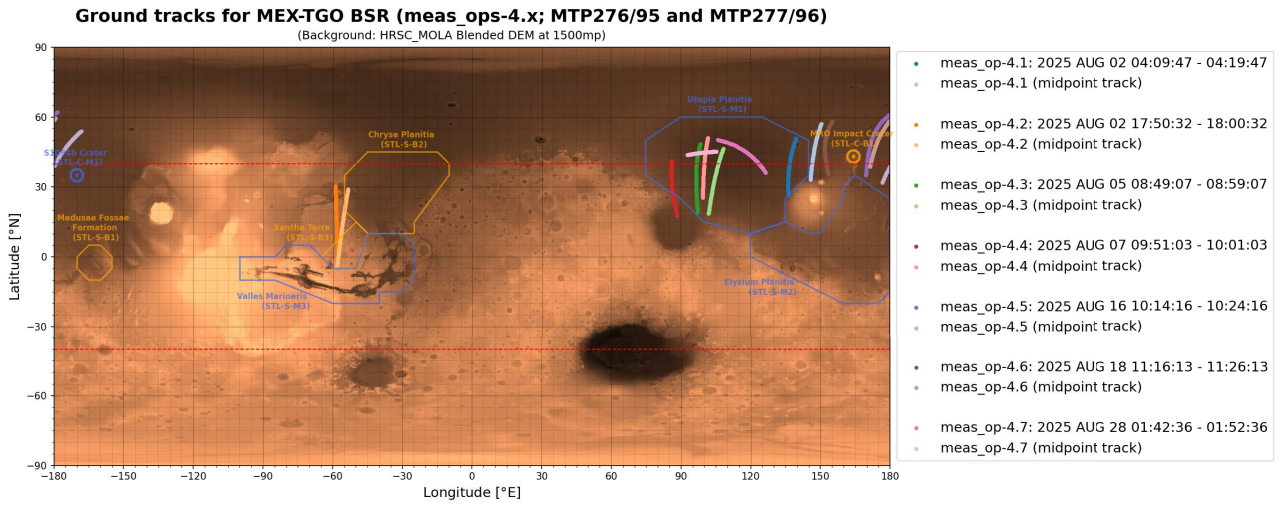
Figure B.5: BSR campaign 4: The midpoint and specular point ground tracks for the August 2025 measurement opportunities requested from ESAC (MTP276/95 and MTP277/96), own work
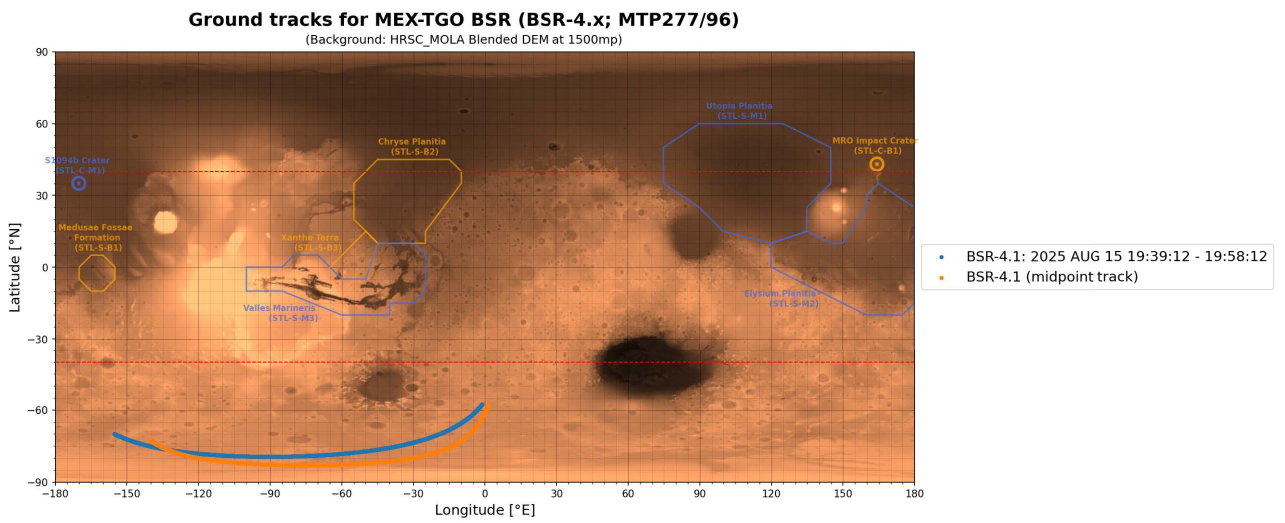
Figure B.6: BSR campaign 4: The midpoint and specular point ground tracks for the August 2025 measurement (MTP277/96), own work
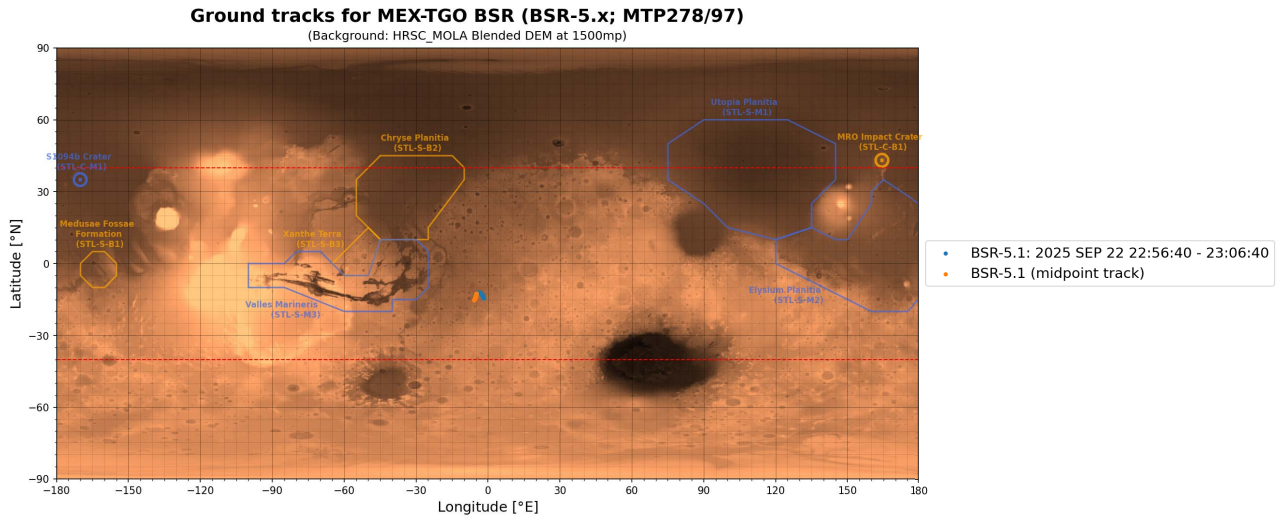
Figure B.7: BSR campaign 5: The midpoint and specular point ground tracks for the September 2025 measurement (MTP278/97), own work
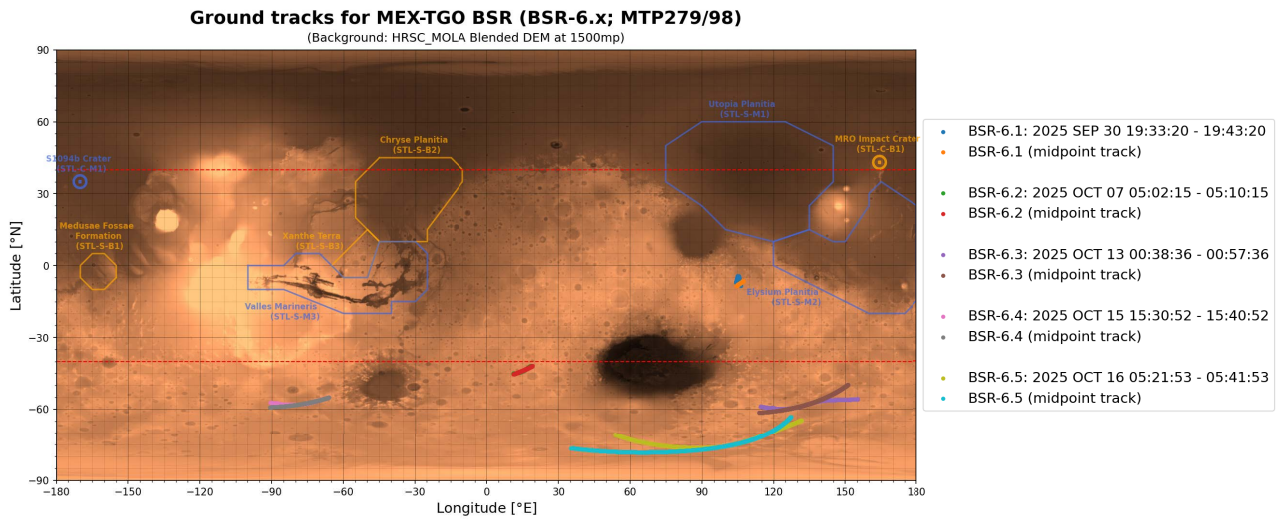
Figure B.8: BSR campaign 6: The midpoint and specular point ground tracks for the September and October 2025 measurements (MTP279/98), own work
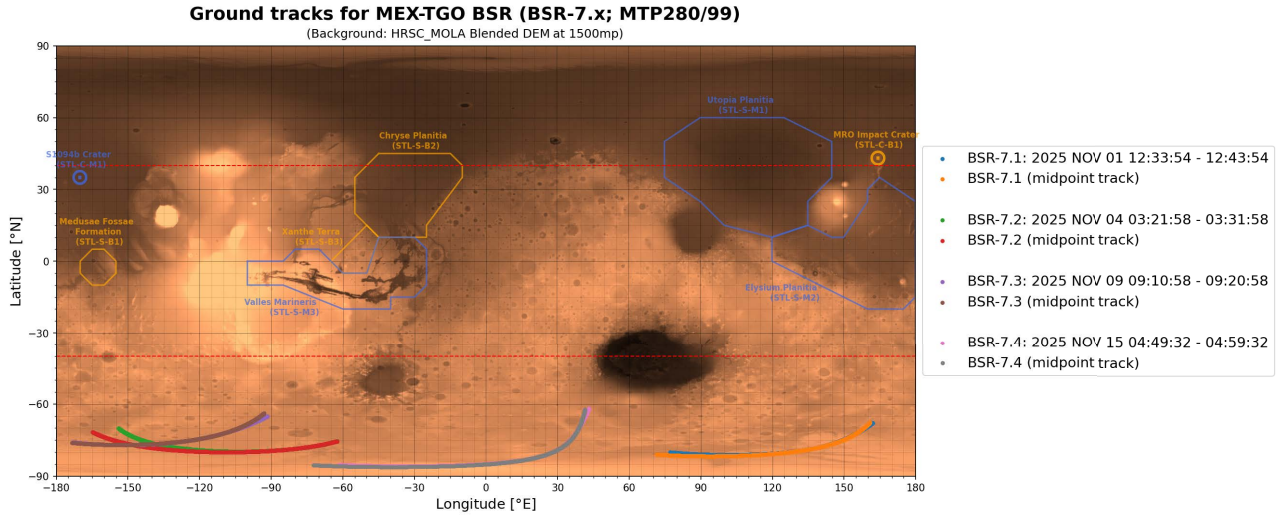
Figure B.9: BSR campaign 7: The midpoint and specular point ground tracks for the November 2025 measurements (MTP280/99), own work
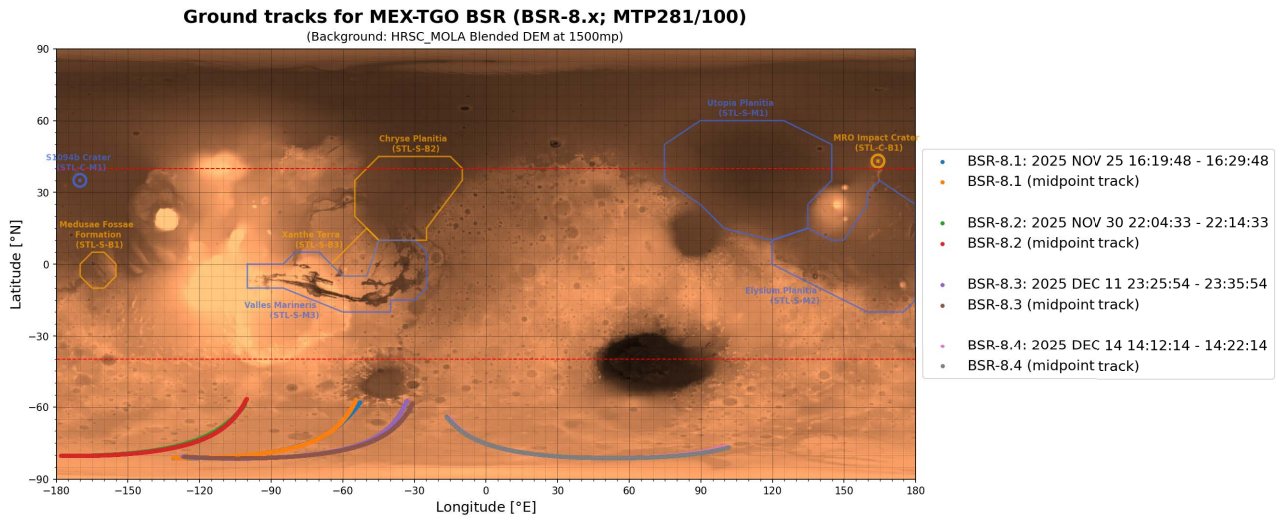
Figure B.10: BSR campaign 8: The midpoint and specular point ground tracks for the November and December 2025 measurements (MTP281/100), own work

C

Mutual Footprints of
All Measurements

This appendix presents the mutual footprints at the start and end of each measurement in both two- and three-dimensional representations (to provide a comprehensive view of the illuminated areas over time). The footprints are bound by the horizon on ellipsoidal Mars as is in view from either S/C, and the following time information is provided inside the plots:

- **'UTC':** The corresponding time stamp in Universal Coordinated Time.

- **'t_step':** The corresponding time stamp, defined as zero at the start of the measurement and counting up for every time step (equal to 1 second for the used temporal resolution in modelling).

Note that the 2D footprints are only given in 4 pixel/degree resolution, as the difference for the increased 16 pixel/degree resolution is not visually discernible from the standard spatial resolution.

Mutual signal footprint for BSR-1.1 (at 4 pixel/degree resolution)
(Background: HRSC_MOLA Blended DEM at 1500mp)
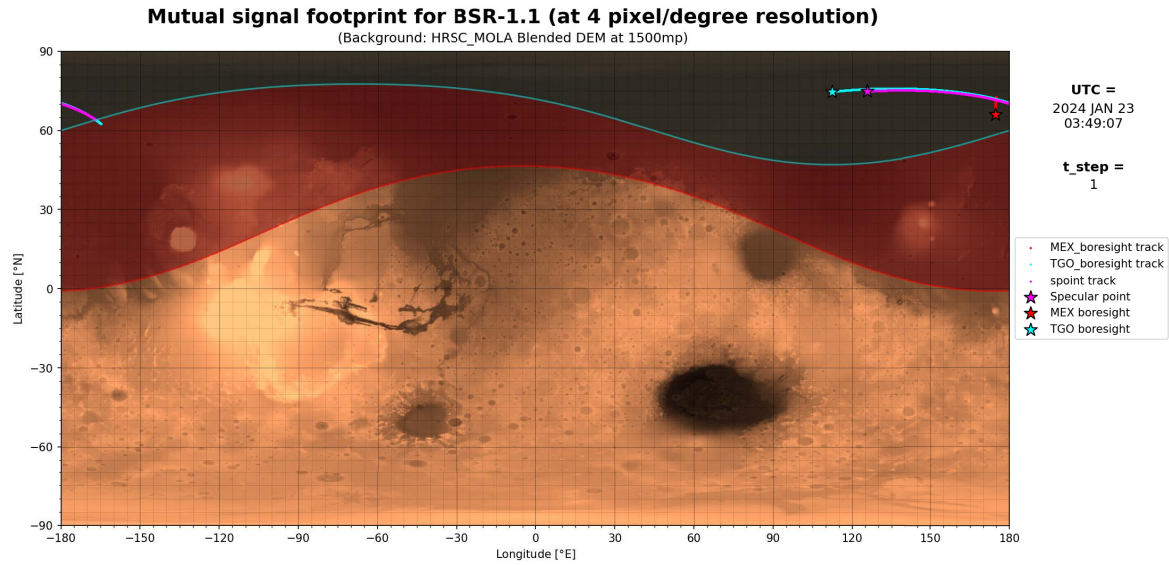
Figure C.1: Mutual signal footprint for BSR-1.1 at start of measurement (23rd of January 2024 03:49:07; using 4 pixel/degree resolution), own work
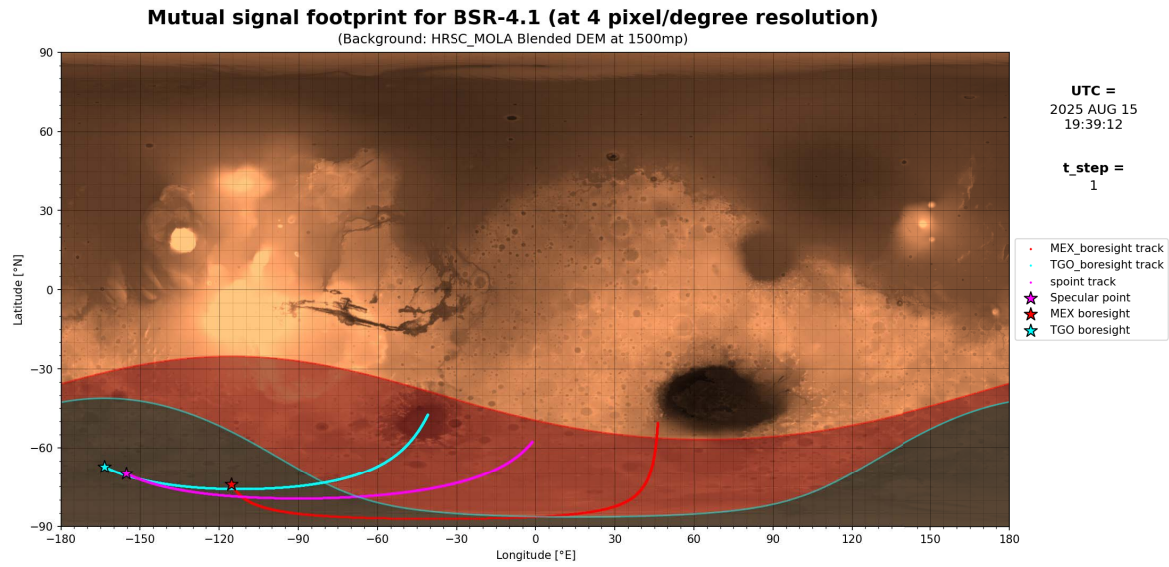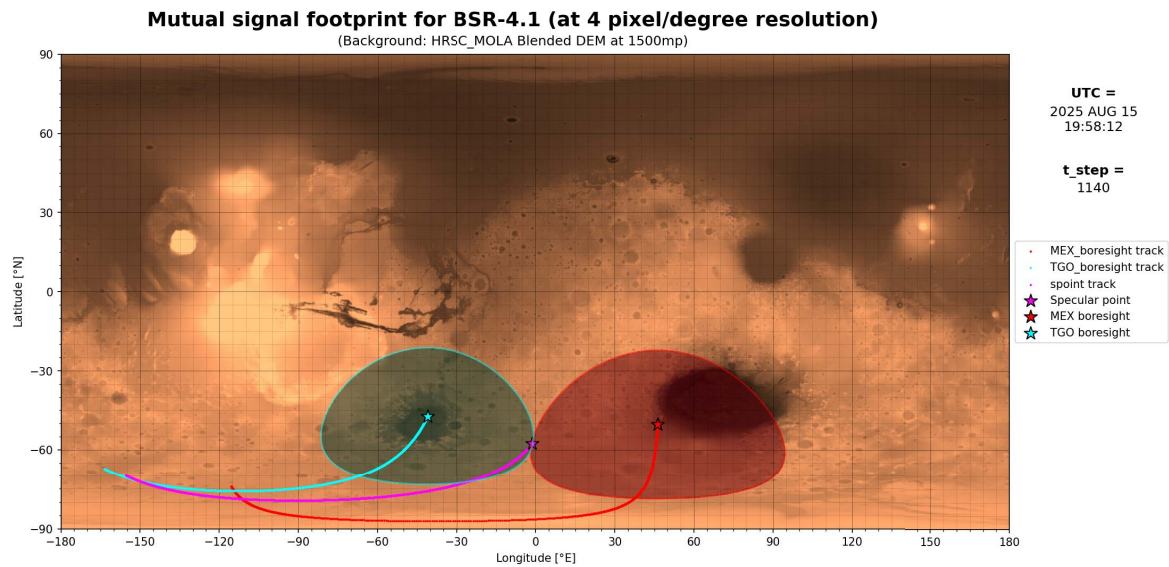
Mutual signal footprint for BSR-1.1 (at 4 pixel/degree resolution)
(Background: HRSC_MOLA Blended DEM at 1500mp)
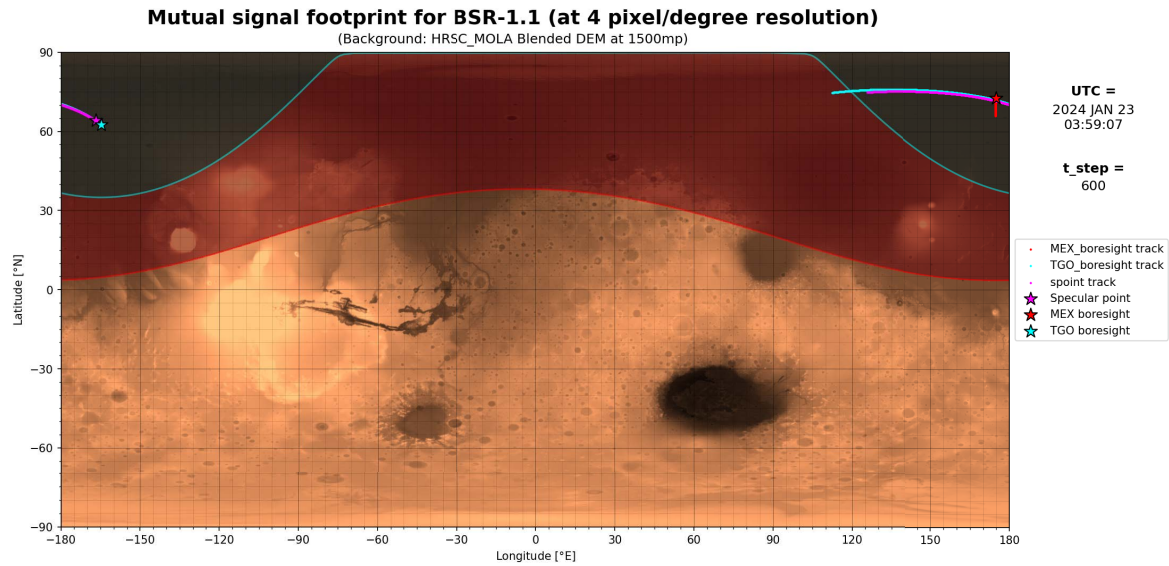
Figure C.2: Mutual signal footprint for BSR-1.1 at end of measurement (23rd of January 2024 03:59:07; using 4 pixel/degree resolution), own work
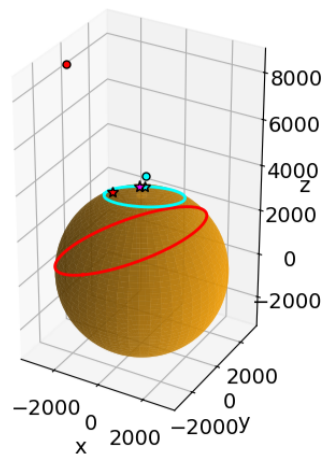
Figure C.3: 3D Mutual footprint for BSR-1.1 at start of measurement (23rd of January 2024 03:49:07), own work
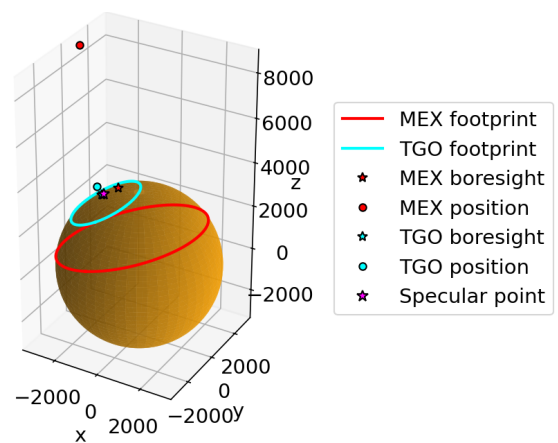
Figure C.4: 3D Mutual footprint for BSR-1.1 at end of measurement (23rd of January 2024 03:59:07), own work
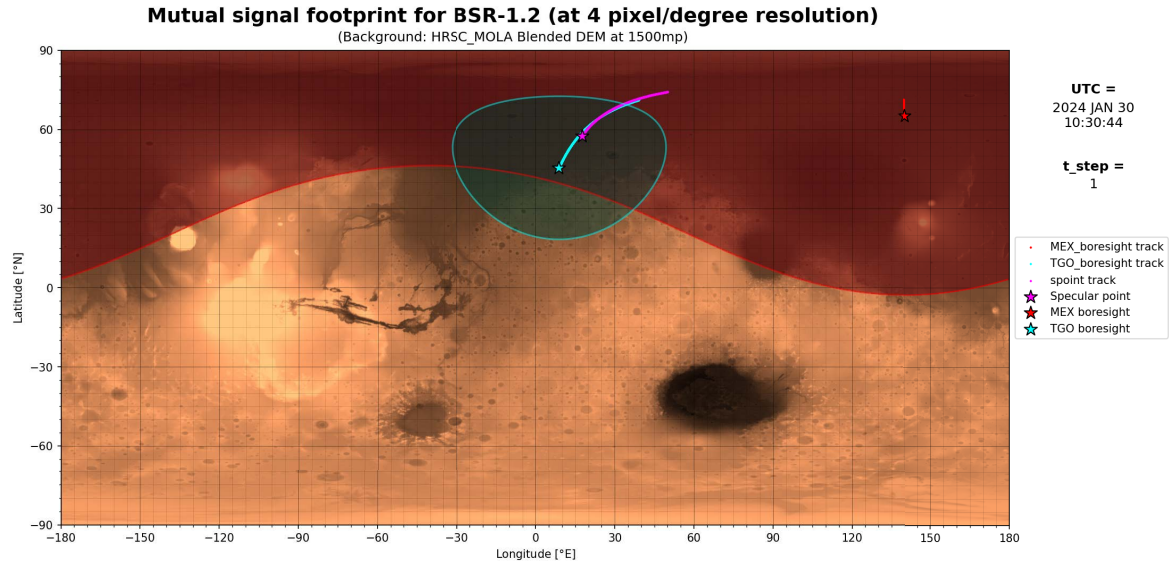
Figure C.5: Mutual signal footprint for BSR-1.2 at start of measurement (30th of January 2024 10:30:44; using 4 pixel/degree resolution), own work
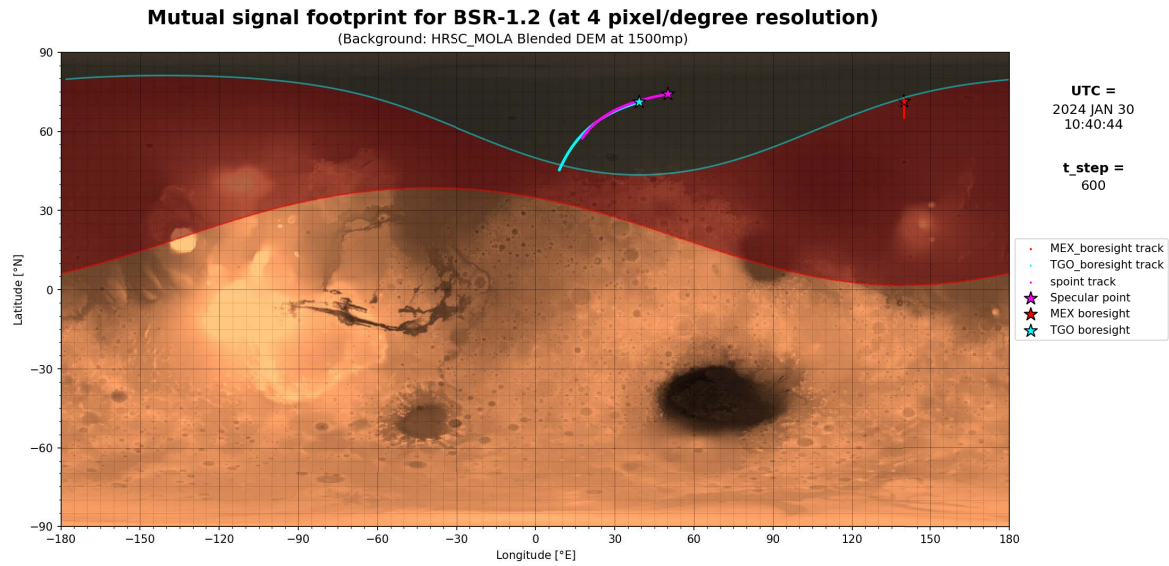
Figure C.6: Mutual signal footprint for BSR-1.2 at end of measurement (30th of January 2024 10:40:44; using 4 pixel/degree resolution), own work
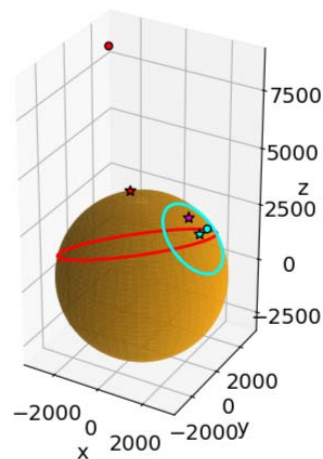
Figure C.7: 3D Mutual footprint for BSR-1.2 at start of measurement (30th of January 2024 10:30:44), own work
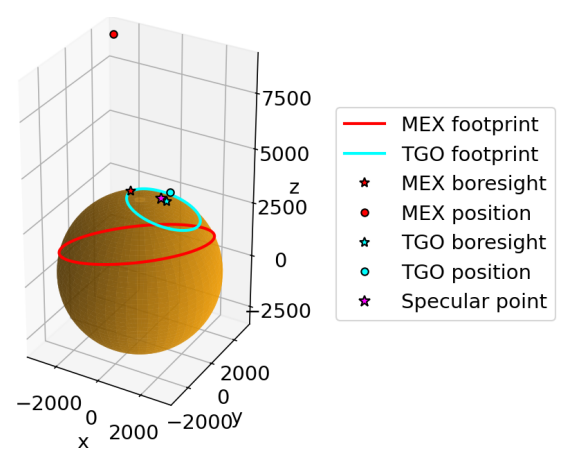
Figure C.8: 3D Mutual footprint for BSR-1.2 at end of measurement (30th of January 2024 10:40:44), own work

Mutual signal footprint for BSR-1.3 (at 4 pixel/degree resolution)
(Background: HRSC_MOLA Blended DEM at 1500mp)
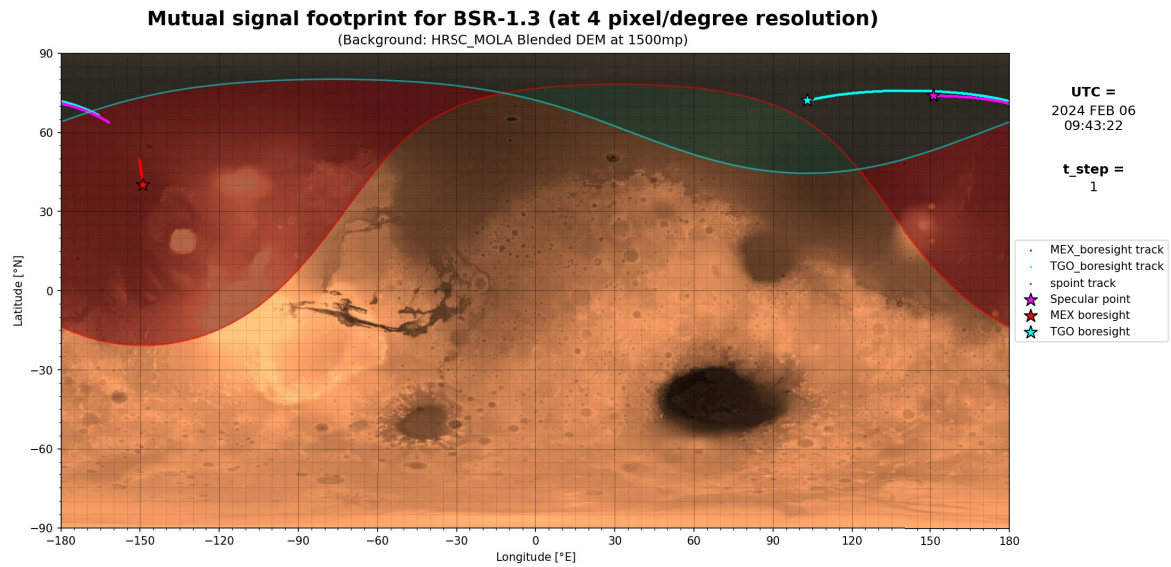
Figure C.9: Mutual signal footprint for BSR-1.3 at start of measurement (6th of February 2024 09:43:22; using 4 pixel/degree resolution), own work

Mutual signal footprint for BSR-1.3 (at 4 pixel/degree resolution)
(Background: HRSC_MOLA Blended DEM at 1500mp)
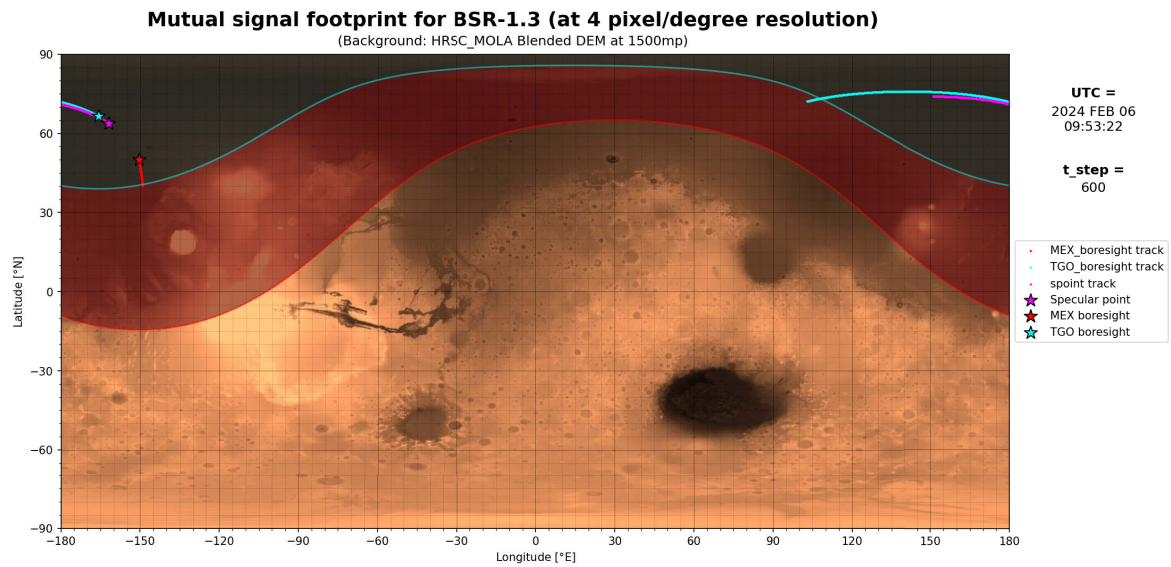
Figure C.10: Mutual signal footprint for BSR-1.3 at end of measurement (6th of February 2024 09:53:22; using 4 pixel/degree resolution), own work
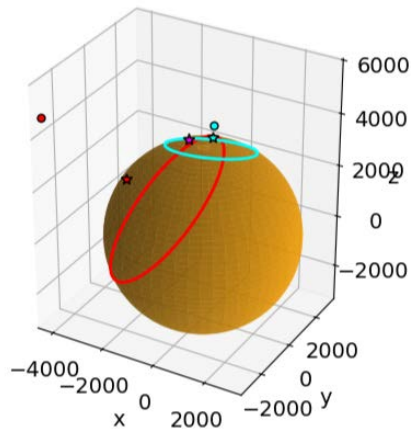
Figure C.11: 3D Mutual footprint for BSR-1.3 at start of measurement (6th of February 2024 09:43:22), own work
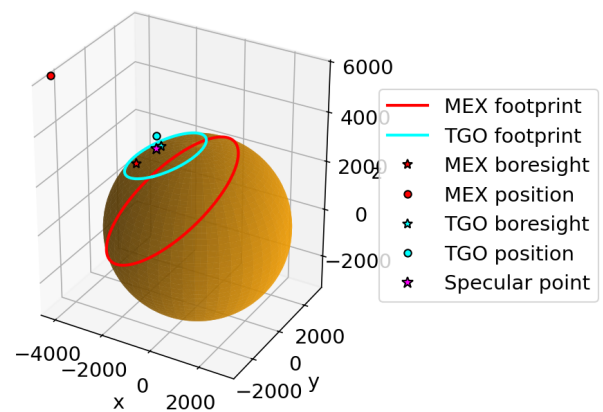
Figure C.12: 3D Mutual footprint for BSR-1.3 at end of measurement (6th of February 2024 09:53:22), own work

Mutual signal footprint for BSR-1.4 (at 4 pixel/degree resolution)
(Background: HRSC_MOLA Blended DEM at 1500mp)
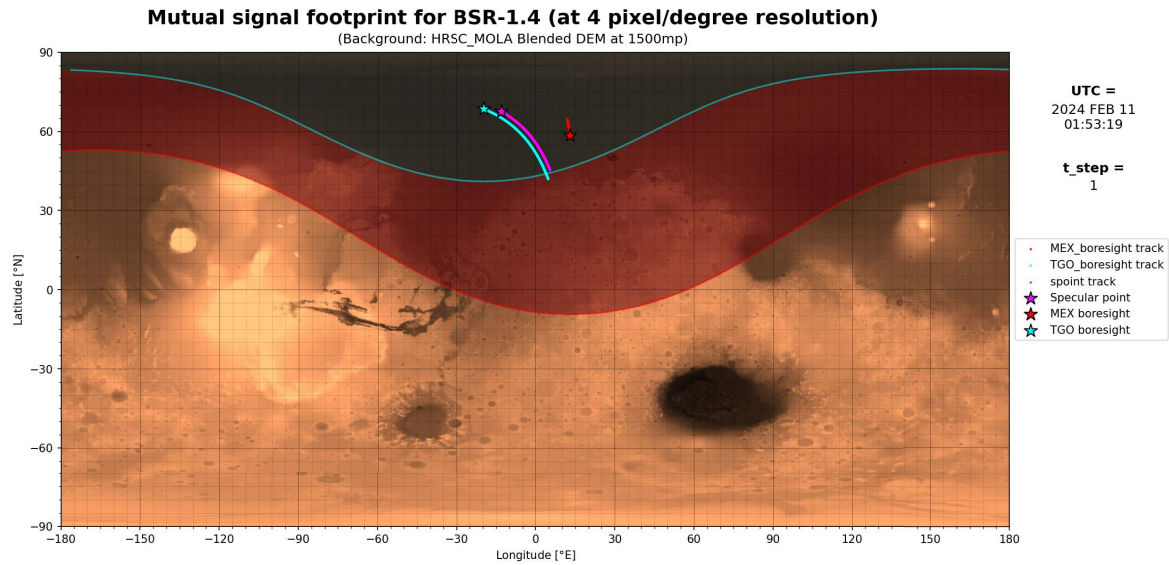
Figure C.13: Mutual signal footprint for BSR-1.4 at start of measurement (11th of February 2024 01:53:19; using 4 pixel/degree resolution), own work

Mutual signal footprint for BSR-1.4 (at 4 pixel/degree resolution)
(Background: HRSC_MOLA Blended DEM at 1500mp)
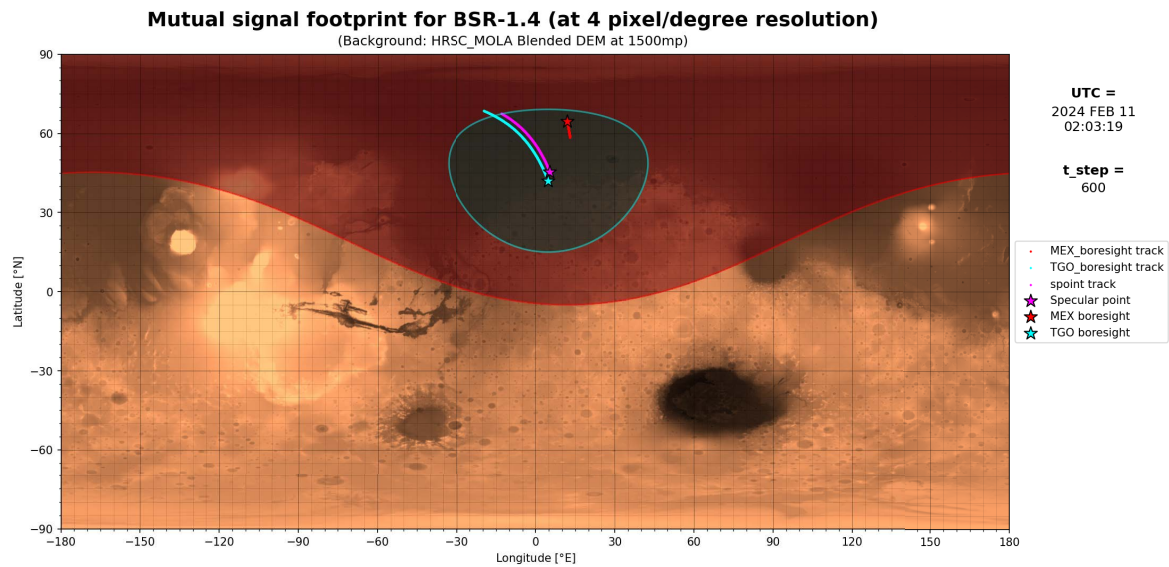
Figure C.14: Mutual signal footprint for BSR-1.4 at end of measurement (11th of February 2024 02:03:19; using 4 pixel/degree resolution), own work
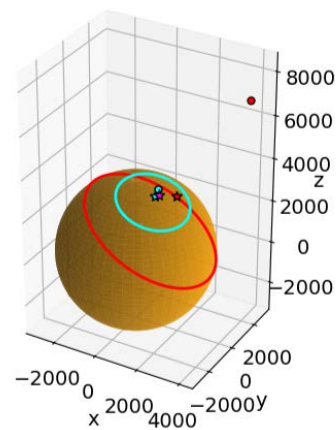
Figure C.15: 3D Mutual footprint for BSR-1.4 at start of measurement (11th of February 2024 01:53:19), own work
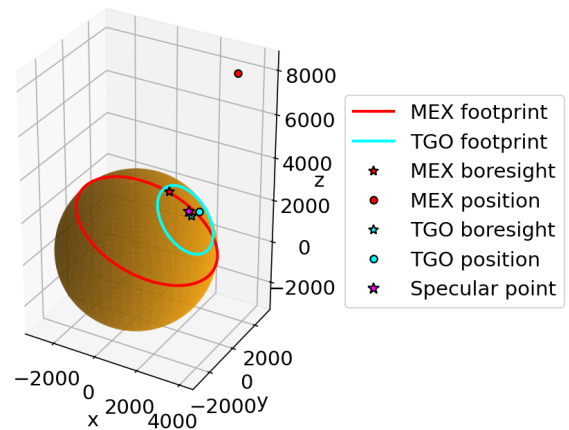
Figure C.16: 3D Mutual footprint for BSR-1.4 at end of measurement (11th of February 2024 02:03:19), own work

Mutual signal footprint for BSR-2.1 (at 4 pixel/degree resolution)
(Background: HRSC_MOLA Blended DEM at 1500mp)
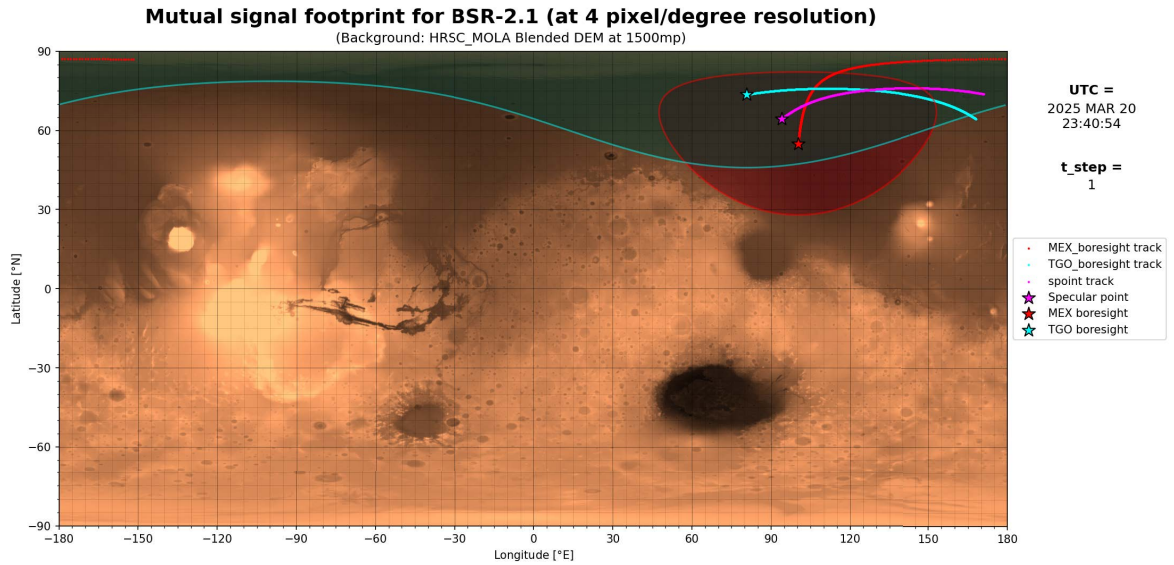
Figure C.17: Mutual signal footprint for BSR-2.1 at start of measurement (20th of March 2025 23:40:54; using 4 pixel/degree resolution), own work

Mutual signal footprint for BSR-2.1 (at 4 pixel/degree resolution)
(Background: HRSC_MOLA Blended DEM at 1500mp)
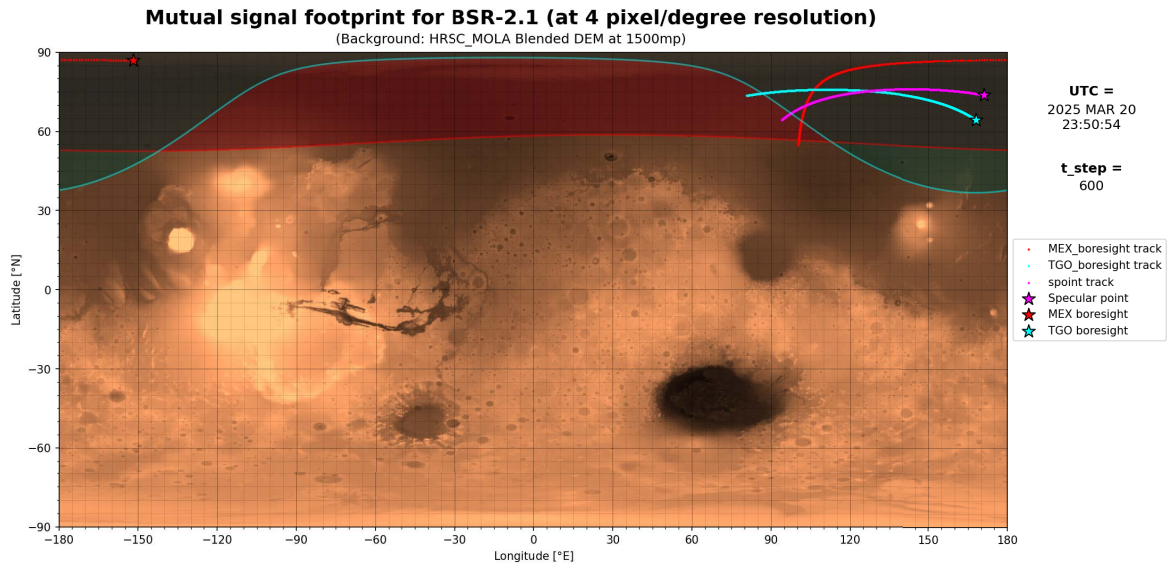
Figure C.18: Mutual signal footprint for BSR-2.1 at end of measurement (20th of March 2025 23:50:54; using 4 pixel/degree resolution), own work
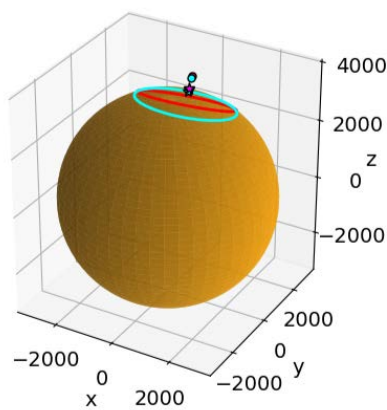
Figure C.19: 3D Mutual footprint for BSR-2.1 at start of measurement (20th of March 2025 23:40:54), own work
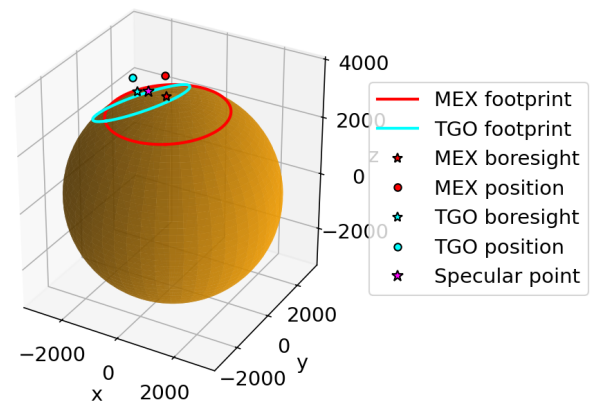
Figure C.20: 3D Mutual footprint for BSR-2.1 at end of measurement (20th of March 2025 23:50:54), own work

Mutual signal footprint for BSR-2.2 (at 4 pixel/degree resolution)
(Background: HRSC_MOLA Blended DEM at 1500mp)
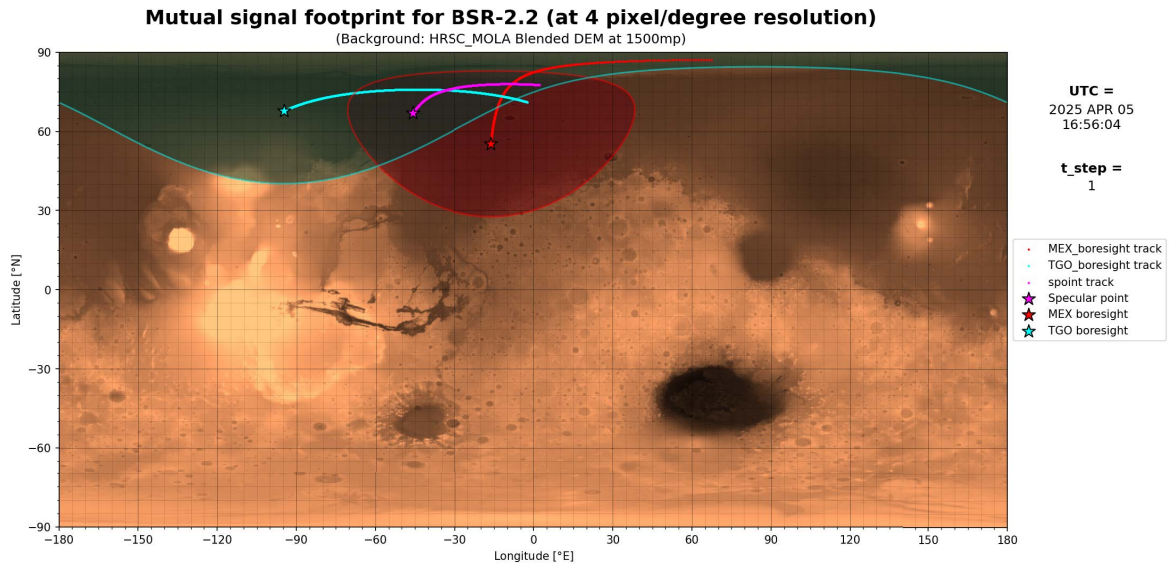
Figure C.21: Mutual signal footprint for BSR-2.2 at start of measurement (5th of April 2025 16:56:04; using 4 pixel/degree resolution), own work

Mutual signal footprint for BSR-2.2 (at 4 pixel/degree resolution)
(Background: HRSC_MOLA Blended DEM at 1500mp)
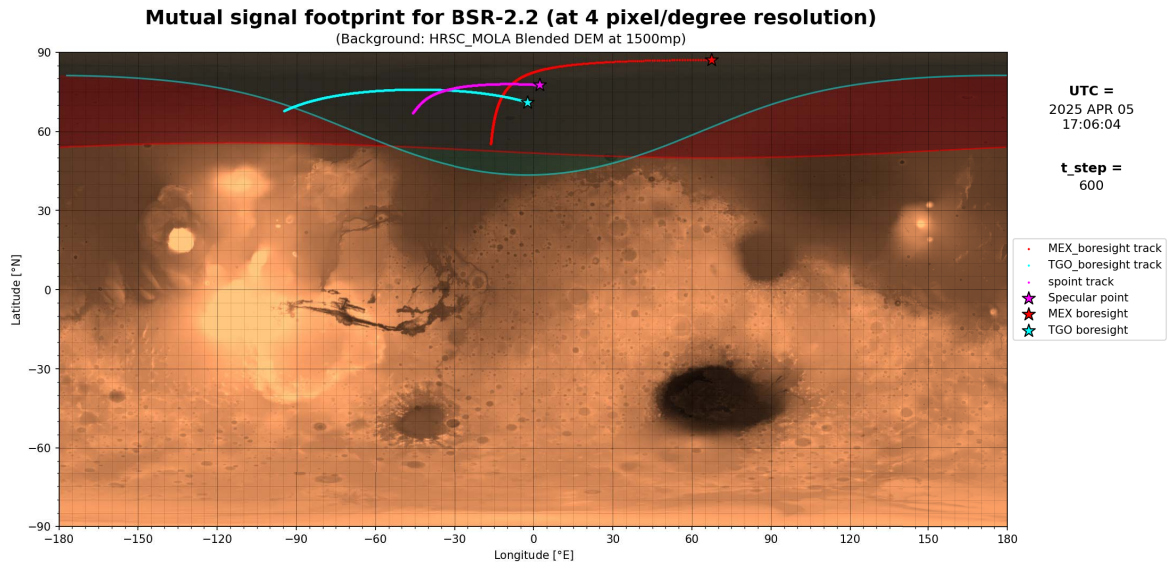
Figure C.22: Mutual signal footprint for BSR-2.2 at end of measurement (5th of April 2025 17:06:04; using 4 pixel/degree resolution), own work
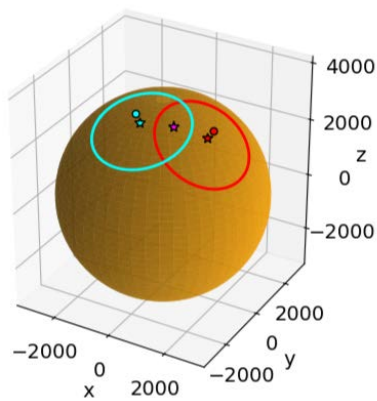
Figure C.23: 3D Mutual footprint for BSR-2.2 at start of measurement (5th of April 2025 16:56:04), own work
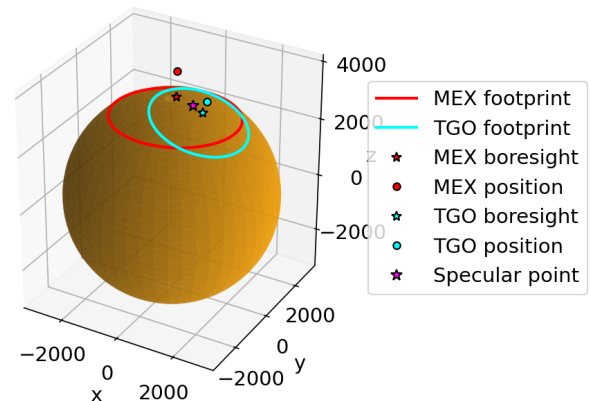
Figure C.24: 3D Mutual footprint for BSR-2.2 at end of measurement (5th of April 2025 17:06:04), own work

Mutual signal footprint for BSR-3.1 (at 4 pixel/degree resolution)
(Background: HRSC_MOLA Blended DEM at 1500mp)
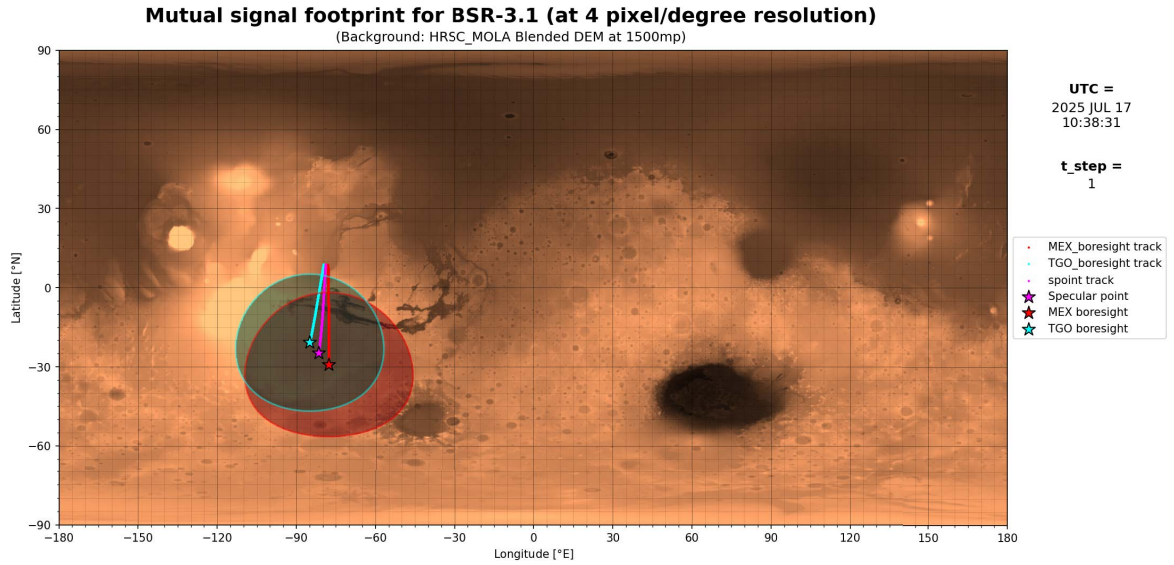
Figure C.25: Mutual signal footprint for BSR-3.1 at start of measurement (17th of July 2025 10:38:31; using 4 pixel/degree resolution), own work

Mutual signal footprint for BSR-3.1 (at 4 pixel/degree resolution)
(Background: HRSC_MOLA Blended DEM at 1500mp)
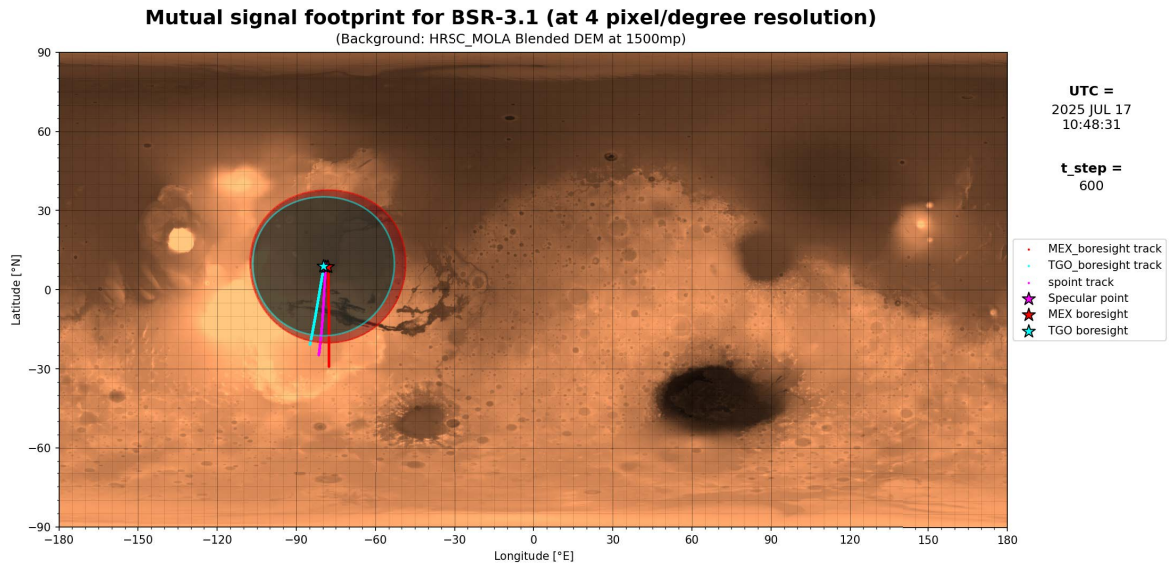
Figure C.26: Mutual signal footprint for BSR-3.1 at end of measurement (17th of July 2025 10:48:31; using 4 pixel/degree resolution), own work
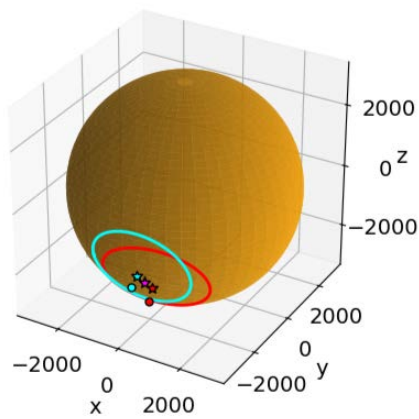
Figure C.27: 3D Mutual footprint for BSR-3.1 at start of measurement (17th of July 2025 10:38:31), own work
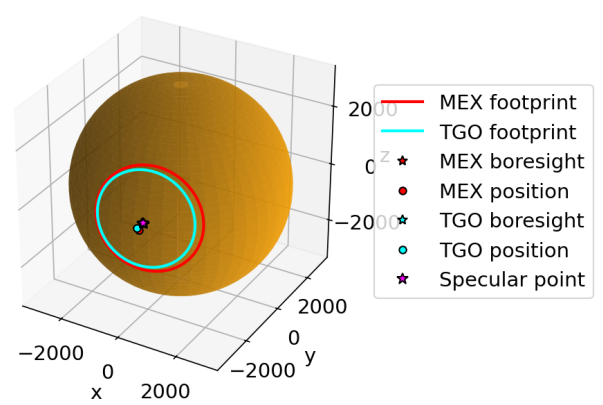
Figure C.28: 3D Mutual footprint for BSR-3.1 at end of measurement (17th of July 2025 10:48:31), own work

Mutual signal footprint for BSR-4.1 (at 4 pixel/degree resolution)
(Background: HRSC_MOLA Blended DEM at 1500mp)

Figure C.29: Mutual signal footprint for BSR-4.1 at start of measurement (15th of August 2025 19:39:12; using 4 pixel/degree resolution), own work

Mutual signal footprint for BSR-4.1 (at 4 pixel/degree resolution)
(Background: HRSC_MOLA Blended DEM at 1500mp)

Figure C.30: Mutual signal footprint for BSR-4.1 at end of measurement (15th of August 2025 19:58:12; using 4 pixel/degree resolution), own work
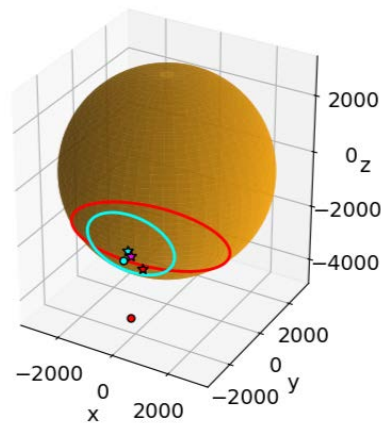
Figure C.31: 3D Mutual footprint for BSR-4.1 at start of measurement (15th of August 2025 19:39:12), own work
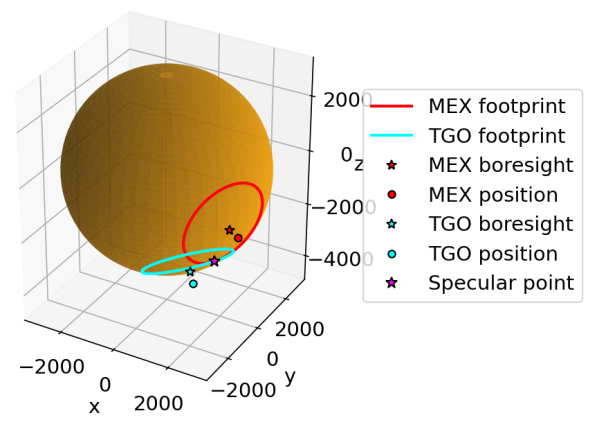
Figure C.32: 3D Mutual footprint for BSR-4.1 at end of measurement (15th of August 2025 19:58:12), own work

D
AGC Data of
All Measurements

This appendix presents the AGC (and converted power) data of all measurements. Each set includes:

- **'AGC data':** The direct readout of the AGC values from the IQ files downlinked by TGO, decoded from an 8-bit string to a value between 0 and 255.

- **'Converted Power data':**

  - **Power in dB:** Converted from the AGC values through an estimated transfer function wherein every AGC count is assumed to correspond to +1 dB in the received signal strength.

  - **Power in W:** Converted from the power in dB through an estimated transfer function which yields realistic expected values (on linear instead of logarithmic scale).

Effectively the shape for each graph is the same, but at a different scale shown on the y-axis.

Figure D.1: AGC data for BSR-1.1 (direct readout from IQ file), own work

Figure D.2: Converted received power data for BSR-1.1, own work

AGC data for BSR-1.2

Data retrieved from IQ___DMEX__05376BCD_2024-030T10-30-15_8F540240300137_00001.EXM
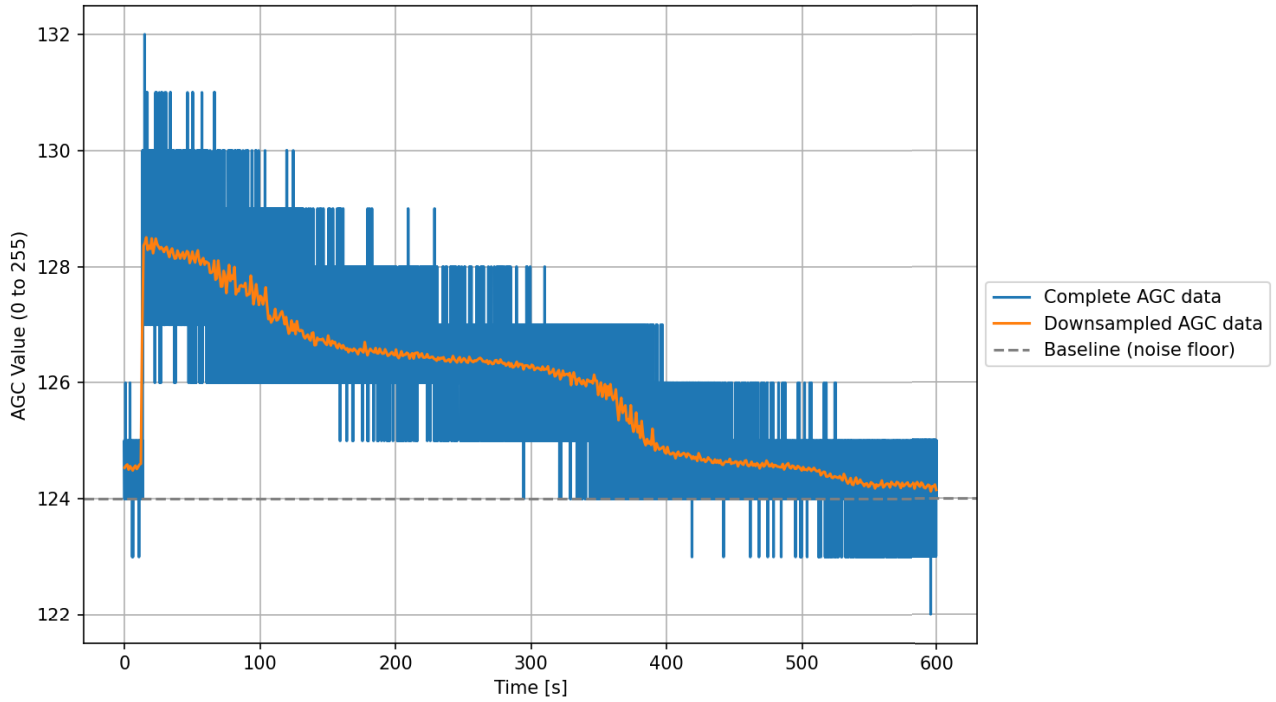
Figure D.3: AGC data for BSR-1.2 (direct readout from IQ file), own work

Converted Power data for BSR-1.2

Data retrieved from IQ___DMEX__05376BCD_2024-030T10-30-15_8F540240300137_00001.EXM
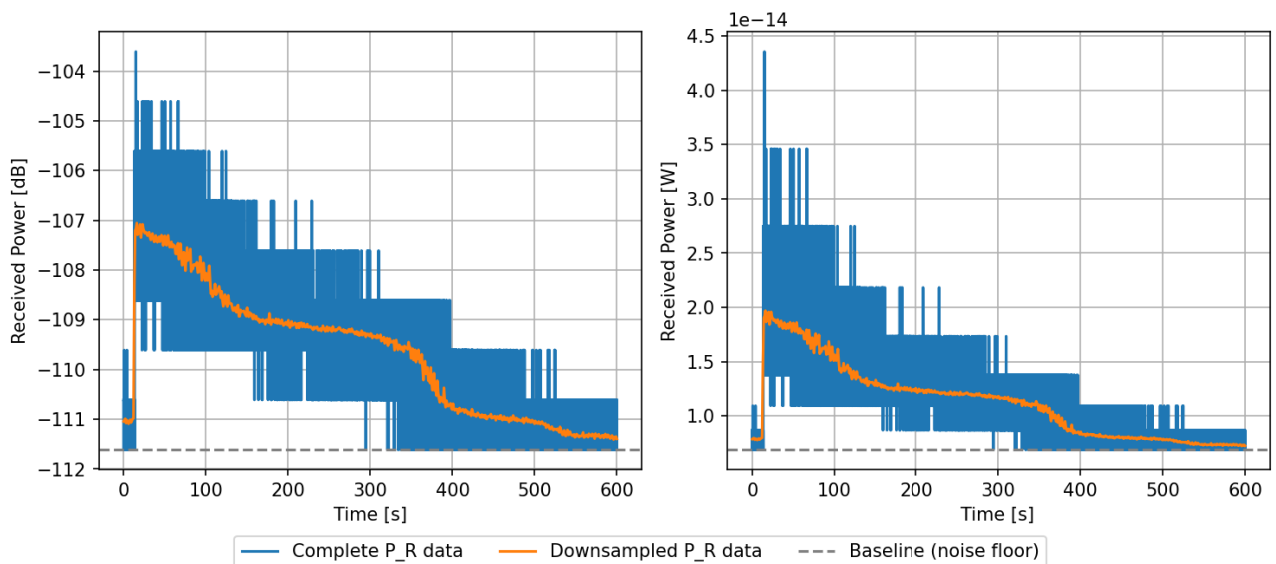
Figure D.4: Converted received power data for BSR-1.2, own work

AGC data for BSR-1.3

Data retrieved from IQ___DMEX__05376C22_2024-037T09-42-58_8F540240370137_00001.EXM
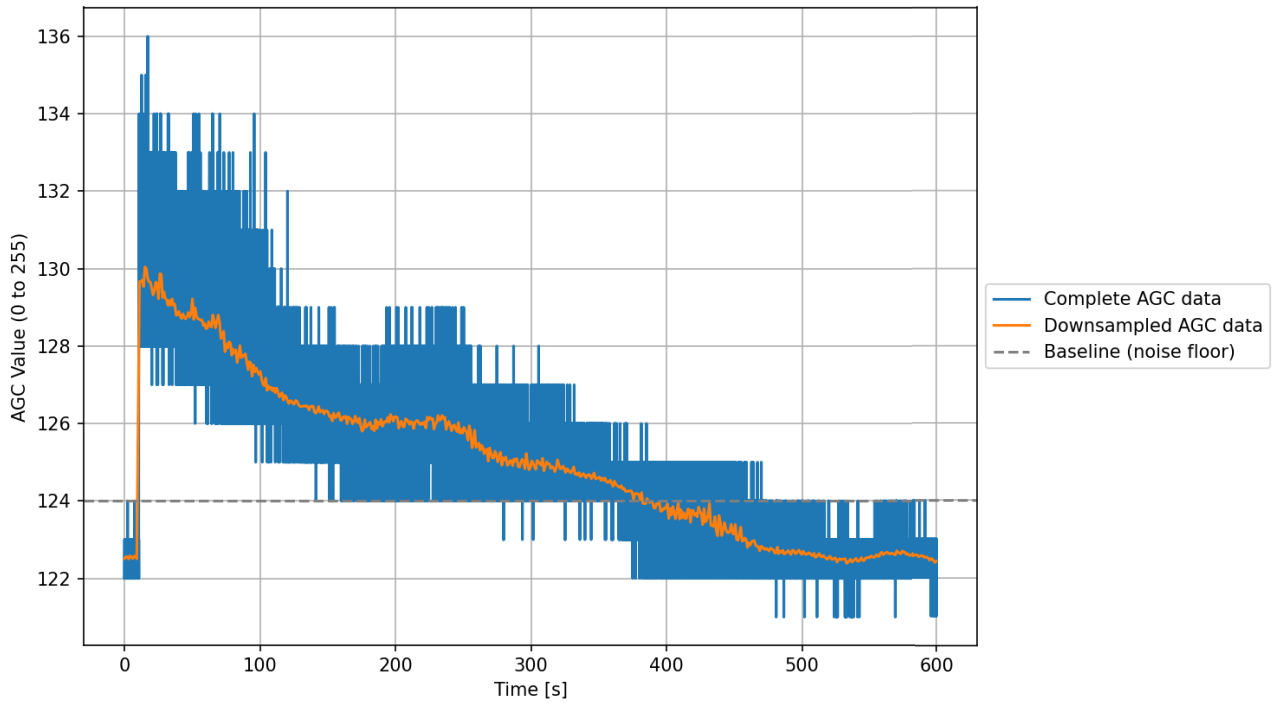
Figure D.5: AGC data for BSR-1.3 (direct readout from IQ file), own work

Converted Power data for BSR-1.3

Data retrieved from IQ___DMEX__05376C22_2024-037T09-42-58_8F540240370137_00001.EXM

Figure D.6: Converted received power data for BSR-1.3, own work

Figure D.7: AGC data for BSR-1.4 (direct readout from IQ file), own work

Figure D.8: Converted received power data for BSR-1.4, own work

Figure D.9: AGC data for BSR-2.1 (direct readout from IQ file), own work

Figure D.10: Converted received power data for BSR-2.1, own work

AGC data for BSR-2.2

Data retrieved from IQ___DMEX__05378060_2025-095T16-55-49_8F540250950137_00001.EXM

Figure D.11: AGC data for BSR-2.2 (direct readout from IQ file), own work

Converted Power data for BSR-2.2

Data retrieved from IQ___DMEX__05378060_2025-095T16-55-49_8F540250950137_00001.EXM
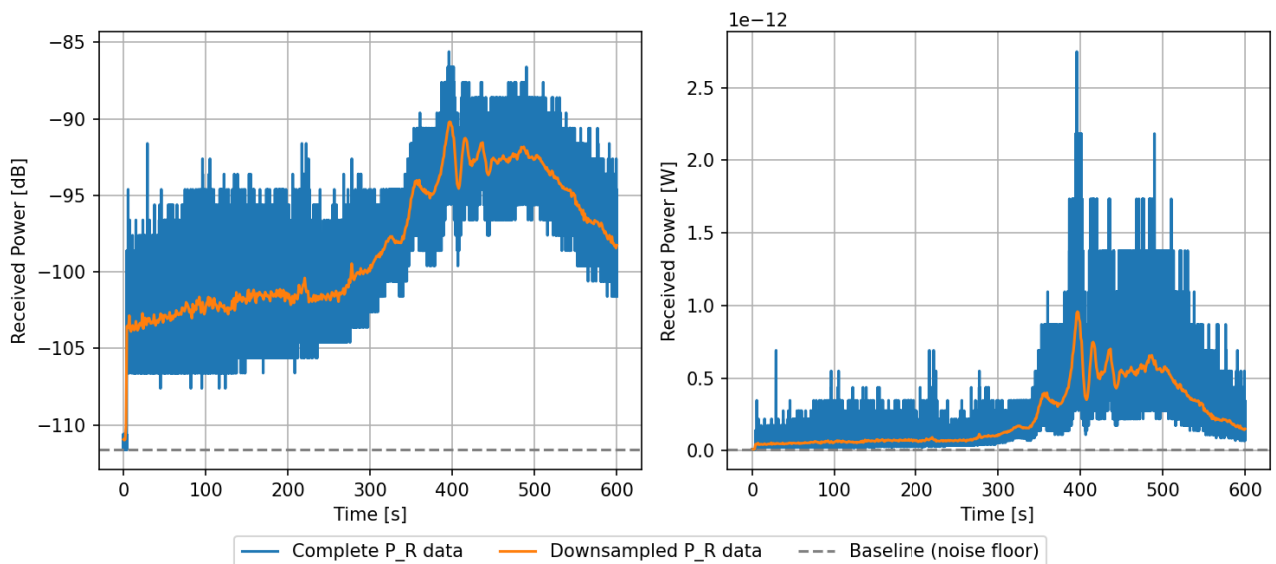
Figure D.12: Converted received power data for BSR-2.2, own work

AGC data for BSR-3.1

Data retrieved from IQ___DMEX__05378500_2025-192T16-16-12_8F540251920137_00001.EXM
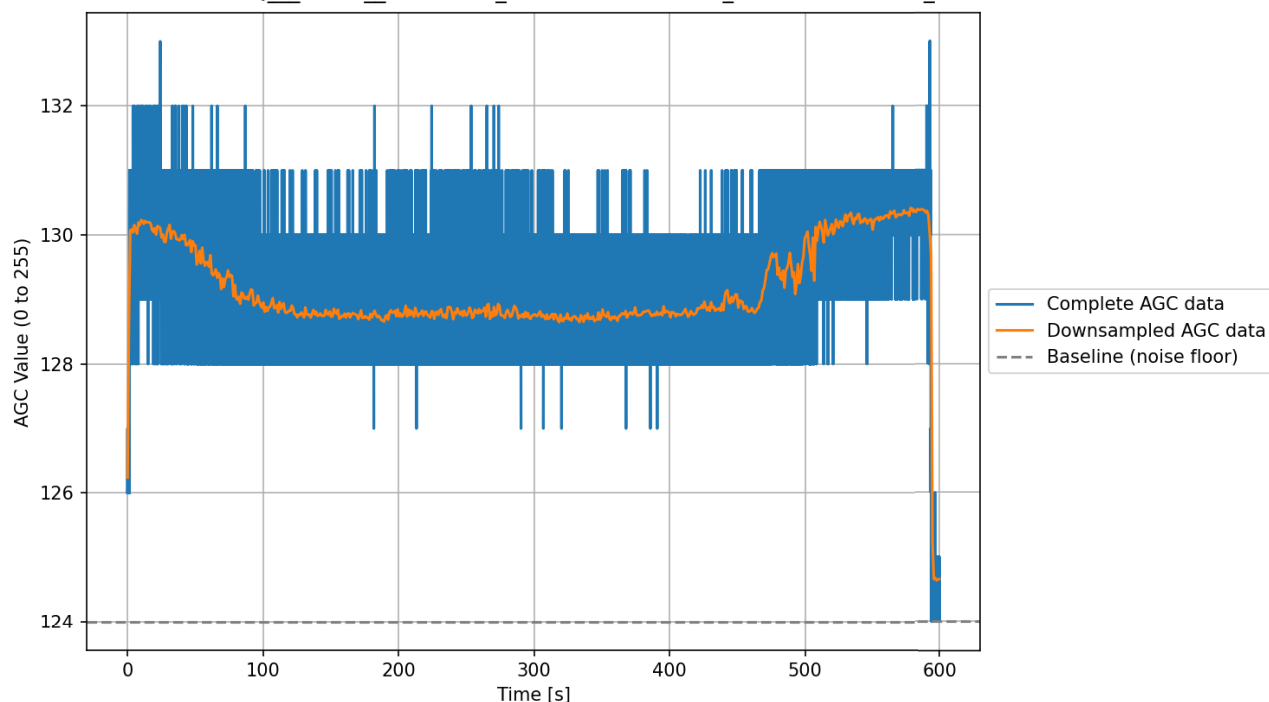
Figure D.13: AGC data for BSR-3.1 (direct readout from IQ file), own work

Converted Power data for BSR-3.1

Data retrieved from IQ___DMEX__05378500_2025-192T16-16-12_8F540251920137_00001.EXM
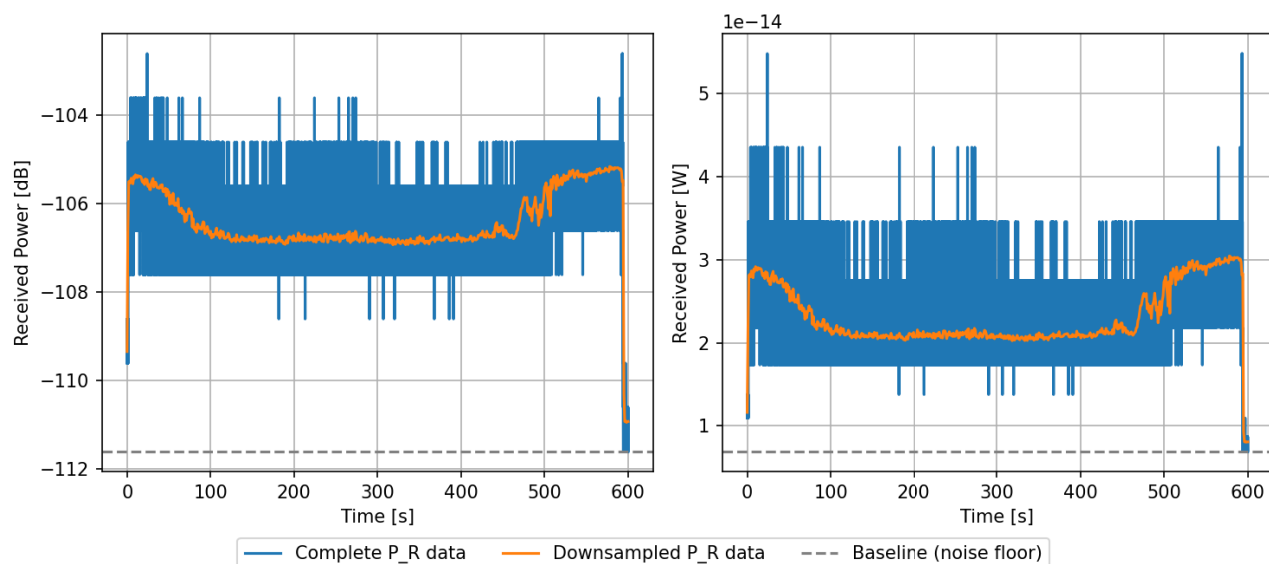
Figure D.14: Converted received power data for BSR-3.1, own work

AGC data for BSR-4.1

Data retrieved from IQ___DMEX__053786AD_2025-227T19-38-57_8F540252270137_00001.EXM
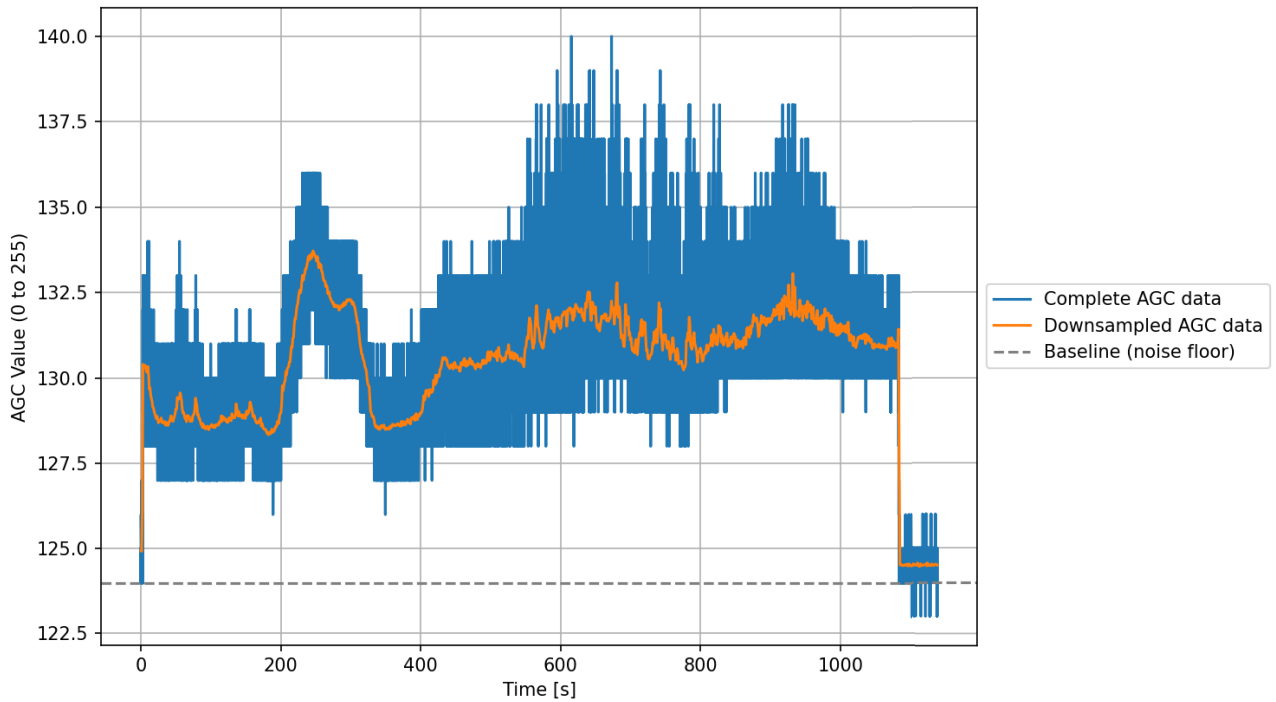
Figure D.15: AGC data for BSR-4.1 (direct readout from IQ file), own work

Converted Power data for BSR-4.1

Data retrieved from IQ___DMEX__053786AD_2025-227T19-38-57_8F540252270137_00001.EXM
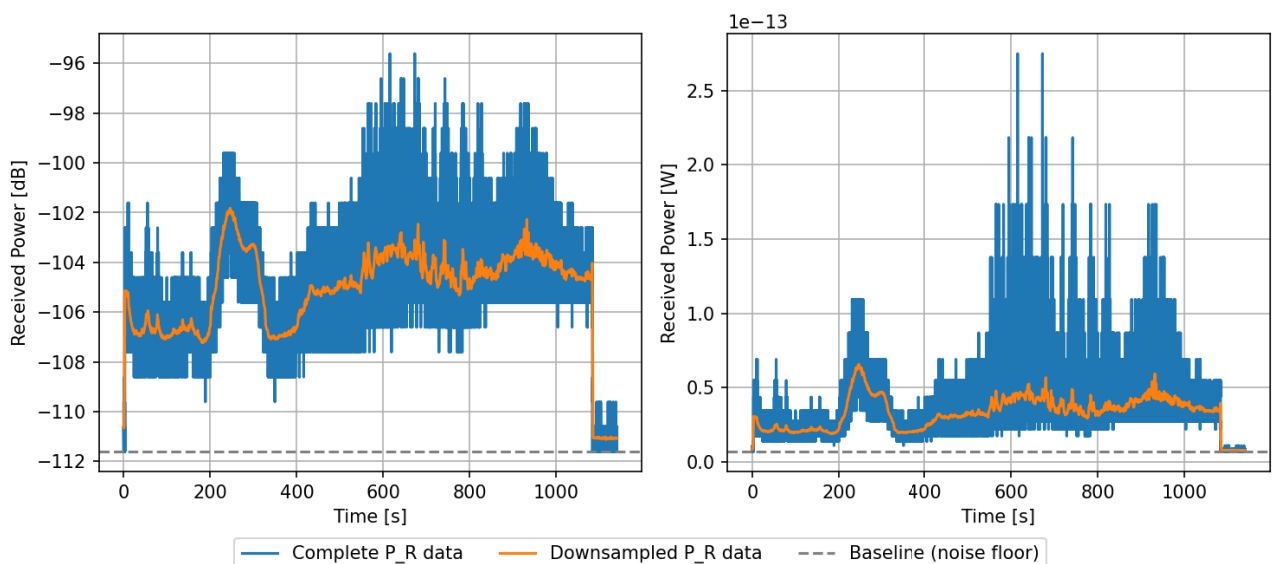
Figure D.16: Converted received power data for BSR-4.1, own work

E

Model Results of All Measurements

This appendix presents the model results of all measurements. It is divided over the following:

- **Section E.1** presents the model results for the 'Effects of the BSR model parameters', i.e. the variation of the BSR parameters throughout the duration of each measurement.
- **Section E.2** presents the model results for the 'Power distribution over the mutual footprint', including:
  - **Subsection E.2.1** presents the actual power distribution over the mutual footprint, plotted as the individual power contribution per gridpoint shown for both the start and end of each measurement.
  - **Subsection E.2.2** presents the comparison of the power contributions (inside the mutual footprint) over time. This includes the total modelled received power, as well as the isolated contributions of the specular point and point of maximum return.
  - **Subsection E.2.3** presents the ground tracks of maximum power return, placed in comparison to the tracks calculated for the specular point, midpoint approximation and both S/C boresights.
- **Section E.3** presents the model results for the 'Free-space direct signal contribution', i.e. the received power and parameters in the direct free-space calculation, throughout the duration of each measurement.
- **Section E.4** presents the model results for the 'Effect of the surface composition', represented by comparing the total received power as follows from using either regolith (ϵ=4.0) or CO_2 ice (ϵ=2.1) as the polar host material for each measurement. It should be noted measurement BSR-3.1 was excluded from these results as it does not pass 60°N nor 60°S latitude, making it irrelevant for this comparison.
- **Section E.5** presents the model results for the 'Periodicity and Topography Effects', represented by isolating the topography factors for the specular point and point of maximum return and plotting their behavior throughout the duration of each measurement.

E.1. Model Results: 'Effects of the BSR Model Parameters'

Model results for BSR-1.1 (at 4 pixel/degree resolution)
Effects of the BSR model parameters
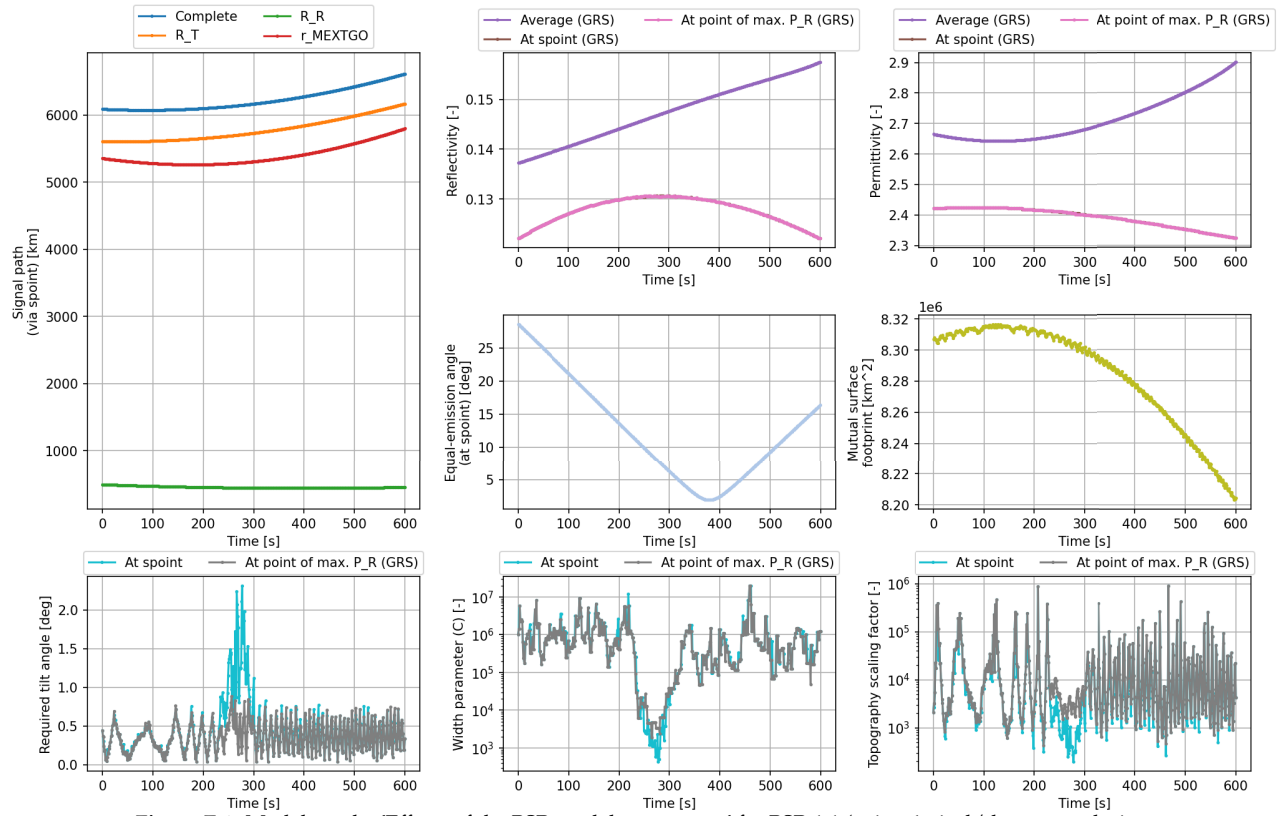
Figure E.1: Model results 'Effects of the BSR model parameters' for BSR-1.1 (using 4 pixel/degree resolution, GRS data and CO_2 ice as the polar host material), own work

Model results for BSR-1.2 (at 4 pixel/degree resolution)
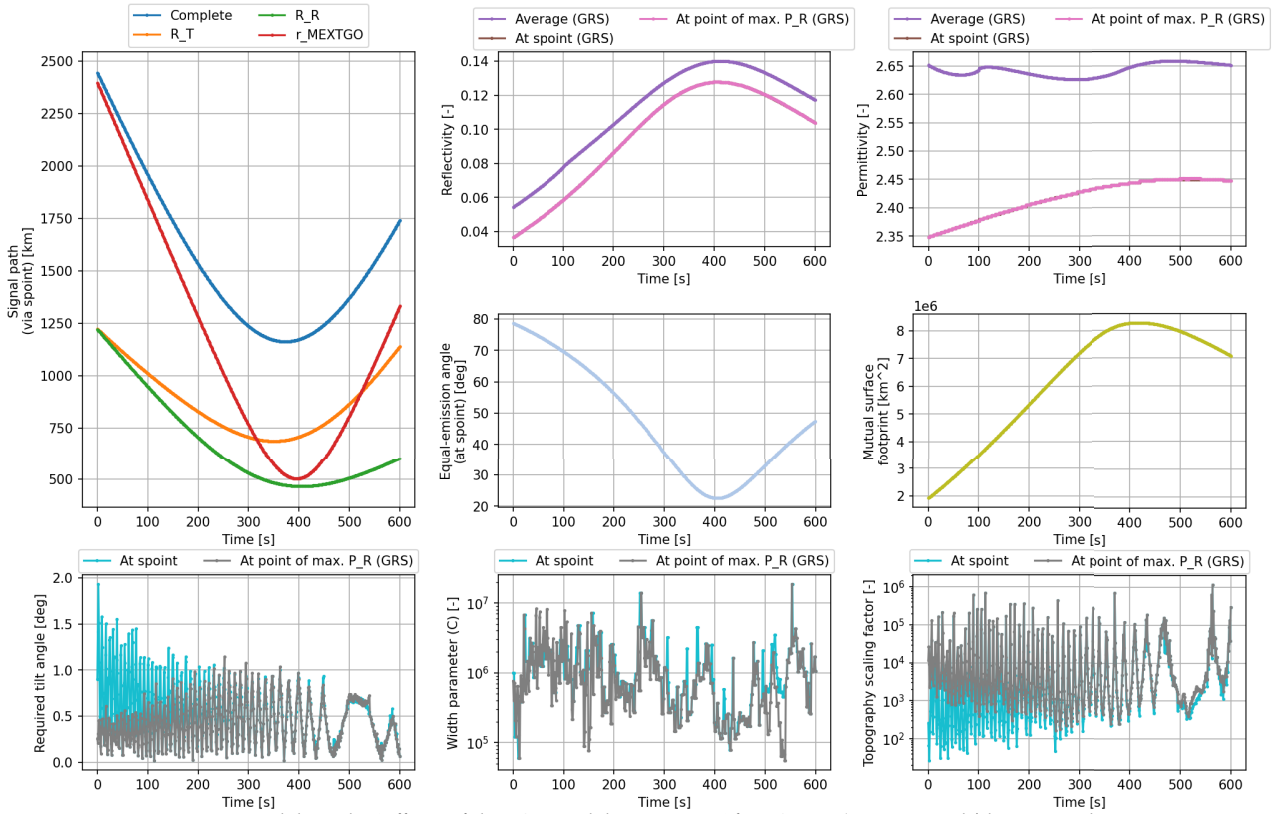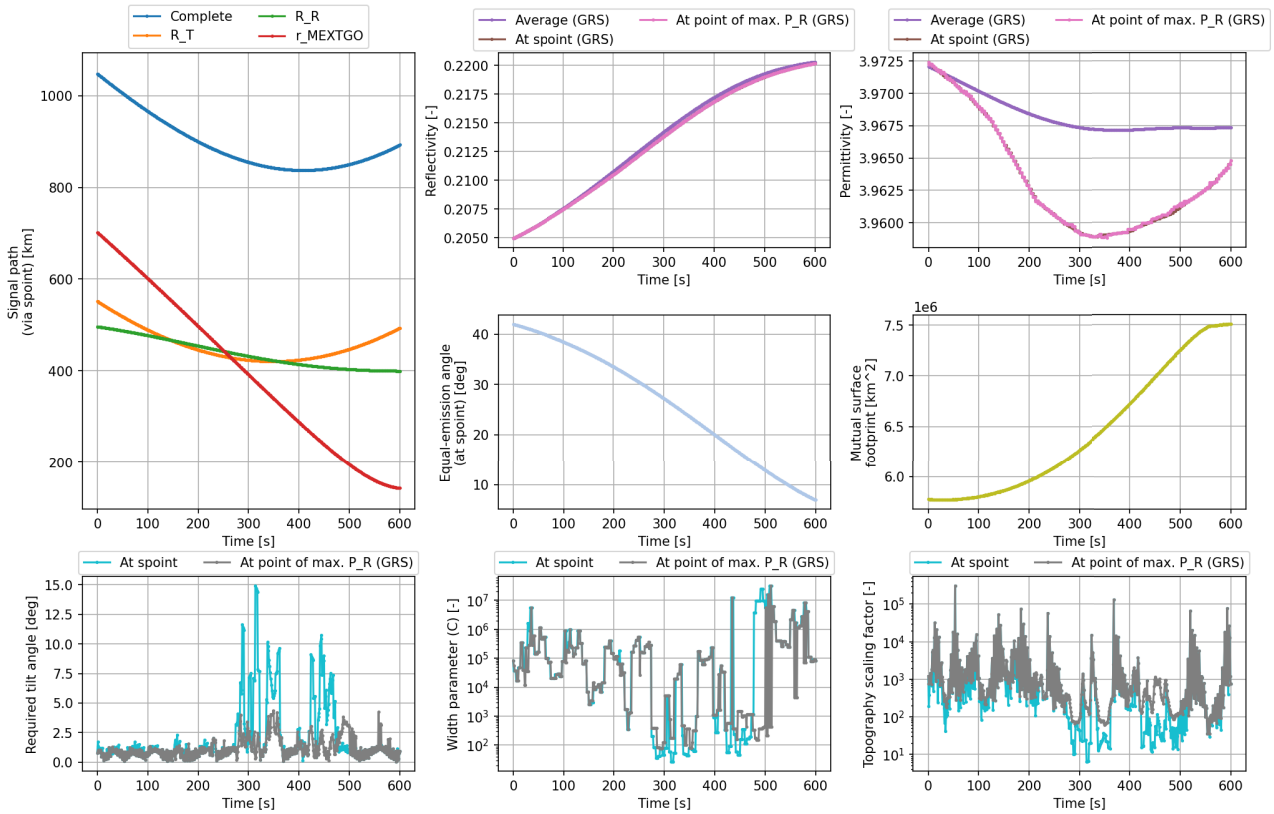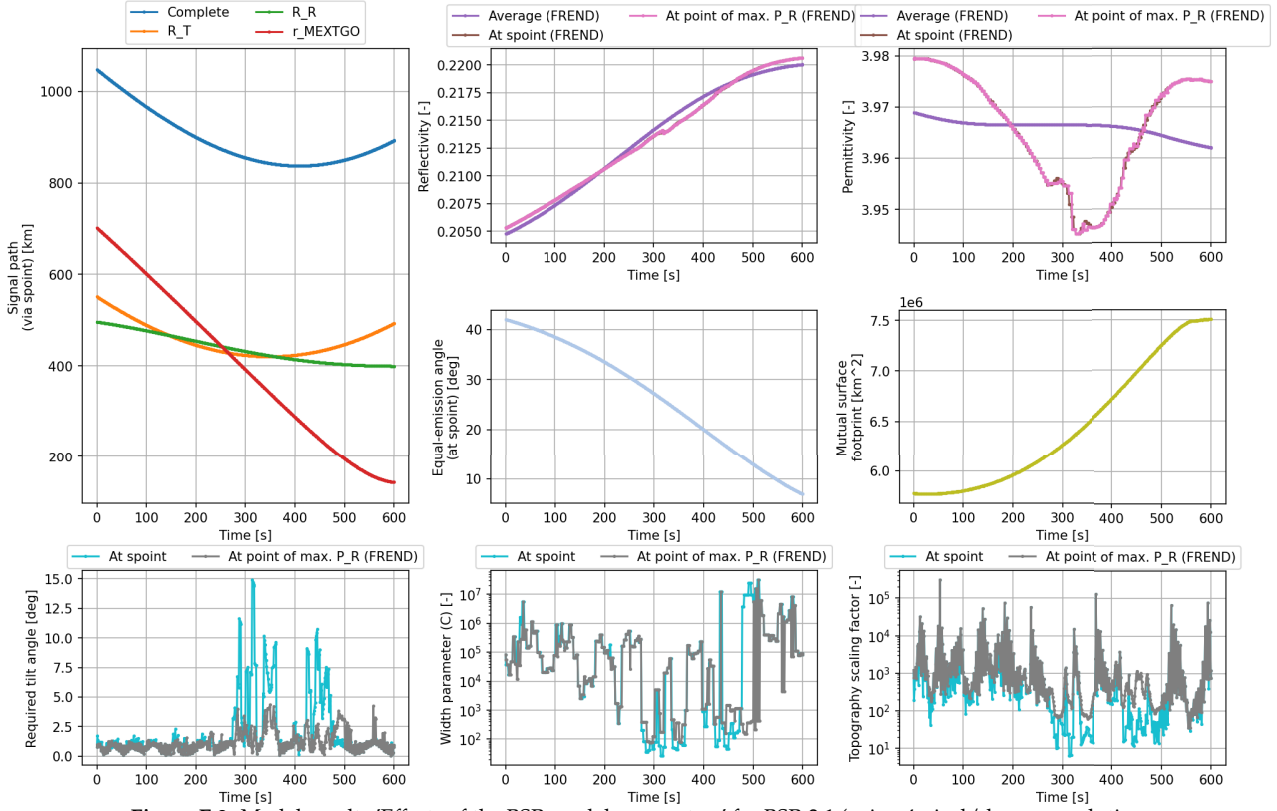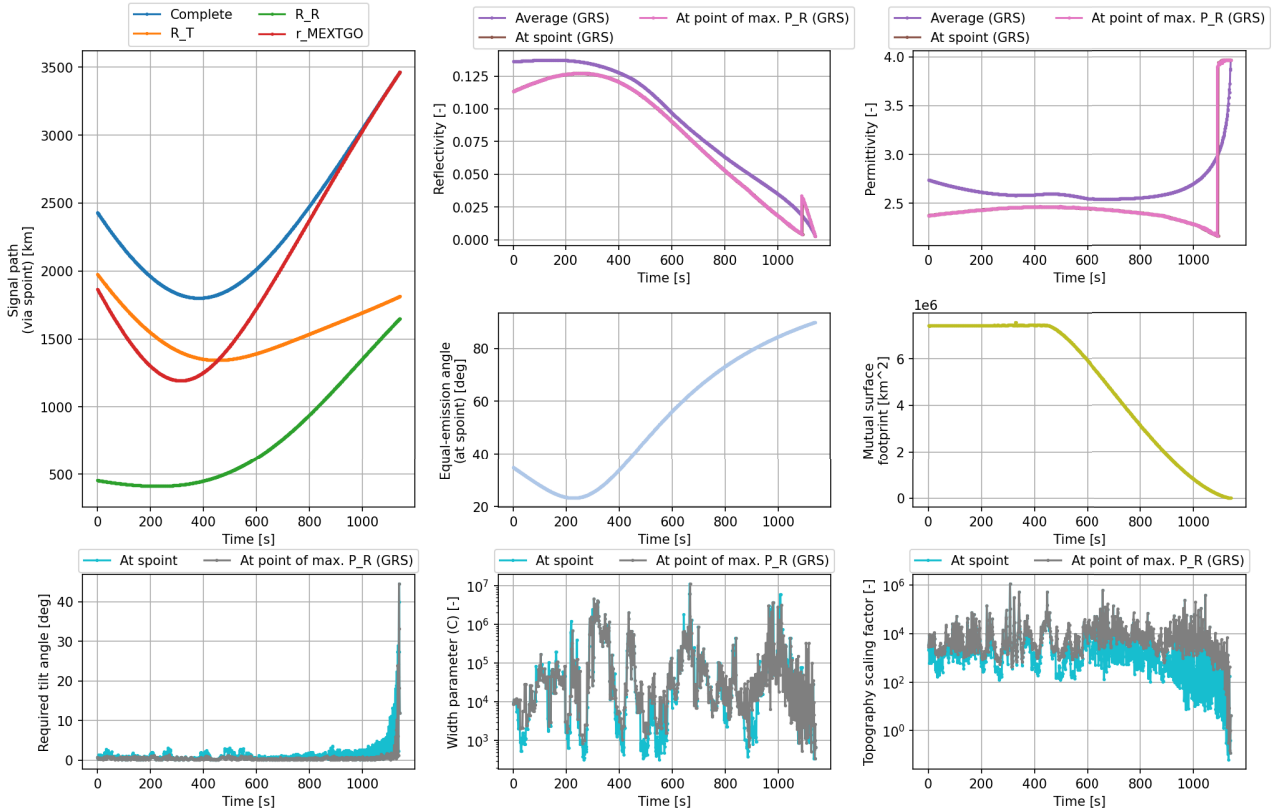### Effects of the BSR model parameters
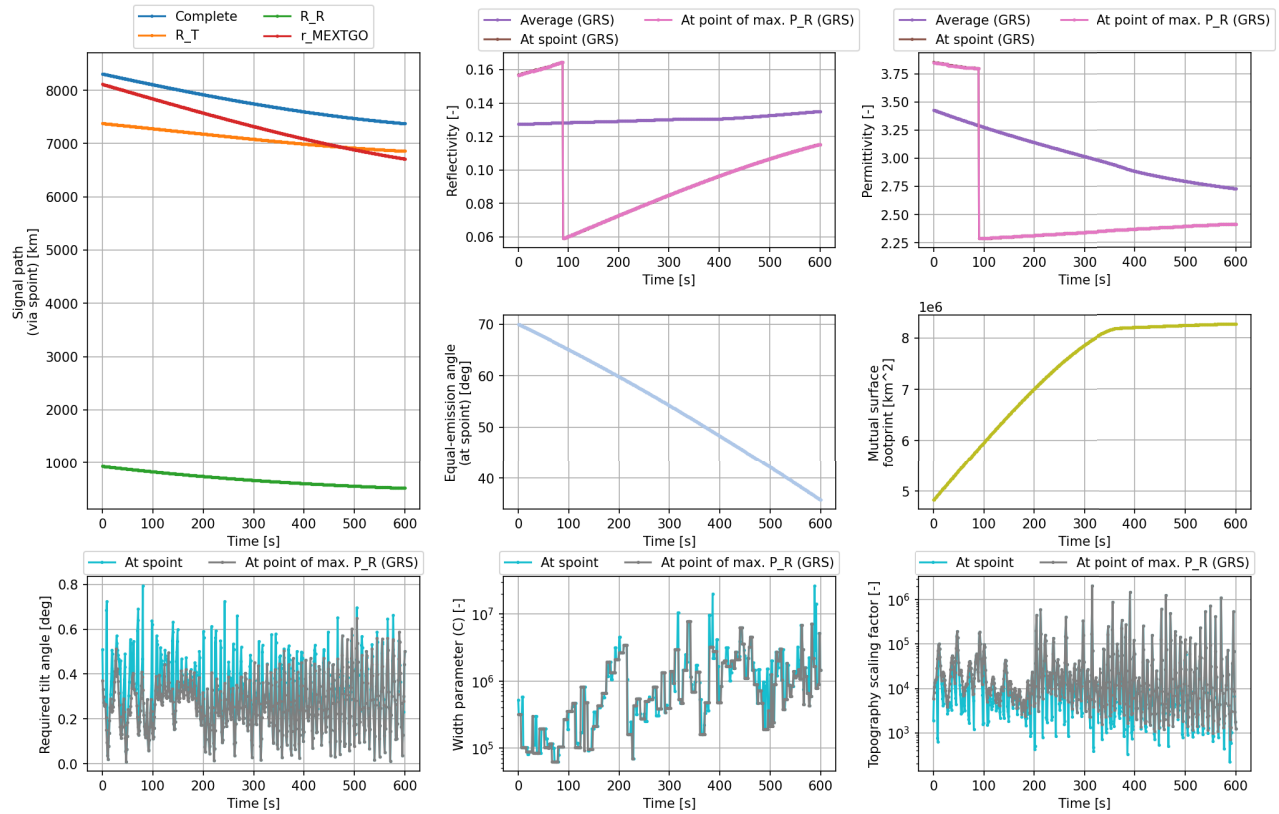
Figure E.2: Model results 'Effects of the BSR model parameters' for BSR-1.2 (using 4 pixel/degree resolution, GRS data and CO_2 ice as the polar host material), own work

Model results for BSR-1.3 (at 4 pixel/degree resolution)
Effects of the BSR model parameters
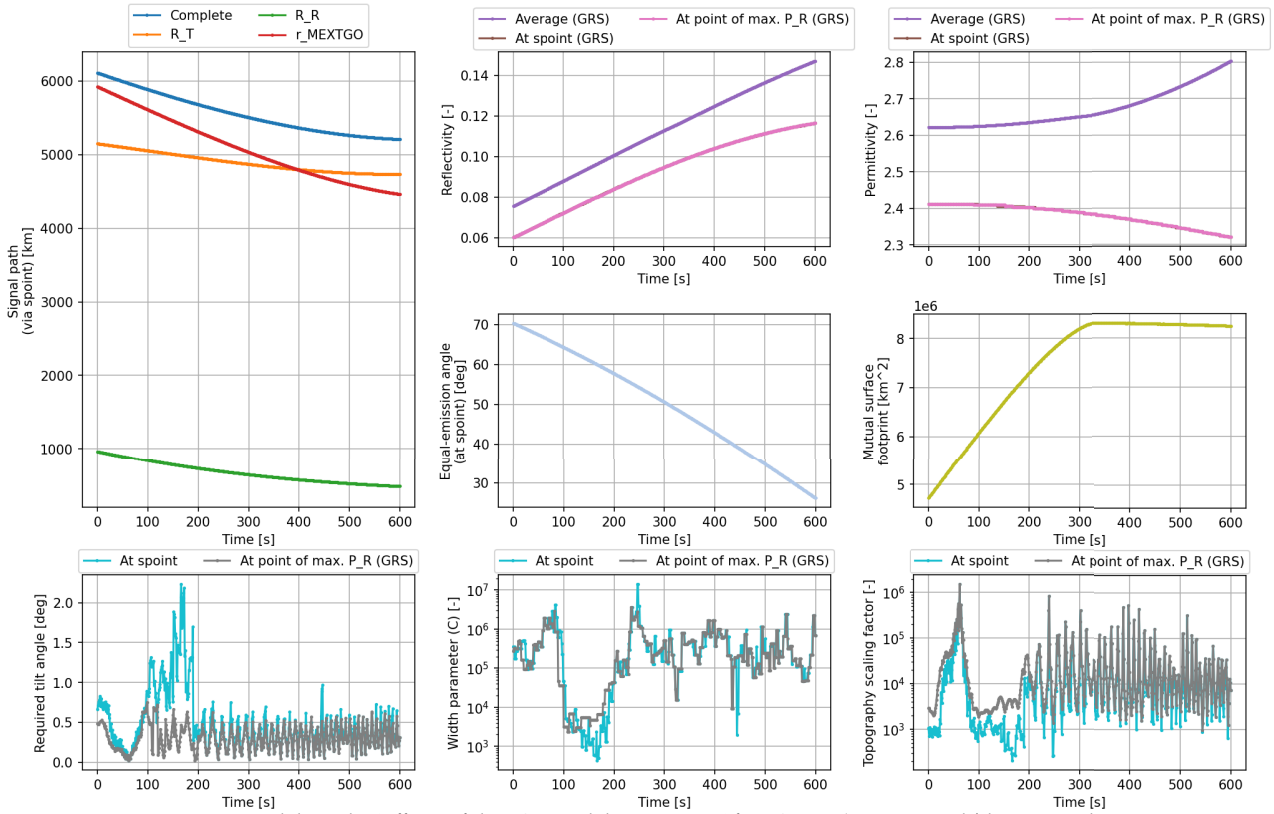
Figure E.3: Model results 'Effects of the BSR model parameters' for BSR-1.3 (using 4 pixel/degree resolution, GRS data and CO_2 ice as the polar host material), own work

Model results for BSR-1.4 (at 4 pixel/degree resolution)
Effects of the BSR model parameters
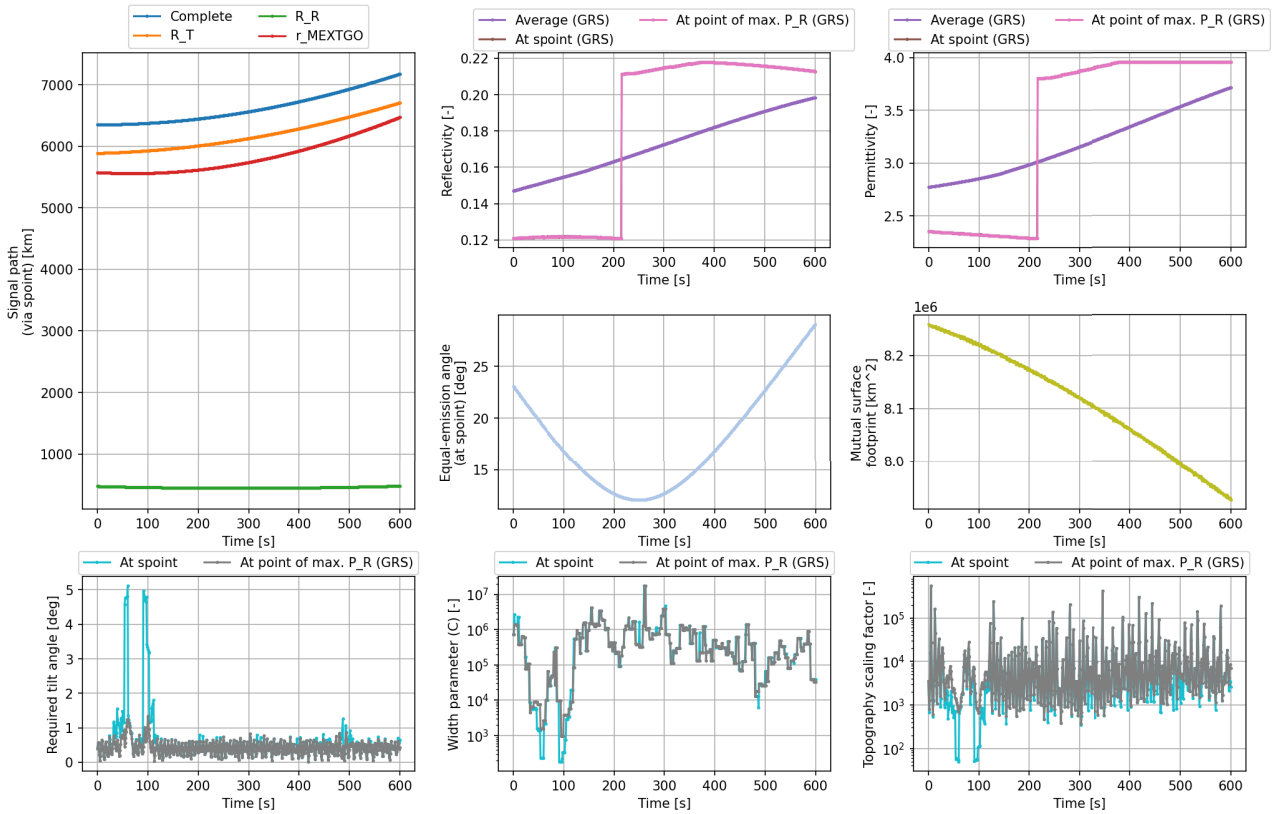
Figure E.4: Model results 'Effects of the BSR model parameters' for BSR-1.4 (using 4 pixel/degree resolution, GRS data and CO_2 ice as the polar host material), own work

Model results for BSR-2.1 (at 4 pixel/degree resolution)
Effects of the BSR model parameters
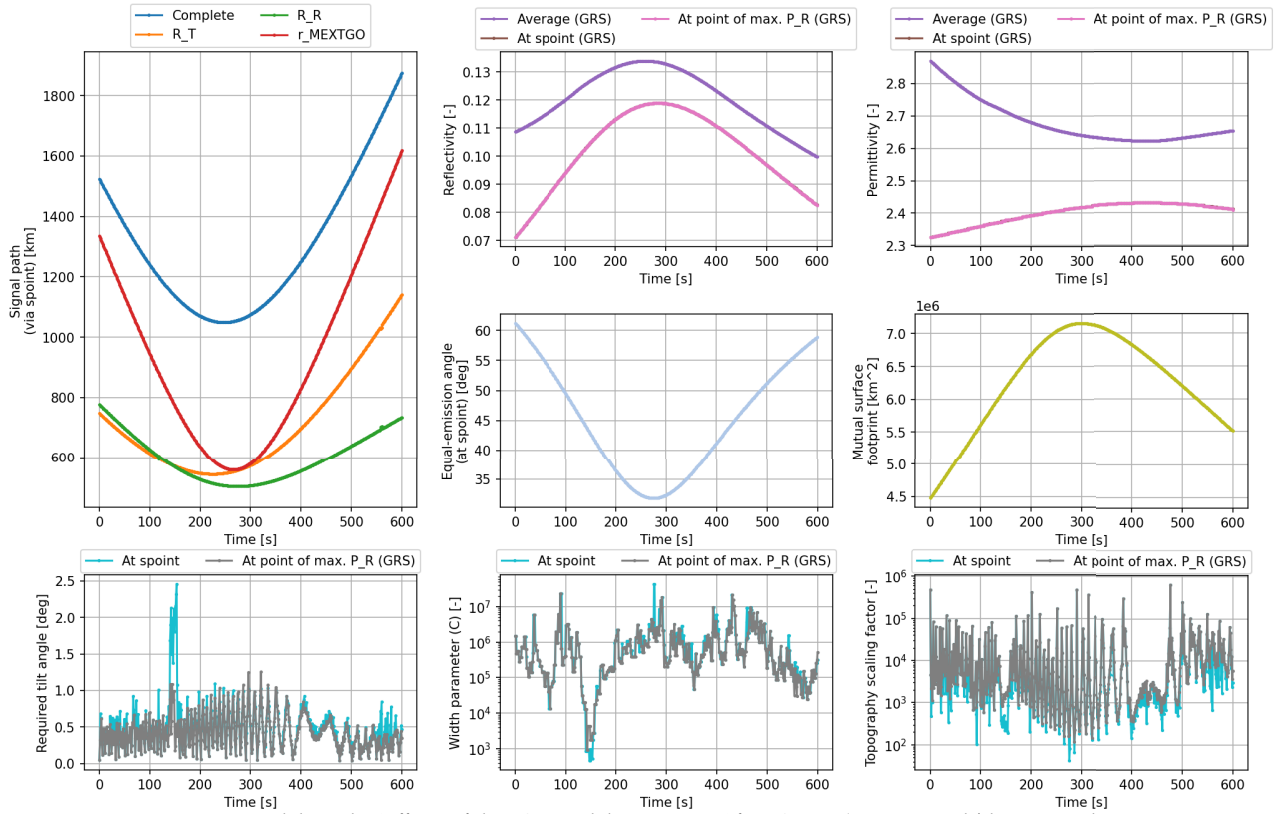
Figure E.5: Model results 'Effects of the BSR model parameters' for BSR-2.1 (using 4 pixel/degree resolution, GRS data and CO_2 ice as the polar host material), own work

Model results for BSR-2.1 (at 16 pixel/degree resolution)
Effects of the BSR model parameters
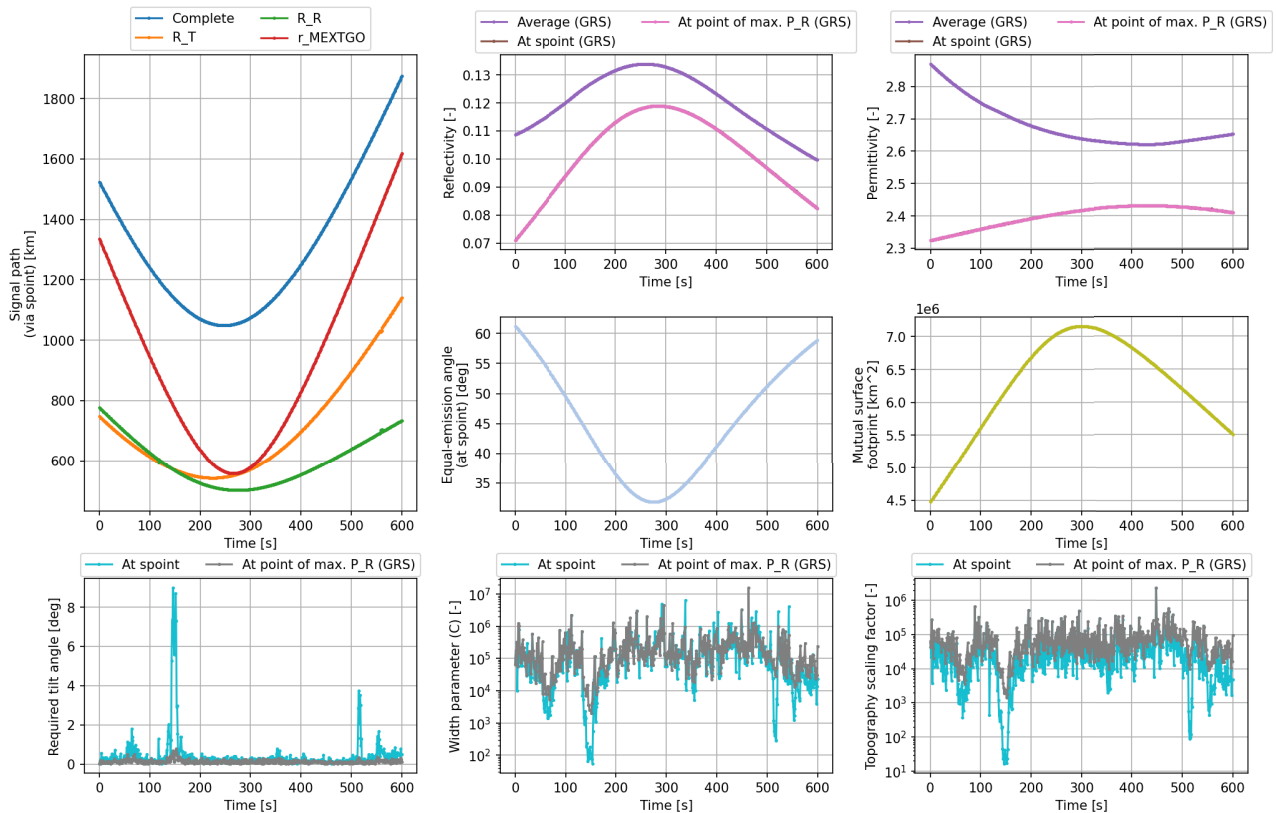
Figure E.6: Model results 'Effects of the BSR model parameters' for BSR-2.1 (using 16 pixel/degree resolution, GRS data and CO_2 ice as the polar host material), own work

Model results for BSR-2.2 (at 4 pixel/degree resolution)
Effects of the BSR model parameters

Figure E.7: Model results 'Effects of the BSR model parameters' for BSR-2.2 (using 4 pixel/degree resolution, GRS data and CO_2 ice as the polar host material), own work

Model results for BSR-3.1 (at 4 pixel/degree resolution)
Effects of the BSR model parameters

Figure E.8: Model results 'Effects of the BSR model parameters' for BSR-3.1 (using 4 pixel/degree resolution, GRS data and CO_2 ice as the polar host material), own work

Model results for BSR-3.1 (at 4 pixel/degree resolution)
Effects of the BSR model parameters

Figure E.9: Model results 'Effects of the BSR model parameters' for BSR-3.1 (using 4 pixel/degree resolution, FREND data and CO_2 ice as the polar host material), own work

Model results for BSR-4.1 (at 4 pixel/degree resolution)
Effects of the BSR model parameters

Figure E.10: Model results 'Effects of the BSR model parameters' for BSR-4.1 (using 4 pixel/degree resolution, GRS data and CO_2 ice as the polar host material), own work

E.2. Model Results: 'Power Distribution over the Mutual Footprint'
E.2.1. Power Distribution over the Mutual Footprint
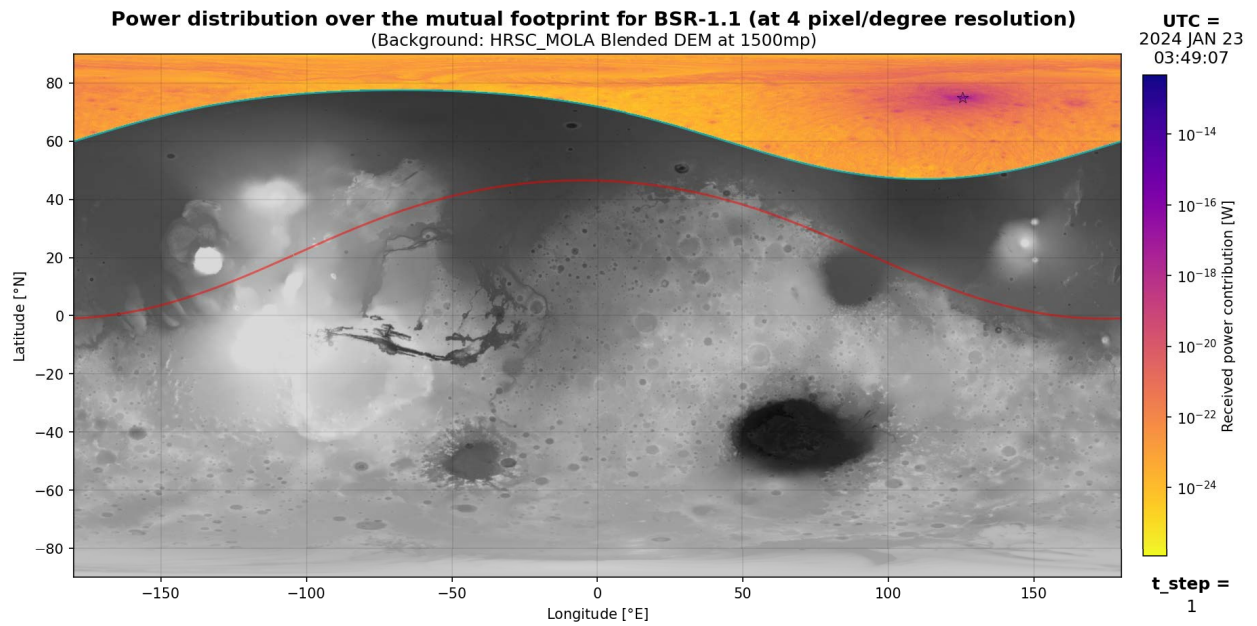
Figure E.11: Model results 'Power distribution over the mutual footprint' for BSR-1.1 at start of measurement (23rd of January 2024 03:49:07; using 4 pixel/degree resolution, GRS data and CO_2 ice as the polar host material), own work
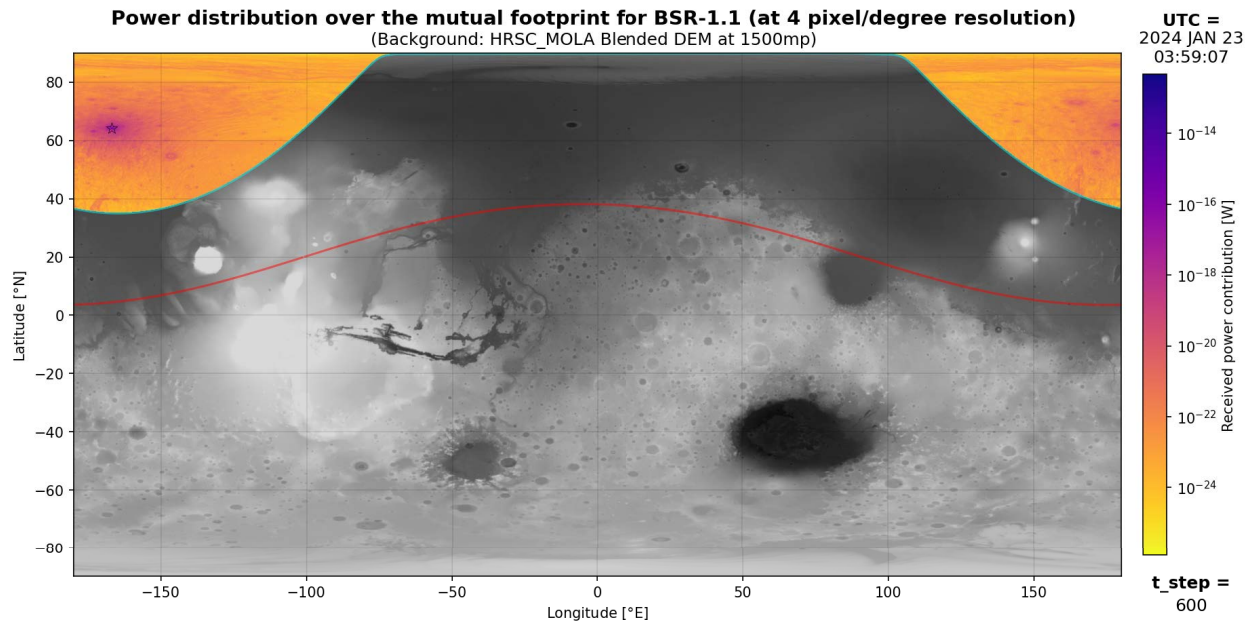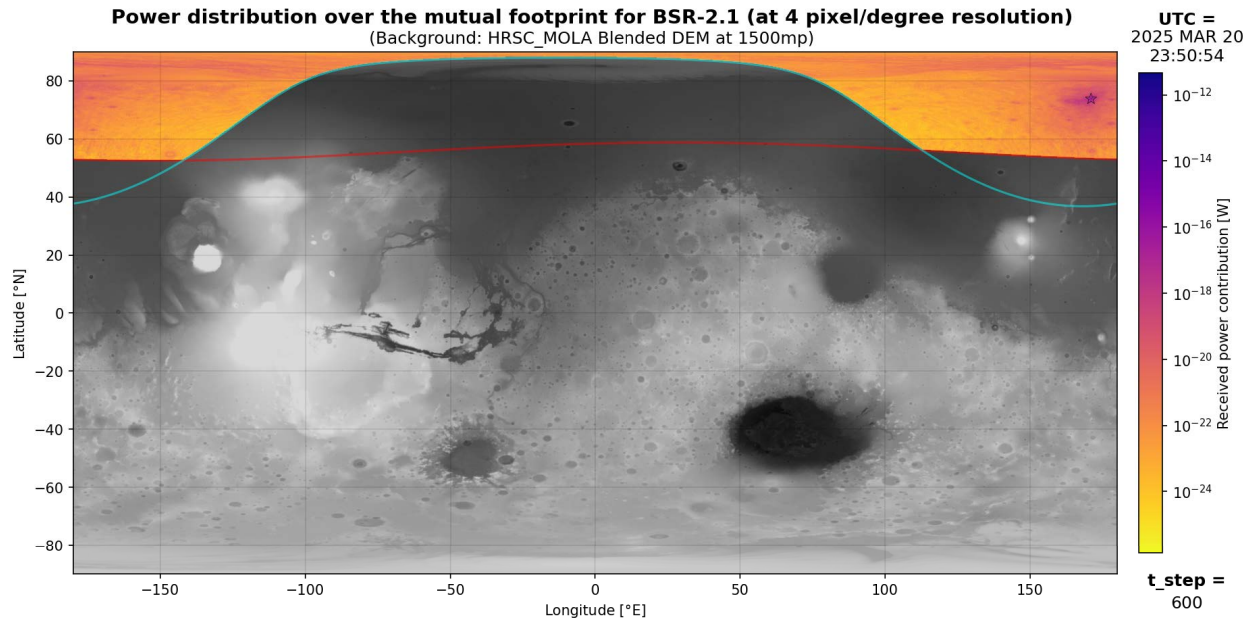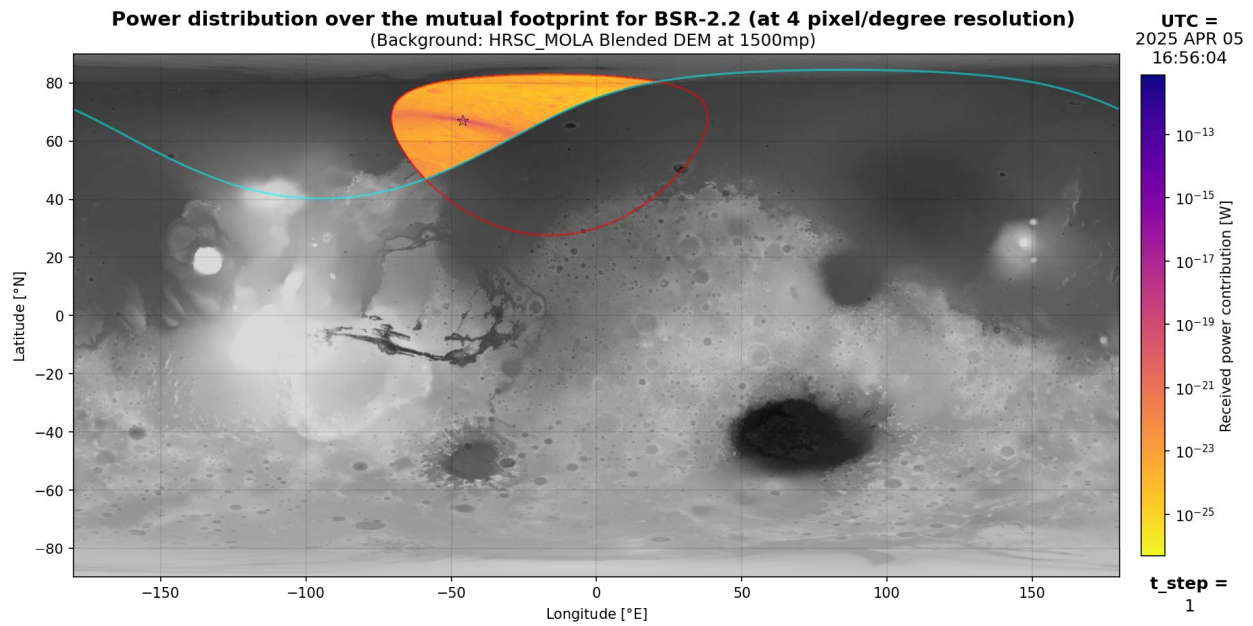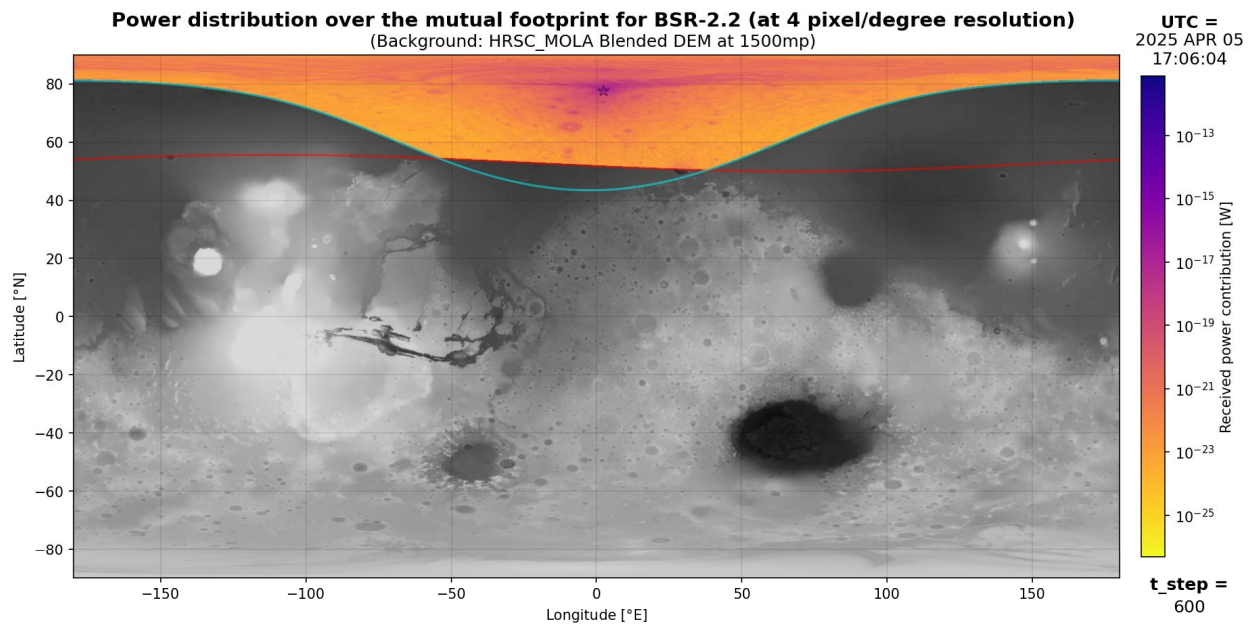

Figure E.12: Model results 'Power distribution over the mutual footprint' for BSR-1.1 at end of measurement (23rd of January 2024 03:59:07; using 4 pixel/degree resolution, GRS data and CO_2 ice as the polar host material), own work
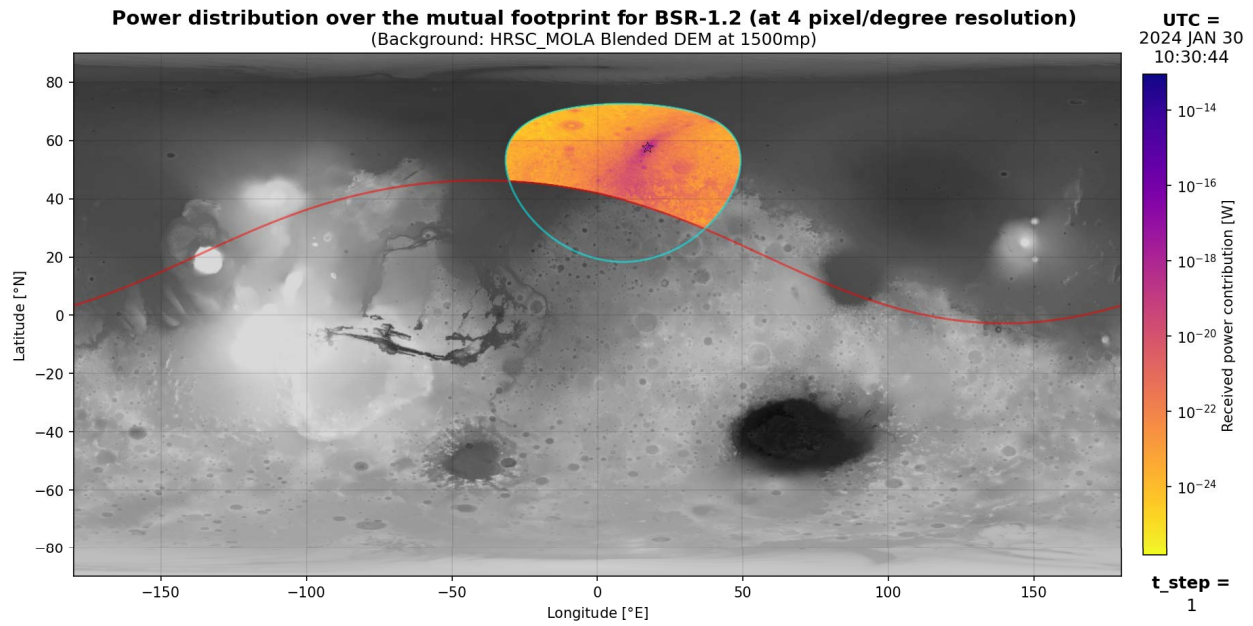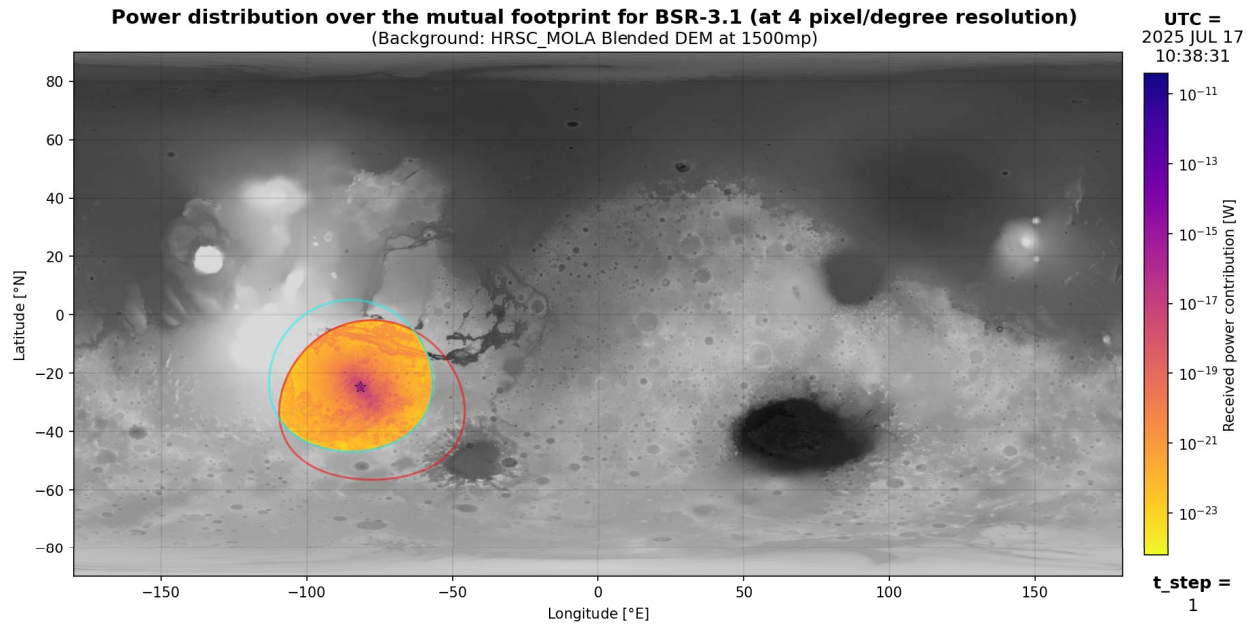
Figure E.13: Model results 'Power distribution over the mutual footprint' for BSR-1.2 at start of measurement (30th of January 2024 10:30:44; using 4 pixel/degree resolution, GRS data and CO_2 ice as the polar host material), own work
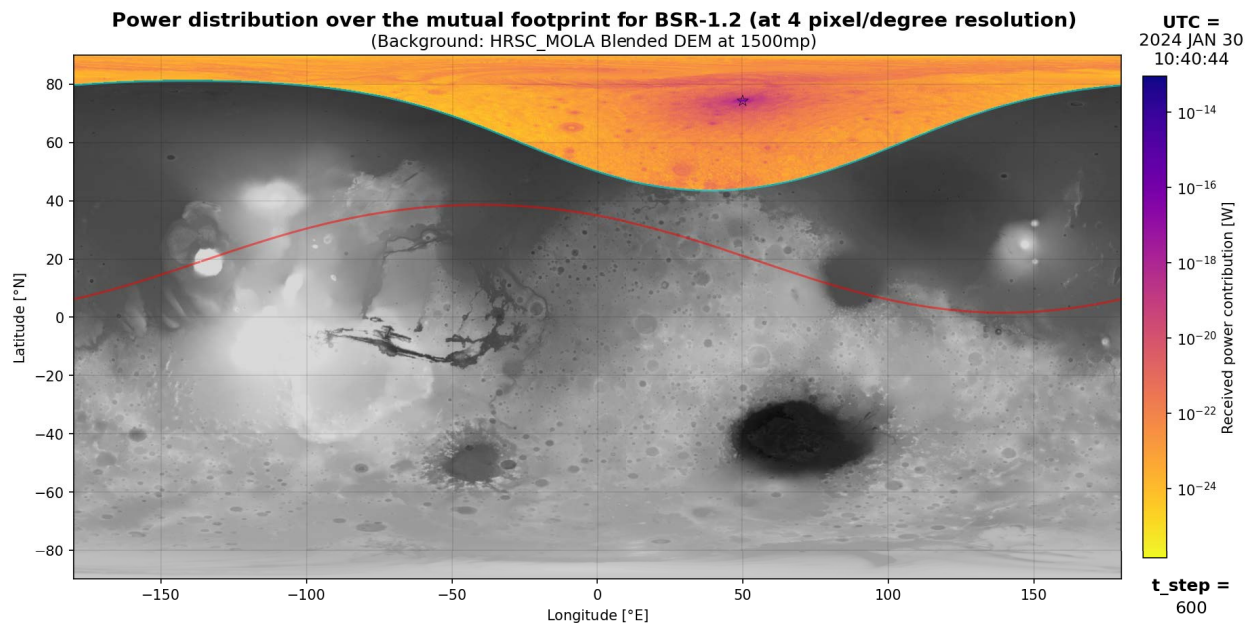
Figure E.14: Model results 'Power distribution over the mutual footprint' for BSR-1.2 at end of measurement (30th of January 2024 10:40:44; using 4 pixel/degree resolution, GRS data and CO_2 ice as the polar host material), own work
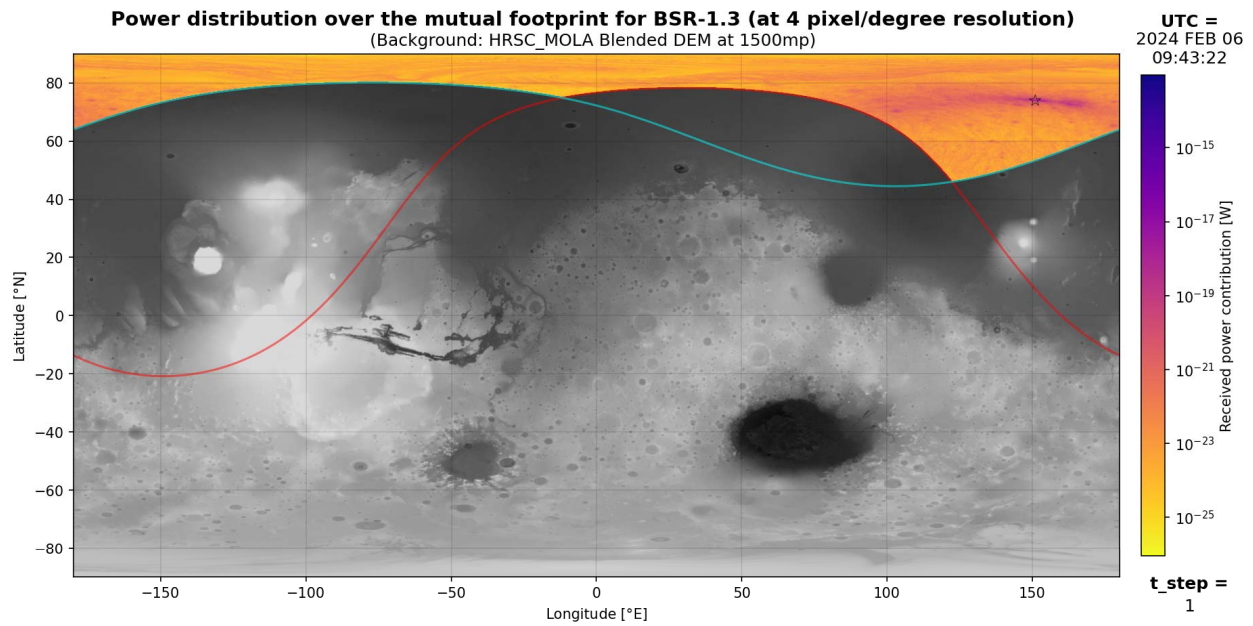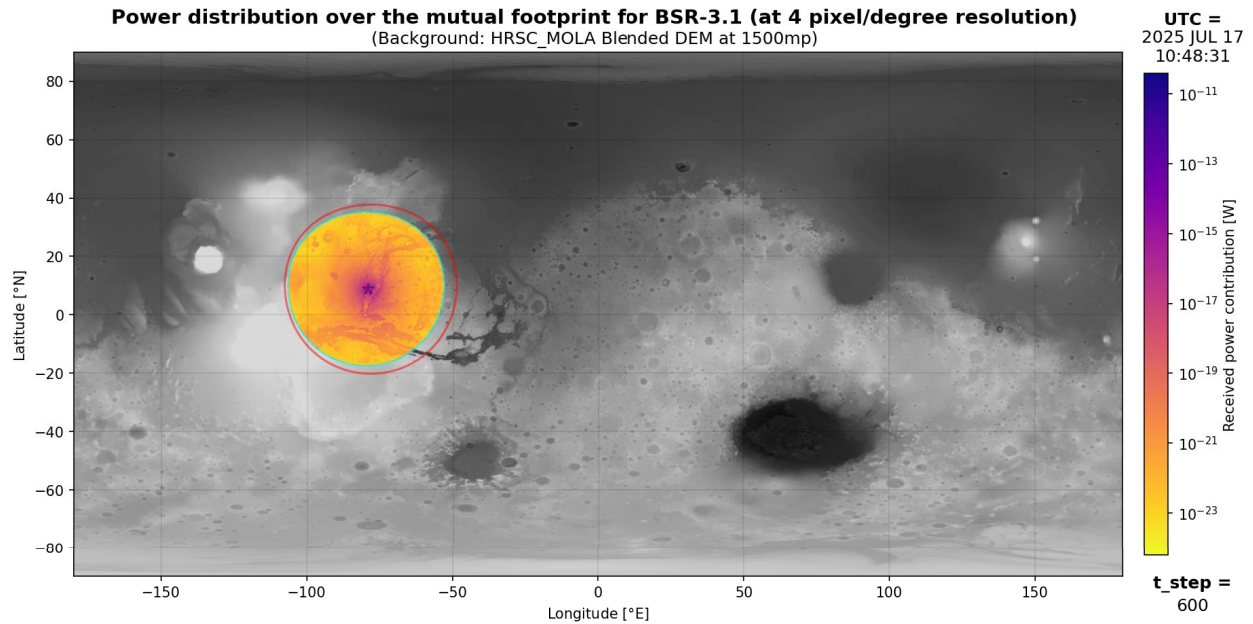
Figure E.15: Model results 'Power distribution over the mutual footprint' for BSR-1.3 at start of measurement (6th of February 2024 09:43:22; using 4 pixel/degree resolution, GRS data and CO_2 ice as the polar host material), own work
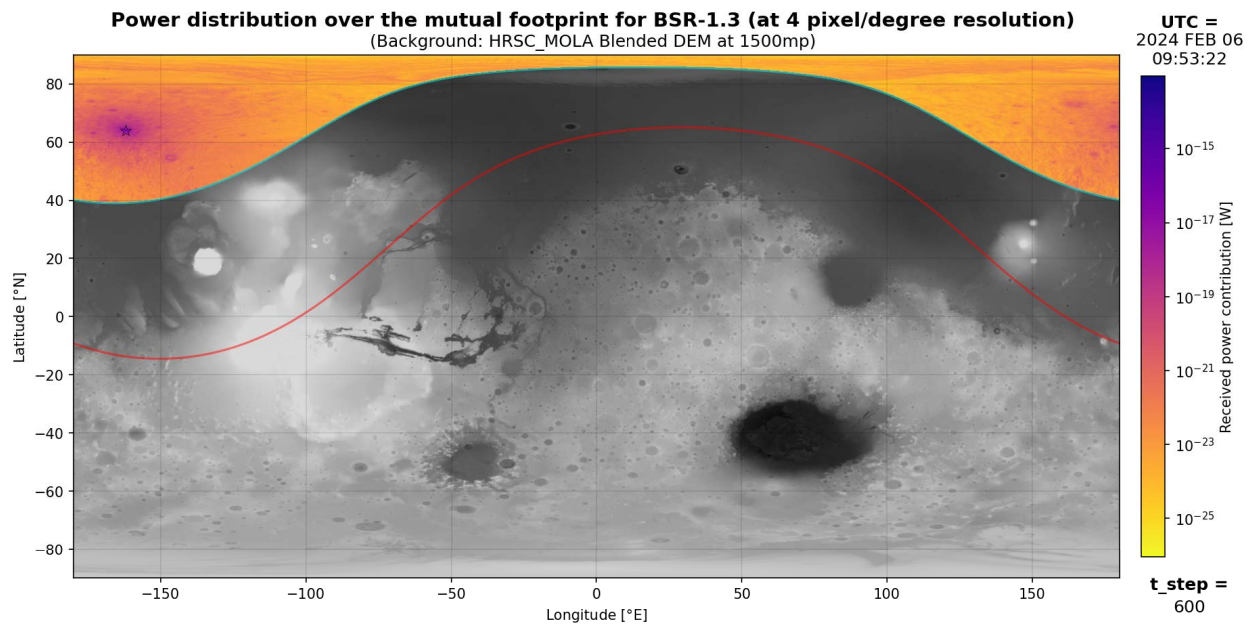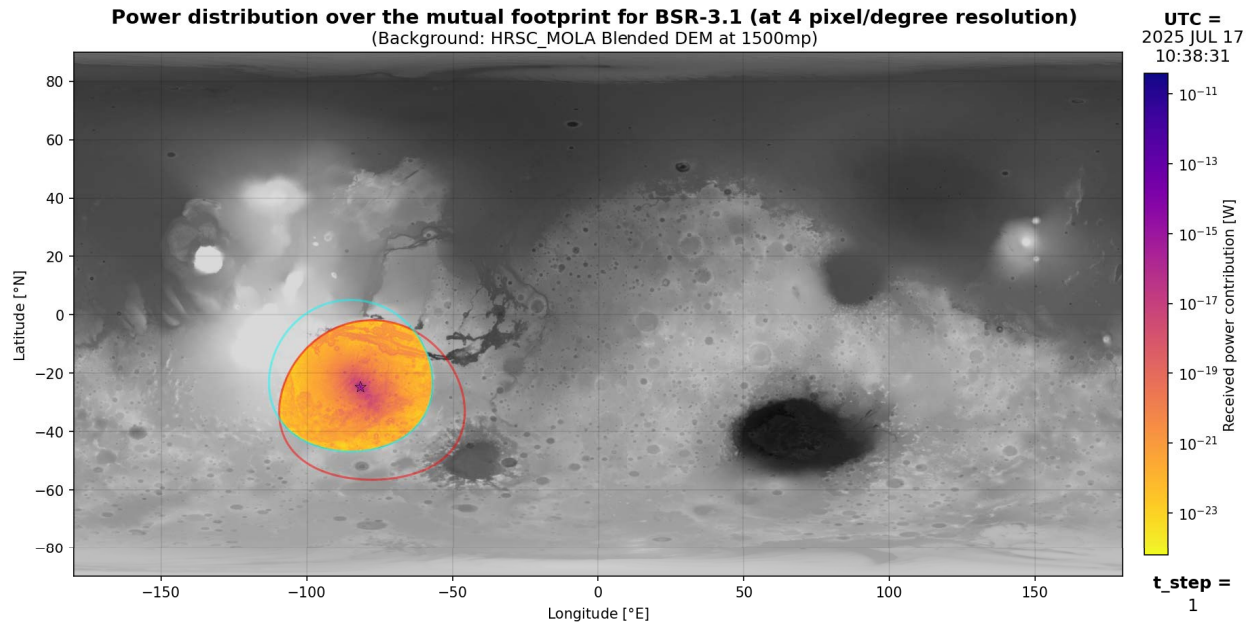

Figure E.16: Model results 'Power distribution over the mutual footprint' for BSR-1.3 at end of measurement (6th of February 2024 09:53:22; using 4 pixel/degree resolution, GRS data and CO_2 ice as the polar host material), own work
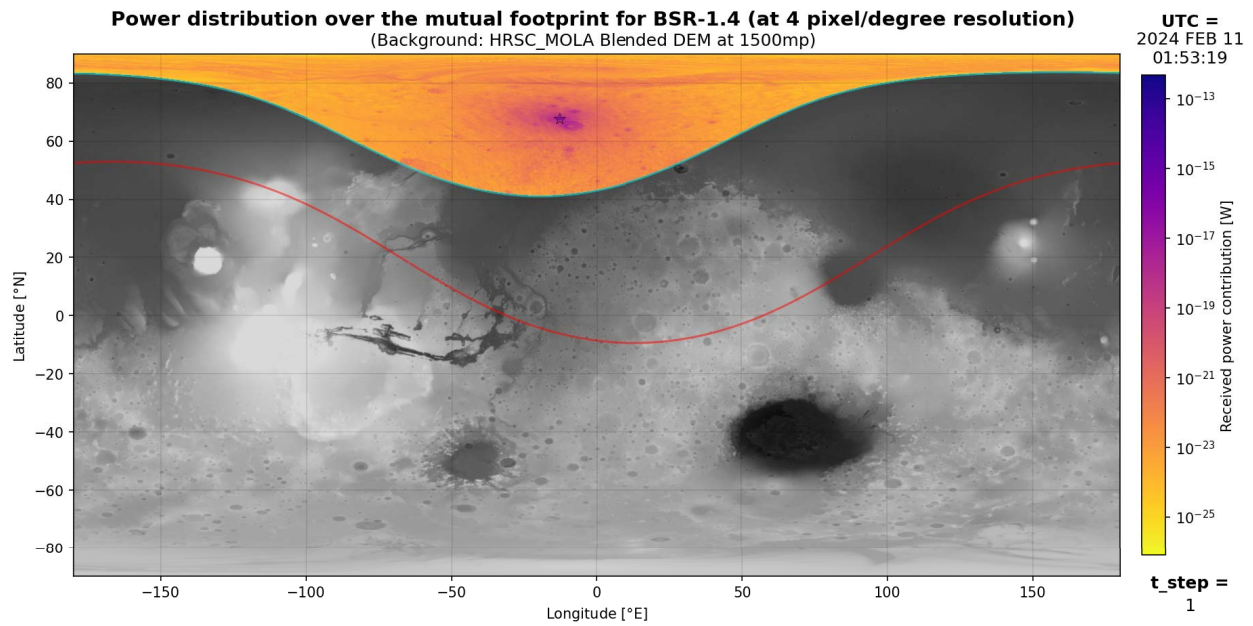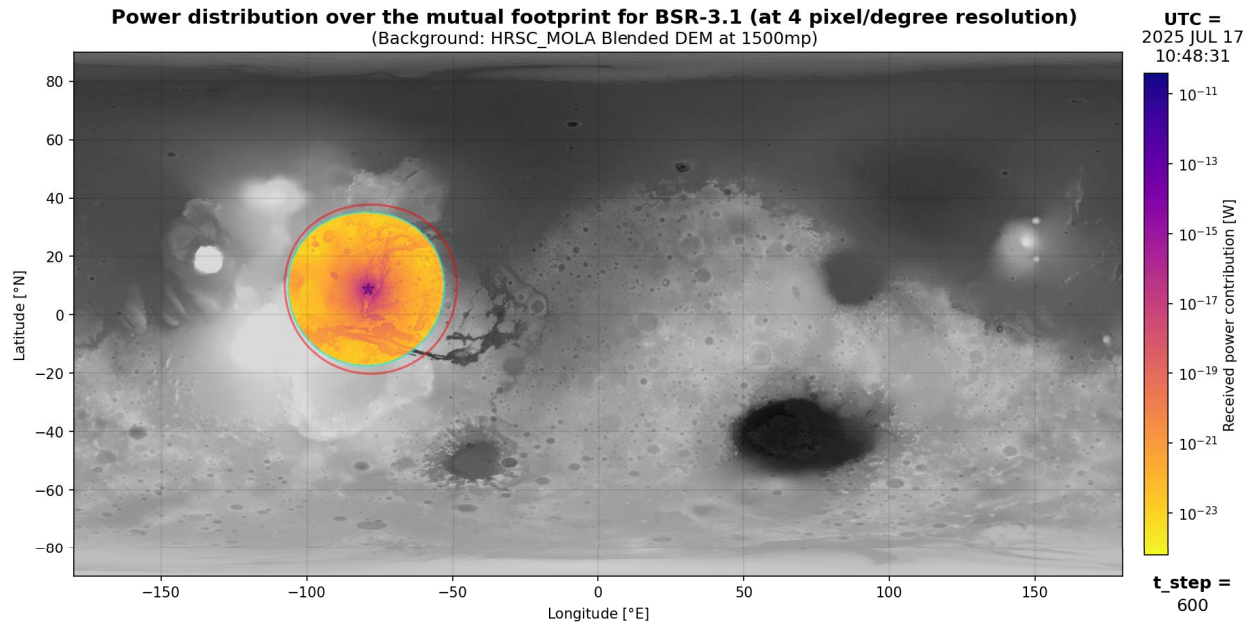
Figure E.17: Model results 'Power distribution over the mutual footprint' for BSR-1.4 at start of measurement (11th of February 2024 01:53:19; using 4 pixel/degree resolution, GRS data and CO_2 ice as the polar host material), own work
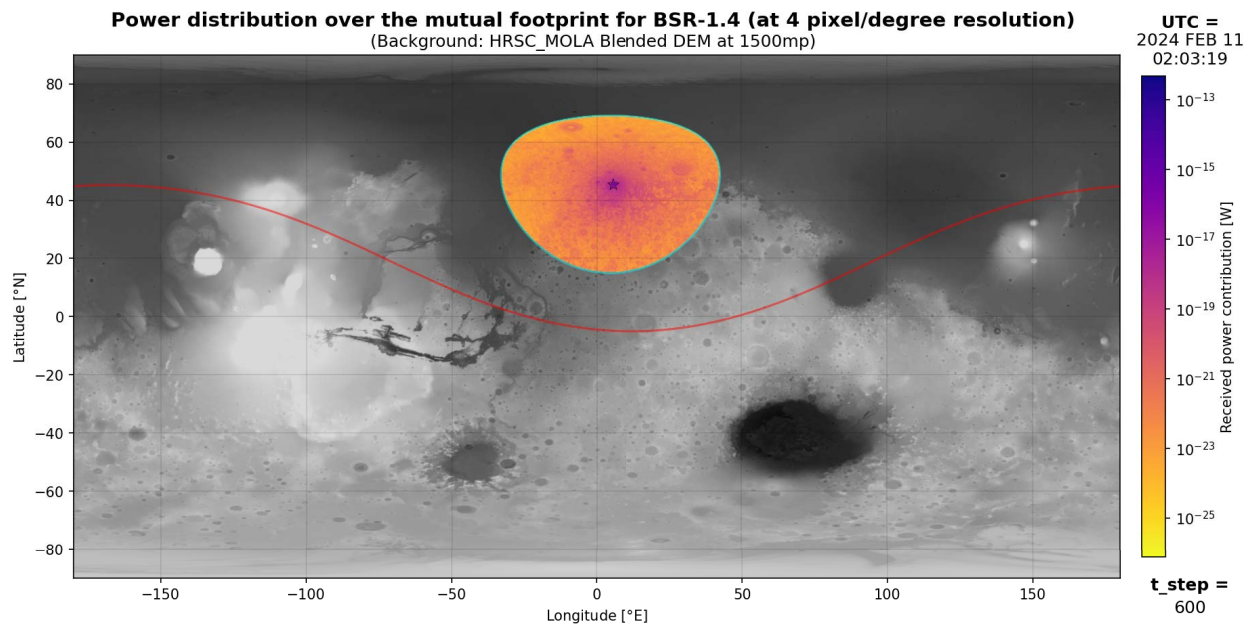
Figure E.18: Model results 'Power distribution over the mutual footprint' for BSR-1.4 at end of measurement (11th of February 2024 02:03:19; using 4 pixel/degree resolution, GRS data and CO_2 ice as the polar host material), own work
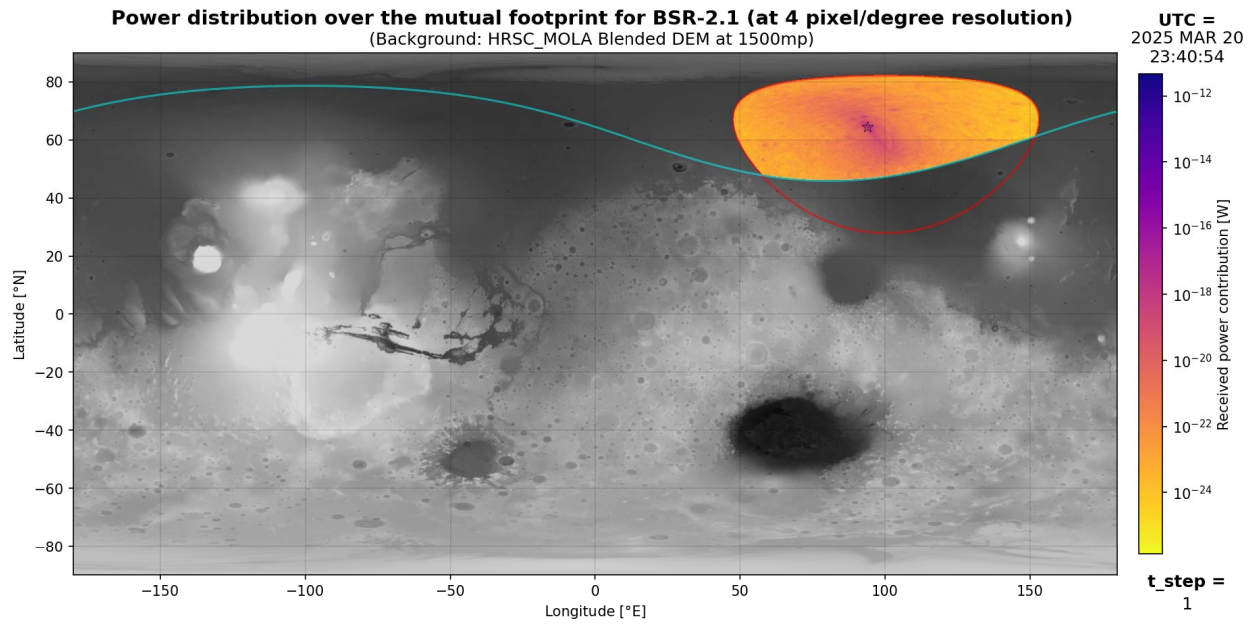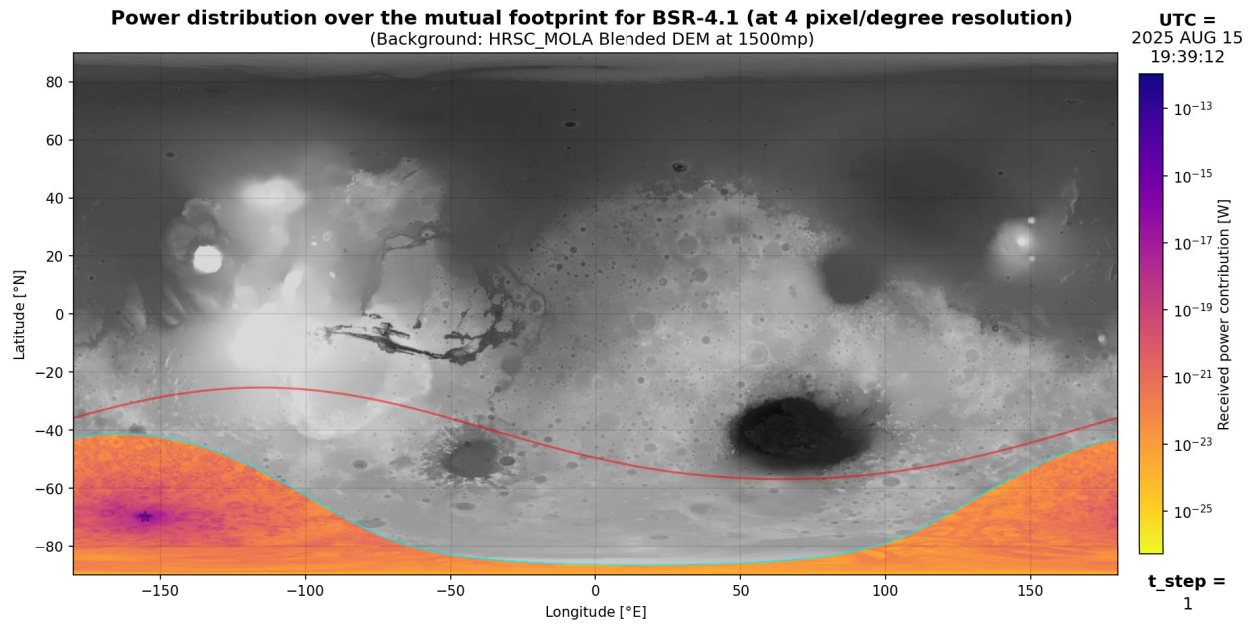
Figure E.19: Model results 'Power distribution over the mutual footprint' for BSR-2.1 at start of measurement (20th of March 2025 23:40:54; using 4 pixel/degree resolution, GRS data and CO_2 ice as the polar host material), own work
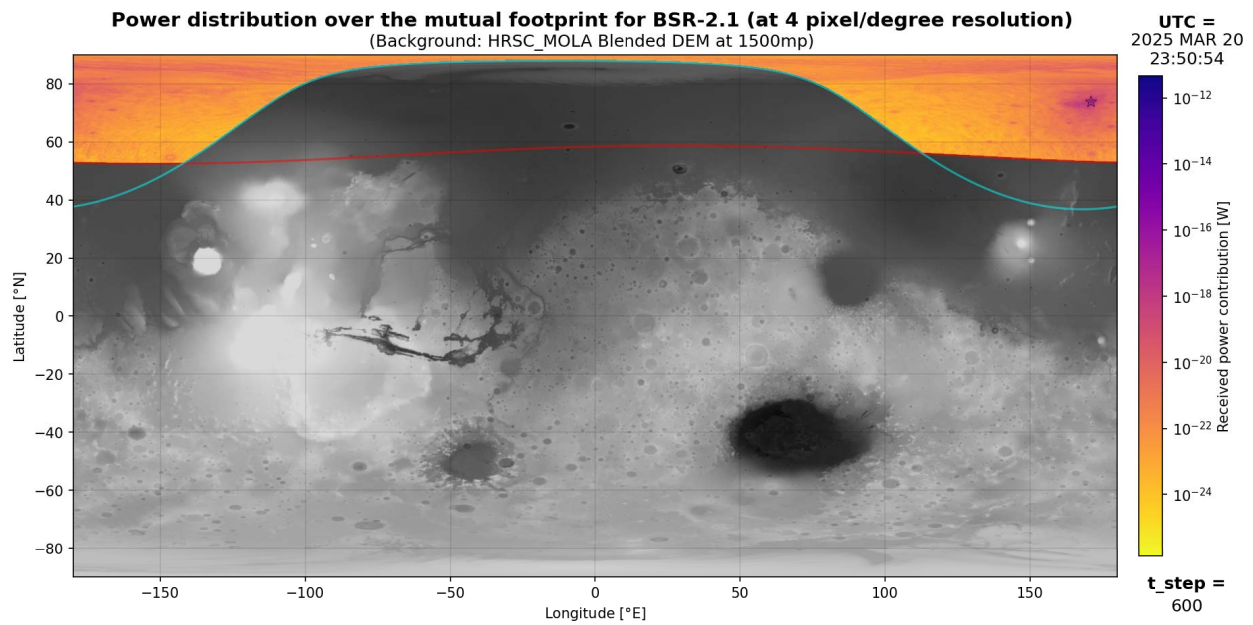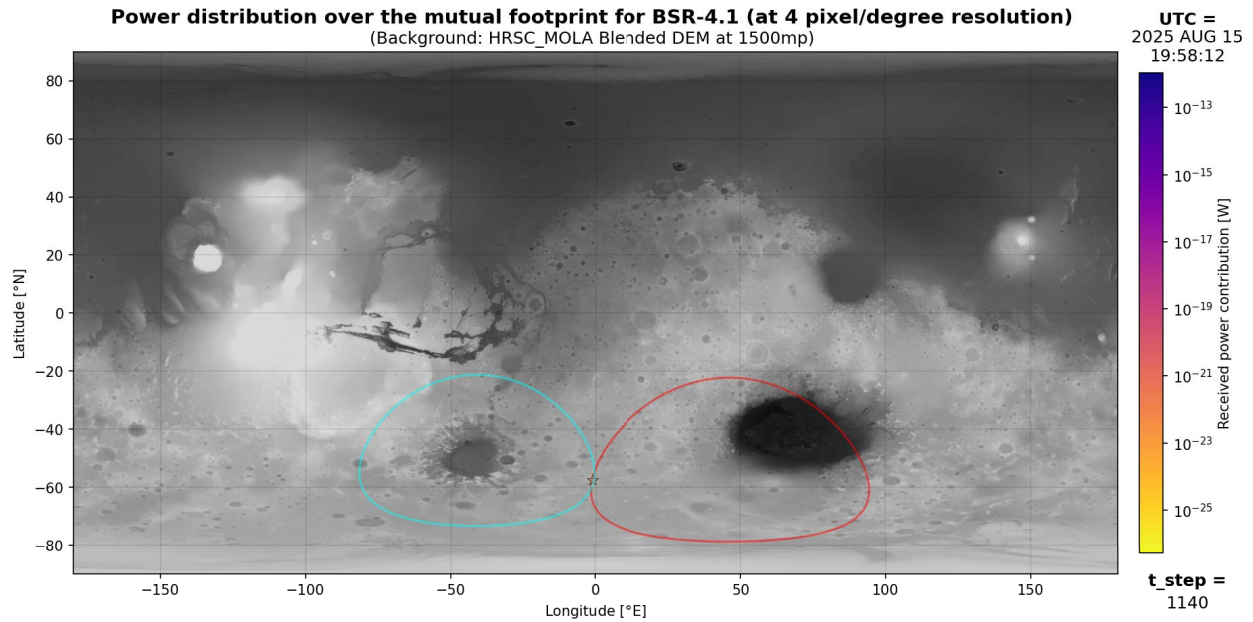

Figure E.20: Model results 'Power distribution over the mutual footprint' for BSR-2.1 at end of measurement (20th of March 2025 23:50:54; using 4 pixel/degree resolution, GRS data and CO_2 ice as the polar host material), own work
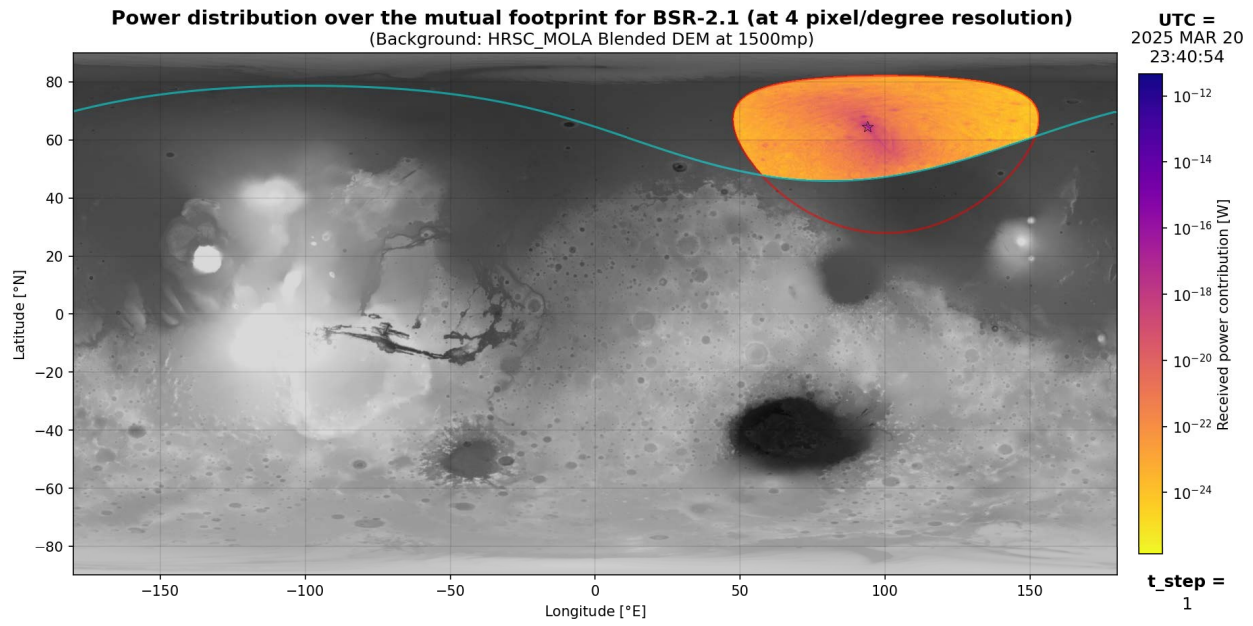
Figure E.21: Model results 'Power distribution over the mutual footprint' for BSR-2.1 at start of measurement (20th of March 2025 23:40:54; using 16 pixel/degree resolution, GRS data and CO_2 ice as the polar host material), own work

Figure E.22: Model results 'Power distribution over the mutual footprint' for BSR-2.1 at end of measurement (20th of March 2025 23:50:54; using 16 pixel/degree resolution, GRS data and CO_2 ice as the polar host material), own work
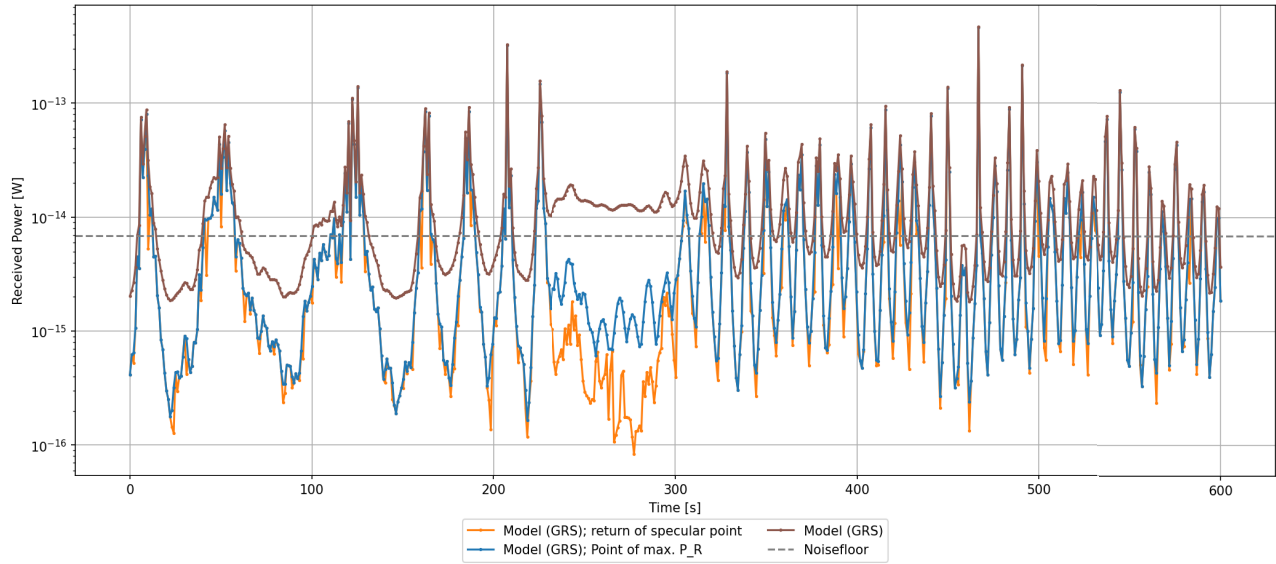
Figure E.23: Model results 'Power distribution over the mutual footprint' for BSR-2.2 at start of measurement (5th of April 2025 16:56:04; using 4 pixel/degree resolution, GRS data and CO_2 ice as the polar host material), own work

Figure E.24: Model results 'Power distribution over the mutual footprint' for BSR-2.2 at end of measurement (5th of April 2025 17:06:04; using 4 pixel/degree resolution, GRS data and CO_2 ice as the polar host material), own work

Figure E.25: Model results 'Power distribution over the mutual footprint' for BSR-3.1 at start of measurement (17th of July 2025 10:38:31; using 4 pixel/degree resolution, GRS data and CO_2 ice as the polar host material), own work

Figure E.26: Model results 'Power distribution over the mutual footprint' for BSR-3.1 at end of measurement (17th of July 2025 10:48:31; using 4 pixel/degree resolution, GRS data and CO_2 ice as the polar host material), own work

Figure E.27: Model results 'Power distribution over the mutual footprint' for BSR-3.1 at start of measurement (17th of July 2025 10:38:31; using 4 pixel/degree resolution, FREND data and CO_2 ice as the polar host material), own work

Figure E.28: Model results 'Power distribution over the mutual footprint' for BSR-3.1 at end of measurement (17th of July 2025 10:48:31; using 4 pixel/degree resolution, FREND data and CO_2 ice as the polar host material), own work

Figure E.29: Model results 'Power distribution over the mutual footprint' for BSR-4.1 at start of measurement (15th of August 2025 19:39:12; using 4 pixel/degree resolution, GRS data and CO_2 ice as the polar host material), own work

Figure E.30: Model results 'Power distribution over the mutual footprint' for BSR-4.1 at start of measurement (15th of August 2025 19:58:12; using 4 pixel/degree resolution, GRS data and CO_2 ice as the polar host material), own work

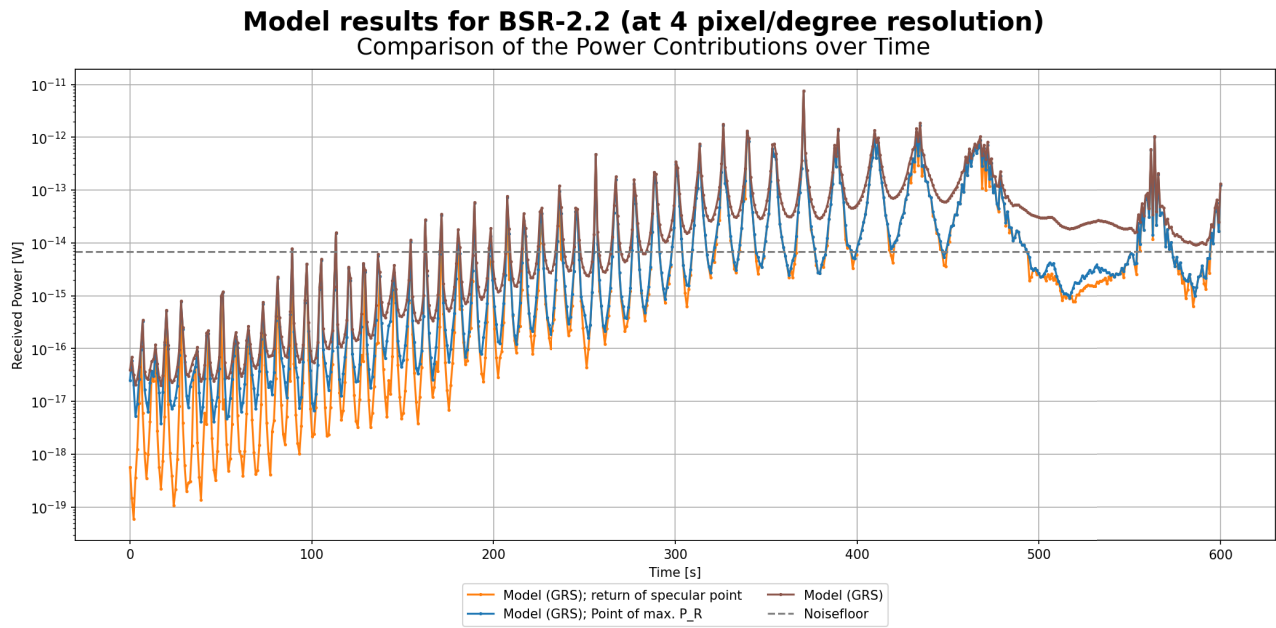### E.2.2. Comparison of the Power Contributions over Time

Figure E.31: Model results 'Power distribution over the mutual footprint' via comparison of the power contributions over time for BSR-1.1 (using 4 pixel/degree resolution, GRS data and CO_2 ice as the polar host material), own work
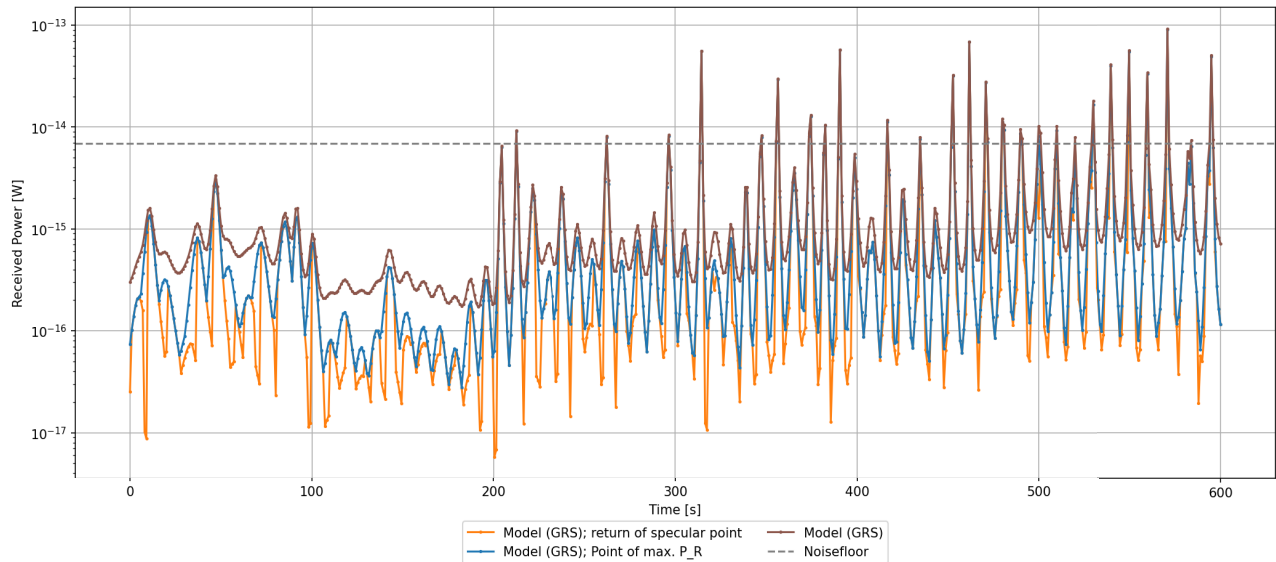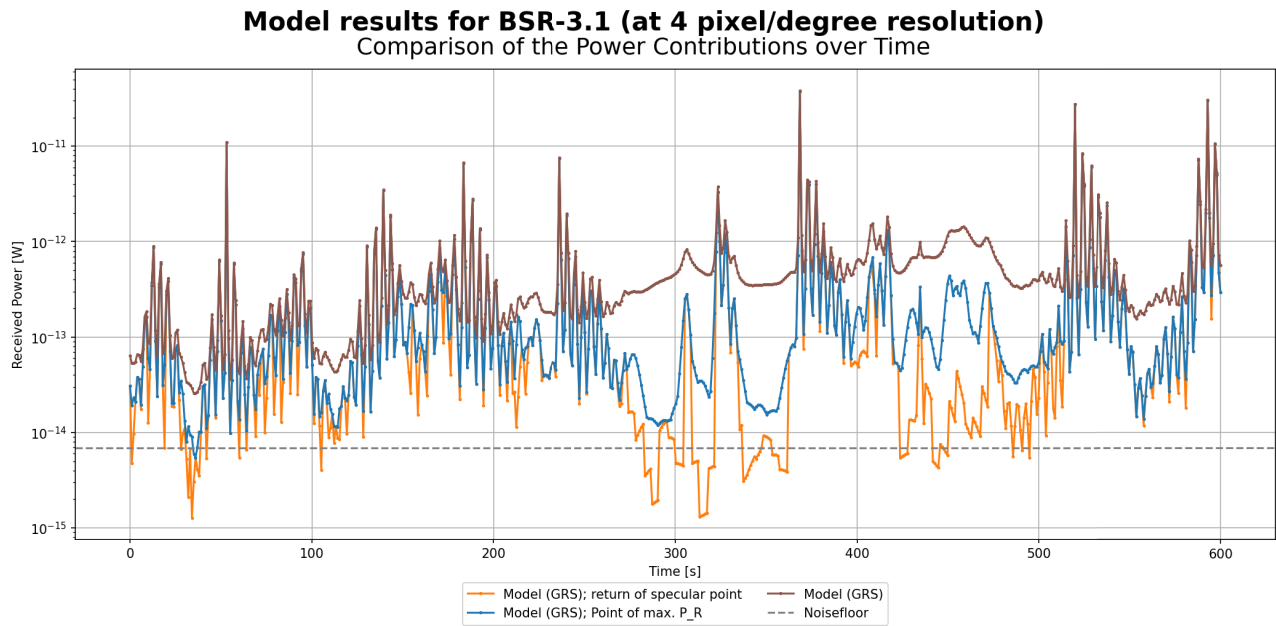

Figure E.32: Model results 'Power distribution over the mutual footprint' via comparison of the power contributions over time for BSR-1.2 (using 4 pixel/degree resolution, GRS data and CO_2 ice as the polar host material), own work

Model results for BSR-1.3 (at 4 pixel/degree resolution)
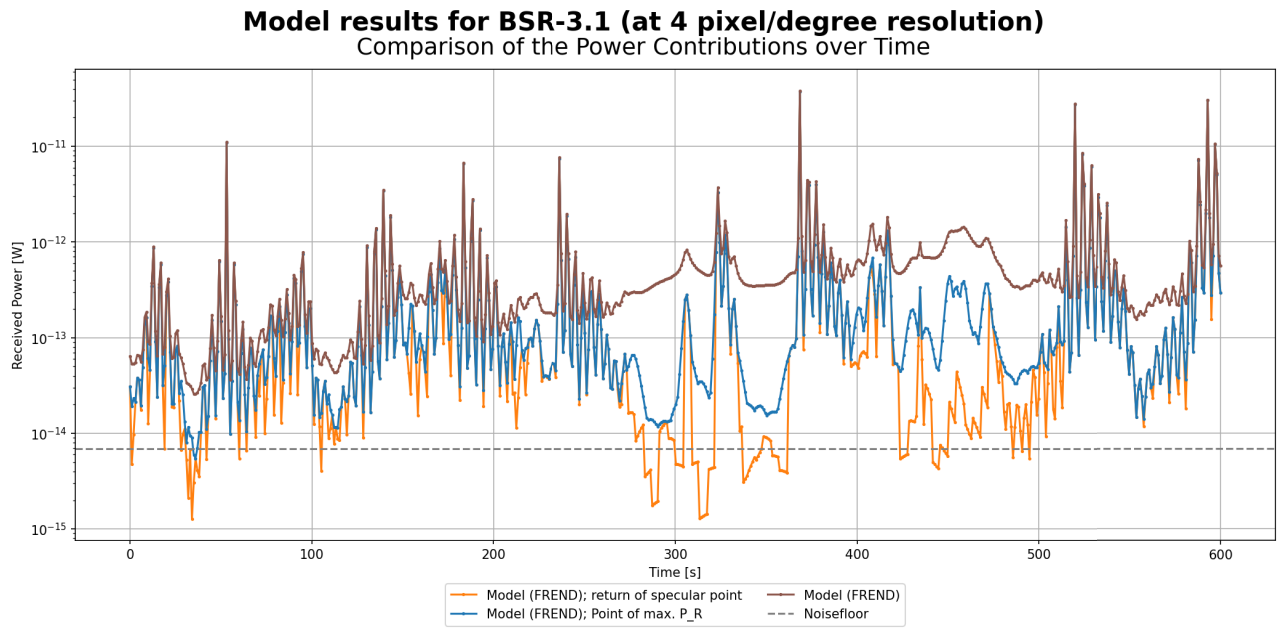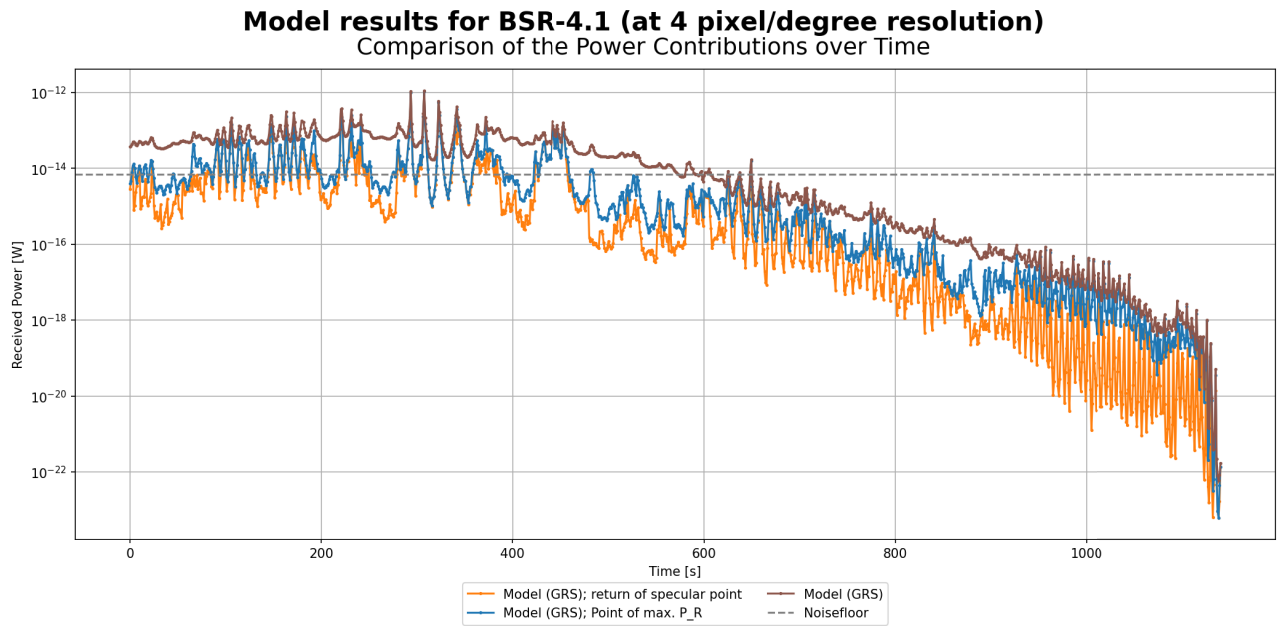### Comparison of the Power Contributions over Time
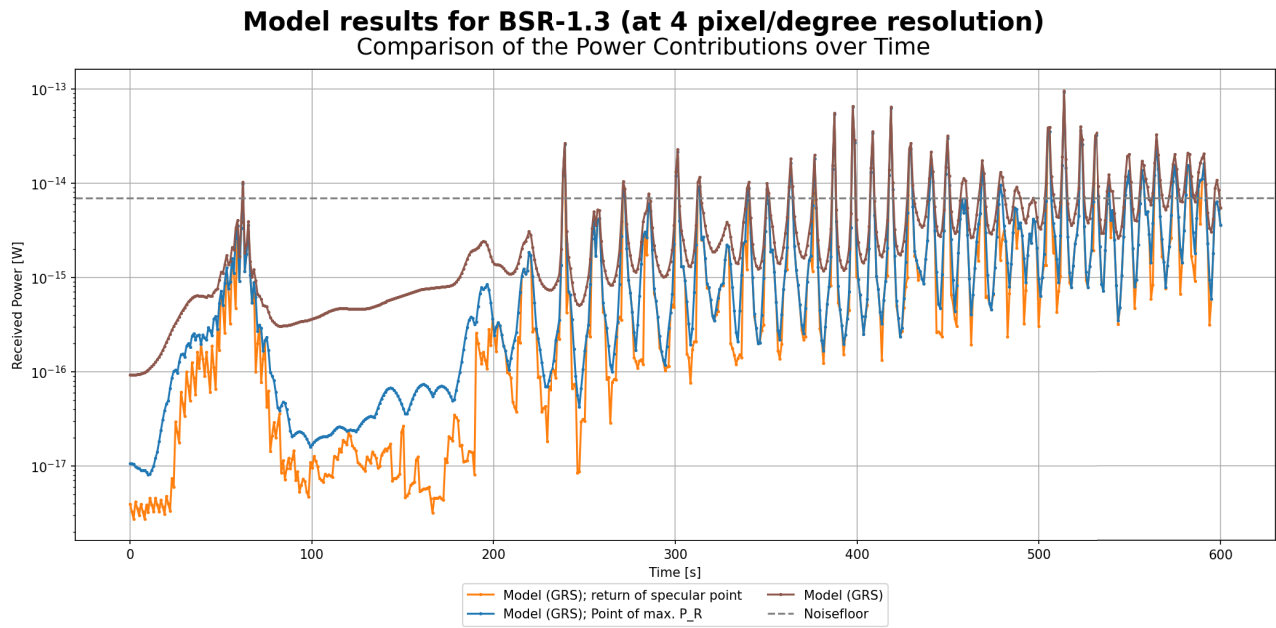
Figure E.33: Model results 'Power distribution over the mutual footprint' via comparison of the power contributions over time for BSR-1.3 (using 4 pixel/degree resolution, GRS data and CO_2 ice as the polar host material), own work

Model results for BSR-1.4 (at 4 pixel/degree resolution)
Comparison of the Power Contributions over Time
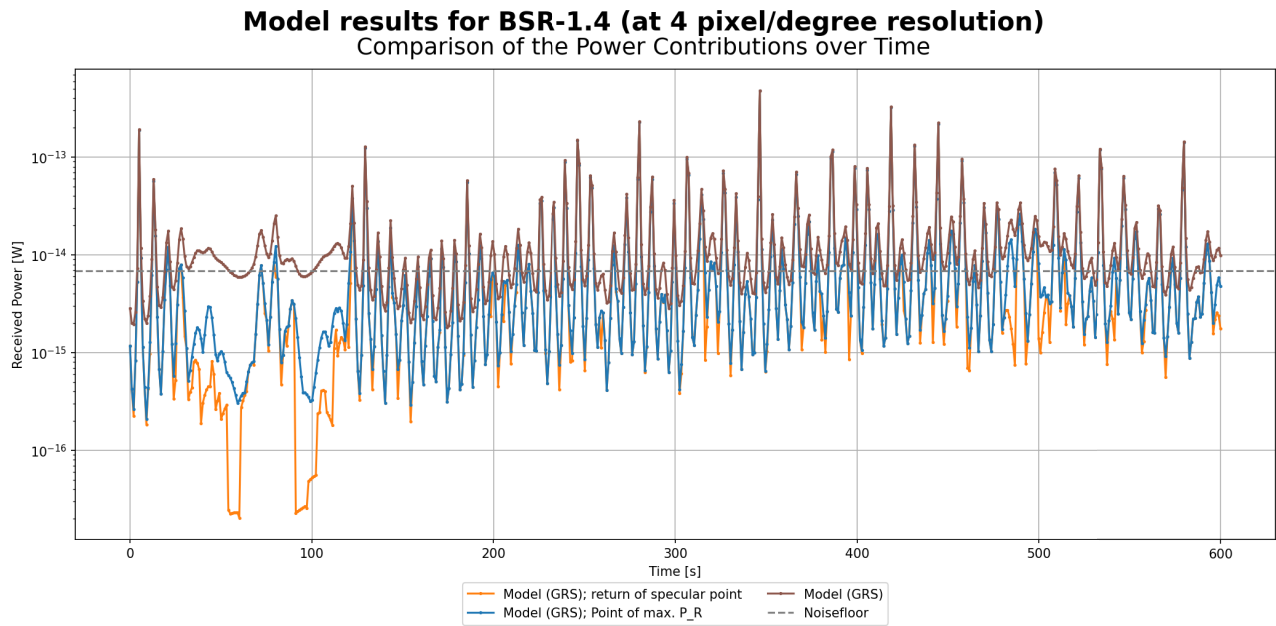
Figure E.34: Model results 'Power distribution over the mutual footprint' via comparison of the power contributions over time for BSR-1.4 (using 4 pixel/degree resolution, GRS data and CO_2 ice as the polar host material), own work

Model results for BSR-2.1 (at 4 pixel/degree resolution)
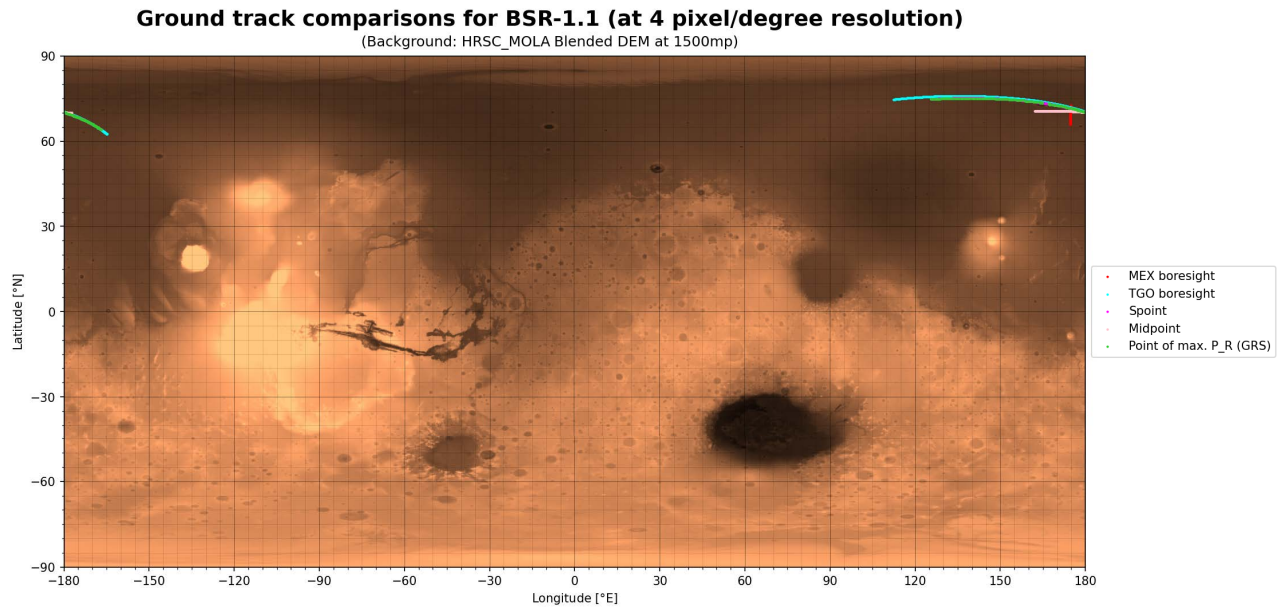### Comparison of the Power Contributions over Time
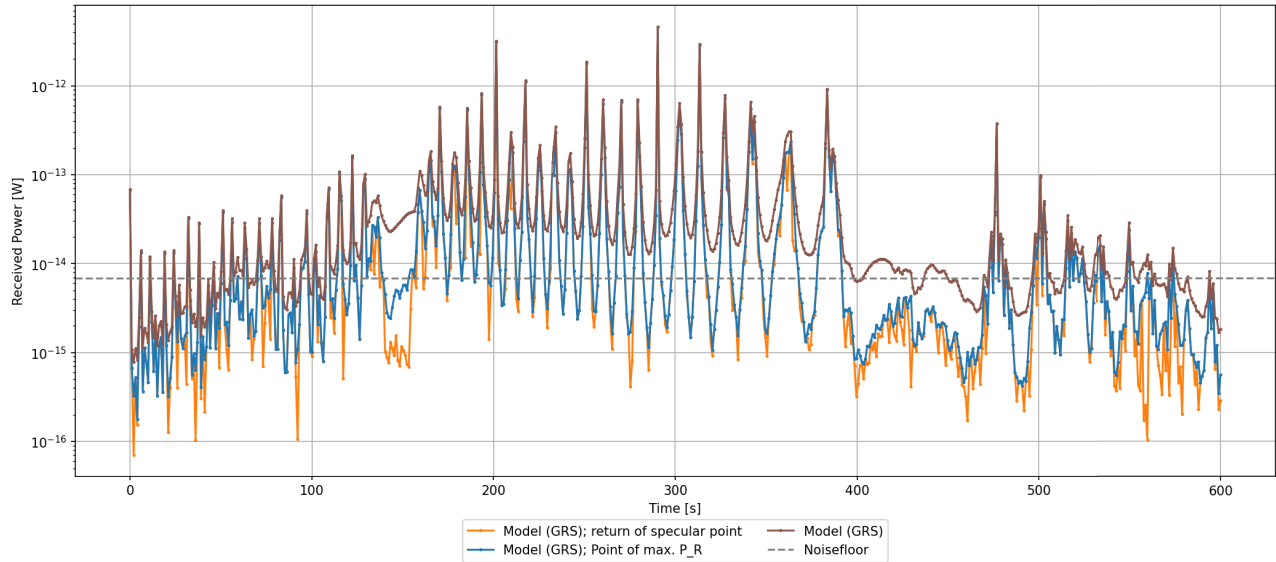
Figure E.35: Model results 'Power distribution over the mutual footprint' via comparison of the power contributions over time for BSR-2.1 (using 4 pixel/degree resolution, GRS data and CO_2 ice as the polar host material), own work

Model results for BSR-2.1 (at 16 pixel/degree resolution)
Comparison of the Power Contributions over Time
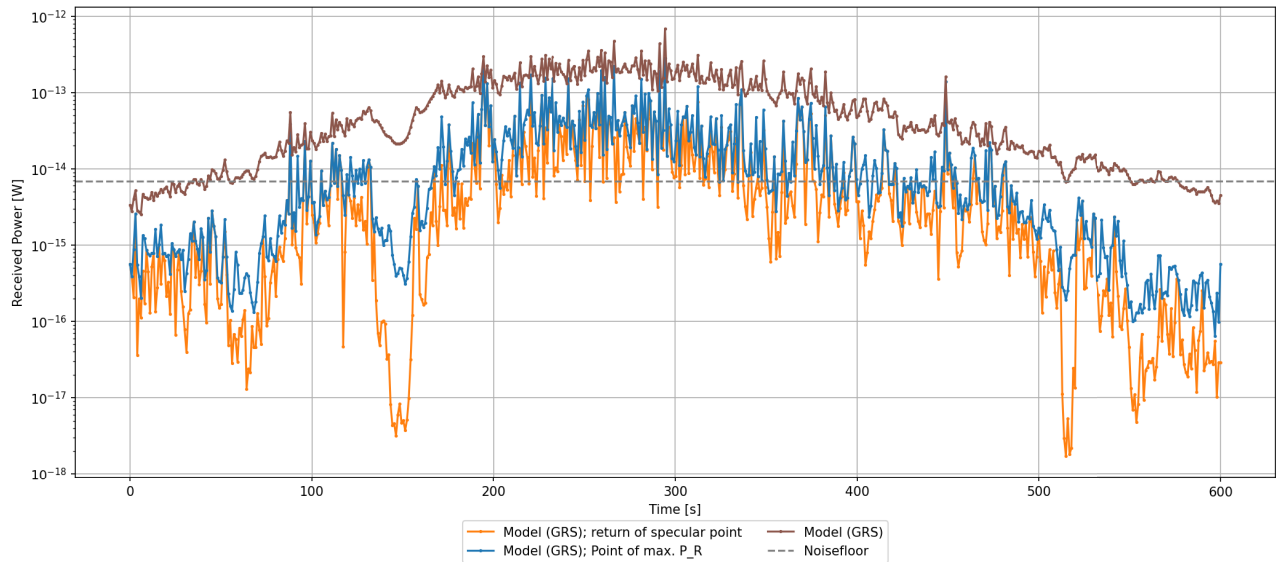
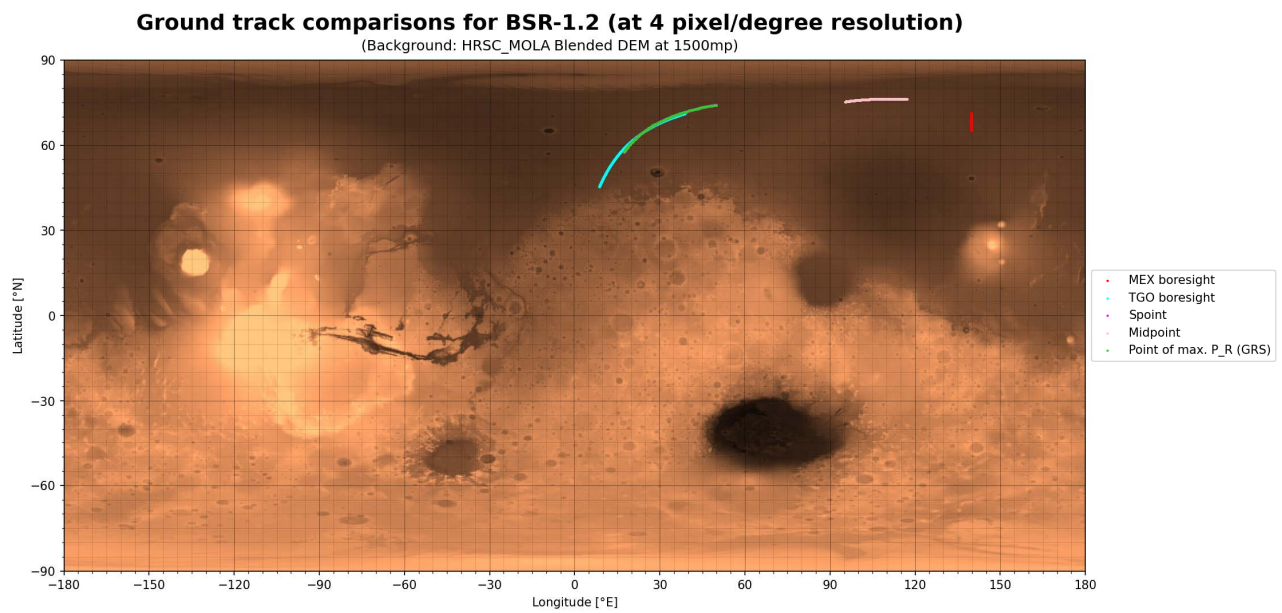**Figure E.36:** Model results 'Power distribution over the mutual footprint' via comparison of the power contributions over time for BSR-2.1 (using 16 pixel/degree resolution, GRS data and CO_2 ice as the polar host material), own work
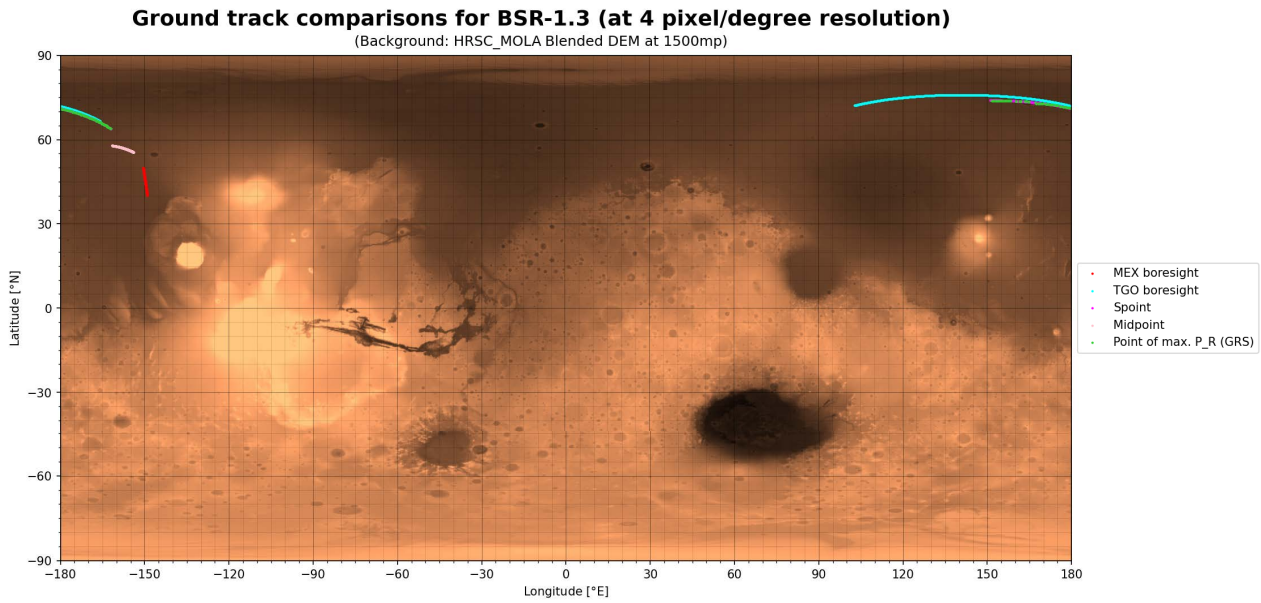
Model results for BSR-2.2 (at 4 pixel/degree resolution)
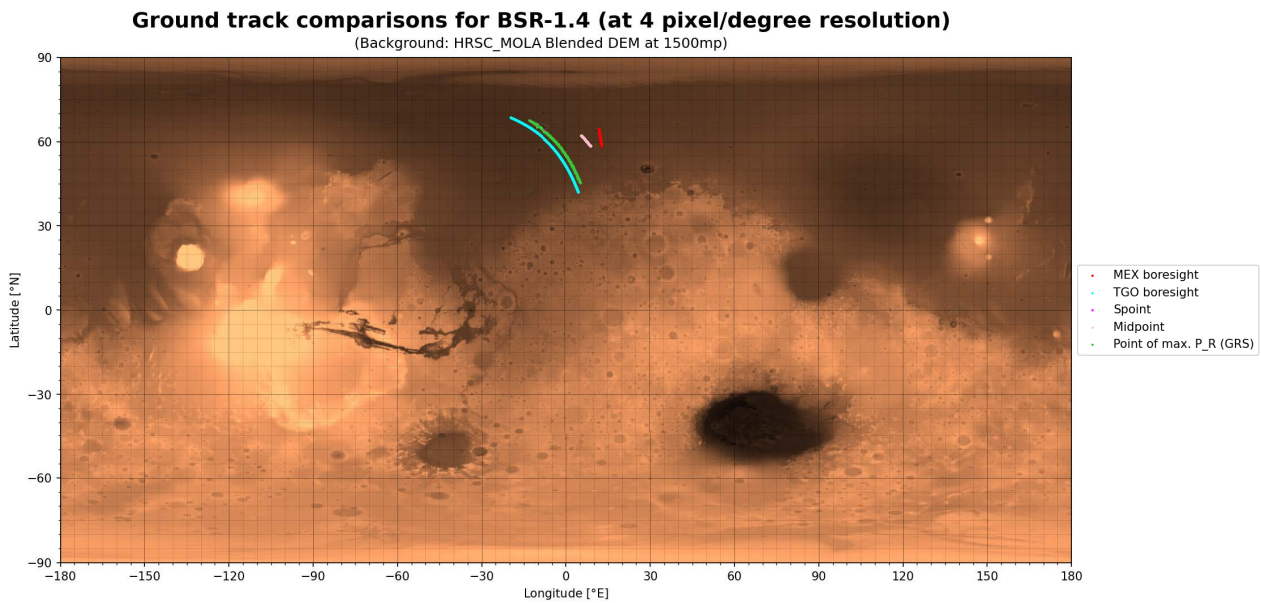### Comparison of the Power Contributions over Time

Figure E.37: Model results 'Power distribution over the mutual footprint' via comparison of the power contributions over time for BSR-2.2 (using 4 pixel/degree resolution, GRS data and CO_2 ice as the polar host material), own work

Model results for BSR-3.1 (at 4 pixel/degree resolution)
Comparison of the Power Contributions over Time
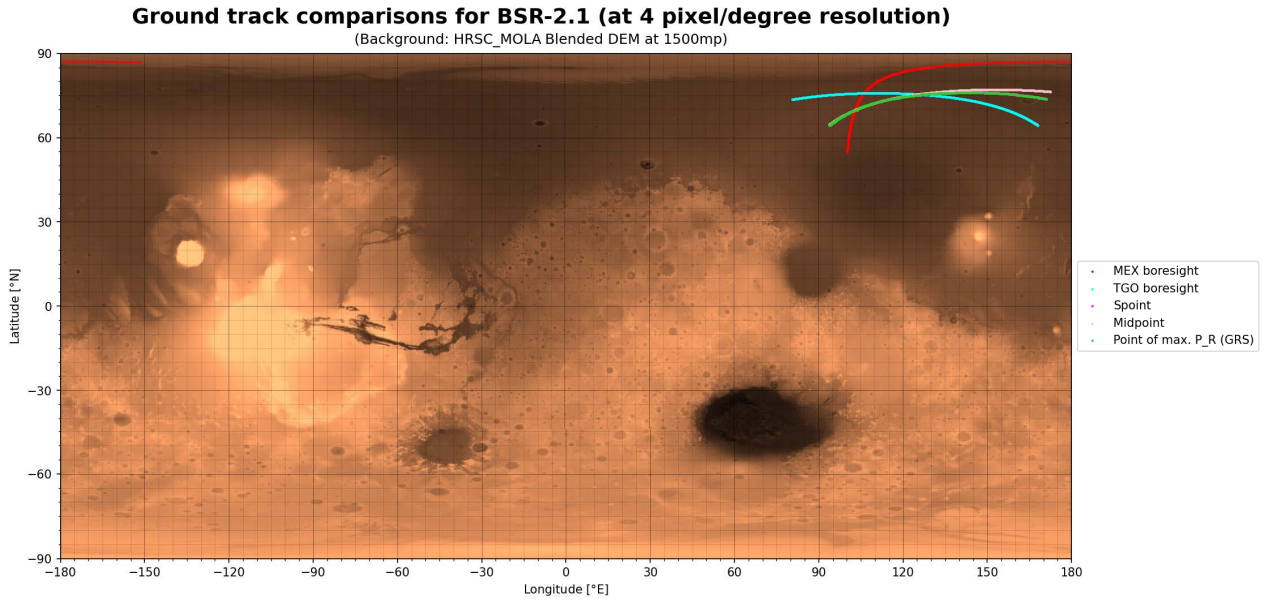

Figure E.38: Model results 'Power distribution over the mutual footprint' via comparison of the power contributions over time for BSR-3.1 (using 4 pixel/degree resolution, GRS data and CO_2 ice as the polar host material), own work

Model results for BSR-3.1 (at 4 pixel/degree resolution)
Comparison of the Power Contributions over Time

Figure E.39: Model results 'Power distribution over the mutual footprint' via comparison of the power contributions over time for BSR-3.1 (using 4 pixel/degree resolution, FREND data and CO_2 ice as the polar host material), own work

Model results for BSR-4.1 (at 4 pixel/degree resolution)
Comparison of the Power Contributions over Time

Figure E.40: Model results 'Power distribution over the mutual footprint' via comparison of the power contributions over time for BSR-4.1 (using 4 pixel/degree resolution, GRS data and CO_2 ice as the polar host material), own work

E.2.3. Ground Tracks of Maximum Power Return

Ground track comparisons for BSR-1.1 (at 4 pixel/degree resolution)
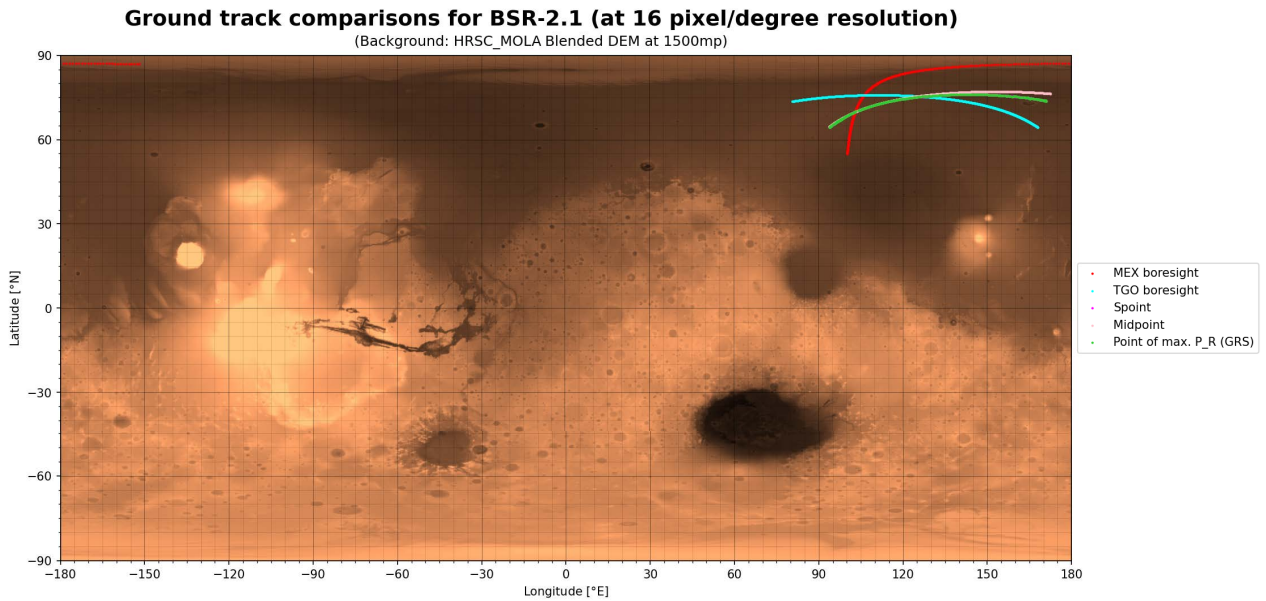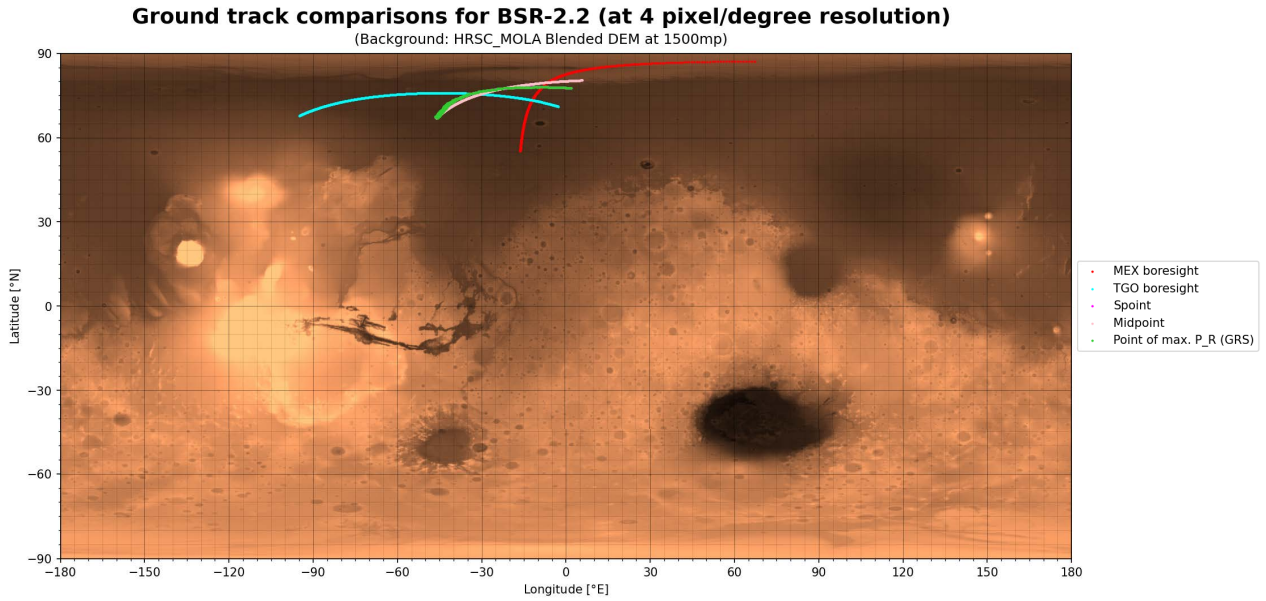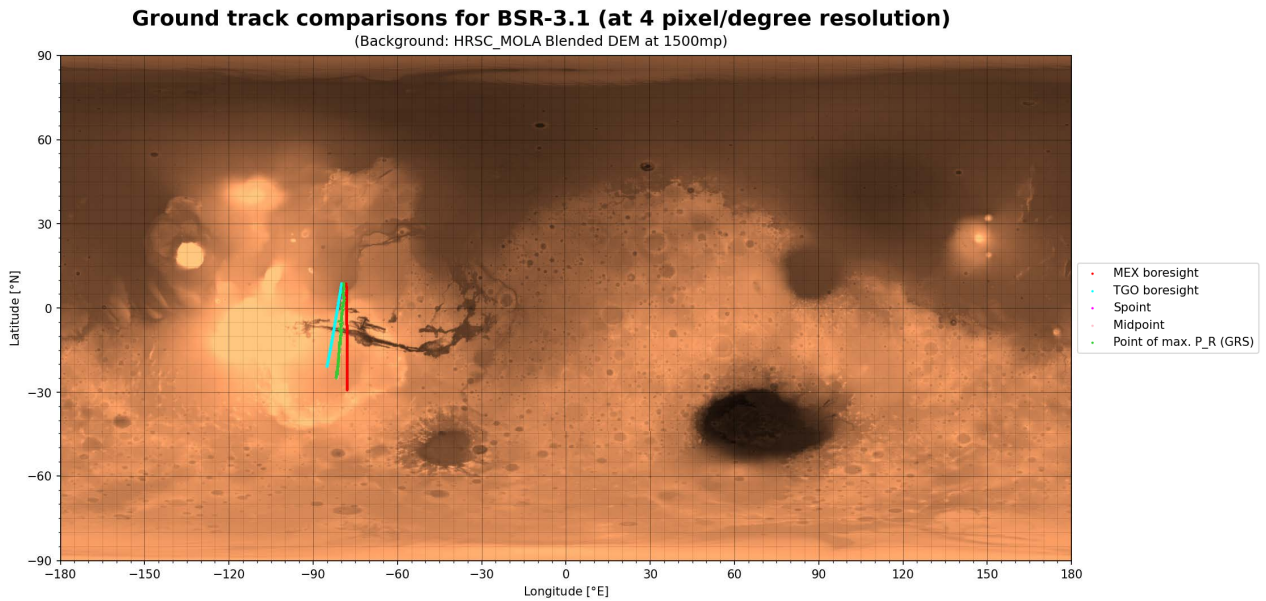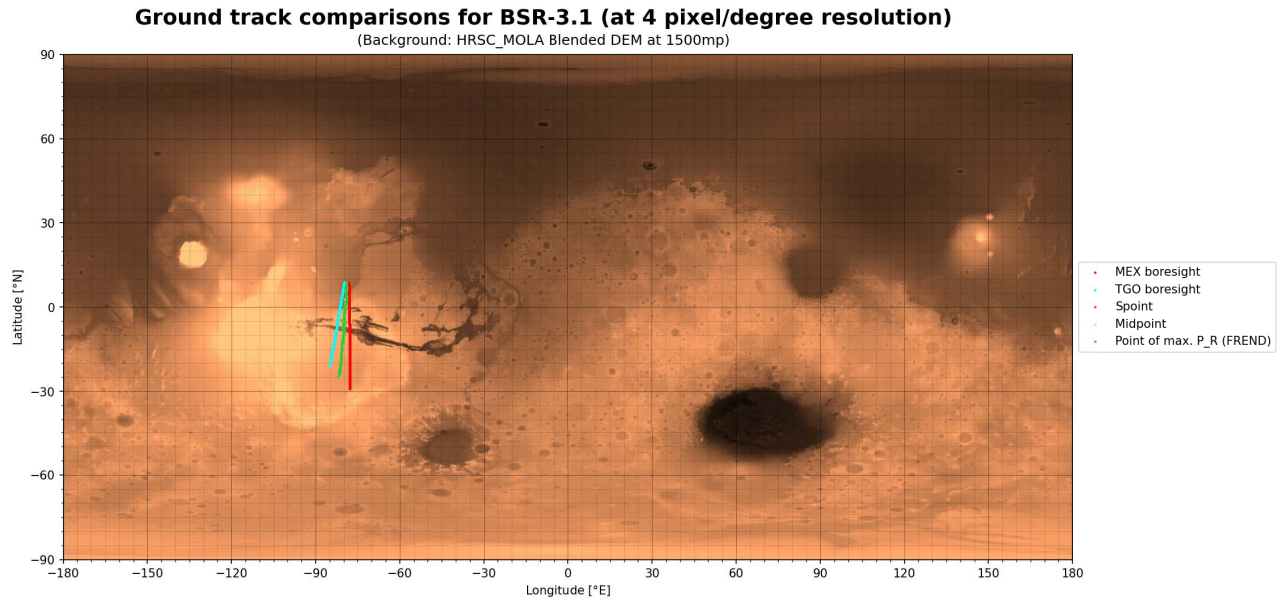(Background: HRSC_MOLA Blended DEM at 1500mp)

Figure E.41: Model results 'Power distribution over the mutual footprint' via comparison of the ground tracks of maximum return for BSR-1.1 (using 4 pixel/degree resolution, GRS data and CO_2 ice as the polar host material), own work

Ground track comparisons for BSR-1.2 (at 4 pixel/degree resolution)
(Background: HRSC_MOLA Blended DEM at 1500mp)

Figure E.42: Model results 'Power distribution over the mutual footprint' via comparison of the ground tracks of maximum return for BSR-1.2 (using 4 pixel/degree resolution, GRS data and CO_2 ice as the polar host material), own work
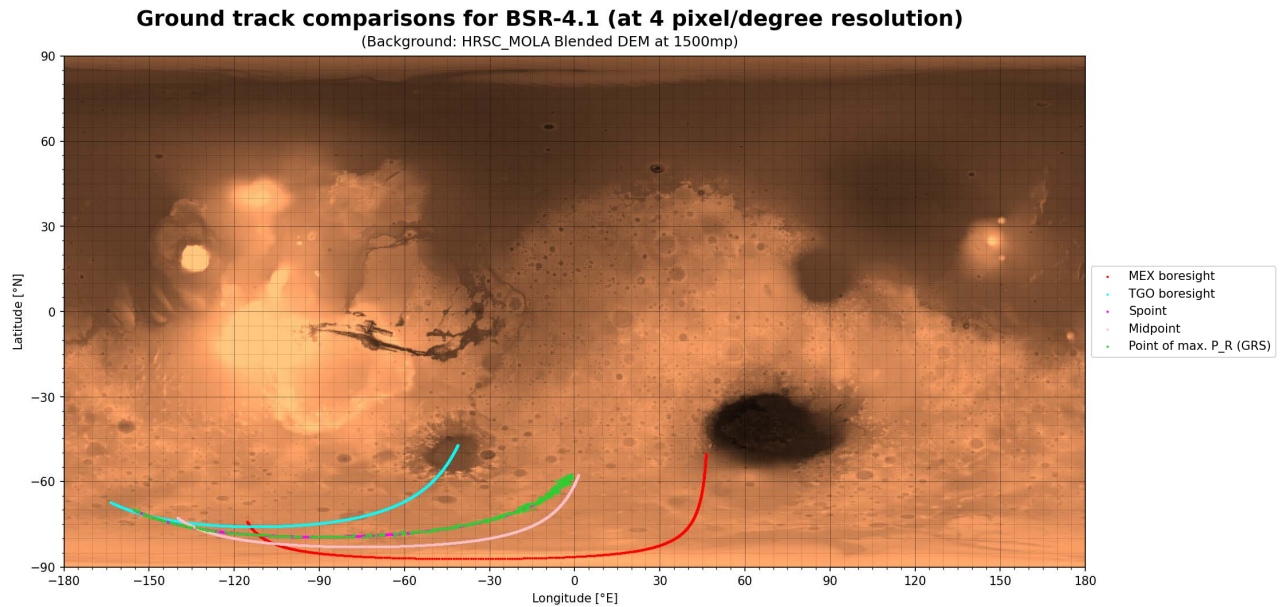
Figure E.43: Model results 'Power distribution over the mutual footprint' via comparison of the ground tracks of maximum return for BSR-1.3 (using 4 pixel/degree resolution, GRS data and CO_2 ice as the polar host material), own work

Figure E.44: Model results 'Power distribution over the mutual footprint' via comparison of the ground tracks of maximum return for BSR-1.4 (using 4 pixel/degree resolution, GRS data and CO_2 ice as the polar host material), own work

Ground track comparisons for BSR-2.1 (at 4 pixel/degree resolution)
(Background: HRSC_MOLA Blended DEM at 1500mp)

Figure E.45: Model results 'Power distribution over the mutual footprint' via comparison of the ground tracks of maximum return for BSR-2.1 (using 4 pixel/degree resolution, GRS data and CO_2 ice as the polar host material), own work

Ground track comparisons for BSR-2.1 (at 16 pixel/degree resolution)
(Background: HRSC_MOLA Blended DEM at 1500mp)

Figure E.46: Model results 'Power distribution over the mutual footprint' via comparison of the ground tracks of maximum return for BSR-2.1 (using 16 pixel/degree resolution, GRS data and CO_2 ice as the polar host material), own work

Figure E.47: Model results 'Power distribution over the mutual footprint' via comparison of the ground tracks of maximum return for BSR-2.2 (using 4 pixel/degree resolution, GRS data and CO_2 ice as the polar host material), own work

Figure E.48: Model results 'Power distribution over the mutual footprint' via comparison of the ground tracks of maximum return for BSR-3.1 (using 4 pixel/degree resolution, GRS data and CO_2 ice as the polar host material), own work

Figure E.49: Model results 'Power distribution over the mutual footprint' via comparison of the ground tracks of maximum return for BSR-3.1 (using 4 pixel/degree resolution, FREND data and CO_2 ice as the polar host material), own work

Figure E.50: Model results 'Power distribution over the mutual footprint' via comparison of the ground tracks of maximum return for BSR-4.1 (using 4 pixel/degree resolution, GRS data and CO_2 ice as the polar host material), own work

E.3. Model Results: 'Free-space Direct Signal Contribution'
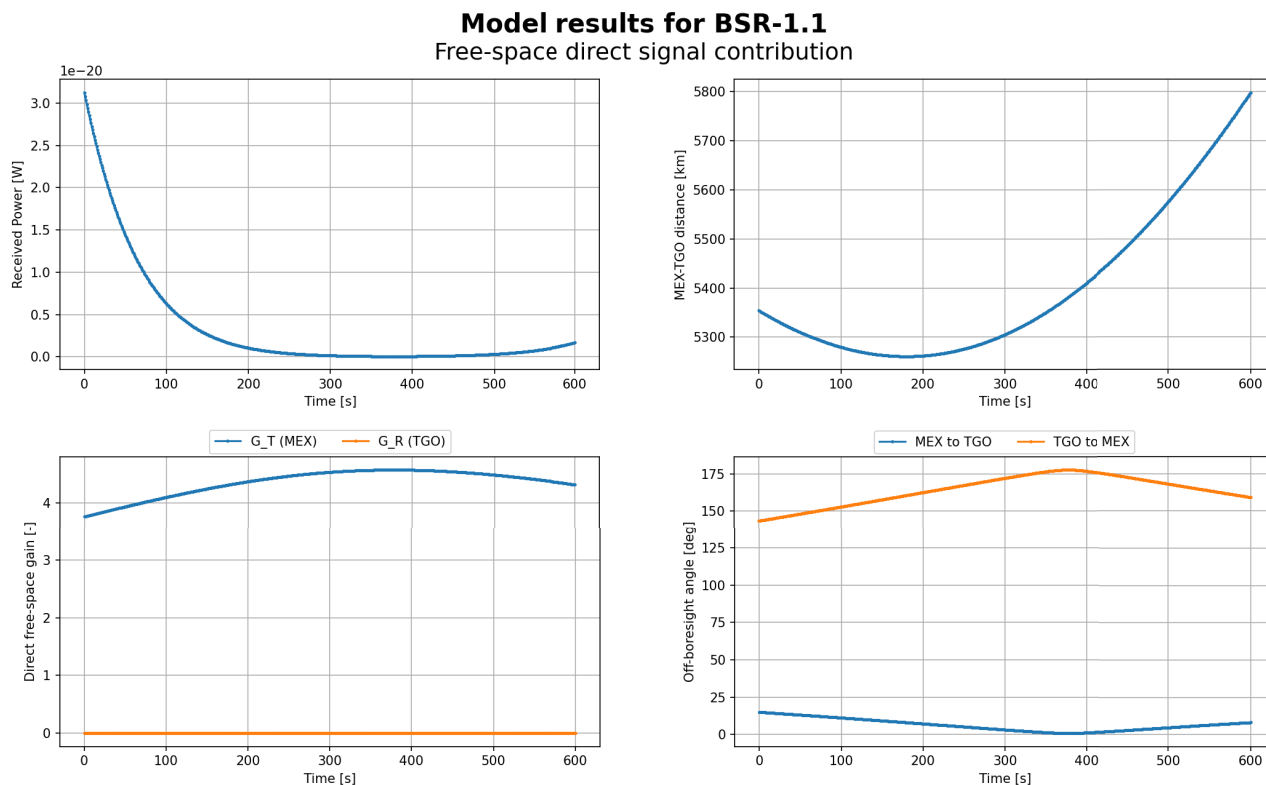
Figure E.51: Model results 'Free-space direct signal contribution' for BSR-1.1, own work
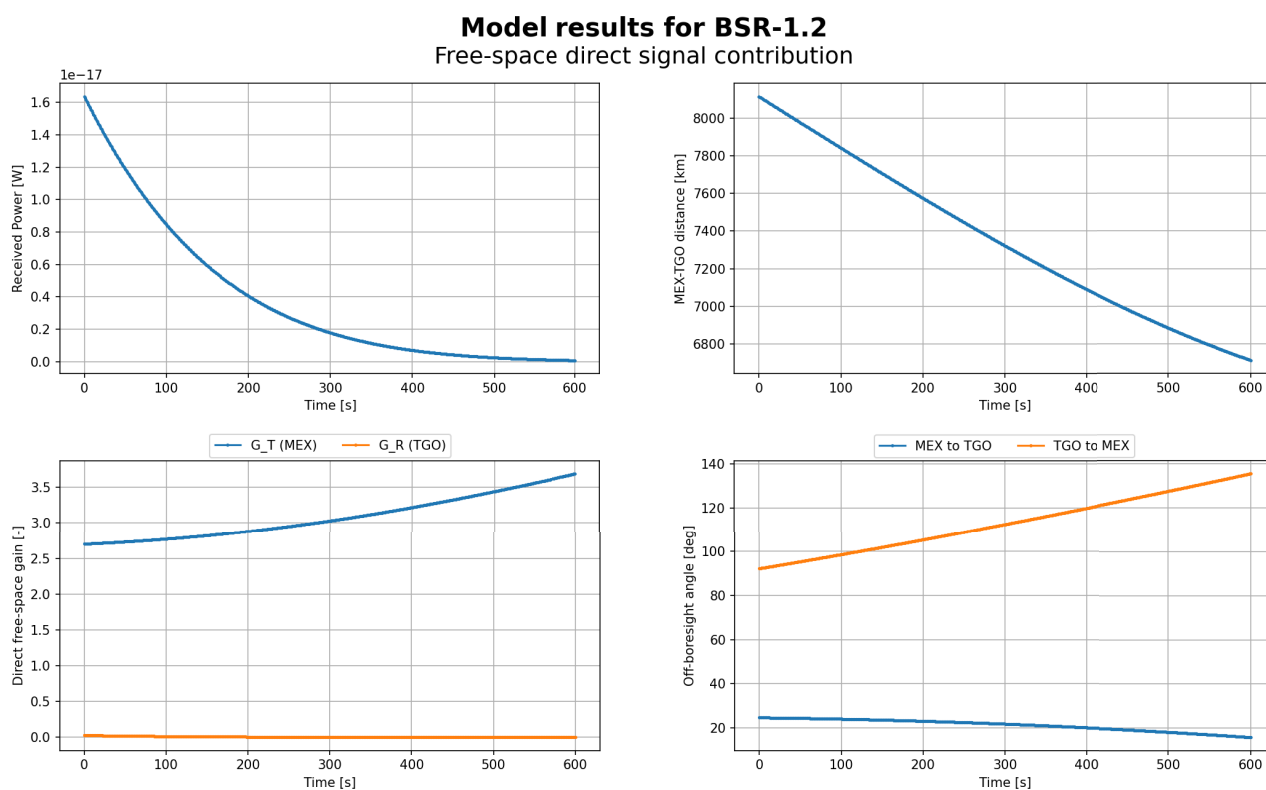
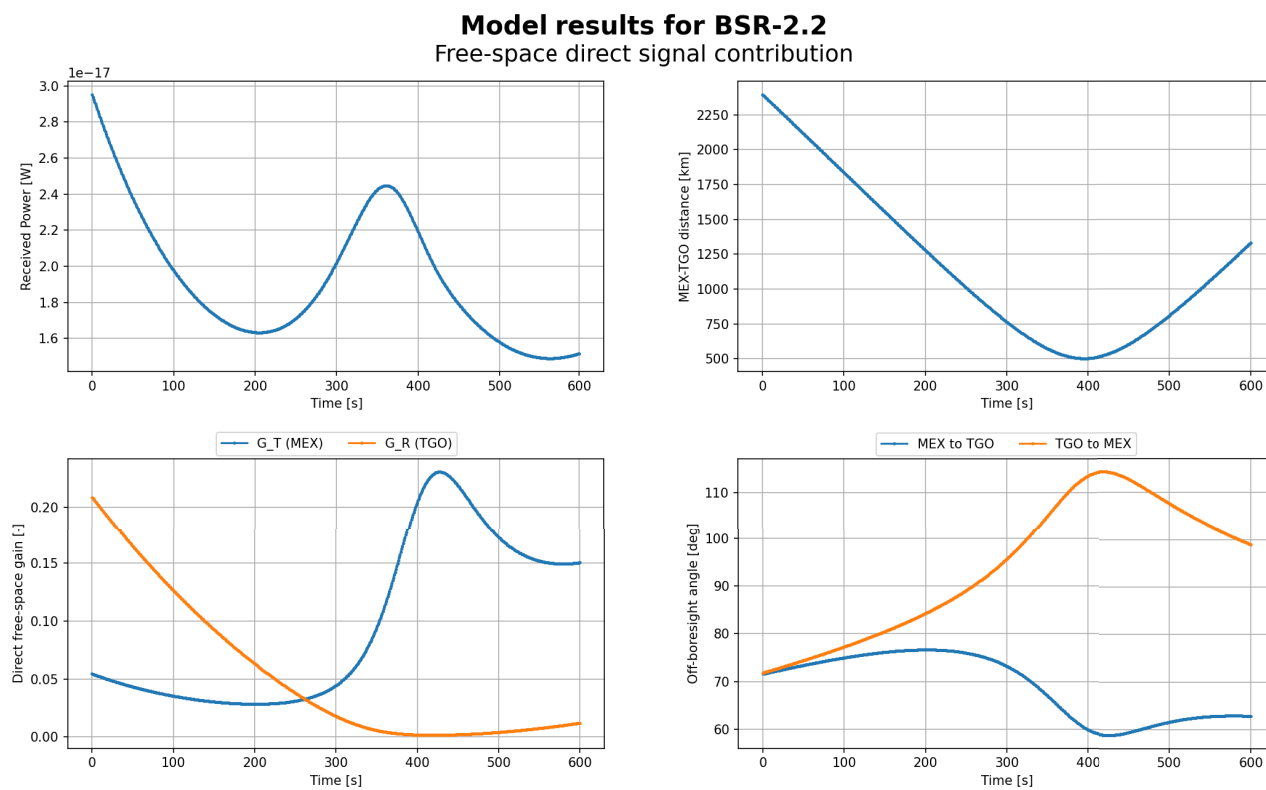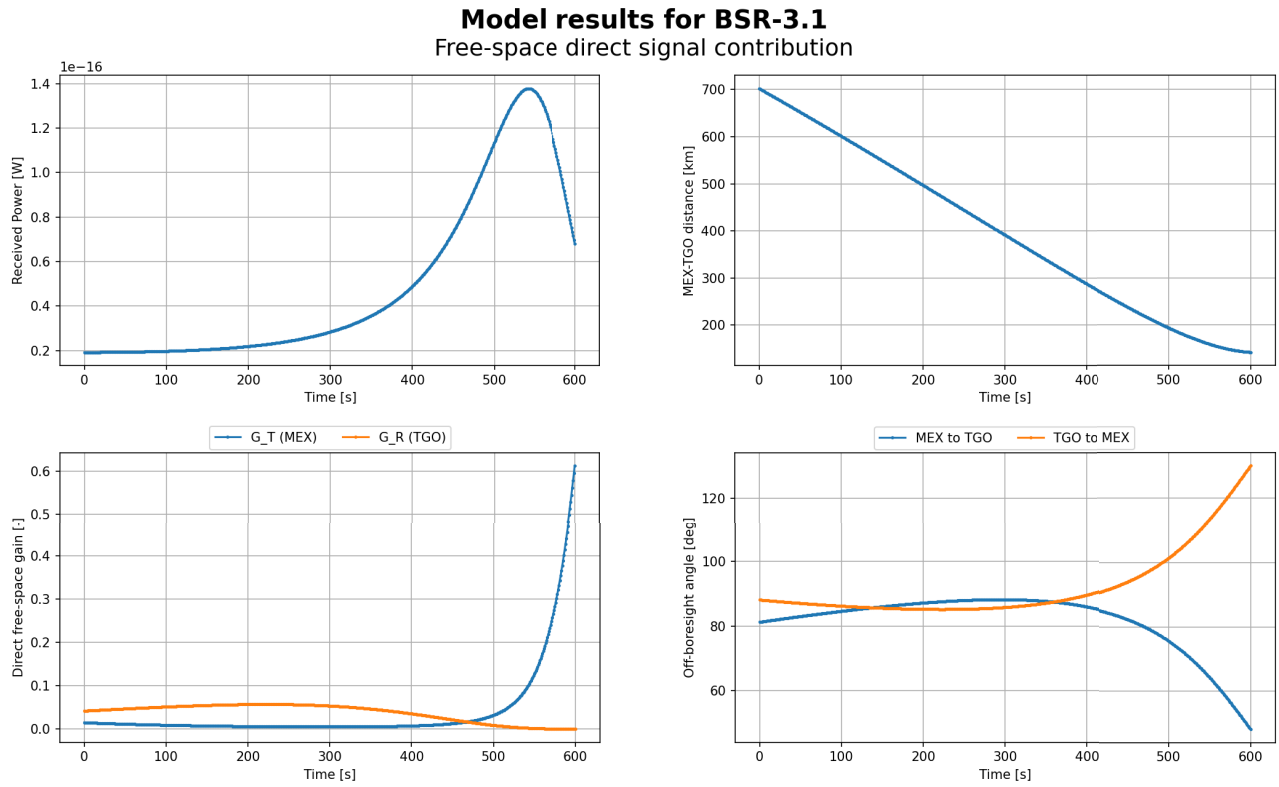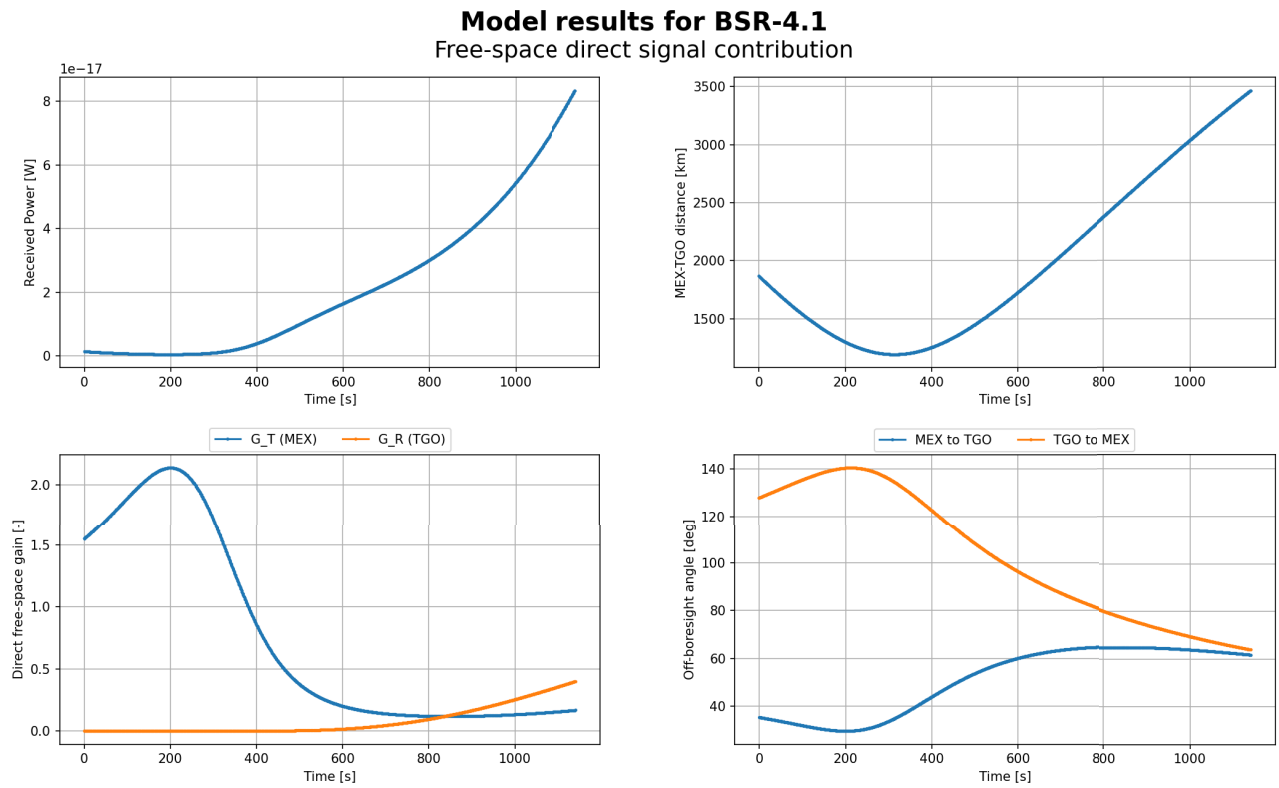**Figure E.52:** Model results 'Free-space direct signal contribution' for BSR-1.2, own work

Model results for BSR-1.3
Free-space direct signal contribution
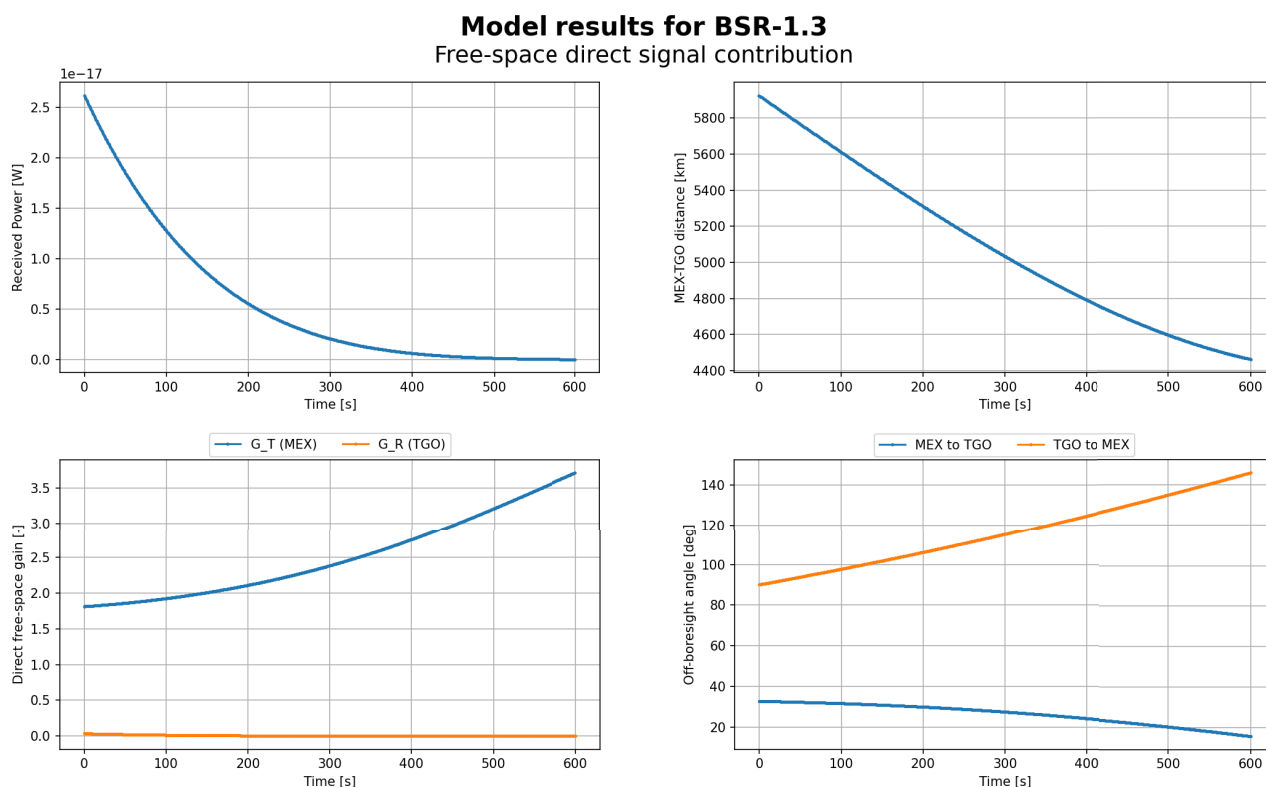
Figure E.53: Model results 'Free-space direct signal contribution' for BSR-1.3, own work

Model results for BSR-1.4
Free-space direct signal contribution
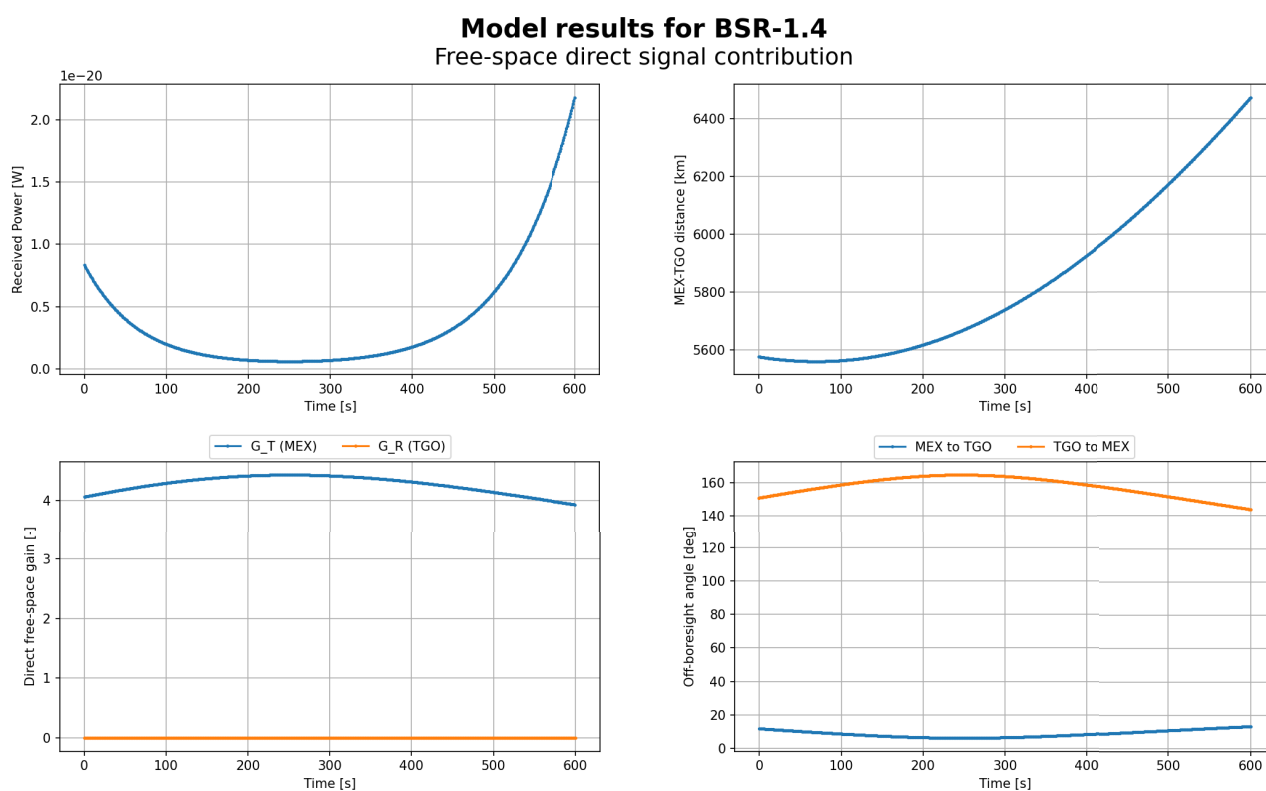
Figure E.54: Model results 'Free-space direct signal contribution' for BSR-1.4, own work

Model results for BSR-2.1
Free-space direct signal contribution
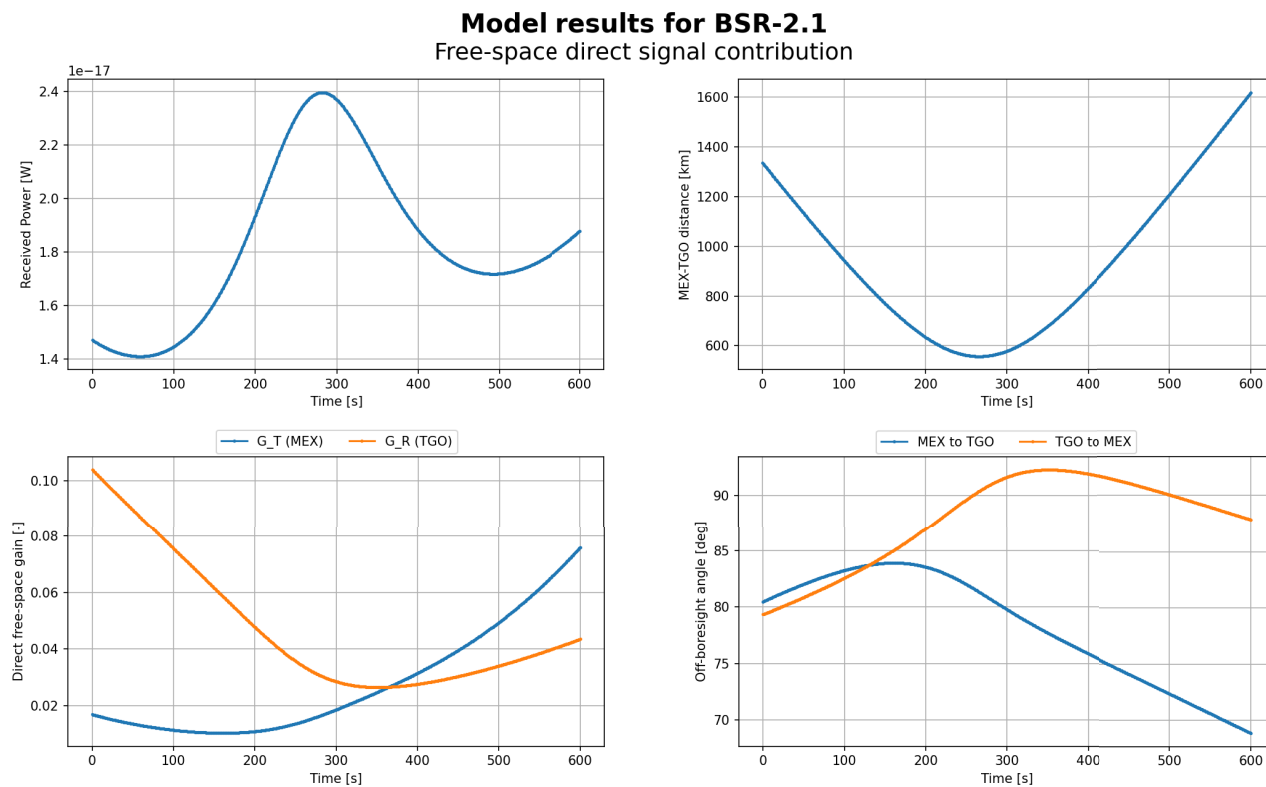
Figure E.55: Model results 'Free-space direct signal contribution' for BSR-2.1, own work

Model results for BSR-2.2
Free-space direct signal contribution

Figure E.56: Model results 'Free-space direct signal contribution' for BSR-2.2, own work

Model results for BSR-3.1
Free-space direct signal contribution

Figure E.57: Model results 'Free-space direct signal contribution' for BSR-3.1, own work

Model results for BSR-4.1
Free-space direct signal contribution

Figure E.58: Model results 'Free-space direct signal contribution' for BSR-4.1, own work

E.4. Model Results: 'Effect of the Surface Composition'
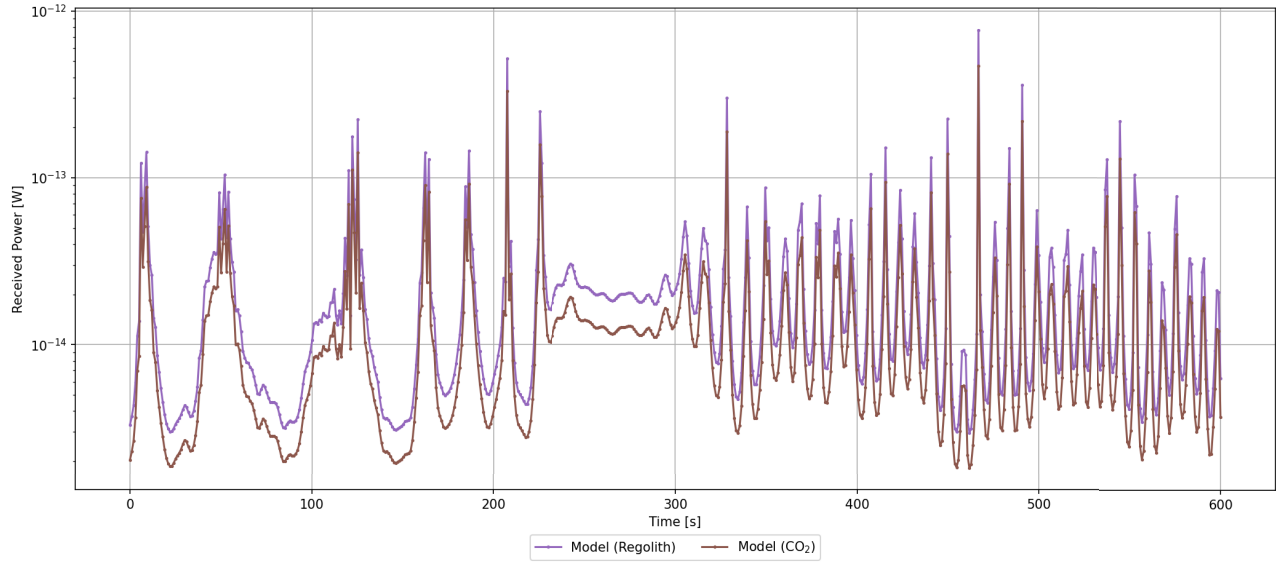
Figure E.59: Model results 'Effect of the Surface Composition: Regolith vs. CO_2 host comparison' for BSR-1.1 (using 4 pixel/degree resolution and GRS data), own work
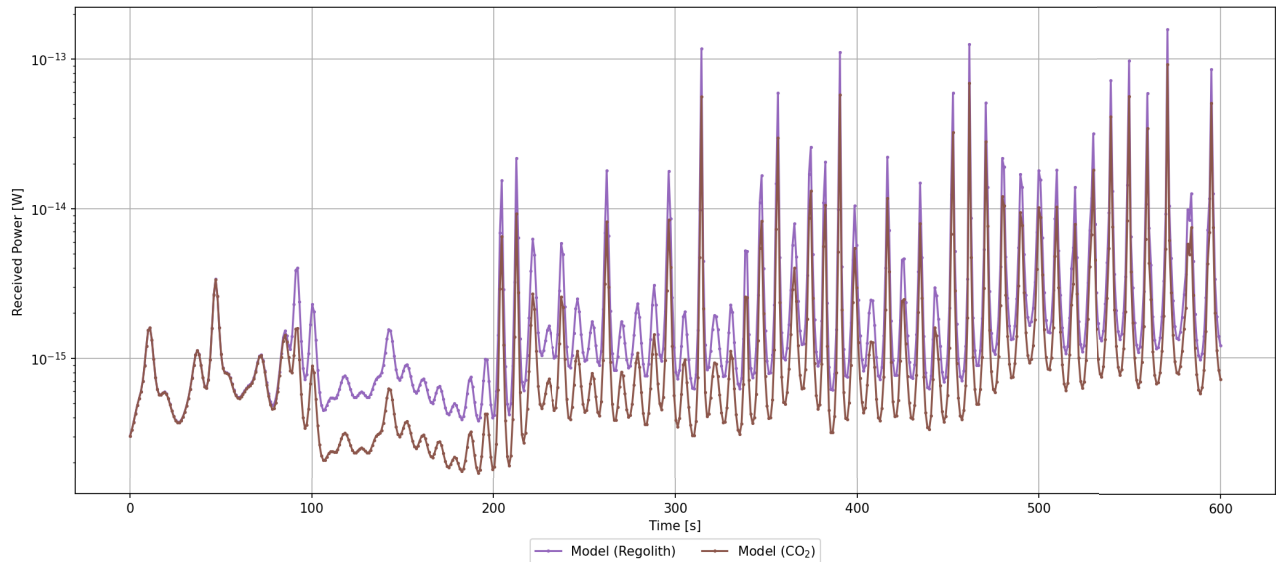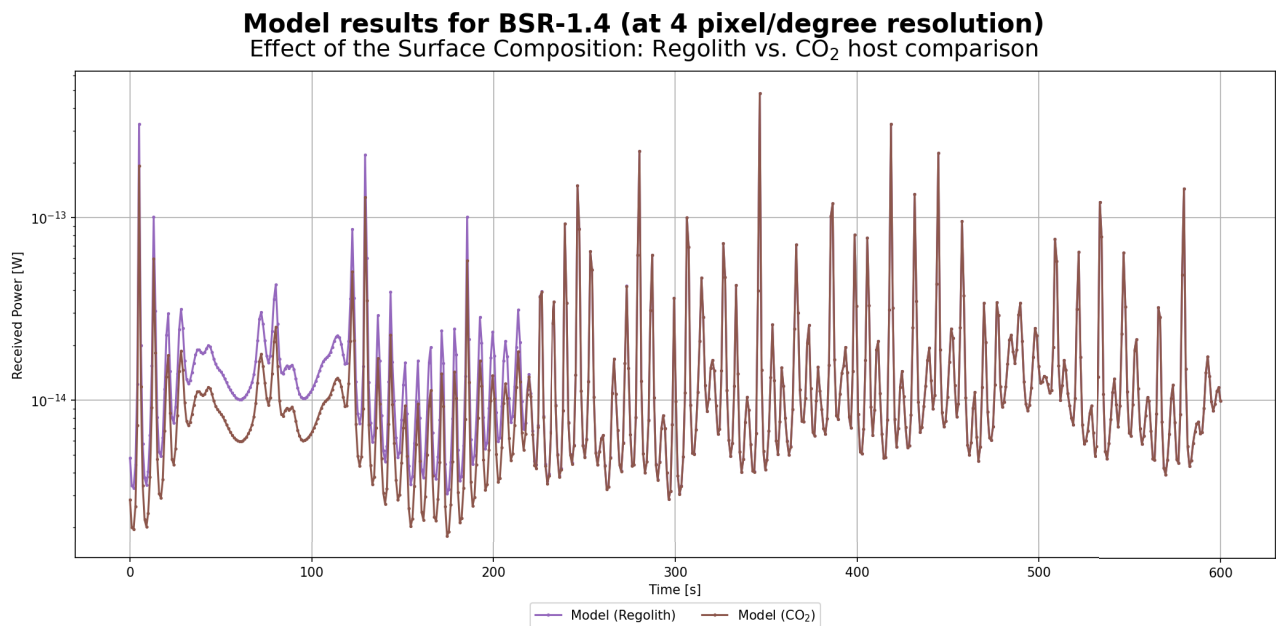

Figure E.60: Model results 'Effect of the Surface Composition: Regolith vs. CO_2 host comparison' for BSR-1.2 (using 4 pixel/degree resolution and GRS data), own work
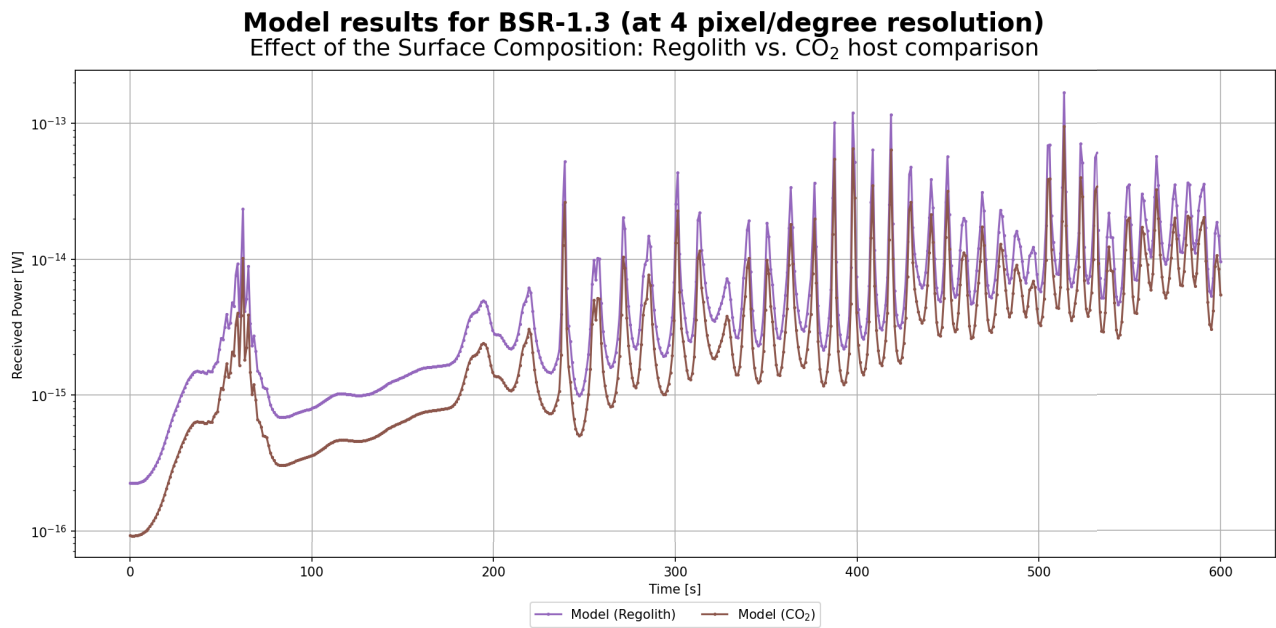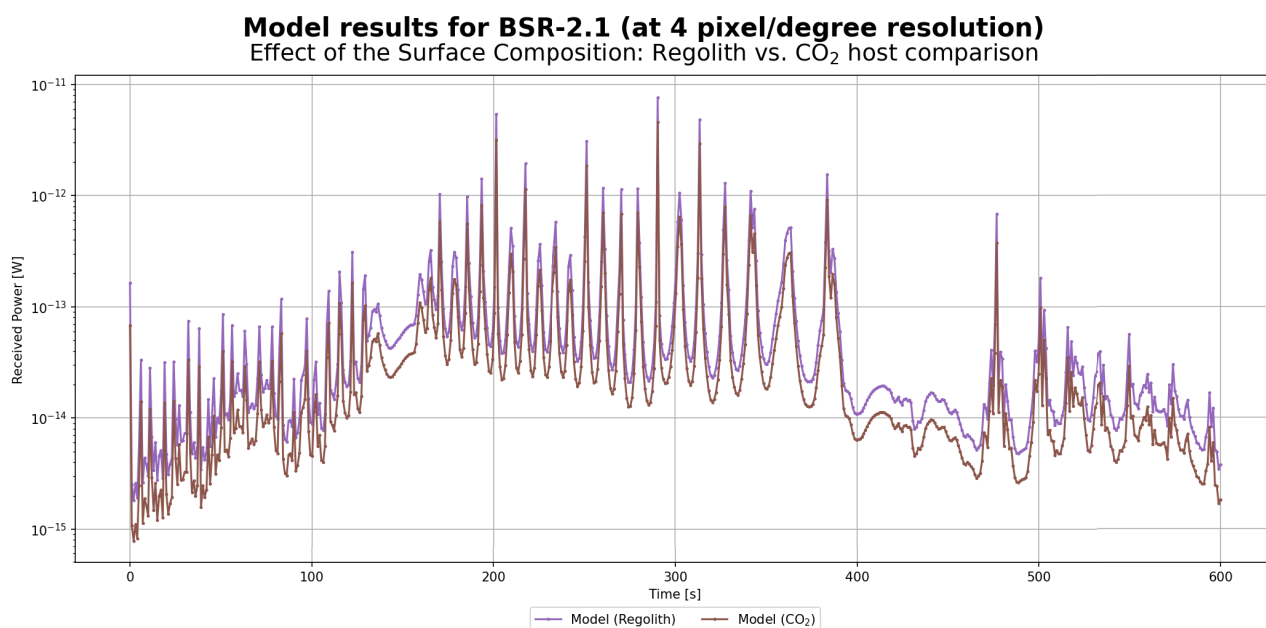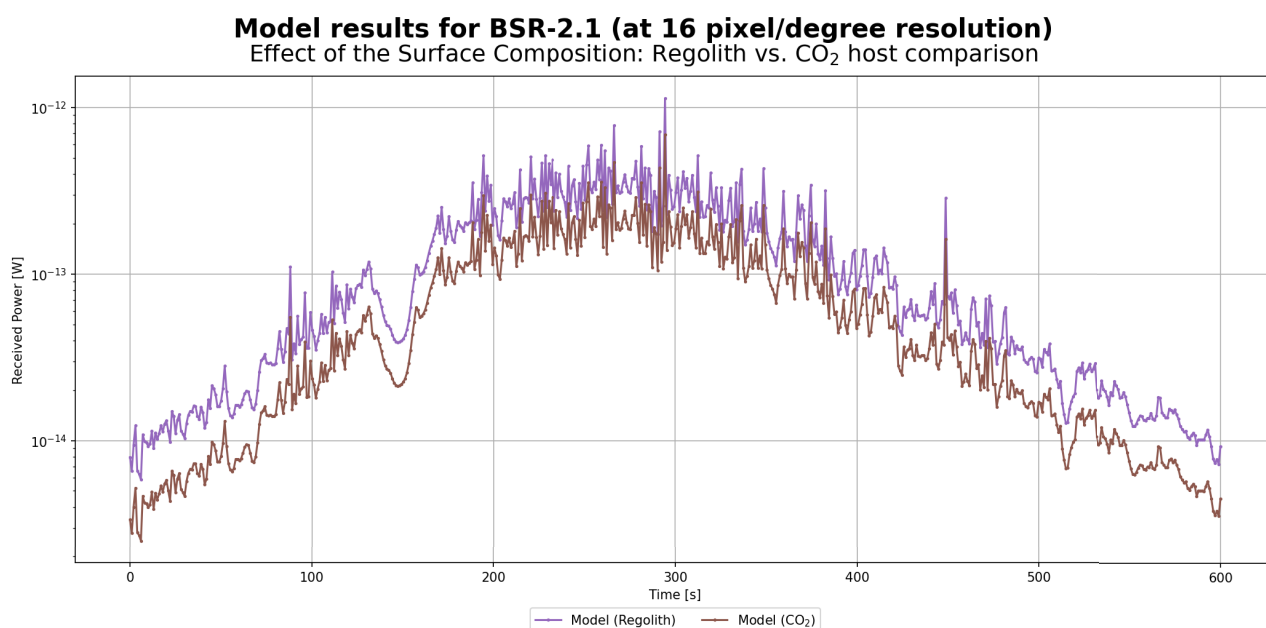
Figure E.61: Model results 'Effect of the Surface Composition: Regolith vs. CO_2 host comparison' for BSR-1.3 (using 4 pixel/degree resolution and GRS data), own work
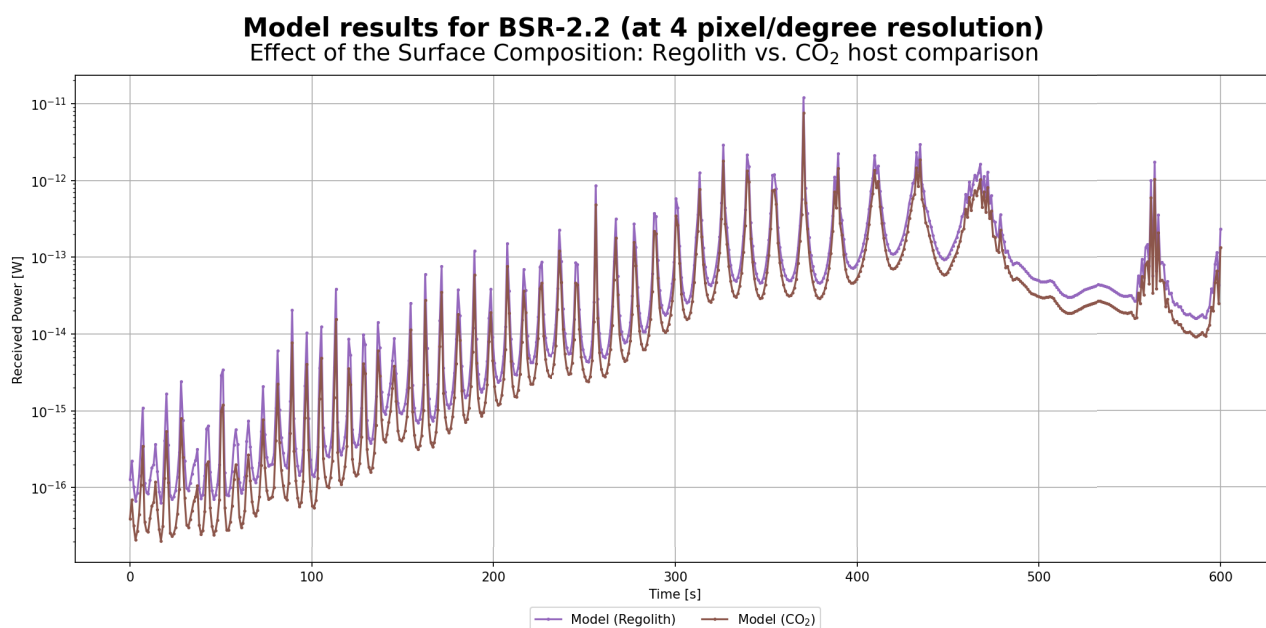

Figure E.62: Model results 'Effect of the Surface Composition: Regolith vs. CO_2 host comparison' for BSR-1.4 (using 4 pixel/degree resolution and GRS data), own work
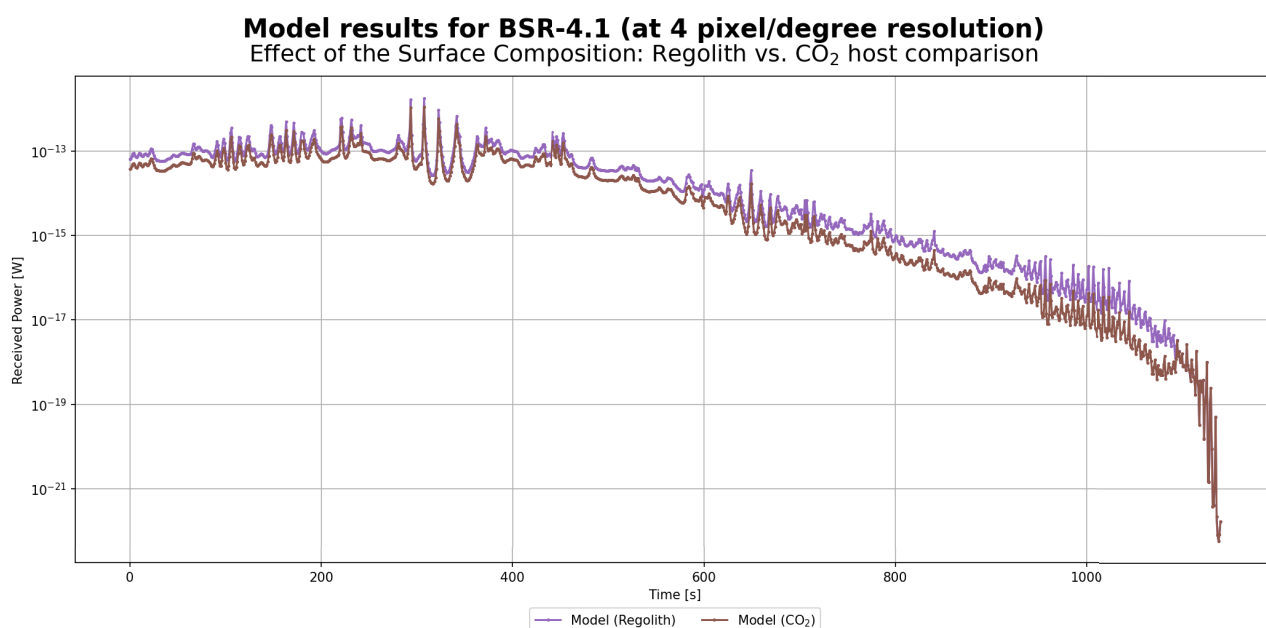
Model results for BSR-2.1 (at 4 pixel/degree resolution)
Effect of the Surface Composition: Regolith vs. CO_2 host comparison

Figure E.63: Model results 'Effect of the Surface Composition: Regolith vs. CO_2 host comparison' for BSR-2.1 (using 4 pixel/degree resolution and GRS data), own work

Model results for BSR-2.1 (at 16 pixel/degree resolution)
Effect of the Surface Composition: Regolith vs. CO_2 host comparison

Figure E.64: Model results 'Effect of the Surface Composition: Regolith vs. CO_2 host comparison' for BSR-2.1 (using 16 pixel/degree resolution and GRS data), own work

Model results for BSR-2.2 (at 4 pixel/degree resolution)
Effect of the Surface Composition: Regolith vs. CO_2 host comparison

Figure E.65: Model results 'Effect of the Surface Composition: Regolith vs. CO_2 host comparison' for BSR-2.2 (using 4 pixel/degree resolution and GRS data), own work

Model results for BSR-4.1 (at 4 pixel/degree resolution)
Effect of the Surface Composition: Regolith vs. CO_2 host comparison

Figure E.66: Model results 'Effect of the Surface Composition: Regolith vs. CO_2 host comparison' for BSR-4.1 (using 4 pixel/degree resolution and GRS data), own work

E.5. Model Results: 'Periodicity and Topography Effects'

Model results for BSR-1.1 (at 4 pixel/degree resolution)
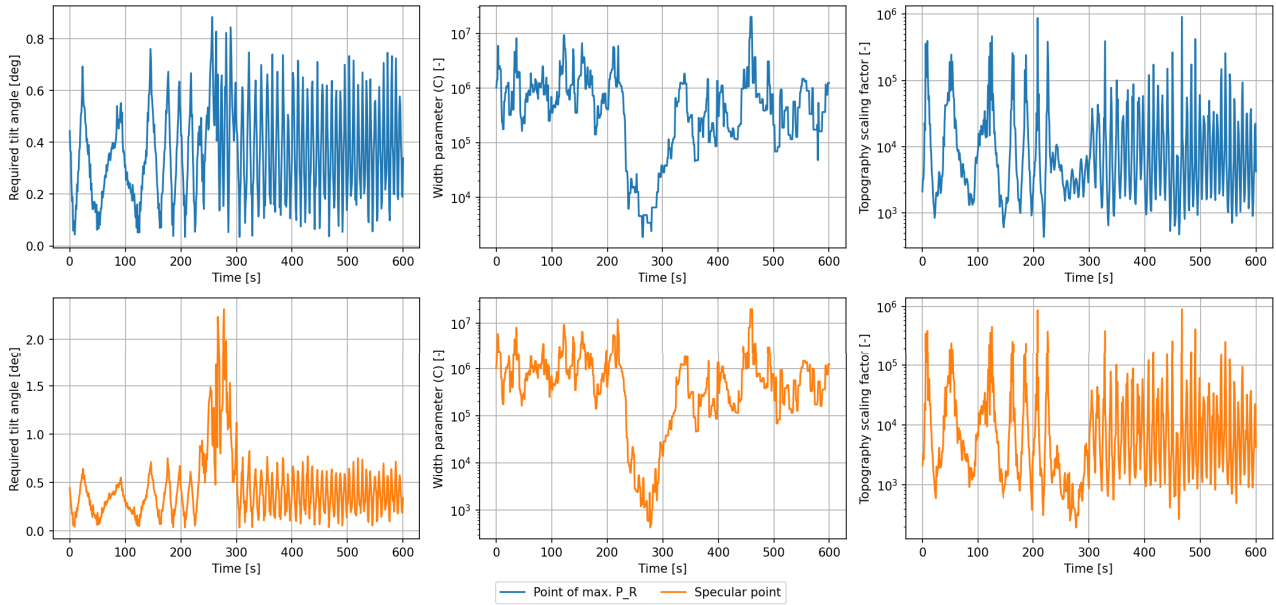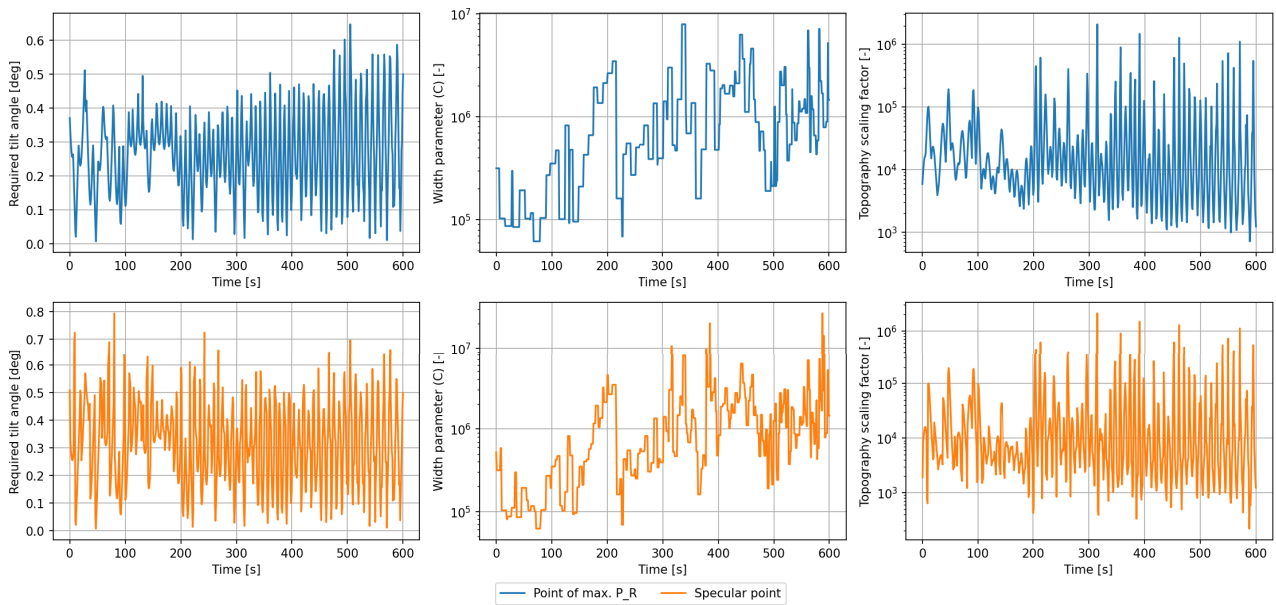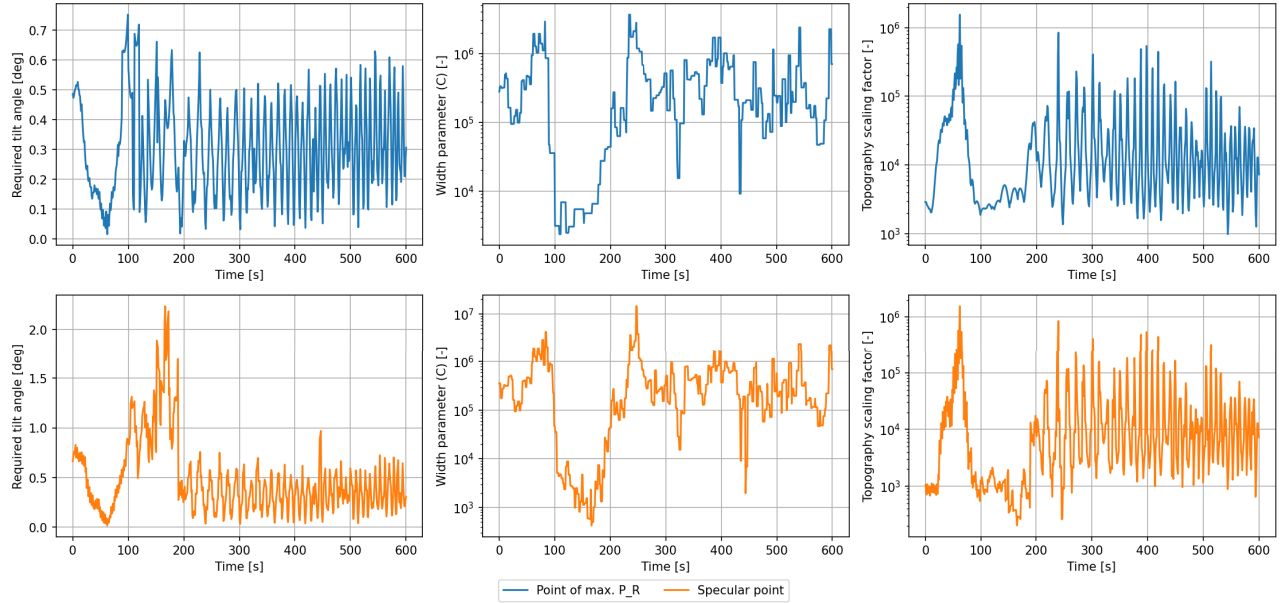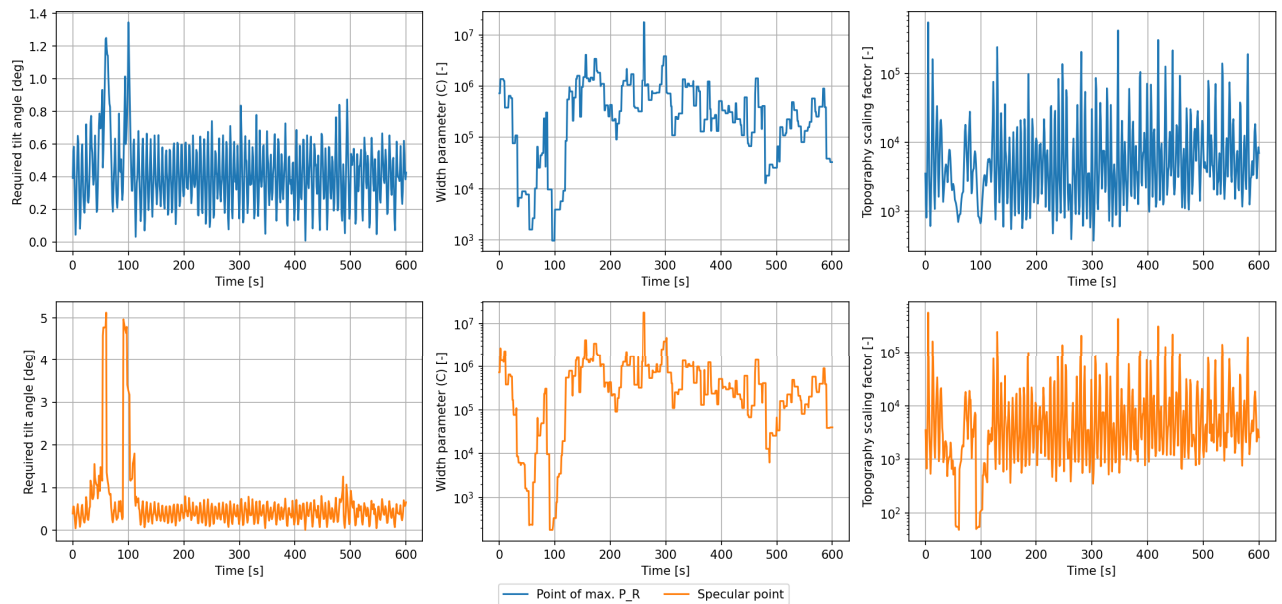Periodicity and Topography Effects

Figure E.67: Model results 'Periodicity and Topography Effects' for BSR-1.1 (using 4 pixel/degree resolution), own work

Model results for BSR-1.2 (at 4 pixel/degree resolution)
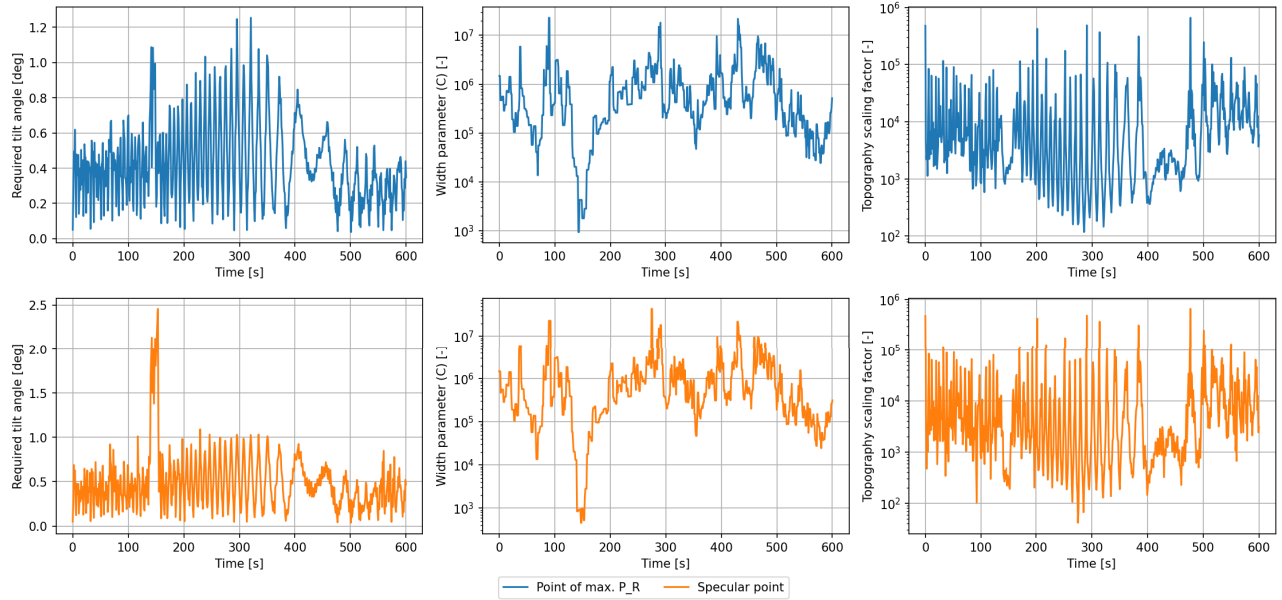Periodicity and Topography Effects

Figure E.68: Model results 'Periodicity and Topography Effects' for BSR-1.2 (using 4 pixel/degree resolution), own work

Model results for BSR-1.3 (at 4 pixel/degree resolution)
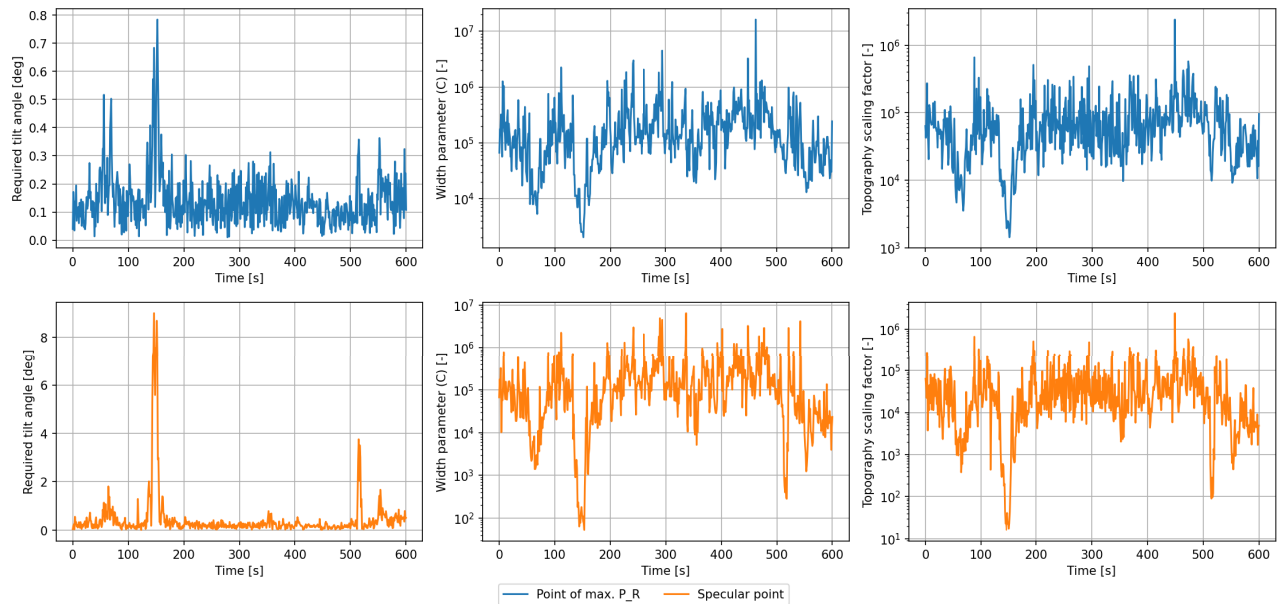### Periodicity and Topography Effects

Figure E.69: Model results 'Periodicity and Topography Effects' for BSR-1.3 (using 4 pixel/degree resolution), own work

Model results for BSR-1.4 (at 4 pixel/degree resolution)
Periodicity and Topography Effects

Figure E.70: Model results 'Periodicity and Topography Effects' for BSR-1.4 (using 4 pixel/degree resolution), own work

Model results for BSR-2.1 (at 4 pixel/degree resolution)
Periodicity and Topography Effects

Figure E.71: Model results 'Periodicity and Topography Effects' for BSR-2.1 (using 4 pixel/degree resolution), own work

Model results for BSR-2.1 (at 16 pixel/degree resolution)
Periodicity and Topography Effects

Figure E.72: Model results 'Periodicity and Topography Effects' for BSR-2.1 (using 16 pixel/degree resolution), own work

Model results for BSR-2.2 (at 4 pixel/degree resolution)
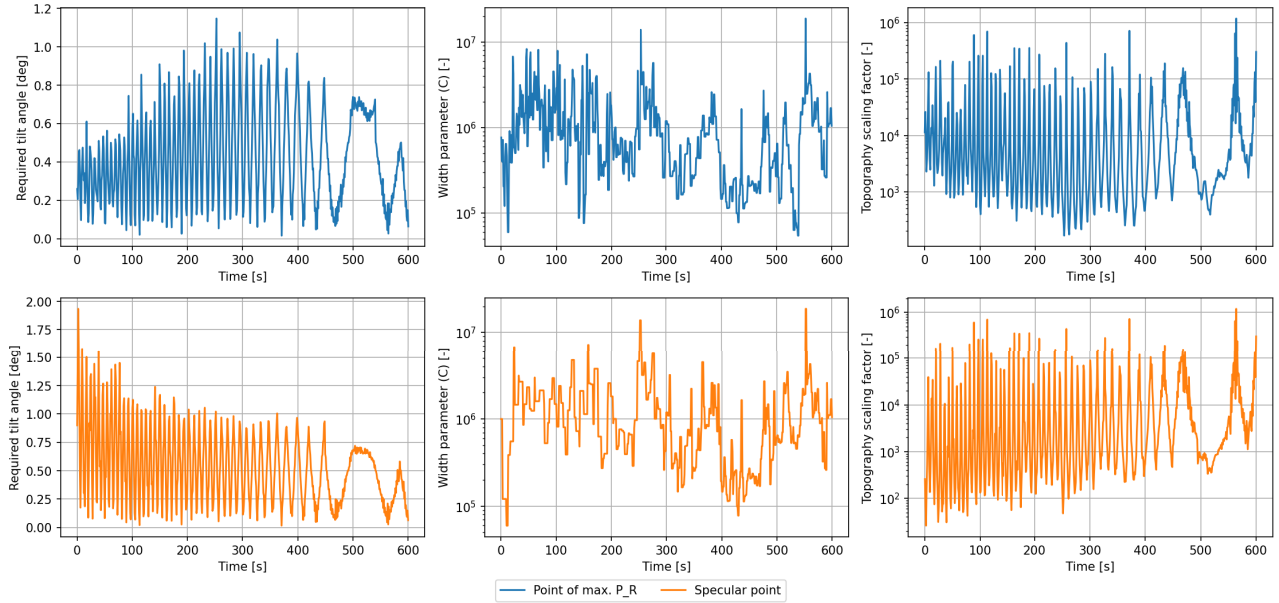### Periodicity and Topography Effects

Figure E.73: Model results 'Periodicity and Topography Effects' for BSR-2.2 (using 4 pixel/degree resolution), own work

Model results for BSR-3.1 (at 4 pixel/degree resolution)
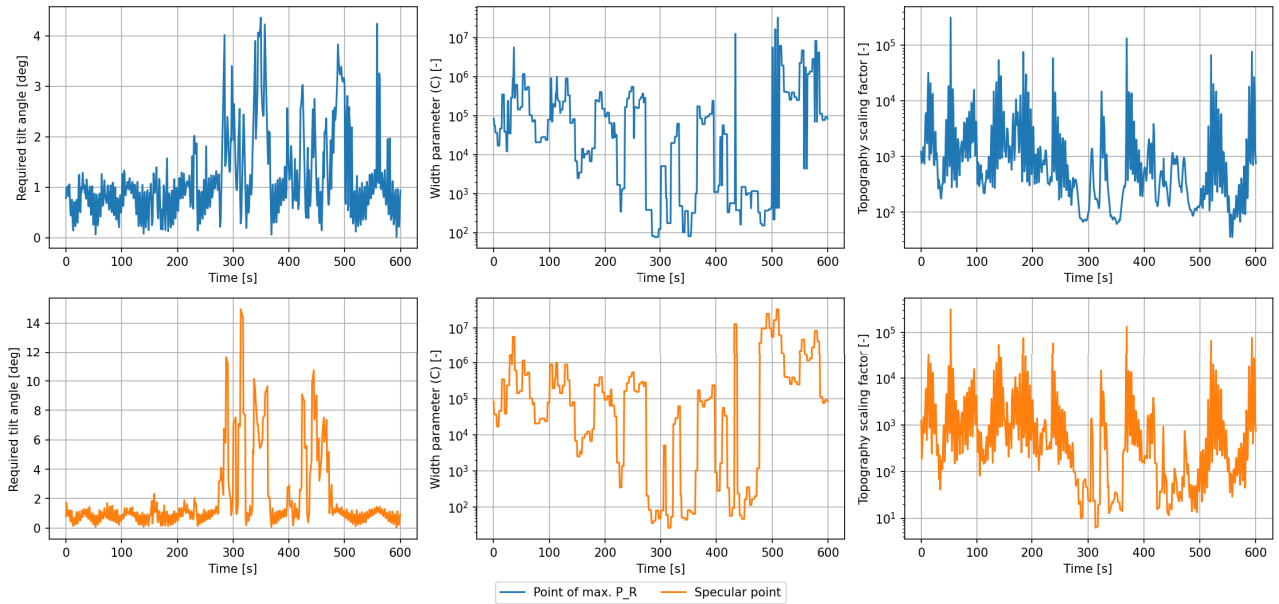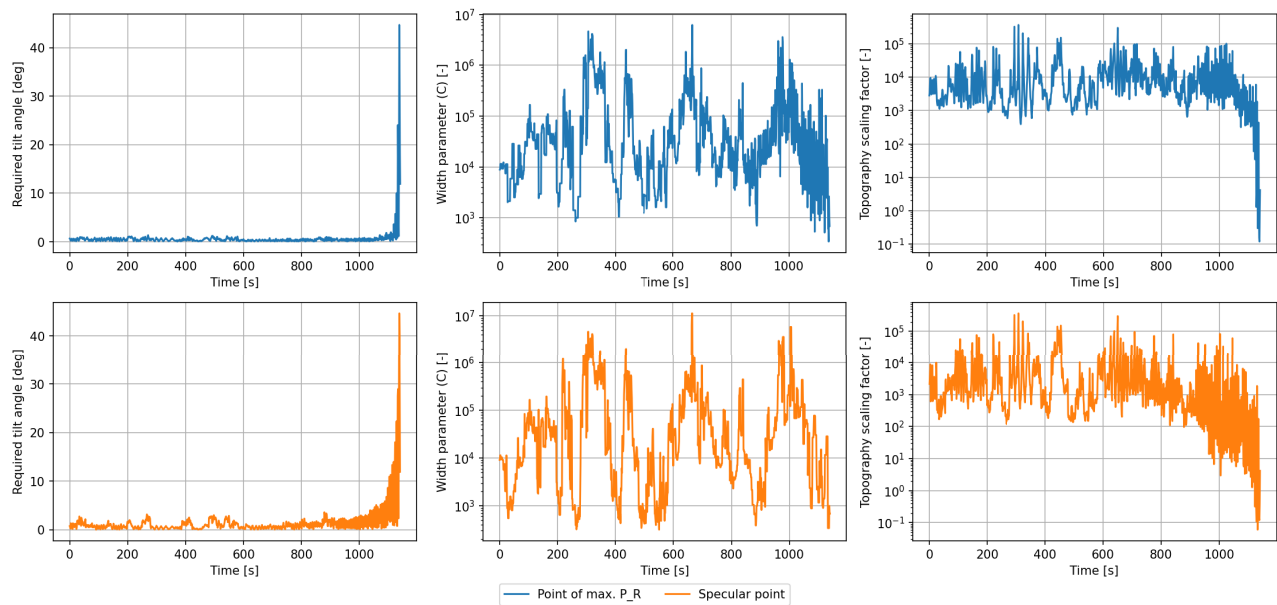### Periodicity and Topography Effects

Figure E.74: Model results 'Periodicity and Topography Effects' for BSR-3.1 (using 4 pixel/degree resolution), own work

Model results for BSR-4.1 (at 4 pixel/degree resolution)
Periodicity and Topography Effects

Figure E.75: Model results 'Periodicity and Topography Effects' for BSR-4.1 (using 4 pixel/degree resolution), own work